ROYAUME DU MAROC
Université Mohammed V - RABAT -
جامعة محمد الخامس – الرباط –
Faculté des sciences
كلية العلوم
CENTRE D'ETUDES DOCTORALES - SCIENCES ET TECHNOLOGIES

N° of order: 3674

THESIS

In order to obtain: ***Doctorate degree***

Research structure: *Laboratory of Condensed Matter and Interdisciplinary Sciences Labeled Research Unit - National Center for Scientific and Technical Research, (LaMCScI-URL-CNRST) -Faculty of Sciences of Rabat*

Discipline: *Physics*

Specialty : *Materials science*

Presented and defended on 10/09/2022 by:

Smahane Dahbi

A DFT study of structural, electronic, optical and transport properties of Lead-free simple, inverse and double perovskite compounds for photovoltaic, photocatalytic and thermoelectric applications

JURY

Abdallah EL KENZ	PES, Mohammed V University, Faculty of sciences in Rabat.	President
Lahoucine BAHMAD	PES, Mohammed V University, Faculty of sciences in Rabat.	Reviewer / Examiner
El Mehdi SALMANI	PH, Mohammed V University, Faculty of sciences in Rabat.	Reviewer / Examiner
Hassane ROUKHE	PH, Superior Institute of Audiovisual and Cinema Professions, in Rabat.	Reviewer / Examiner
Abdelilah BENYOUSSEF	Expert, PES Hassan II academy of sciences and techniques in Rabat.	Examiner
Omar EL BOUNAGUI	PH, Mohammed V University, Faculty of sciences in Rabat.	Thesis Co-director
Najim TAHIRI	PA, Mohammed V University, Faculty of sciences in Rabat.	Thesis Co-director
Hamid EZ-ZAHRAOUY	PES, Mohammed V University, Faculty of sciences in Rabat.	Thesis Director

Academic year: 2021/2022

✉ Faculté des Sciences, avenue Ibn Battouta, BP. 1014 RP, Rabat –Maroc
☎ 00212(0) 5 37 77 18 76 🖷 00212(0) 5 37 77 42 61 ; http://www.um5a.ac.ma

Dedication

I am dedicating this thesis to my family and especially to my parents. I thank my beloved mom from the bottom of my heart, no words can express how I feel towards her, she taught me to be patient and to never give up. My father who gave me his strength and who always trusted my choices and supported me, nothing would have been possible without my dear mom and dad. A big thank to all my sisters, brothers, brothers in law, nephew, and nieces who were always there for me.

A thesis represents a lot of work and investment and I would like to thank all those who have contributed and who have supported me during these four years. It was a strong scientific and personal experience in which I met a lot of kind, helpful and enthusiastic people.

Thanks to everyone (family, professors and friends) who have given yourselves that I have been able to go this far.

DAHBI Smahane

Acknowledgments

First and foremost, praises and prayers to Allah, the almighty, for guiding me when I bewilder in the darkness of ignorance and enlighten my ways, for giving me the strength, as well as the daring to overcome all difficulties throughout my thesis work, the chance and endurance to complete my thesis.

This work was carried out at the Laboratory of Condensed Matter and Interdisciplinary Sciences (LaMCScI) at Mohammed V University, Faculty of Sciences Rabat under the supervision of Mister Professor **Hamid EZ-ZAHRAOUY**. I would like to thank him for entrusting me with the thesis subject and for leading me to achieve it. I express to him my gratitude for his availability, for the fruitful and interesting discussions we were able to have and also for providing me with the knowledge and material used during my research. I would particularly like to thank him for the freedom of action he has given me at every stage.

My sincere thanks to Mister **Najim TAHIRI** Professor at Mohammed V University, Faculty of Sciences Rabat for his patience, advices, great help as well as a shoulder to lean on during the hours of need, for his availability and scientific help. I thank him from my heart for guiding and encouraging me. I hope that I have been able to prove that I am deserving his trust and that this work is nally fullling his expectations.

My deepest thanks and gratitude go to Mister Professor **Omar El BOUNAGUI,** from Mohammed V University, Faculty of Sciences Rabat for his seriousness, kindness and good advice useful critiques to value my thesis, for his availability each time I need help.

I am grateful to the thesis committee for examining my work and providing informative and relevant feedbacks in the completion of this modest project. It is a tremendous honor for me that they consented to review this work. My sincere thanks are first addressed to Mister Professor **Abdallah EL KENZ** from Mohammed V University, Faculty of Sciences Rabat for the interest he has shown for this work and by giving us the honor of being president of the jury members of this thesis.

I would also like to offer my thanks to Mister Professor **Lahoucine BAHMAD** from Mohammed V University, Faculty of Sciences Rabat, for reporting and reviewing this PhD thesis dissertation.

My sincere thanks also go to Mister Professor **El Mehdi SALMANI** from Mohammed V University, Faculty of Sciences Rabat, for reporting and reviewing this PhD thesis dissertation.

I would like also to extend my thanks to Mister Professor **Hassane ROUKHE** from Superior Institute of Audiovisual and Cinema Professions, Rabat for having agreed to examine and report this thesis.

I would like also to show my greatest appreciation to Mister Professor **Abdelilah BENYOUSSEF** expert from Hassan II Academy of sciences and techniques of Rabat, for having agreed to examine and report this thesis.

Abstract

In the framework of this Ph.D. thesis, first-principle calculations based on the density functional theory is employed to reveal and fully understand structures and physical properties of simple, double and inverse perovskites nanomaterials. In this context, three different applications are considered: absorbing materials for photovoltaic application and semiconductor for photocatalytic water splitting application for hydrogen production. The first part of this thesis deals with simulating structural, electronic and optical properties of non-toxic zirconate perovskites $AZrO_3$ (A = Ca, Ba and Sr) doped with chalcogens impurities. And it was found that the wide forbidden band decreases with the increase of chalcogens' concentration, especially for Tellurium and Selenium doped $AZrO_3$. In the second part, the effects of Sulfur, Selenium, or Tellurium doped $CaZrO_3$, $CaHfO_3$ and $SrHfO_3$ on the electronic, optical and photocatalytic properties and structures stability with the presence of the intrinsic F-center defect in oxide materials were carried out. The findings show that there is a huge improvement of the absorption coefficient along the visible spectrum when chalcogens' impurities meet an F-center defect in understudy compounds due to the enhancement of carrier concentrations. The third part investigates the spin orbit coupling effects on physical properties of the non-toxic Lead-free vacancy ordered double perovskites halides X_2TeY_6 (X = Cs, Rb, and Y = I, Br, Cl) using first-principles calculations. The results confirm that the inclusion of spin orbit coupling is crucial for the correct characterization of the electronic properties of the X_2TeY_6 compound. The final part projects a detailed information on physical properties of Ca_3PN, Ca_3AsN, Ca_3SbN and Ca_3BiN inverse perovskites.

Keywords: Non-silicon-based compounds, Solar cells, DFT, Perovskites compounds, Absorption coefficient, Ab-initio simulations, Stability, Forbidden band gap.

Résumé

Dans le cadre de cette thèse, les calculs de premier principe basés sur la théorie de la fonctionnelle de la densité sont utilisés pour révéler et comprendre les structures et les propriétés physiques des nanomatériaux pérovskites simples, doubles et inverses. Dans ce contexte, trois applications différentes sont envisagées : les matériaux absorbants pour l'application photovoltaïque et les semi-conducteurs pour les applications photocatalyse pour la séparation de l'eau pour la production d'hydrogène et la thermoélectricité. La première partie de cette thèse porte sur la simulation des propriétés structurales, électroniques et optiques des pérovskites zirconates $AZrO_3$ (A = Ca, Ba et Sr) dopées par les éléments de chalcogènes. Et il a été constaté que la large bande interdite diminue avec l'augmentation de la concentration des chalcogènes, en particulier pour l'$AZrO_3$ dopé par tellure ou par sélénium. Dans la deuxième partie, les effets des $CaZrO_3$, $CaHfO_3$ et $SrHfO_3$ dopés par le soufre, sélénium ou tellure sur les propriétés électroniques, optiques et photocatalyse et la stabilité de ces structures avec la présence d'une lacune d'oxygène dans les matériaux oxydes ont été étudiés. Les résultats montrent qu'il y a une énorme amélioration du coefficient d'absorption le long du spectre visible lorsque les impuretés des chalcogènes rencontrent les lacunes d'oxygène grâce à l'amélioration des concentrations de porteurs de charges (trou et/ou électron). Dans la troisième partie de cette thèse, nous avons étudié les effets du spin-orbite sur les propriétés physiques des doubles halogénures pérovskites type X_2TeY_6 (X = Cs, Rb et Y = I, Br, Cl). Les résultats confirment que l'inclusion du spin-orbite est cruciale pour la caractérisation correcte des propriétés électroniques du composé X_2TeY_6. La dernière partie projette une information détaillée sur les propriétés physiques des pérovskites inverses Ca_3PN, Ca_3AsN, Ca_3SbN et Ca_3BiN.

Mots clés : Composés sans silicium, Cellules solaires, DFT, Composés pérovskites, Coefficient d'absorption, Simulations ab-initio, Stabilité, Bande interdite.

Résumé détaillé

Les composés pérovskites simples, doubles, triples et inverses ont récemment suscité un intérêt considérable de la part des équipes de recherche, car ils peuvent conduire à des développements substantiels de dispositifs photovoltaïques industriels efficaces et peu coûteux pour répondre à la croissance socio-économique. De plus, l'application des composés pérovskites en tant que couches absorbant de la lumière dans les cellules solaires conduit à une efficacité impressionnante de plus de 25,5 % dans les conditions de laboratoire. Cependant, pour les applications industrielles, les problèmes fondamentaux concernant leur large valeur de bande interdite, leur faible absorption le long du spectre visible et la toxicité du Plomb doivent être résolus.

Dans le cadre de cette thèse, les calculs de premier principe basés sur la théorie de la fonctionnelle de la densité sont utilisés pour révéler et comprendre les structures et les propriétés physiques des matériaux pérovskites simples, doubles et inverses sans Plomb. Dans ce contexte, trois applications différentes sont envisagées : les matériaux absorbants pour l'application photovoltaïque et les semi-conducteurs pour l'application photocatalyse pour la séparation de l'eau pour la production d'hydrogène. La première partie de cette thèse porte sur la simulation des propriétés structurales, électroniques et optiques des pérovskites zirconates $AZrO_3$ (A = Ca, Ba et Sr) dopées par les éléments de chalcogènes (soufre (S), sélénium (Se) ou tellure (Te). Et il a été constaté qu'avec l'augmentation de la concentration des chalcogènes, la large bande interdite est diminué en particulier pour l'$AZrO_3$ dopé par Te ou par sélénium Se.

Dans la deuxième partie, les effets de dopage du $CaZrO_3$, $CaHfO_3$ et $SrHfO_3$ par le soufre, sélénium ou tellure sur les propriétés électroniques, optiques, photocatalyse et la stabilité de ces structures avec la présence d'une lacune d'oxygène ont été étudiés. Les résultats montrent qu'il y a une énorme amélioration du coefficient d'absorption le long du spectre visible lorsque les impuretés des chalcogènes rencontrent les lacunes d'oxygène grâce à l'amélioration des concentrations de porteurs de charges (trou et/ou électron) dans ces matériaux ce qui est tout à fait remarquable pour les deux technologies étudiées. Et tous les structures étudier sont thermodynamiquement stable et peuvent être facilement synthétisé.

Dans la troisième partie de cette thèse, nous avons étudié les effets du couplage spin-orbite sur les propriétés physiques des doubles pérovskites type X_2TeY_6 (X = Cs, Rb et Y = I, Br, Cl).

Les résultats confirment que l'inclusion du couplage spin-orbite est cruciale pour la caractérisation correcte des propriétés électroniques du composé X_2TeY_6.

La dernière partie projette une information détaillée sur les propriétés structurales, élastiques, électroniques, transport et optiques des pérovskites inverses Ca_3PN, Ca_3AsN, Ca_3SbN et Ca_3BiN. Et nous avons constaté que grâce à ses propriétés exceptionnelles, Ca_3PN, Ca_3AsN, Ca_3SbN et Ca_3BiN peuvent être utilisé comme des nouvelles couches absorbantes dans les cellules solaires son Silicium.

ملخص

مؤخرًا جذبت مركبات البيروفسكايت الفردية والمزدوجة والثلاثية والمعكوسة اهتمامًا كبيرًا من فرق البحث العلمي، حيث يمكن أن تؤدي إلى تطورات كبيرة في الأجهزة الكهروضوئية الصناعية الفعالة وغير المكلفة لتلبية النمو الاجتماعي والاقتصادي. علاوة على ذلك، فإن استخدام مركبات البيروفسكايت كطبقات ماصة للضوء في الخلايا الشمسية يؤدي إلى كفاءة مبهرة تزيد عن 25.5٪ في ظروف المختبر. ومع ذلك، بالنسبة للتطبيقات الصناعية، يجب معالجة القضايا الأساسية المتعلقة بقيمة فجوة النطاق الواسعة، والامتصاص المنخفض على طول الطيف المرئي، وسمية عنصر الرصاص. في هذه الأطروحة، استخدمت حسابات المبدأ الأول القائمة على نظرية الكثافة الوظيفية لكشف وفهم الهياكل والخصائص الفيزيائية للمواد النانوية المفردة والمزدوجة والمعكوسة من البيروفسكايت. في هذا السياق، تم أخذ ثلاثة تطبيقات مختلفة في الاعتبار: المواد الماصة للتطبيقات الكهروضوئية وأشباه الموصلات للتطبيق التحفيزي الضوئي لفصل الماء لإنتاج الهيدروجين. يتعامل الجزء الأول من هذه الأطروحة مع محاكاة الخصائص التركيبية والإلكترونية والبصرية لـ $AZrO_3$ زيركونات البيروفسكايت (A= Ca, Ba, Sr) مخدر بعناصر الكالكوجين (S, Se, Te) . وقد وجد أن فجوة الحزمة العريضة تتناقص مع زيادة تركيز الكالكوجين، خاصة بالنسبة ل $AZrO_3$ المخدر بلتيلوريوم أو السيلينيوم. وفي الجزء الثاني، تمت دراسة تأثيرات الكبريت والسيلينيوم أو التيلوريوم كمخدر ل CaZrO3 و $CaHfO_3$ و $SrHfO_3$ على الخواص الإلكترونية والبصرية والتحفيزية الضوئية واستقرار هذه الهياكل مع وجود خلل نقص أكسجين في مواد الأكسيد. أظهرت النتائج أن هناك تحسنًا كبيرًا في معامل الامتصاص على طول الطيف المرئي عند تواجه شوائب الكالكوجين وخلل نقص الأكسجين بسبب تعزيز تركيزات حاملات الشحن. في الجزء الثالث من هذه الأطروحة، درسنا تأثيرات المدار الدوراني على الخواص الفيزيائية لهاليدات البيروفسكايت المزدوجة من النوع X_2TeY_6 (X= Cs, Rb ; Y= I, Br, Cl). تؤكد النتائج أن إدراج المدار الدوراني أمر بالغ الأهمية للتوصيف الصحيح للخصائص الإلكترونية المركبات X_2TeY_6. يعرض الجزء الأخير معلومات مفصلة عن الخصائص الفيزيائية للبيروفسكايت المعكوس Ca_3PN و Ca_3AsN و Ca_3SbN و Ca_3BiN.

الكلمات المفتاحية: المركبات الخالية من السيليكون، الخلايا الشمسية، DFT، مركبات البيروفسكايت، معامل الامتصاص، حسابات Ab-initio ، الاستقرار.

List of publications

1. **S. Dahbi**, N. Tahiri, O. El Bounagui and H. Ez-Zahraouy, The new eco-friendly lead-free zirconate perovskites doped with chalcogens for solar cells: Ab initio calculations, Optical Materials 109 (2020) 110442.

2. **S. Dahbi**, N. Tahiri, O. El Bounagui, H. Ez-Zahraouy, Calcium hafnate perovskite from an insulator to a semiconductor for photovoltaic and photocatalytic hydrogen production from water splitting applications, Superlattices and Microstructures 160 (2021) 107058.

3. N. Tahiri, **S. Dahbi**, I. Dani, O. El Bounagui and H. Ez-Zahraouy, Magnetic, magnetocaloric and thermoelectric investigations of perovskite $LaFeO_3$ compound: First principles and Monte Carlo calculations, Computational and theoretical chemistry 1204 (2021) 113421.

4. N. Tahiri, **S. Dahbi**, I. Dani, O. El Bounagui and H. Ez-Zahraouy, Magnetocaloric and thermoelectric properties of the perovskite $LaMnO_3$ material: A DFT study and Monte Carlo thechnique, Phase Transitions 94 (2021) 826-834.

5. **S. Dahbi**, N. Tahiri, O. El Bounagui and H. Ez-Zahraouy, Electronic, optical, and thermoelectric properties of perovskites $BaTiO_3$ compound under the effect of compressive strain, chemical Physics 544 (2021) 111105.

6. **S. Dahbi**, N. Tahiri, O. El Bounagui, H. Ez-Zahraouy, Chalcogens' impurities and a single F-center in perovskite $SrHfO_3$ compound: Ab initio calculations, Materials Science in Semiconductor Processing 138 (2022) 106271.

7. **S. Dahbi**, N. Tahiri, O. El Bounagui and H. Ez-Zahraouy, Importance of spin-orbit coupling on photovoltaic properties of Pb-free vacancy ordered double perovskites halides X_2TeY_6 (X = Cs, Rb, and Y = I, Br, Cl): first-principles calculations, International Journal of Energy Research 46 (2022) 8433-8442.

8. B. Mouhib, **S. Dahbi**, A. Douayar, N. Tahiri, O. El Bounagui and H. Ez-Zahraouy, Theoritical investigations of electronic structure and optical properties of S, Se or Te doped perovskite $ATiO_3$ (A = Ca, Ba, and Sr) materials for eco-friendly solar cells. Micro and Nanostructures 163 March (2022) 107124.

9. B. Akenoun, **S. Dahbi**, N. Tahiri, O. El Bounagui, H. Ez-Zahraouy, and A. Benyoussef, The effect of chalcogens-doped with dilation strain on the electronic, optic, and thermoelectric properties of $BaSnO_3$ perovskite, Journal of the Korean Ceramic Society. https://doi.org/10.1007/s43207-022-00212-1.

10. **S. Dahbi,** N. Tahiri, O. El Bounagui and H. Ez-Zahraouy, Earth-Abundant Nontoxic ternary calcium nitrides inverse perovskites for single-junction solar cells; ab-initio simulations, Materials Science in Semiconductor Processing 150 (2022) 106959.

11. **S. Dahbi,** N. Tahiri, O. El Bounagui, H. Ez-Zahraouy, and A. Benyoussef, Effects of oxygen group elements on thermodynamic stability, electronic structures and optical properties of the pure and pressed $BaTiO_3$ perovskite, Computational Condensed Matter 32 (2022) e00728.

12. **S. Dahbi,** N. Tahiri, O. El Bounagui, H. Ez-Zahraouy, and O. Mounkachi, First-principles calculations of an oxygen vacancy and chalcogens impurities in Lead-Free calcium zirconate perovskite for non-toxic solar cells (under review).

13. A. El Badraoui, **S. Dahbi**, N. Tahiri, O. El Bounagui, and H. Ez-Zahraouy, Electronic structure, optical, and thermoelectric properties of $AgTaO_{3-X}Y_X$ (Y = S, Se, Te) perovskite for photovoltaic applications: A DFT study (submitted).

14. A. El Badraoui, **S. Dahbi**, N. Tahiri, O. El Bounagui, and H. Ez-Zahraouy, A DFT study on electronic structure and optical properties of V-doped, N-doped and V+N co-doped $CaZrO_3$: photovoltaic applications (submitted).

List of communications

1. Poster communication at the 2nd annual Inter-lab-LaMCScI-Meeting, December -11&13, 2019, Rabat, Morocco.

2. Poster communication at the 7th International Renewable and Sustainable Energy Conference, November -27-30, 2019, Morocco.

3. Oral communication at the 1st Multidisciplinary Doctoral Days, January -29&30, 2022, kenitra, Morocco.

4. Oral communication at the 1st Multidisciplinary Doctoral Days, July -18-22, 2022, Rabat, Morocco.

Table of Content

Liste of Figures

Liste of Tables

List of abbreviations

Pb : Lead	**CZO :** $CaZrO_3$
BZO : $BaZrO_3$	**SZO :** $SrZrO_3$
CHO : $CaHfO_3$	**SHO :** $SrHfO_3$
CTI : Cs_2TeI_6	**CTB :** Cs_2TeBr_6
CTC : Cs_2TeCl_6	**RTI :** Rb_2TeI_6
RTB : Rb_2TeBr_6	**RTC :** Rb_2TeCl_6
CHI : Cs_2HfI_6	**CPN :** Ca_3PN
CAN : Ca_3AsN	**CSN :** Ca_3SbN
CBN : Ca_3BiN	**λ :** Wavelength
UV : UltraViolet	**Vis :** Visible
IR : InfraRed	***k*** **:** wave vector
S : Sulfur	**Se :** Selenium
Te : Tellurium	**PV :** PhotoVoltaic
HH : Half Half	**VB :** Valence Band
CB : Conduction Band	**DPs :** Double perovskite
BO : Born-Oppenheimer	**HF :** Hartree-Fock
Eg : Forbidden band energy	**CdTe :** Cadmium Telluride
CIS : Copper Indium Selenide	**PSCs :** Perovskite solar cells
DSSCs : Dye-sensitized solar cells	**CZTS :** Copper Zinc Tin Sulfide

PCE : Power Conversion Efficiency	**HOMO :** Highest Occupied Molecular Orbital
CIGS : Copper, Indium Gallium dieSeline	**DFT :** Density Functional Theory
B : Bulk modulus	**G :** Shear modulus
B' : Pressure derivative	**E :** Young's modulus
Θ_D : Debye temperature	**v_m :** Average wave velocity
h : Plank's constant	**B/G :** Pugh's ratio
u : Poisson's ratio	**E :** electric field
a : Lattice parameter	**m^* :** Effective mass
D : Recombination ratio	**TE :** Thermoelectric
S : Seebeck coefficient	**κ :** Thermal conductivity
σ : Eelectrical conductivity	**Ov :** Oxygen Vacancy
ΔH_f: Enthalpy of formation	**HPs :** Halide Perovskites
TM : Melting Temperature	**KB :** Boltzmann's constant
C_{ij} : Elastic stiffness constants	**A :** Elastic anisotropy factor
R_{MT} : Muffin-Tin radius	**SOC :** Spin-Orbit Coupling
TDOS : Total Densities Of States	**VBM :** Valence Band Maxima
v_t : Transverse elastic wave velocities	**v_l :** Longitudinal elastic wave velocities
CBM : Conduction Band Minima	**YS-PBE0 :** Yukawa screened PBE0l
HTT : High-Temperature Technology	**TBC :** Thermal Barrier Coatings
LDA : Local Density Approximation	**GGA :** Generalized gradient approximation

DHPs : Double Halide Perovskites	**LUMO :** Lowest Unoccupied Molecular orbital
TB-mBJ : modified Tran-Blaha Becke-Johson potential	**NASA :** National Aeronautics and Space Administration
MOSFETs : Metal-Oxide-Semiconductor Field-Effect Transistors	**Meta-GGA :** Tao et al-Generalized gradient approximation
WC-GGA : Wu-Cohen- Generalized gradient approximation	**EV-GGA :** Engel and Vosko- Generalized gradient approximation
PW-GGA : Perdew and Wang- Generalized gradient approximation	**PBE-GGA :** Perdew, Burke and Ernzerhof- Generalized gradient approximation
S@OI: The substitution of Sulfur at oxygen sites by a percentage of 4.1667%	**S@OII:** The substitution of oxygen by Sulfur with a percentage of 8.3333%
S@OIII: The substitution of oxygen by Sulfur with a percentage of 12.5000%	**S@OI+Ov:** The substitution of oxygen by Sulfur with a percentage of 4.1667% with an oxygen vacancy
S@OII+Ov: The substitution of oxygen by Sulfur with a percentage of 8.3333% with an oxygen vacancy	**S@OIII+Ov:** The substitution of oxygen by Sulfur with a percentage of 12.5000% with an oxygen vacancy

General introduction

The need of heat, power and fuel continues to increase day by day. However, the conventional energies systems such as coal, oil, natural gas and nuclear power, are the origin of the emission of greenhouse gases levels in Earth's atmosphere, namely carbon dioxide, methane and nitrous oxide, which are directly responsible for the deterioration of the Ozone layer, climate change issues and global warming. Consequently, the emissions of greenhouse gas emissions as the principal culprit of global warming by creating a greenhouse effect in the Earth's atmosphere represent a severe menace to mankind's civilization.

Under the actual global warming circumstances and according to the surveys reported on previously, the world's CO_2 emissions could rise to 43.3 Gt by 2035 [1]. Consequently, this leads to a considerable and negative impact on the surrounding environment including sea levels rising by 18−59 cm and an increased intensity of tropical storms [2]. Additionally, within the scope of the latest worldbank [3] survey, it has been reported that the consequences of climate change on maritime cities will occur in the near future. Besides, the emission of greenhouse gas, we have a limited supply of fossil fuels on Earth. Consequently, there will be no fossil fuel left within 2110. Therefore, to rescue the human civilization, it is contemplated to replace the non-renewable energies sources by durable, clean, environmental-friendly, sustainable and renewable energies sources, which is potentially quite cheaper than the existing non-renewable energies sources on the Earth which are currently and in the coming years major research subjects.

The photovoltaic technology, whereby energy from the sun is converted into electricity, offers the possibility of a clean source of electricity without the pollution concerns of gas or coal-fired power stations, or the safety concerns associated with nuclear energy. Thus, an important research area is the development of new materials for solar cells. Therefore, the development of industry and the rise in scientific research has led to the birth of the disciplines of nanoscience and nanotechnology; this caused a development of nano-material manufacturing and their various applications. The study of nanoscale matter is the subject of several works over the past two decades, due to the technological advances in the development, characterization and low-price of nanomaterials.

Perovskite solar cells (PSCs) nanomaterials are the most "talked-about" absorbing materials for solar cells because it is a promising technology that provides a simple manufacturing and a high-power conversion efficiency with low production costs, these PSCs have been improved considerably in a shirt time. The rapid growth in solar cell technology has made the PSCs as a shining star in the photovoltaics industry. Furthermore, the PSCs technology also holds a huge potential for better engineering, with a boom in power conversion efficiency (PCE) from 3.5% in 2009 to 25.5% today going over the maximum efficiency achieved in traditional mono- and poly-crystalline silicon cells [4], and are expected to reach a breakthrough cell PCE of over 30% of PCE within the year. The PSCs technology is estimated to grow at 34% between 2020 to 2027. Although this their high PCE, factors as instabilities as well as the use of toxic elements especially Lead (Pb) hinder their commercialization in the cells market. This is the major factor that the PSCs technology is still in development stage and has been extremely studies since it discovered and it tops scientific breakthroughs. Accordingly, the Pb free perovskite solar cells with high PCE are needed. Thus, in this thesis the Lead-free simple, double and inverse perovskites were studied, and this thesis is outlined as follows;

Chapter I, gives a succinct overview of the state of the art of the current energy consumption, photovoltaic effect, solar panel generations perovskites materials,…, to emphasize the main goals of our research.

Chapter II, describes theoretical method, and softwares used to investigate structural, electronic, optical, and thermoelectric poetries used in this thesis.

Chapter III, delas the effects of chalcogens-doped zirconate oxides perovskites $AZrO_3$ (A = Ca, Ba and Sr) on electronic and optical properties using Density Functional Theory coupled to Full-Potential Linearized Enhanced Plane Wave within the WIEN2K software, and Local Density Approximation added to modified Becke and Johnson potential of Trans and Blaha as correlation.

Chapter IV, sheds new light on calcium zirconate, calcium halfnate, and strontium halfnate perovskites, in this part we got the challenge to enable to the understudy insulators to be applied as semiconductors for photovoltaic and photocatalytic hydrogen production from water splitting devices by the substitution of oxygen atoms by chalcogens impurities (Sulfur, Selenium

and Tellurium) with different concentrations up to 12.5%, taking into account a neutral intrinsic defect in oxide materials which is the F-center defect.

The objective of **Chapiter V** of this thesis is to investigate the role of spin orbit coupling on physical properties of the ordered-vacancy double halides perovskites X_2TeY_6 (X = Cs, Rb and Y = I, Br, Cl) due to the presence of heavy elements. Due to the obtained results, our study will improve knowledge and serve as a base of future studies X_2TeY_6 compounds.

Projection of a detailed information on structural thermodynamic and mechanical stabilities, elastic properties, electronic structure, chemical bonding nature, the charge carrier effective masses, recombination ratio, thermopower, electrical and heat conductivities, absorption coefficient, reflectivity and transmittance of non-silicon based inverse perovskites Ca_3MN (M= P, As, Sb and Bi) using first principals calculations are drawn in **Chapiter VI.**

All the chapters are connected with the basic motivation of sustainable materials for a single junction PSCs. For details of the methods and discussion of results, the readers are encouraged to read the original papers and manuscripts attached at the top of the thesis.

I. 1. Introduction

Throughout history and starting from the discovery of fire, man has developed and expanded his ability to use and harvest energy in all its forms. Thereafter, the global energy demand and consumption are increasing exponentially due to many socioeconomic factors such as; human population and economic growth, urbanization, industrialization, and technological development, causing more energy needs to fulfill this growth. Therefore, this necessary demand is expected to rise 48% in the next 20 years [5]. As shown in the **Figure I.1** [6], the mentioned factors lead to a continuous expansion of the global world energy demand and production.

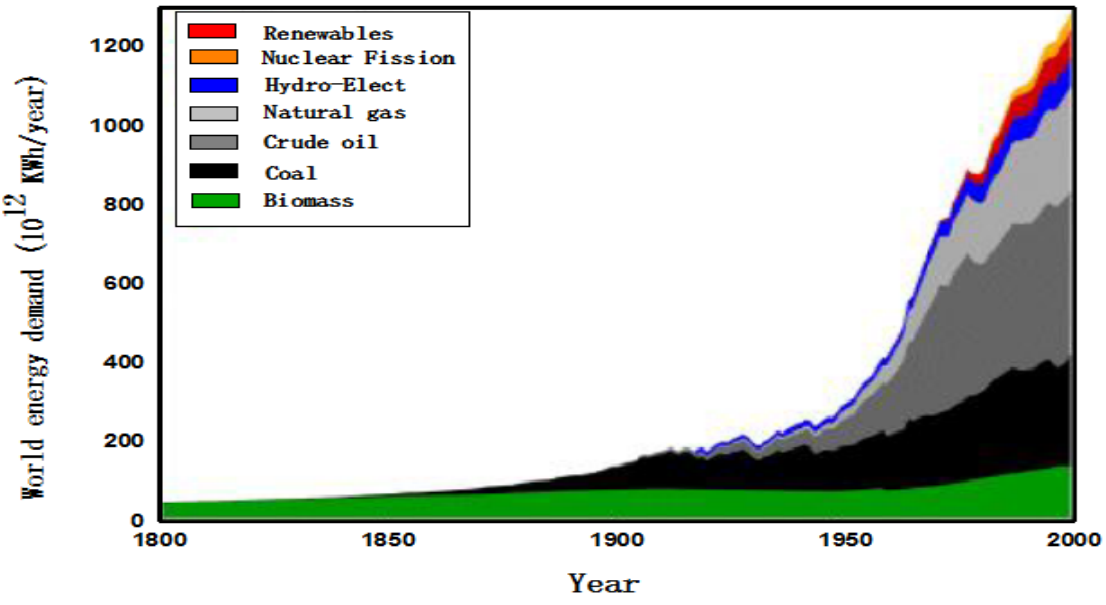

Figure I.1: The global world energy consumption over years from 1800 to 2000s

.

Since 1880s, the humanity's increased use of fossil fuels caused the increasing of the heat-trapping greenhouse gas (carbon dioxide, methane, nitrous oxide,…) levels in Earth's atmosphere which so-called global warming and climate change issues [7-9]. According to National Aeronautics and Space Administration's (NASA) temperature record, the past eight years are the warmest years since modern recordkeeping began in 1880.

Continuing the Earth's long-term warming trend, NASA uses the period from 1951-1980 as a baseline to see how global temperature changes over time, and it was found that the global temperature in 2021 was 1.5 degrees Fahrenheit above NASA's baseline period (See **Figure I.2)** [9,10] .

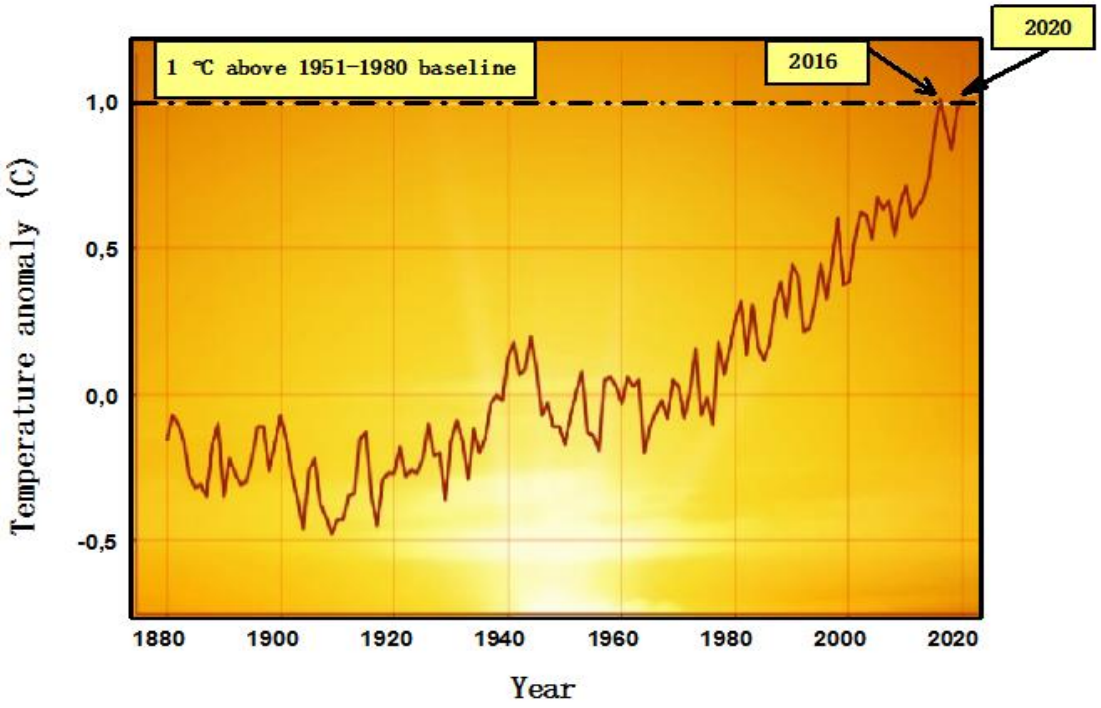

Figure I.2: The temperature anomaly (°C) over years from 1880 to 2021s

At the current energy consumption rate, the extensive use of limited availability of the exhaustible primary energy resources, the global warming, as well as the air pollution reflect the urgency to develop new strategies to effectively utilize sustainable, inexhaustible and clean energies (Solar energy, Wind energy,...). Scientists, researchers and industries have collaborated over the years to find an answer to the constant demand of energy to sustain the reduction of the environmental pollution and future growing of the energy consumption is getting more and more important and attractive.

I. 2. Solar energy

The most renewable, sustainable and environment-friendly energy source known to humankind is solar energy. Therefore, solar energy is the long-term and cheap replacement of electricity produced from crude oil [11], which could as well generate a substantial amount of renewable and green energies. Every single year, around 1 Zetta-Watt-hour of energy falls onto the Earth's

surface [12,13]. By using 10% of efficient solar panels, the solar energy fulfills more than double energy humanity need projected in 2050s.

I. 2. 1. The Sun and its irradiance spectrum

The sun is a dense and glowing sphere (1,392,000 Km, 2×10^{30} Kg are the diameter and mass respectively) which is made up of 70% of hydrogen, 28% of helium, 1.5% of carbon, nitrogen and oxygen while many other hot gases such as neon, iron, silicon, magnesium and sulfur make up 0.5% [14], its surface temperature is 5772 Kelvin (K) [15].

The sun's radiant power (or solar irradiation) received by Earth's outside atmosphere is about 1353 W/m^2 (at normal incidence the solar irradiation is constant) [16]. **Figure I. 3**. shows that the solar irradiation undergoes attenuation after passing through the atmosphere approximately 30% is absorbed and/or reflected by different atmosphere gas, aerosols, dust and clouds scattering before reaching the earth's surface.

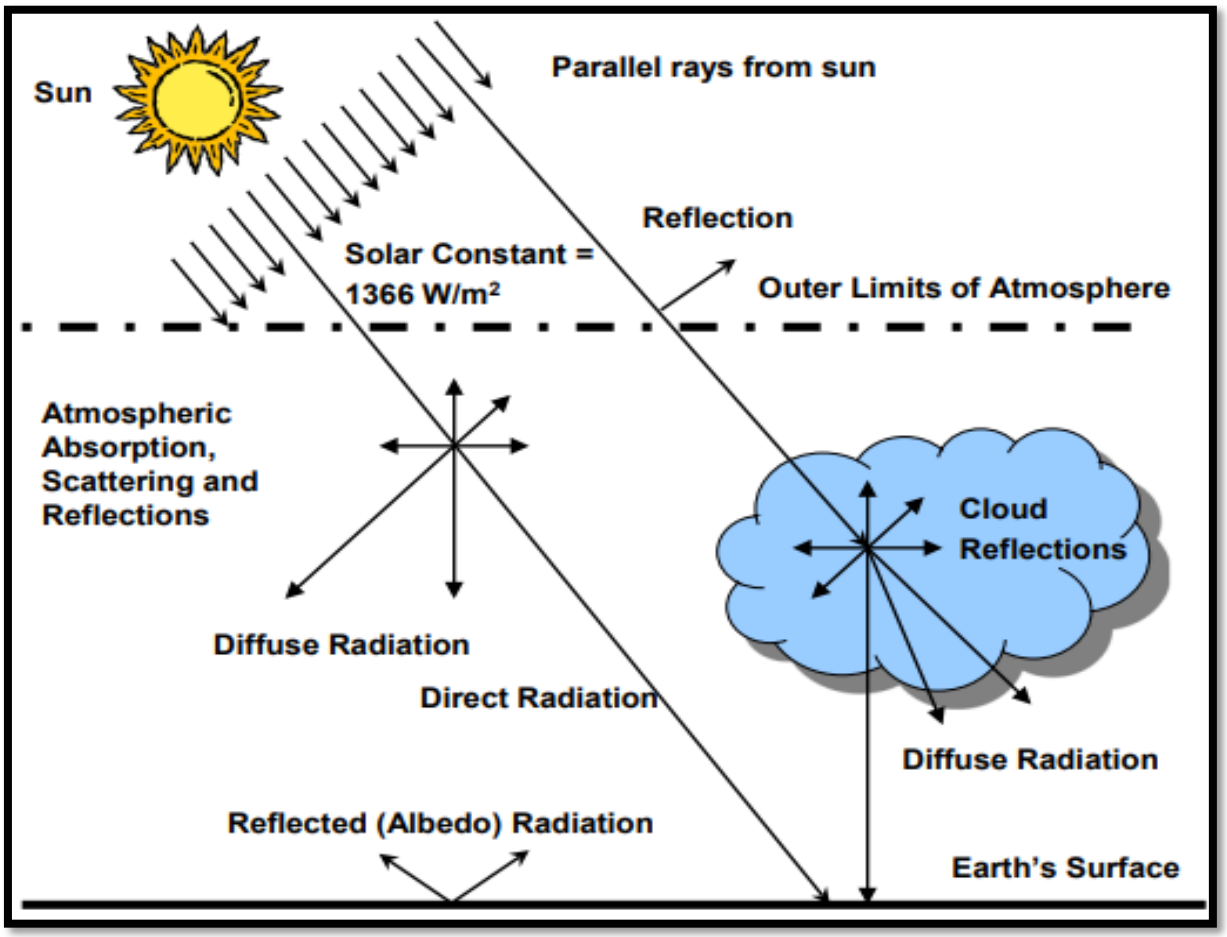

Figure I.3: Total global solar radiation: direct and diffuse radiations

Therefore, the typical peak value is 1000 W/m^2 on a terrestrial surface facing the sun on a clear day around solar noon at sea level. Furthermore, latitude, altitude, air pollutants, time of day and year, wavelength and weather patterns can significantly reduce the density irradiation. Moreover, the sunshine is from turning hydrogen into helium via nuclear fusion process give rise to different wavelengths (λ) which are UltraViolet (UV) (λ < 400 nm), Visible (Vis) (400 nm < λ < 700 nm) and InfraRed (IR) (λ > 700 nm) radiations. Meanwhile, these irradiations make up 8%, 46%, and 46% of the total solar radiation [17]. This distribution must be considered while searching for solar-absorbing materials.

I. 2. 2. Photovoltaic effect

In 1839s, French physicist Alexandre Edmond Becquerel discovered the PhotoVoltaic (PV) effect [18]. This effect is the principle of producing the electricity directly from electromagnetic radiation (photons) or sun irradiation without any chemical or mechanical reactions through photovoltaic solar cells by converting the photon energy into mobile electrons, thus electricity. Depending on its wavelength, when a PV cell is subject to the sunlight the incident photons will be absorbed, reflected or passed through the matter (See **Figure I.4**).

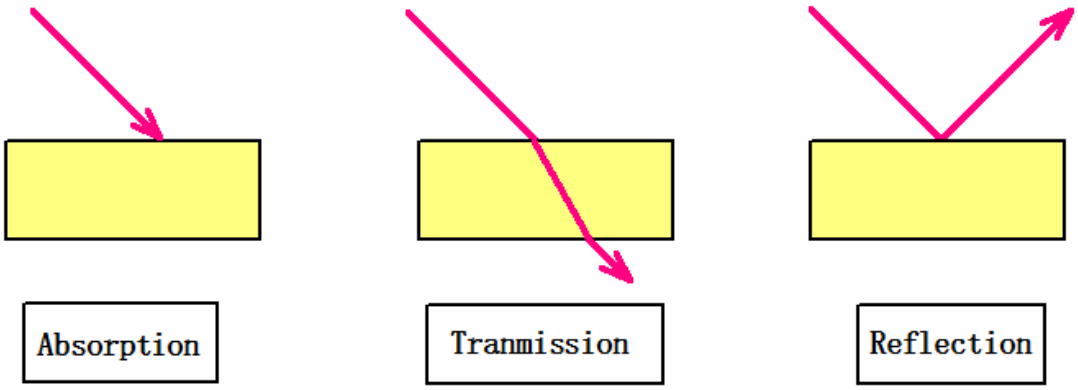

Figure I.4: Schematic illustration of radiation-matter interaction: absorption, transmission and reflection

I. 2. 3. Generation and Recombination

The electrons (e) in the atoms of nanomaterials are energized by the energy of the absorbed photons. This energy ejects electrons from their equilibrium states in the valence band (VB) bump into the excited states in the conduction band (CB) within the matter which in-turn leave "holes" in the valence band. Therefore, an electrical imbalance is creating within matter resulting in electron-hole pairs. Generally, the excited electrons relax back quickly to their

equilibrium states in the VB (recombination) by transforming their electrical energy into thermal one by inelastic shocks between electrons, which results in a heat evacuation which is so-called thermalization.

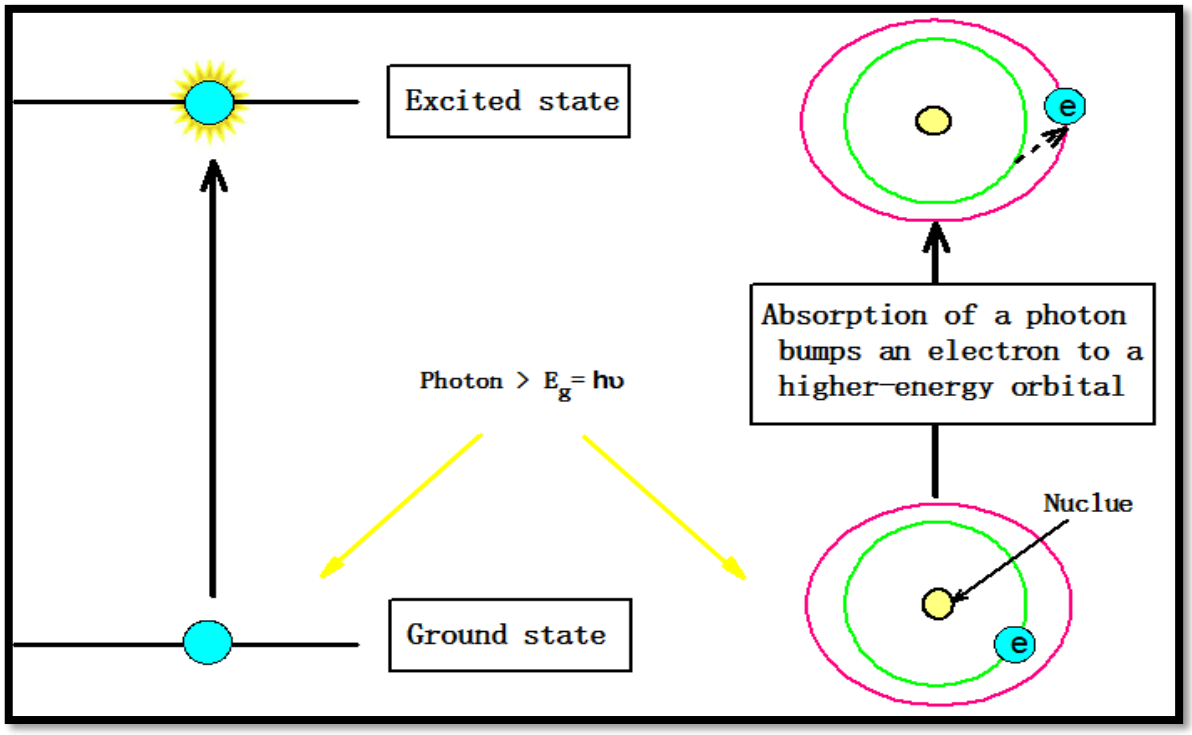

Figure I.5: Illustration of photon absorption by an electron (e) at atomic level

I. 2. 4. Materials types

Moreover, the energy differences between the initial and final states so-called the forbidden band energy (is given by $E_g = h\nu$). Particularly, this occurs when the energy of the photons making up the sun light is larger than the forbidden band gap of the matter. This forbidden band energy differs depending on the type of matter. On one hand, in conductor materials the VB and CB overlap (none forbidden band), thus all wavelengths could be absorbed. Unfortunately, the generated electron-hole pairs instantly recombine, leaving no possibility to exploiting them.

One the other hand, insulator materials are characterized by wide forbidden band energy values of at least 6 eV which indicates that the incident photons must provide energies greater than the forbidden band to interact with the electron, which corresponds to lengths wave less than 200 nm (UV region), a range that does not cover solar radiation [19].

Fourteenthly, the semiconductor materials have forbidden band gap values considerably less than the insulator materials (from 1 to 3 eV) which indicates that wavelengths of solar radiation

could be absorbed and converted to electrical energy this is the reason why the semiconductor compounds are used as photovoltaic cells.

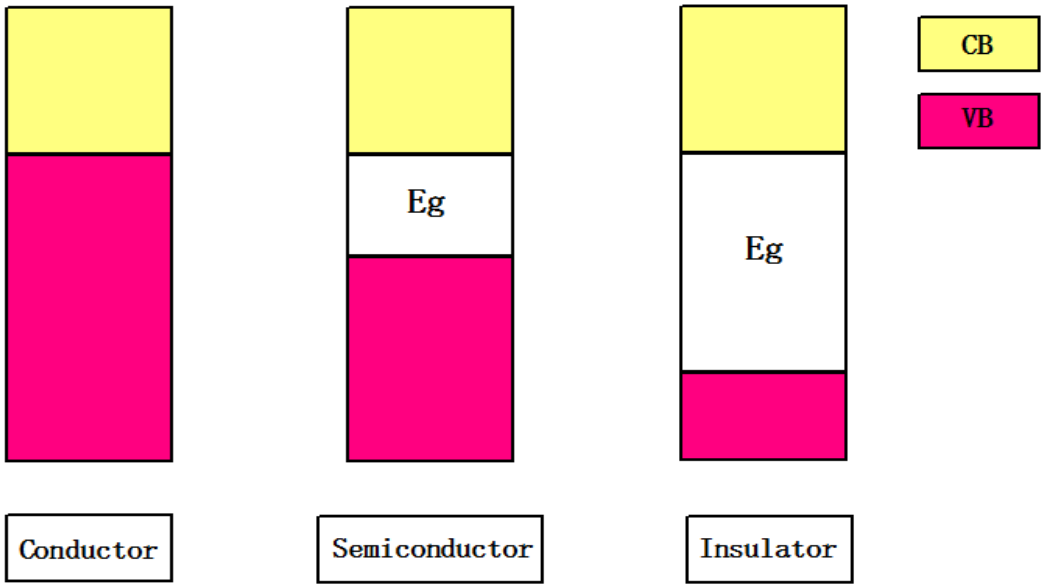

Figure I.6: Schematic illustration of valence band, conduction band and the forbidden band gap of conductor, semiconductor and insulator

I. 2. 5. Direct and indirect materials

Semiconductor and insulator materials could be either direct or indirect forbidden band gap, two different transitions therefore may occur. Note that, when the highest occupied molecular orbital (HOMO) and the lowest unoccupied molecular orbital (LUMO) occur at the same momentum (wave vector value *k*) the generation and the recombination are therefore direct without changing the wave vector. Hence, promoting a more efficient absorption of the photon.

A semiconductor or insulator those the HOMO and LUMO do not occur at the momentum is called an indirect forbidden band material. These materials require such an electron to interact not only with the photon to gain energy, but also with a lattice vibration called a phonon in order to either gain or lose momentum. In order to explain this phenomenon an energy versus momentum crystal diagram is used (see **Figure I.7**).

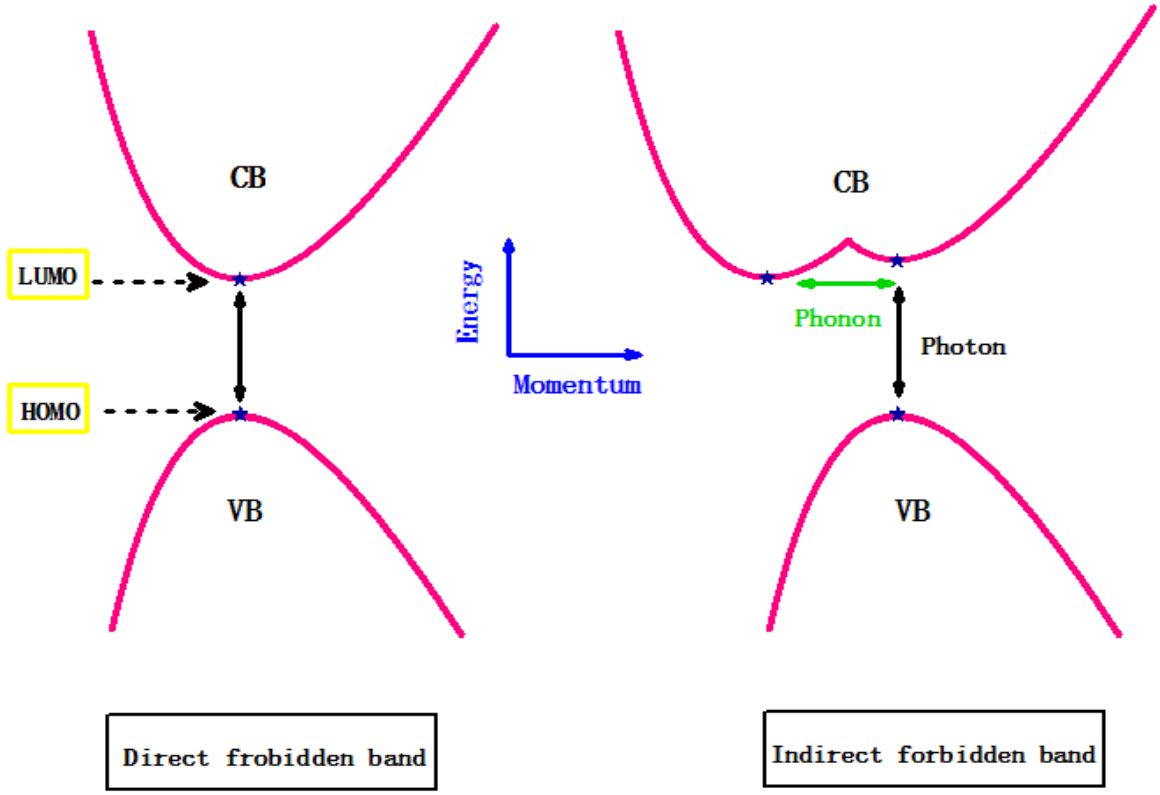

Figure I.7: Schematic illustration of direct and indirect materials

I. 2. 6. The p-n junction

Generally, in a semiconductor matter the electron-hole pairs are not collected because they recombine (the excited electrons relax back quickly to their equilibrium states in the VB). Thus, a semiconductor material itself cannot generate an electric current and the separation of these electron-hole pairs is needed. Therefore, to create this a p-type semiconductor (holes are the majority carries and electrons are minority carriers) is put into contact with a n-type semiconductor (electrons are the majority carries and holes are minority carriers), the junction between the two semiconductors is known as a p–n junction.

In the junction region, the electrons flow readily through the n-type semiconductor and holes flow readily through p-type semiconductor in which some of the electrons from the n-type semiconductor will move by normal diffusion into the p-type semiconductor and occupy electron vacancies.

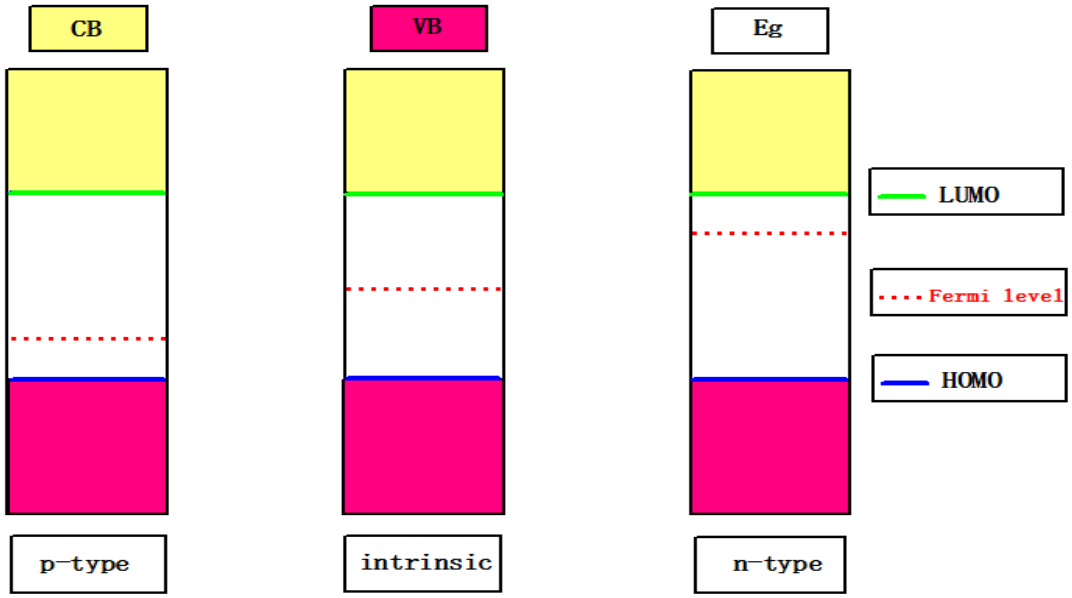

Figure I.8: Energy band profiles for a p-type, intrinsic and n-type semiconductor

Each time this happens, an electron-hole pair is left behind in the n-type semiconductor. So, accompanying the actual motion of an electron from the n-to the p-type semiconductor, a hole has effectively been moved from the p-type material into the n-type semiconductor. Because both semiconductors were electrically neutral to begin with, the loss of electrons from the n-type semiconductor, and the loss of holes from the p-type semiconductor, leaves behind net positive and negative charges, respectively, in the two semiconductors. The presence of these net positive and negative charges on either side of the junction creates an electric field across the junction. The electric field thus developed in the junction will force any free electron that happens to be in the junction region to move in the direction toward the n-type semiconductor. If there is also a hole in the junction region, it will effectively move in the direction toward the p-type material [20].

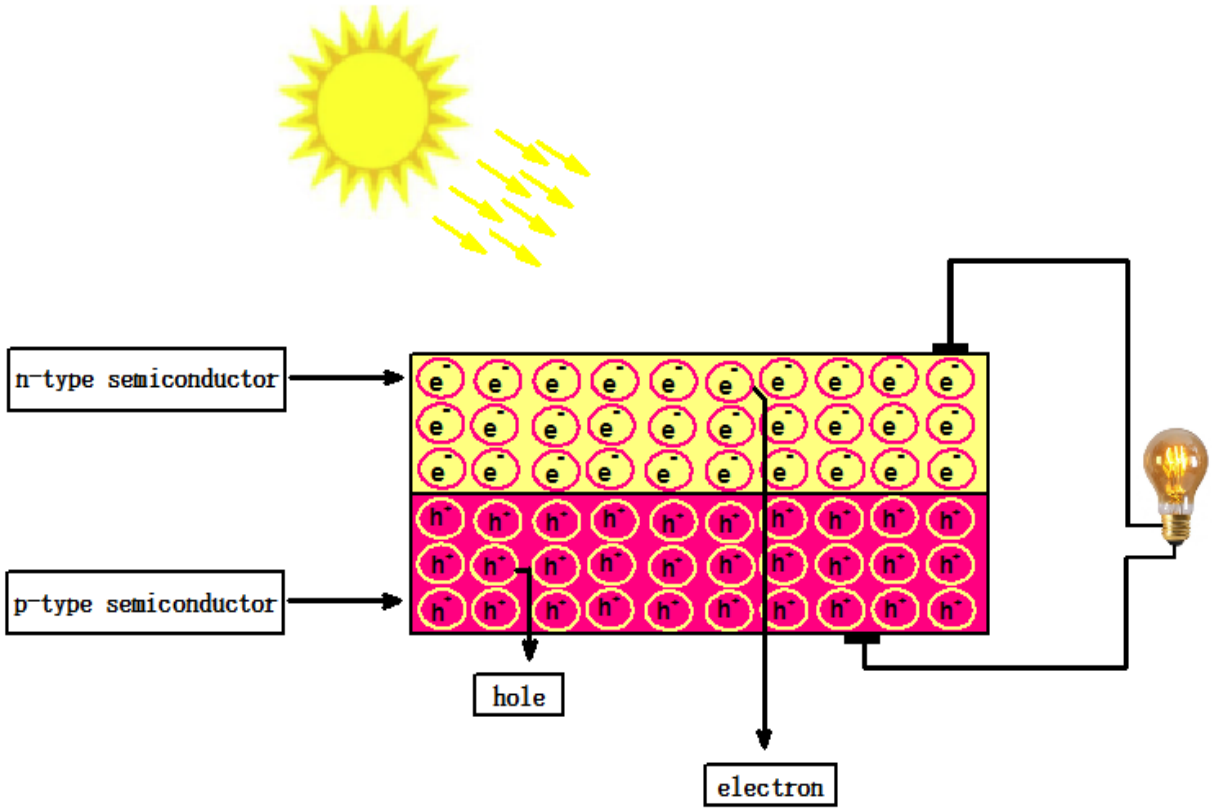

Figure I.9: Mechanism of charge carriers' movement (electrons and holes) in a photovoltaic cell

Thus, electric current is made to flow through an external load, and solar energy is being converted into electric energy. The strength of the internal electric field is reflected in the voltage produced across the terminals of the solar cell. The maximum current that the cell can deliver will be determined by the rate at which incident photons raise electrons into the conducting state. This is the reason why the p-n junction is crucial to the operation of a photovoltaic cell.

I. 2. 7. Basic structure of a solar cell

In general, the PV cell could be considered as a stack of materials, and most of them are made up of:

- Anti-reflecting coating or doped layer is placed at the front of the cell in order to improve the cell performance: better absorption of the light, and better charge carries diffusion in the semiconductors, etc.

- The active or the absorbing layer is made up of a p-n junction, in its simplest form, the base (p-type) region is joined at a junction with emitter (n-type) region leading to majority electrons in the n-type side close to the junction to diffuse of to the p-type side and majority hole from the p-type to diffuse n-type side.

- Front and rear contacts are usually made of metals. They are necessary to collect the current generated by a solar cell.

I. 3. Photovoltaic and solar cells technologies

There is a wide variety of photovoltaic cell technologies in the marketplace today, using different types of materials, and an even larger number will be available in the future. Depending on the absorbing material used, the photovoltaic cell technologies are generally divided into three broad generations [21 – 23].

I. 3. 1. The first solar cell generation

The most widely used material for the various types of fabrication is crystalline silicon both in its simple crystalline from (mono-crystalline) as well as in the multi-crystalline from. Usually, solar cells made of crystalline silicon are called as traditional or conventional solar cells This generation represents over 95% (fully commercial) of global commercial PV module production in its various forms [24]. This technology dominates the world market due to the high abundance of silicon on Earth's surface and none-toxic element with a solar panel lifetime up to 20 years. Coming to the efficiency, these solar cells tops the list. Polycrystalline silicon solar cells generate a good efficiency of 22.3% (under the laboratory conditions) while the monocrystalline solar cells have the highest lab efficiency of 26.7% (see **Fig. I. 10**).

Otherwise, even though silicon is abundant in the earth's surface, it is relatively expensive to purify it sufficiently to make a semiconductor. However, the inherent limitation to a real broad scale-up of the first-generation PV technologies is determined by the very laborious and energy consuming processing of Silicon wafers, representing more than 60% of the manufacturing costs of Silicon-based photovoltaic cells, leading to a large amount of waste as well as their indirect forbidden band which inspired engineers and scientists to look for a 2nd generation solar cells that addressed factors such as simple and low-cost production as well as high performance.

I. 3. 2. The second solar cell generation

The Second generation of solar cells is based on thin film photovoltaic technology, and generally include three main families: Amorphous silicon and micro amorphous silicon; cadmium telluride (CdTe); and copper indium selenide (CIS) and copper, indium gallium dieseline (CIGS). As the name itself indicates these cells are thin, these film layers thickness ranges from few nanometers to tens of micrometers and therefore minimizing the cost manufacturing and materials.

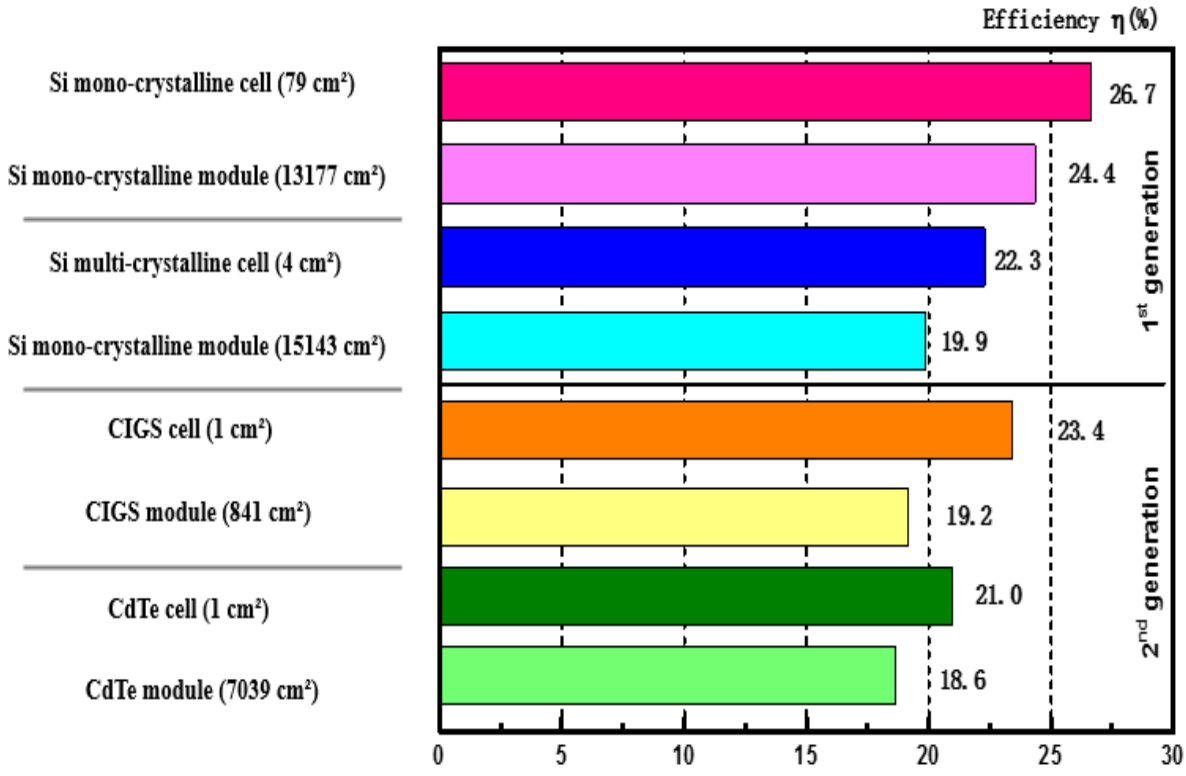

Figure I.10: Efficiency achieved for the first second generations of solar cells

Their low thickness makes them flexible, light weighted and easy to install while the implementation processes are complex and quite expensive. The maximum efficiency obtained under the laboratory conditions is 23.4% and the market share covered by this technology is 5% [25]. The toxicity of cadmium telluride, the degradation of amorphous silicon output power (15%–35%) when exposed to the sun.

I. 3. 3. The third solar cell generation

The 3rd solar cells generation brings together very high efficiencies and lifetime with very diversified technologies. With the development of new absorbers, new manufacturing methods

can be considered to decrease manufacturing costs. This generation of PV cells includes Dye-sensitized solar cells (DSSCs) or Grätzel cells [26], Copper zinc tin sulfide solar cell (CZTS), and derivates CZTSe and CZTSSe [27], Quantum dot solar cells [28,29], carbon nanotubes [30,31], hot carrier [32,33],Organic solar cells [34], perovskites. This generation is potentially able to overcome the Shockley–Queisser limit of 31–41% power efficiency for single forbidden band gap solar cells [35], and it is a compromise compared to other existing ones in terms of efficiency, cost, respect for the environment and chemical durability (See **Figure I. 11**. [36]). They are still the subject of intense research work without a significant industrialization to date.

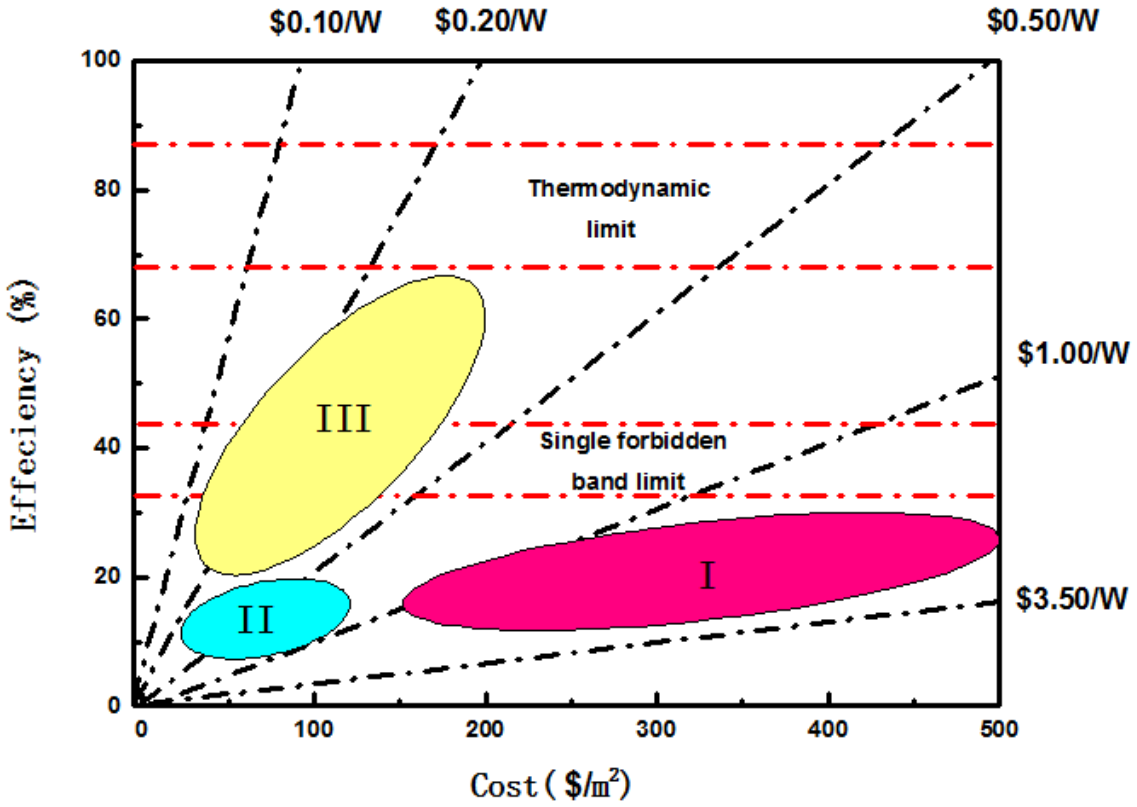

Figure I.11: Efficiency-cost trade-off for the first three generations of solar cells

I. 3. 3. 1. Perovskites solar cells

Perovskite materials were discovered over 160 years ago by a German scientist, Gustav Rose, during a trip to Russia, in the Ural Mountains, which was named "perovskite" in honor of the Russian mineralogist Lev von Perovski [37]. About half a century later, H.L. Wells et al. at Sheffield Scientific School, a pre-World War I unit of Yale University, prepared the first synthetic halide perovskite based on cesium and lead, although its perovskite structure was determined only during the 1950s by C.K. Møller at the Royal Veterinary and Agricultural College in Copenhagen, Denmark. Møller.

The perovskite solar cells stem from dye-sensitized solar cells, which have demonstrated remarkable optoelectronic properties due to their superior photoelectric and catalytic properties which boost the performance of existing solar cell technology. Perovskite solar cells based on organometal halides have attracted great attention from the scientific community all over the world, as well as they are considered to be from the top 10 scientific breakthroughs in 2013 [38]. The perovskite compounds can be used not only as light absorbing layer, but also as an electron/hole transport layer due to its high charge mobility, long carrier diffusion distance, high extinction coefficient, and long carrier lifetime.

In 2009, photoelectric PCE was around 3–4%. By optimizing the perovskite coating conditions, the perovskite solar cells' photoelectric PCE was doubled after two years. Recently, the perovskite solar cells' photoelectric PCE is boosted from 3.8% in 2009 to 25.5% in 2021 [38 – 42]. Therefore, perovskite solar cells have gained a significant position in the photovoltaic family within this short duration of time. It has become one of the promising photovoltaic technologies for the future which can meet our energy needs at a low cost and more efficient way.

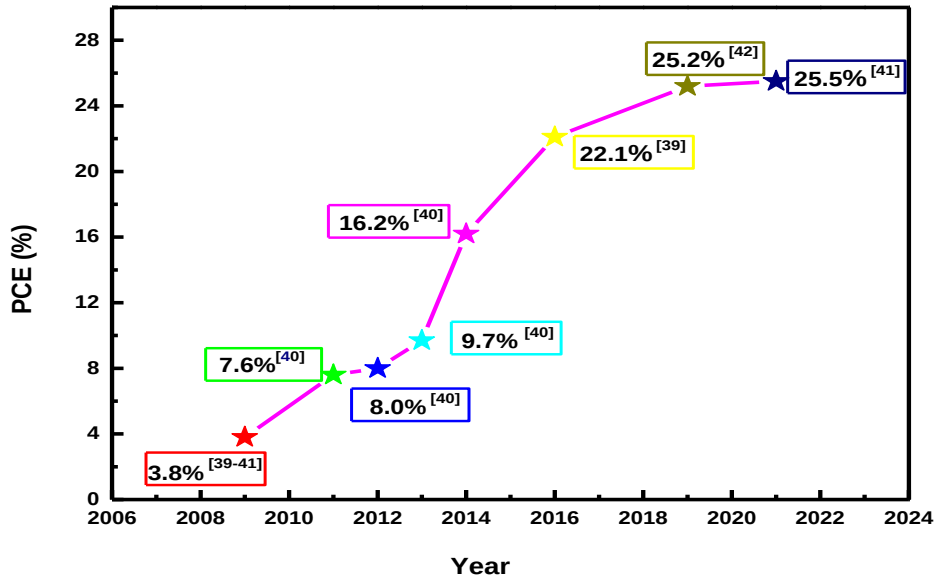

Figure I.12: Progress in perovskite solar cell efficiency

I. 3. 3. 1. 1. Simple perovskites solar cells

The simple perovskite is a compound that has the same crystal structure as the mineral calcium titanium oxide $CaTiO_3$.Generally, the chemical formula for perovskite compounds is

ABX_3 where the A site is occupied by a large cation, and the B site is occupied by a smaller metal cation and X is an oxide or halide anion that bonds to both. A wide number of different chemical elements can be combined together to form perovskite ABX_3 ($^{XII}A^{2+VI}B^{4+}X^{2-}{}_3$). In organic-inorganic metal halides case this species A is replaced by the organic cation. The cubic structure (space group Pm3m) is the ideal structure of this kind of perovskite solar cells in which the large A cation occupies the eight adjacent octahedra in three-dimensional space. The X-atoms are mostly substituted by the oxygen atoms or halogen atoms. The B transition metal (TM) cation occupies the body center position surrounded by six nearest X oxide or halide anion forming together a BX_6 octahedral arrangement.

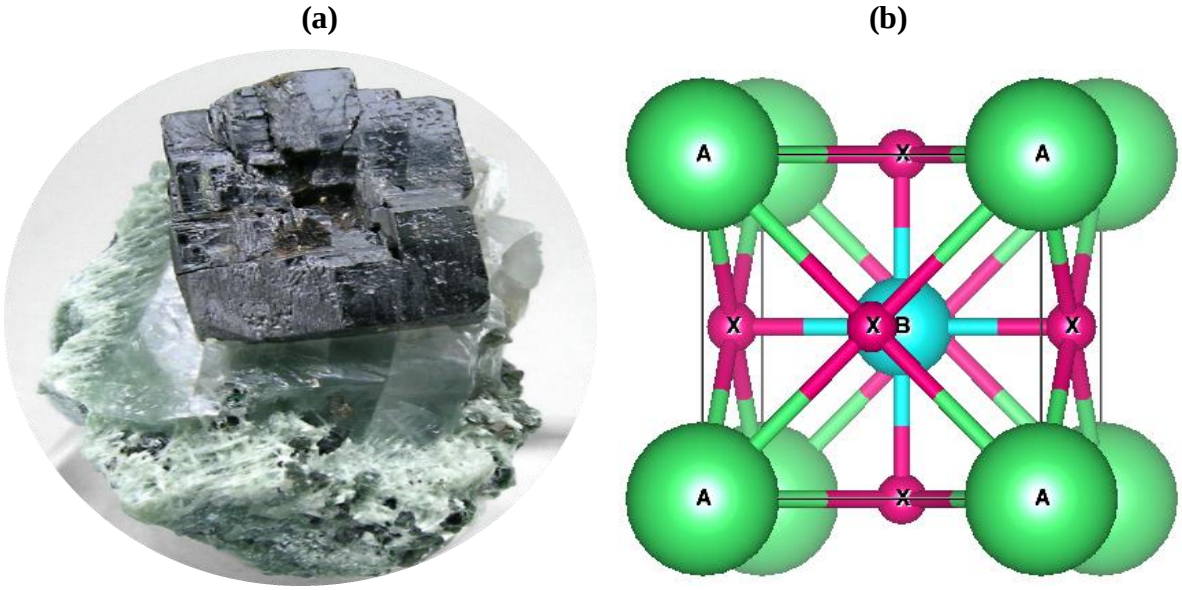

Figure I.13: (a) Crystals of $CaTiO_3$ perovskite on matrix, (b) the cubic structure of perovskite with general chemical formula ABX_3

ABX_3 undergoes a sequence phase transitions, a paramagnetic transition at high temperature and ferroelectric transition at low temperature. looking at one of ABX_3 compounds, strontium Hafnate simple oxide perovskite with chemical formula $SrHfO_3$ undergoes a sequence phase transitions; a paramagnetic transition: cubic (Pm-3m) $^{1360K}\rightarrow{}^{1000\text{ to }1353K}$ tetragonal (I4/mcm) and a ferroelectric transition; tetragonal (I4/mcm) $^{1000\text{ to }1353K}\rightarrow{}^{870K}$ orthorhombic (Cmcm) $\rightarrow{}^{300\text{ to }670K}$ Orthorhombic (Pnma) [43].

I. 3. 3. 1. 2. Double perovskites solar cells

Double perovskite (DPs) chemical formula can be derived out from the simple perovskite chemical formula ABX_3. Partial cation substitution is one of the common methods for tailoring the properties of perovskite materials. Otherwise, this substitution can be in varying degrees

and take place either at A or B site. Recently, the half of the *B*-site cations are substituted with another B' cation case has been taking a particular interest. In this case and as schematically shown in **Figure I.13**, by doubling the unit formula ABX_3 where one of the B cations in the formula is replaced by B' cation, may remain disordered at the *B* site, or they can order, giving rise to the so-called *B*-site ordered double-perovskite with chemical formula $A_2BB'X_6$. For this purpose, DPs $A_2BB'X_6$ feature an ordered rock-salt like arrangement of corner-sharing BO_6 and $B'O_6$ units in the crystal structure (see **Figure I.14**) are a versatile class of compounds.

Therefore, DPs compounds with the presence of two different TM elements at B sites (B and B') and possible presence of even two different rare-earth and alkaline earth elements at A sites, offer even better flexibility and degrees of freedom to play around, compared to simple perovskite structure with one A cation and one B cation sites. Besides, From the ordered double-perovskite $A_2BB'X_6$, it derivatives the vacancy-ordered double perovskites family (A_2BX_6) by removing the B' cation. The periodicity is therefore twice that of the ideal perovskite (cubic (Pm-3m)). This, the ideal double perovskites belong to a cubic system with space group Fm-3m.

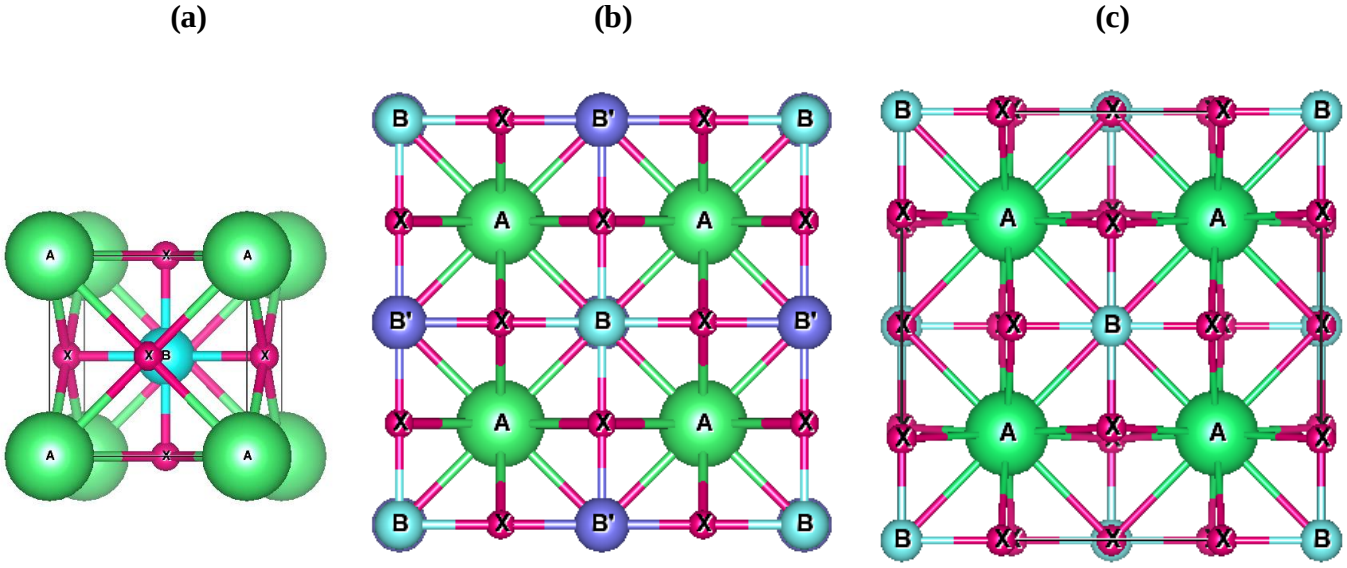

Figure I.14: Schematic representation of a vacancy-ordered double perovskite structure A_2BX_6 (c), derived from double perovskite structure $A_2BB'X_6$ (b), derived starting from a perovskite structure ABX_3 (a)

I. 3. 3. 1. 3. Triple perovskites solar cells

In the so-called "triple perovskite solar cells", the inequivalent B and B' cations positions are on a rock-salt ordered lattice as the double perovskites. On the other hand, the B cation is twice much as B' cation in the unit cell. Therefore, the triple perovskites have $A_3B_2B'X_9$ chemical formula in which one of both B and B' have a mix of the two elements (B and B') [44]. The order over the rock-salt positions therefore will not be a complete order of one element. In different ratios, therefore keeping the both positions inequivalent. The Triple perovskites, usually have hexagonal, orthorhombic, monoclinic, and trigonal structures.

I. 3. 3. 1. 4. Inverse perovskites solar cells

From the simple perovskite chemical formula ABX_3, we can get the chemical formula of inverse perovskite (anti-perovskite) by switching the anion and cation positions XBA_3 (XAB_3) (or A_3BX (AB_3X)). Researchers have been demonstrating that the simple and inverse perovskite materials except not just at the photovoltaic applications, but also various range of applications including hydrogen production from photocatalytic water splitting technology.

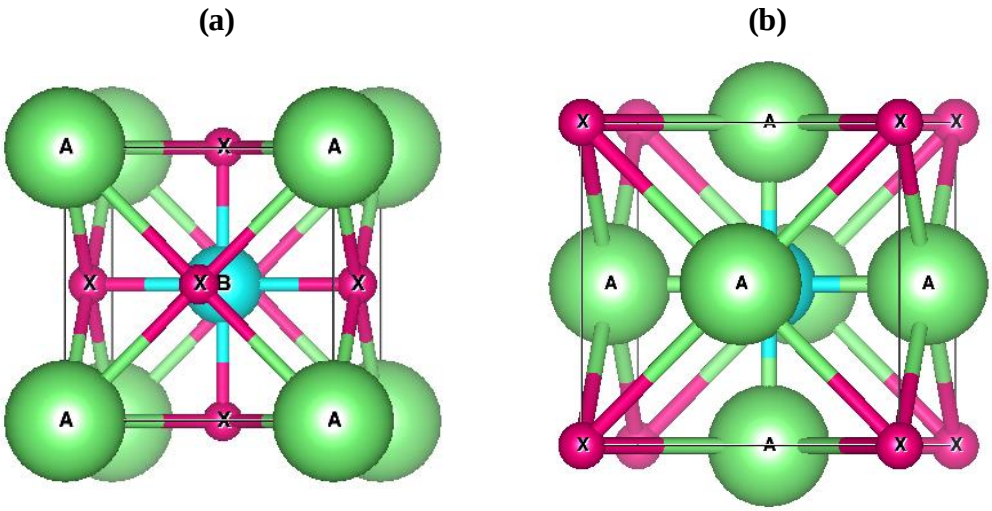

Figure I.15: Schematic representation of a simple perovskite structure ABX_3 (a), and inverse perovskite structure XBA_3 (b)

I. 4. Photocatalytic effect

Hydrogen (H_2) has been considered as an emerging promising energy vector, owns a remarkably high energy density of about 140 MJ kg^{-1} with respect to other chemical fuels, showing its potential to replace the fossil-based energy [45]. Now days, the most widely

hydrogen produced in industry is made via steam- natural gas reforming process with a production of 48% [46]. In this process, a high temperature (700-1000°C) is used to produce H_2 from a natural gas. However, this process leads to unwelcome environmental pollution gases such as carbon monoxide and carbon dioxide.

In contrast, the hydrogen production from water splitting is an efficient and eco-friendly way to produce H_2. Moreover, water represents the most convenient option owing to its availability, therefore the production of hydrogen with no carbon pollution that is very prevalent in the production methods involving the decomposition of hydrocarbons.

Overall water splitting into H_2 and O_2 molecules is an endothermic reaction with a standard free enthalpy of 237.1 $kJ.mol^{-1}$ under standard conditions (25°C, 1 atm) [47], which implies that an energy input is required to initiate the reaction. Among the easiest approaches to supply the needed energy is through an electrochemical reaction.

Photocatalytic water splitting in a photo-electrochemical cell extract electrical energy from sunlight. Four holes and two electrons are needed to produce an O_2 molecule and a H_2 molecule for driving the oxidation and reduction procedure respectively for giving rise to hydrogen through water splitting based on photocatalysis. The mechanism basically involves four main steps [47];

- The generation of electron–hole pairs from light irradiation on the photo-anode.
  - Absorption of light: **Semiconductor + hν (>Eg) → e^-_{CB} + h^+_{VB}**
- The oxidation of water by photo-generated holes on the photo-anode surface to produce O_2 and four protons (H^+).
  - Water oxidation: **$2H_2O + 4h^+ \rightarrow O_2 + 4H^+$**
- The transfer of photo-generated electrons through an external circuit to the cathode and the reduction of H^+ by photo-generated electrons on the cathode surface to produce H_2.
  - Proton reduction: **$2H^+ + 2e^- \rightarrow H_2$**
- Hydrogen is then captured as a gas and can be used for beneficial purposes.
  - The overall all reaction is: **$2H_2O \rightarrow 2H_2 + O_2$**

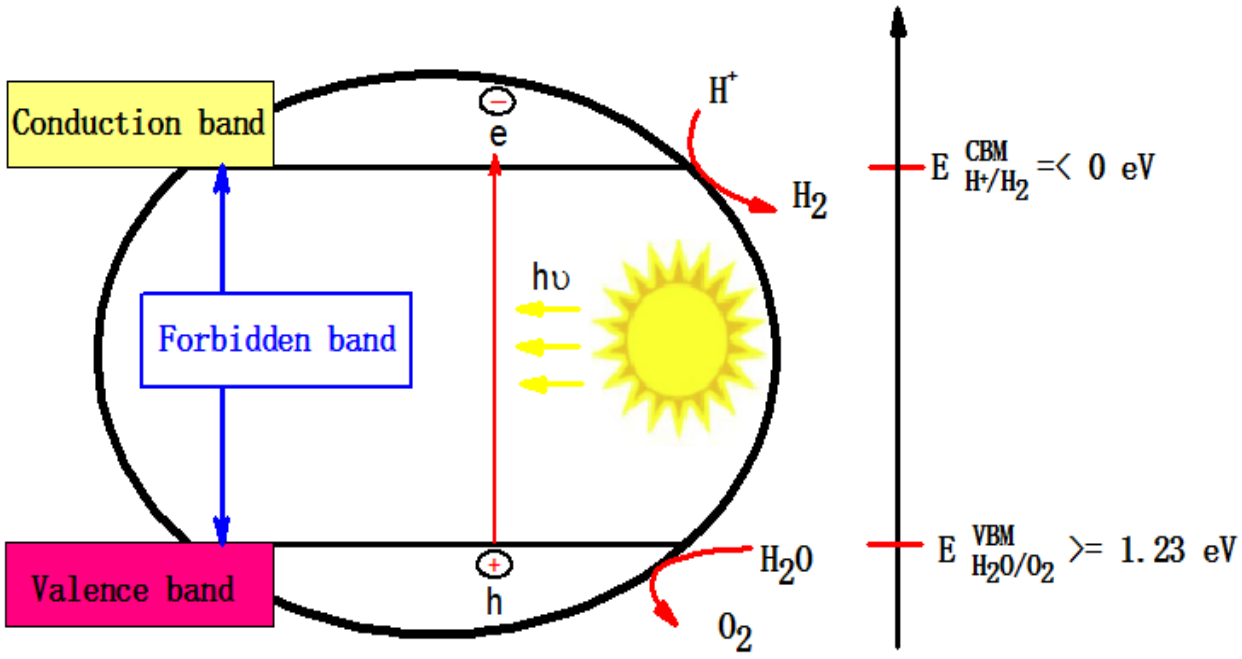

Figure I.16: Schematic illustration of photocatalytic water splitting in a photo-electrochemical

Besides, the positions of HOMO and LUMO are necessary for photocatalytic water splitting to evaluate the oxidation and reduction ability of semiconductor. The HOMO must be positioned below the water oxidation potential $E_{H2O/O2}^{HOMO} \geq 1.23\ eV$, and the LUMO must situated above the proton reduction potential $E_{H+/H2}^{LUMO} \leq 0\ eV$. The minimum forbidden band is therefore 1.23 eV for a suitable water splitting.

I. 5. Conclusion

In this chapiter, we have first presented the current global world energy consumption and environmental issues associated with the use of conventional energies. Then we have mentioned the greatest substantial renewable energy which is the solar energy. Next, we have described the photovoltaic and photocatalytic effects, as well as the perovskite materials which have been presenting admirable physical, chemical, electronic, magnetic and thermoelectrical properties. These properties are making them a promising candidate for many applications.

II. 1. Introduction

The density functional theory (DFT) is one of the most important computational quantum mechanical modeling methods used in material science, chemistry, and physics. The DFT method enabled us to identify the physical properties of many-body quantum system including; structural, electronic, optical, elastic, and thermodynamic properties in details by comparing the theoretical results with the experimental ones. Moreover, to obtain theoretical results agrees with the experimental results or data, various factors must be taken into consideration including; the approximations used as well as the interactions taken into account. In the following section, a basic description of DFT method will be given along with the approximations as well as the software and packages used in this thesis are presented.

II. 2. The many particles' problems

The basic of theoretical solid-state physics is the non-relativistic time independent Schrodinger equation [48], which is described a particle by its wave function, for a system consisting of M nuclei and N electrons this equation is described by:

$$\hat{H}\psi(\{\mathbf{r_i}\},\{\mathbf{R_j}\}) = \mathbf{E}\psi(\{\mathbf{r_i}\},\{\mathbf{R_j}\}) \qquad \textbf{(Eq. II.1)}$$

Where $\psi(\{r_i\},\{R_j\})$ presents the wave function of multi-particles (N-body) system, $\{r_i\}$ and $\{R_i\}$ terms describe the electrons and the nuclei respectively, while $\hat{H}$ is the Hamiltonian operator given by:

$$\hat{H} = \hat{T}_e + \hat{T}_N + \hat{V}_{e-e} + \hat{V}_{e-N} + \hat{V}_{N-N} \qquad \textbf{(Eq. II.2)}$$

In the above equation, $\hat{T}_e$ and $\hat{T}_n$ are the kinetic energies of electrons and nuclei while $\hat{V}_{e-e}$, $\hat{V}_{n-n}$, and $\hat{V}_{e-n}$ represent the electron-electron interaction, the nucleus-nucleus repulsion, and the electron-nucleus attraction, respectively. The Hamiltonian of a system with n electrons and N nucleus can be written as:

$$\hat{H} = \underbrace{-\frac{\hbar^2}{2m_e}\sum_i \nabla_i^2}_{\hat{T}_e} \underbrace{-\frac{\hbar^2}{2}\sum_I \frac{\nabla_I^2}{M_I}}_{\hat{T}_N} + \underbrace{\frac{1}{2}\sum_{i\neq j}\frac{e^2}{4\pi\varepsilon_0 r_{ij}}}_{\hat{V}_{e-e}} \underbrace{-\sum_{i,I}\frac{e^2 Z_I}{4\pi\varepsilon_0 R_{iI}}}_{\hat{V}_{e-N}} + \underbrace{\frac{1}{2}\sum_{I\neq J}\frac{e^2 Z_I Z_J}{4\pi\varepsilon_0 R_{IJ}}}_{\hat{V}_{N-N}} \quad \textbf{(Eq. II.3)}$$

Where, ħ is the Plan constant, ∇ is the Laplacian, m_e and M_I are the i^{th} and I^{th} electrons and nuclei masses, respectively. e represents the electron's charge, ε_0 is the free space permittivity, r_{ij} is the distance between the electron i and the electron j, while Z_I and Z_J are the atomic numbers of I^{th} and J^{th} nucleus respectively (See **Figure II.I**) [49].

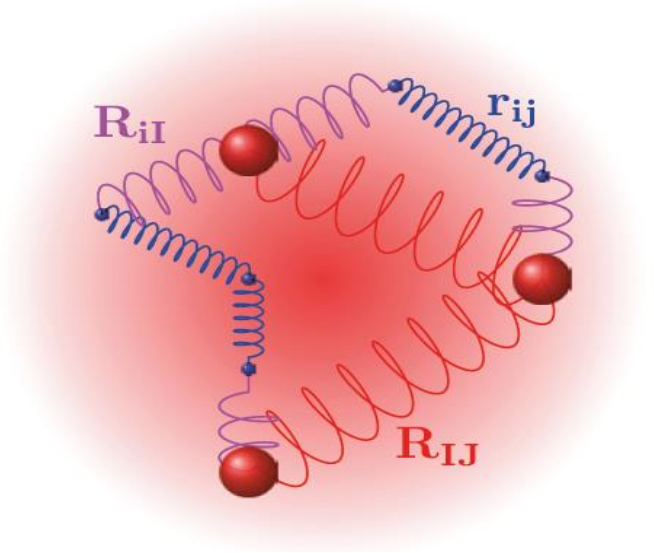

Figure II.1: Schematic representation of randomly located of electrons and nucleus in many-particle system. The blue and red balls outline electrons and nucleus respectively. The blue, red and magenta illustrate electron-electron, nuclei-nuclei and electron-nuclei interactions, respectively.

The analytical solution for the equation mentioned above is limited to the small and simple systems, such as, hydrogen atom and molecule. A solid with multi-particles n electrons and N nucleus which are mutually interacting and moving in an electromagnetic field presents a complicity in the resolution of the Schrödinger equation. Therefore, some approximations must be involved to solve the non-relativistic time independent Schrödinger for N-body systems.

II. 2. 1. Born – Oppenheimer approximation

In 1927s, Born and Oppenheimer assume that there is a large difference in mass between nuclei and electron because the nuclei-electron masses ratio is slightly more than 1836, which indicates that the nuclei are heavy and slow and the electrons are small and fast [50]. Thus, the dynamics of nuclei could be neglected by considering then frozen (or fix) compared to electrons movement, this is the basis of so-called Born-Oppenheimer (BO) approximation. Therefore, the kinetic energy of the nuclei can be considered equal to zero $T_n = 0$, the interaction energy of the nuclei (Coulomb energy caused by the repulsion between the nuclei) $V_{n-n} = cte$ is a constant value which can be neglected. Hence, the total wavefunction in **Eq.II.3** can be rewritten as follows:

$$\widehat{H} = \underbrace{-\frac{\hbar^2}{2m_e}\sum_i \nabla_i^2}_{\widehat{T}_e} + \underbrace{\frac{1}{2}\sum_{i\neq j}\frac{e^2}{4\pi\varepsilon_0 r_{ij}}}_{\widehat{V}_{e-e}} - \underbrace{\sum_{i,I}\frac{e^2 Z_I}{4\pi\varepsilon_0 R_{iI}}}_{\widehat{V}_{e-N}} \qquad (\mathbf{Eq.\ II.4})$$

It is worthwhile to mention that the BO approximation is successfully reduced the complexity for solving the many-body Schrödinger equation which is become more simplified, and all methods of solving the Schrödinger equation are based on this approximation because it is the first step of the resolution. Although the great simplification of the BO approximation, this approximation alone is not sufficient to solve the Schrödinger equation due to the complexity of the interactions between electrons and further approximations are needed.

II. 2. 2. Hartree and Hartree-Fock approximation

The mutual interactions between electrons complicate the resolution of **Eq.II.4**. In 1928s, Hartree proposed his approximation for the first time [51], this approximation assumed that the electrons are independent and each electron can move in a medium external filed generated by nuclei and other electrons which allows to calculate the wave functions for multi-electronic system (many-body) making them as a mono-electronic wave function orbitals product. The wave function of the system is written as:

$$\boldsymbol{\psi}(\boldsymbol{r_1}, \boldsymbol{r_2}, \boldsymbol{r_3}, \ldots\ldots\ldots \boldsymbol{r_n}) = \boldsymbol{\varphi_1}(\boldsymbol{r_1})\boldsymbol{\varphi_2}(\boldsymbol{r_2})\boldsymbol{\varphi_3}(\boldsymbol{r_3})\ldots\ldots\ldots\boldsymbol{\varphi_n}(\boldsymbol{r_n}) \qquad \textbf{(Eq. II.5)}$$

In 1930s, Fock highlighted that the total wave function must be anti-symmetric which is not respected in the Hartree approximation. Therefore, the exclusion principal of Pauli is taken into consideration in the Hartree-Fock (HF) approximation. Accordingly, two electrons cannot exist simultaneously in the same quantum state. In the HF approximation the multi-electronic wave function is written in the form of a N mono-electronic wave functions by a Slater determinant [52]:

$$\boldsymbol{\psi}(\boldsymbol{r_1}, \boldsymbol{r_2}, \boldsymbol{r_3}, \ldots\ldots\ldots \boldsymbol{r_n}) = \frac{\mathbf{1}}{\sqrt{n!}}\begin{bmatrix} \boldsymbol{\psi_1}(\boldsymbol{r_1}) & \boldsymbol{\psi_2}(\boldsymbol{r_1}) & \boldsymbol{\psi_n}(\boldsymbol{r_1}) \\ \boldsymbol{\psi_1}(\boldsymbol{r_2}) & \boldsymbol{\psi_2}(\boldsymbol{r_2}) & \boldsymbol{\psi_n}(\boldsymbol{r_2}) \\ \boldsymbol{\psi_1}(\boldsymbol{r_3}) & \boldsymbol{\psi_2}(\boldsymbol{r_3}) & \boldsymbol{\psi_n}(\boldsymbol{r_3}) \\ \vdots & \vdots & \vdots \\ \vdots & \vdots & \vdots \\ \vdots & \vdots & \vdots \\ \vdots & \vdots & \vdots \\ \boldsymbol{\psi_1}(\boldsymbol{r_n}) & \boldsymbol{\psi_2}(\boldsymbol{r_n}) & \boldsymbol{\psi_n}(\boldsymbol{r_n}) \end{bmatrix} \qquad \textbf{(Eq. II.6)}$$

Herein, $\frac{1}{\sqrt{n!}}$ Represents the normalization factor for an n-electron determinant.

The HF approximation is considered as an approach which can solve the Schrödinger equation for a quantum system for many particles system. Nevertheless, the HF approximation is extremely computationally intensive for large molecular systems. For this reason, an efficient and less computationally intensive methods are needed.

II. 3. Density Functional Theory

In the mid-1960s, Pierre Hohenberg, Walter Kohn and Lu Sham have created the current model of DFT formalism [53 – 56]. The Hartree-Fock method is based essentially on multi-electronic wave functions and it presents some problems of calculations and requests numerical efforts, especially for the case of transition metal materials including electronic correlations, while DFT is given to solve the Schrödinger equation for a multi-body system using only the multi-electronic wave function proposed by Hartree-Fock, which states that all ground properties of a given system composed by N-electrons with punctual nuclei are uniquely determined by the electron density and the probability of the presence of an electron in a volume element correspond to the electron density. It is very necessary to note that the DFT formalism takes into account the electron correlation which is very useful for the calculations and modeling of various extensive system, including materials with rare earth elements. The DFT is extensively used in recent years because in the most cases the DFT results agree with the experimental results or data, simplifies the calculations along with the computational costs of DFT calculations are less than other traditional methods [57].

II. 3. 1. Hohenberg - Kohn theorems

DFT is based on the description of the electron density ρ(r) which is an observable (unlike the wave function). This theory, introduced in the 1964s by Kohn, Hohenberg and Sham, is based on two theorems [54,58].

*** The first theorem:**

For any system of interacting particlules, there is a correspondence between the electronic density and the extermal potential, indicating that the total ground state energy is unique functional of electron density:

$$\mathbf{E = E\ (\rho(r))} \qquad \textbf{(Eq. II.7)}$$

This theorem highlights a unique correspondence between the external potential and electronic density. Since the electronic density determines the number of electrons, it also uniquely determines the wave function and thus the electronic properties of the system. Nd the exact form of this function is not accurately identified.

*** The second theorem:**

For any system of interacting particlules, the total energy of a system with an external potential reaches its minimum value when the density $\rho(r)$ is the exact ground state density $\rho_0(r)$:

$$\boldsymbol{E}\left(\boldsymbol{\rho_0}(\mathbf{r})\right) = \mathbf{min}\, \boldsymbol{E}\left(\boldsymbol{\rho}(\mathbf{r})\right) \qquad \textbf{(Eq. II.8)}$$

Thus, Hohenberg and Kohn have shown that the true or the exact density of the ground state is that which minimizes the energy E(ρ(r)) as shown in **Figure. II.2** (red star) and all the other properties are also functional of this density. The ground state energy of an electronic system in an external potential is determined by the variational method. The main advantage of this theorem is the enormous simplification of the solution of the Schrödinger equation, because of the problem with 3N variables is reduced to a problem of a scalar function in 3-dimensional space.

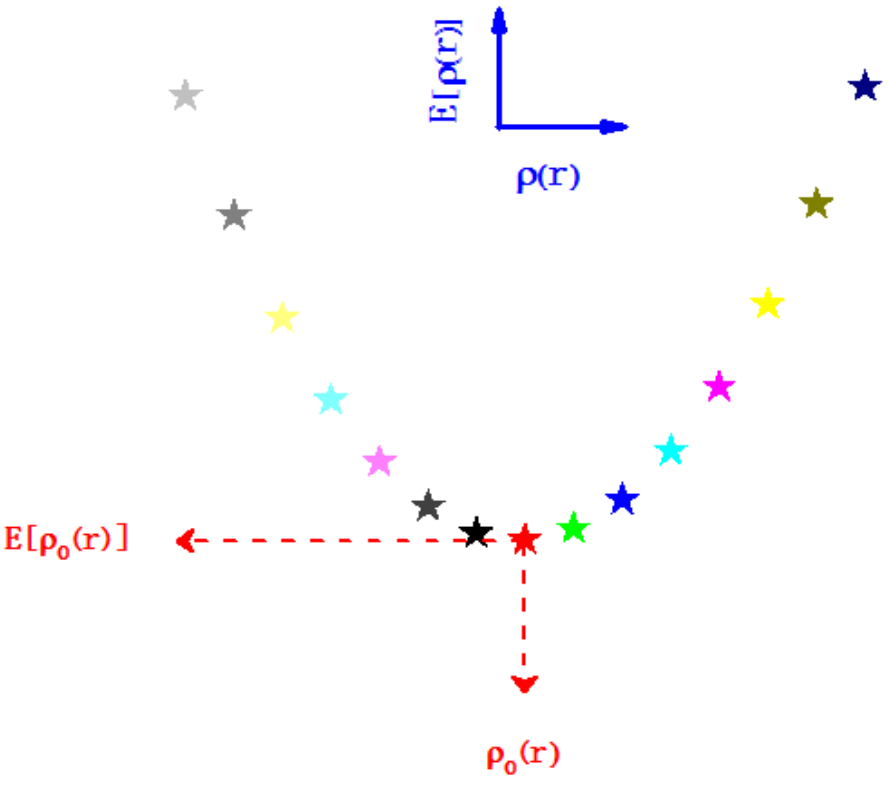

Figure II.2: Schematic of the energy as a functional of the electron density

II. 3. 2. Kohn-Sham formalism

As mentioned above, Hohenberg-Kohn theorems assumed that for an external potential $V_{\text{extern}}(\mathrm{r})$, exists a unique functional $F_{HK}[\rho(\mathrm{r})]$ when the charge density ρ (r) is equal to the charge density of the ground state $\rho_0(\mathrm{r})$. Thus, these lead to get the ground-state energy by minimizing the energy functional:

$$\mathbf{E}[\boldsymbol{\rho}(\mathbf{r})] = \boldsymbol{F_{HK}}[\boldsymbol{\rho}(\mathbf{r})] + \iiint \mathbf{V_{extern}}(\mathbf{r})\boldsymbol{\rho}(\mathbf{r})\mathbf{dr} \qquad \textbf{(Eq. II.9)}$$

Although the Hohenberg-Kohn established the existence of a universal functional $F_{HK}(\rho(\mathrm{r}))$ without stating its exact form or defining the ground state density. Thereafter, in 1965s, Kohn and Sham replaced the interacting electrons system with an auxiliary non-interacting electrons system by mapping the kinetic energy (T) of the real system to the exact kinetic energy (T_S) of the auxiliary system that have the same density [59]. Hence, the kinetic energy of the non-interacting system (T_S) can be written as a function of the Kohn-Sham orbitals ψ_i^{KS}:

$$\boldsymbol{T_S}\left[\left\{\boldsymbol{\psi_i^{KS}}\right\}\right] = -\frac{\mathbf{1}}{\mathbf{2}}\sum_{i=1}^{N}\int \boldsymbol{\psi_i^{KS}}\boldsymbol{\nabla^2}(\boldsymbol{r})\boldsymbol{\psi_i^{KS}}(\mathbf{r})\boldsymbol{dr} \qquad \textbf{(Eq. II.10)}$$

$F_{HK}[\rho(\mathrm{r})]$ functional in the equation (II.9) can be expressed as follows:

$$\boldsymbol{F_{HK}}[\boldsymbol{\rho}(\mathbf{r})] = \mathbf{Ts}[\boldsymbol{\rho}(\mathbf{r})] + \mathbf{E_H}[\boldsymbol{\rho}(\mathbf{r})] + \mathbf{E_{xc}}[\boldsymbol{\rho}(\mathbf{r})]$$

Herein, $T_S[\rho(\mathrm{r})]$ is the exact kinetic energy of electrons system without interaction, $E_H[\rho(\mathrm{r})]$ Corresponds to the energy of Hartree representing the electrostatic interaction between the electrons while $E_{xc}[\rho(\mathrm{r})]$ is the exchange-correlation energy of interacting electrons. Thus, the total energy function can be determined from the resulting density through the following equation:

$$\boldsymbol{E}[\boldsymbol{\rho}(\boldsymbol{r})] = \boldsymbol{T_S}[\boldsymbol{\rho}(\boldsymbol{r})] + \int \boldsymbol{V_{ext}}(\boldsymbol{r})\boldsymbol{\rho}(\boldsymbol{r})\boldsymbol{dr} + \frac{\mathbf{1}}{\mathbf{2}}\iint \frac{\boldsymbol{\rho}(\boldsymbol{r})\boldsymbol{\rho}(\boldsymbol{r_2})}{|\boldsymbol{r}-\boldsymbol{r_2}|}\boldsymbol{dr}\,\boldsymbol{dr_2} + \boldsymbol{E_{XC}}[\boldsymbol{\rho}(\boldsymbol{r})] \qquad \textbf{(Eq. II.12)}$$

The analytical expression of the exchange-correlation energy ($E_{XC}[\rho(\mathrm{r})]$) is unknown. Fortunately, the Kohn-Sham formalism implementation able to find a good approximation for $E_{XC}[\rho(\mathrm{r})]$. Based on the second Hohenberg – Kohn theorem, the Kohn-Sham minimization energy functional as function of the density $\rho(\mathrm{r})$ by the self-consistent solution which leads to set Schrödinger type single-particle equation the so-called Kohn-Sham equation:

$$\widehat{\boldsymbol{H_{KS}}}\boldsymbol{\psi_i}(\boldsymbol{r}) = \left[-\frac{\hbar^2}{\boldsymbol{em_e}}\boldsymbol{\nabla^2} + \boldsymbol{V_{KS}}\right]\boldsymbol{\psi_i}(\boldsymbol{r}) = \boldsymbol{\varepsilon_i}\boldsymbol{\psi_i}(\boldsymbol{r}) \qquad \textbf{(Eq. II.13)}$$

Here, ε_i and $\psi_i(r)$ are the Kohn-Sham eigenvalues and the Kohn-Sham orbital while V_{KS} represents the Kohn-Sham effective potential which can be obtained from a combination of the external (V_{ext}) and the Hartree (V_H) potentials, and it is given by:

$$\boldsymbol{V_{KS}(r) = V_{ext}(r) + V_H(r) + V_{xc}(r)} \qquad \textbf{(Eq. II.14)}$$

Where:

$$\boldsymbol{V_H[\rho(r)] = \frac{1}{2}\int \frac{\rho(r')}{|r - r'|}\, dr'} \qquad (\textbf{Eq. II. 15})$$

$$\boldsymbol{V_{xc}(r) = \frac{\delta E_{xc}[\rho(r)]}{\delta \rho(r)}} \qquad (\textbf{Eq. II. 16})$$

Hence, the ground state density can be expressed as:

$$\boldsymbol{\rho(r) = \sum_{i=1}^{N} |\psi_i(r)|^2} \qquad \textbf{(Eq. II.17)}$$

The Kohn-Sham formalism leads to the exact ground state of an interacting many-body system because the Kohn-Sham equation (**Eq.II.13**) is similar to the Schrödinger equation. As can be seen from the figure bellow, the total energy of system using DFT method can be obtained through sequence steps; the first step is needed to construct the potential from the given atomic positions. Then, we need to make initial guess for electron density. Next, we should calculate the effective potentials using this density functional theory. The following step leads to calculate the Kohn-Sham equations using effective potentials to calculate new electron densities. Therefore, the Kohn-Sham equations has to be solved self-consistently following an iterative method. At the end, the self-consistent solution ensures that the true ground state density has been achieved.

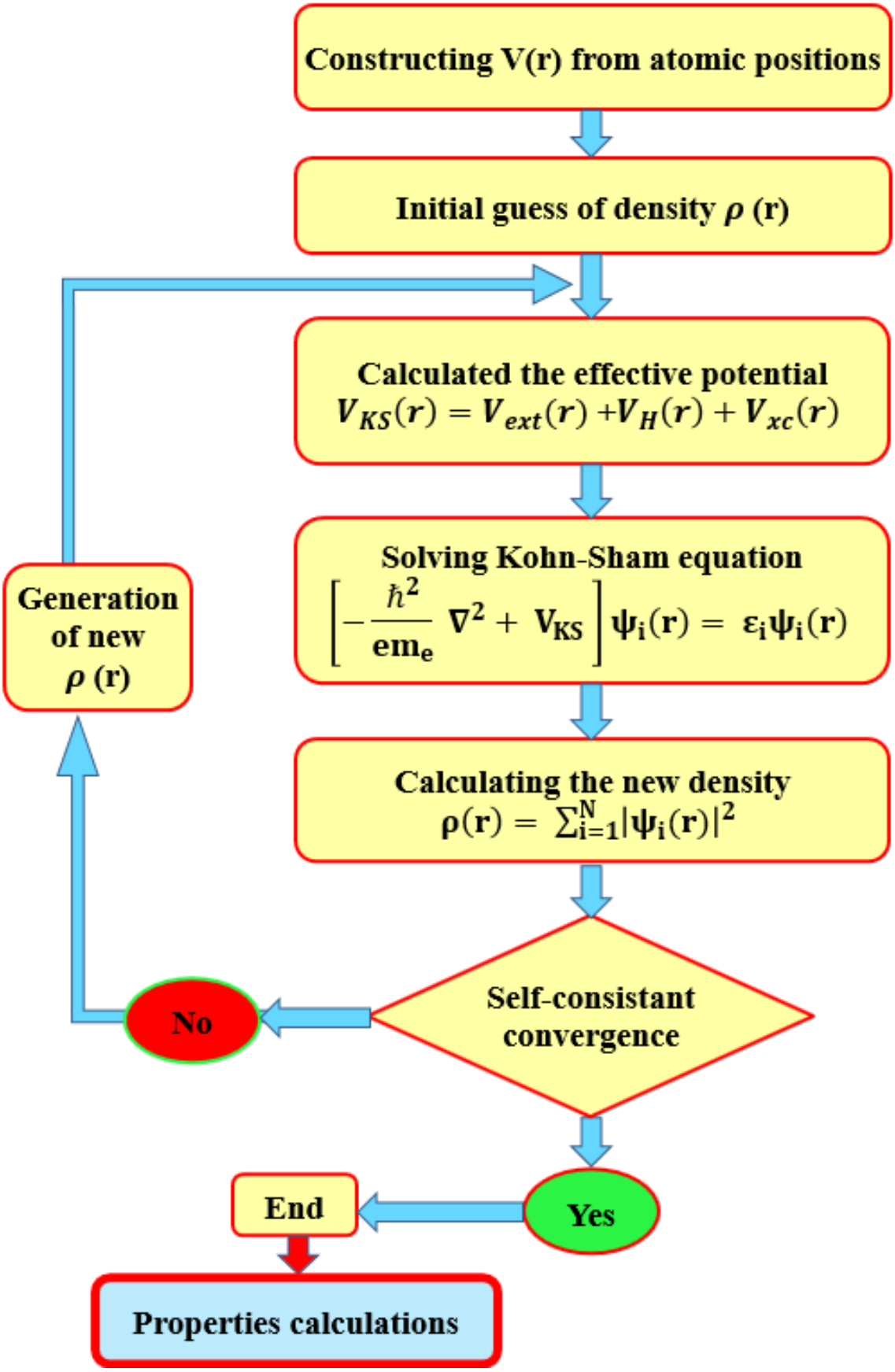

Figure II.3: Algorithm for calculation the properties from DFT

II. 3. 3. Exchange correlation approximation

As previously stated, the formalism of Kohn and Sham provides an exact expression for the total energy by replacing the real with auxiliary non-interacting system. Unfortunately, the Kohn-Sham equation is still not possible to solve and the only ambiguity here is that all Kohn-Sham equation terms can be evaluated except that of exchange correlation functional term which is unknow and the complexity of this term makes the Kohn-Sham equation resolution difficult. It is worthwhile noting that the more precise of the exchange correlation potential form, the more precisely the density will be obtained. However, getting the right and optimal approximation for the exchange-correlation potential is inherently a challenging and unsolved research task. It is therefore necessary to approximate this exchange-correlation potential to be able to apply the DFT. In this section, approximative expressions for this functional used in this thesis are presented.

II. 3. 3. 1. Local density approximation

In 1965s, Kohn and Sham proposed the first approximation which is the Local Density Approximation (LDA) [60]. The LDA based on the uniform and homogenous electron gas model. It considers that the charge density is slowly varied in each small volume (local density). Therefore, the exchange-correlation energy of electron at distance point r in the electron gas, is the exchange-correlation energy per electron gas which has the same density as the electron gas at r point. This approximation is the simplest approach to describe the exchange correlation energy which can be written as:

$$\mathbf{E_{xc}^{LDA}[\rho(r)] = \int \rho(r)\varepsilon_{xc}^{unifor}[\rho(r)]\ dr} \qquad \textbf{(Eq. II.18)}$$

Noting that $\varepsilon_{xc}^{unifor}[\rho(r)]$ donates the energy of the exchange and correlation of a uniform electron gas. The energy density $\varepsilon_{xc}^{unifor}[\rho(r)]$ further be divided into two parts, and it is represented as a sum of exchange ($\boldsymbol{\varepsilon_x}$) and correlation ($\boldsymbol{\varepsilon_c}$) energies as follows:

$$\boldsymbol{\varepsilon_{xc}^{unifor}[\rho(r)] = \varepsilon_x[\rho(r)] + \varepsilon_c[\rho(r)]} \qquad \textbf{(Eq. II.19)}$$

Where:

$$\boldsymbol{\varepsilon_x[\rho(r)] = -\frac{3}{4}\left[\frac{3[\rho(r)]}{\pi}\right]^{\frac{1}{3}}} \qquad \textbf{(Eq. II. 20)}$$

Regrettably, the correlation energy term is unknown. Fortunately, the analytical form of $\boldsymbol{\varepsilon_c[\rho(r)]}$ is described by Perdew-Zunger and Perdew-Wang using Monte Carlo simulation technique performed by Ceperley and Alder for uniform electron gas at different densities. Indeed the despite of simplicity, LDA surprisingly well and explains majority of metals or semiconductors as well as insulators systems properties.

II. 3. 3. 2. Generalized gradient approximation

Hohenberg and Kohn proposed an improvement of LDA by including the gradient of the electronic density in the term of exchange and correlation functional creating the Generalized gradient approximation (GGA). The main goal of the use of the GGA is that various systems have very different forms than uniform homogeneous (non-local and non-homogenies) electron gas from [61]. For this reason, the GGA is a non-local method. Hence, the $E_{xc}^{GGA}[\rho(r)]$ depends on the electronic density $\rho(r)$ and its gradient $\nabla[\rho(r)]$ as follows:

$$\boldsymbol{E_{xc}^{GGA}[\rho(r)] = \int \rho(r)\varepsilon_{xc}^{unifor}\left[\rho(r), \nabla[\rho(r)]\right]d(r)} \qquad \textbf{(Eq. II.21)}$$

Moreover, different GGA formulas were improved. Therefore, the GGA have several versions and well-know are:

- PW-GGA introduced by Perdew and Wang in 1992 [62],
- PBE-GGA introduced by Perdew, Burke and Ernzerhof in 1996 [63],
- Meta-GGA introduced by Tao et al in 2003 [64],
- WC-GGA introduced by Wu-Cohen in 2006 [61],
- EV-GGA introduced by Engel and Vosko 2017 [65].

On one hand, the LDA describes different physical properties for a large range of systems. on the other hand, the LDA fails in the description of the chemical properties especially the bonding energy of the molecules while the introduction of GGA provide a better description of the bonding energy. That explains the widespread use of the GGA by the chemical community in 1990s. The successes of the semi-local approach (LDA and GGA) rely on the accuracy is usually good enough to be useful, in particular for geometrical parameters and other quantities such as bulk modules calculations. Despite the many successes of LDA and GGA, we cannot say that these approaches are perfect for approximating the exchange-correlation potential. Therefore, other approximations are needed.

II. 3. 3. 3. Tran-Blaha modifssied Becke-Johnson potential

As mentioned above, the LDA and GGA are usually underestimate the electronic forbidden band of semiconductors and insulators. Hence, they underestimate the electronic properties on which the optical and all others properties are depend. This is the reason why in 2006, Becke and Johnson proposed a version of the exchange potential which based on the Optimized Potential Method [66]. This version of the exchange potential modified by Tran and Blaha in 2009 in order to be subsequently optimized effective potential. The modified Becke-Johson potential (mBJ) formalism is so-called the modified Tran-Blaha Becke-Johson potential (TB-mBJ) [67]. The BJ exchange is used in conjunction with LDA or GGA correlation. The TB-mBJ potential has been shown to be the perfect exchange potential with better precision and allowing to achieve an excellent agreement with the experimental results. The TB-mBJ potential is written according to the following form:

$$U_{\chi,\sigma}^{TB-mBJ}(r) = cU_{\chi,\sigma}^{BR}(r) + (3c-2)\frac{1}{\pi}\sqrt{\frac{5}{12}}\sqrt{\frac{2t_\sigma(r)}{\rho_\sigma(r)}} \qquad \textbf{(Eq. II.22)}$$

Where:

c is a system-dependent parameter which can be written as follows:

$$c = \alpha + \beta\left(\frac{1}{V_{cell}}\int\frac{|\nabla\rho(r)|}{\rho(r)}dr\right)^{\frac{1}{2}} \qquad (\textbf{Eq. II. 23})$$

α and β are parameters (α = - 0.012 and β=1.023 $Bohr^{\frac{1}{2}}$) which obtained according to the adjustment of the experimental results, and V_{cell} being the unit cell volume.

$U_{\chi,\sigma}^{BR}(r)$ term represents the Becker-Roussel potential which was originally proposed to model the Coulomb potential in 1989 corresponding to the exact exchange hole, it is given by the following formula:

$$U_{\chi,\sigma}^{BR}(r) = -\frac{1}{b_\sigma(r)}\left(1 - e^{-x_\sigma(r)} - \frac{1}{2}x_\sigma(r)e^{-x_\sigma(r)}\right) \qquad (\textbf{Eq. II. 24})$$

Herrin σ being the spin notation while b_σ (r) term can be determined from the following equation:

$$b_\sigma(r) = \left[\frac{x_\sigma^3(r)e^{-x\sigma}}{8\pi\rho_\sigma}\right]^{\frac{1}{3}} \qquad (\textbf{Eq. II. 25})$$

Where the electron density and kinetic energy density terms are presented as follows, respectively:

$$\boldsymbol{\rho_\sigma(r) = \sum_{i=1}^{N_\sigma} \left|\psi_{i,\sigma}(r)\right|^2} \qquad \textbf{(Eq. II. 26)}$$

$$\boldsymbol{T_\sigma = \frac{1}{2}\sum_{i=1}^{N_\sigma} \nabla\, \psi^*_{i,\sigma}(r)\, \nabla\, \psi_{i,\sigma}(r)} \qquad \textbf{(Eq. II. 27)}$$

II. 3. 3. 4. Hybrid exchange-correlation functional

Since 90s, new generation of functionals have been emerged so-called Hybrid Functional (HF) introduced by Axel Becke [68]. The HF is a combination of two parts, the exact exchange from Hartree-Fock to select relativity orbitales and the correlation energy of analytic density functional. The complete description of the electronic exchange and correlation is obtained by combining an exchange functional and a correlation functional by using the HF exchange part associated with GGA functional also called Half Half (HH) as following:

$$\boldsymbol{E_{xc} = 1/2(E_x(HF) + E_c(DFT))} \qquad \textbf{(Eq. II.28)}$$

The conversion of a reference system "without interaction" into an interacting system is the origin of the adiabatic term connection which can be decremented using the following formula:

$$\boldsymbol{E_{xc} = \int_0^1 \langle \psi(J)|V_{xc}(J)|\psi(J)dJ\rangle} \qquad \textbf{(Eq. II. 29)}$$

Where J describes the strength of the electronic coupling or the extent of the electronic interactions. J = 0 when the particles are independent presenting any interaction between electrons while J = 1 where the system particles are in complete interaction (real system). HF has been provided a great precision of the forbidden band, as well as it achieves an excellent agreement with the experiment value. Besides, the HF have serval types, in this thesis work we used the Yukawa screened PBE0 (YS-PBE0) [69].

II. 3. 4. Wien2k software

II. 3. 4. 1. Full Potential Linearized Augmented Plane Wave plus local orbital

To simplify the resolution of Kohn Sham's equations several methods can be used. In this part, the Full-Potential Linearized Augmented Plane Wave plus local orbital (FP-LAPW+lo) [70,71] introducing by Slater [72] implemented in the WIEN2k software [73] will be outlined. As can be seen from **Figure II. 4**., the FP-LAPW+lo method divides the crystal unit cell in two regions:

Region I: None-overlapping atomic spheres (A and B) centralized on atomic sites which known as Muffin-Tin radius (R_{MT}).

Region II: Interstitial region between atomic spheres (A and B).

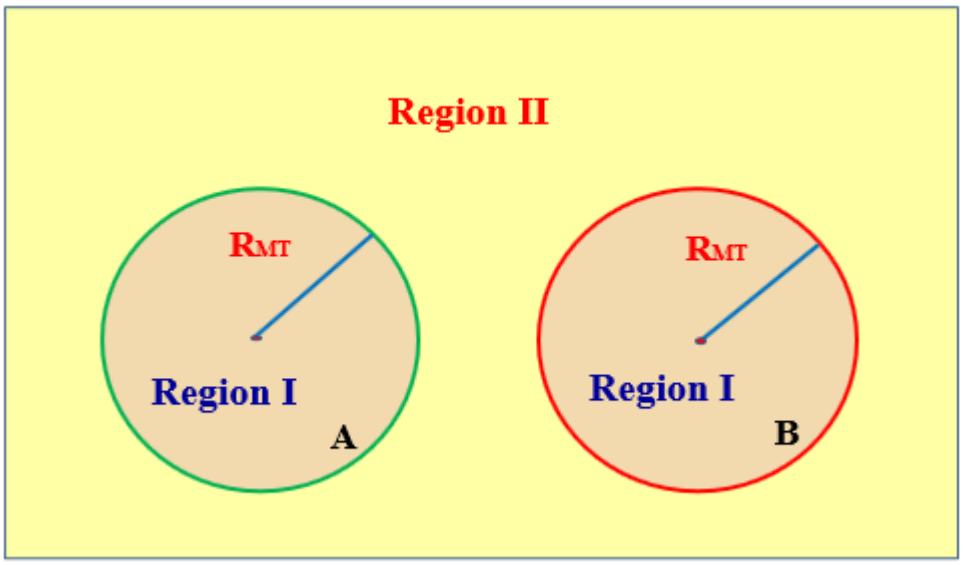

Figure II.4: Schematic illustration of two atomic spheres A and B with radius RMT (region I) and the interstitial region between the spheres (region II)

As highlighted in **Figure II.4**, the potential inside region I is expanded in a linear radial wavefunctions and spherical harmonics combination in which the nucleus are firmly affected by electrons. On the other hand, the potential inside region II is described by plane waves combination, hence the nucleus are less effected by electrons. At the boundary of these two regions, the potential values should coincide which is a regular solution of radial Schrödinger equation, and this model describes the system correctly. The FP-LAPW +lo method expands the potential differently in the following from:

$$\mathbf{V(r)} = \begin{cases} \sum_{\mathbf{LM}} \mathbf{V_{LM}(r)Y_{LM}(r)} & \textbf{Region I} \\ \sum_{\mathbf{K}} \mathbf{V_K e^{iK.r}} & \textbf{Region II} \end{cases} \qquad \textbf{(Eq. II. 30)}$$

Similarly, the charge density is developed in the following form:

$$\rho(\mathbf{r}) = \begin{cases} \sum_{LM} \rho_{LM}(\mathbf{r})\rho_{LM}(\mathbf{r}) & \textbf{Region I} \\ \sum_{K} \rho_{K} e^{iK.r} & \textbf{Region II} \end{cases} \qquad (\textbf{Eq. II. 31})$$

II. 3. 4. 2. Overview of Wien2k software

Since 1990s, Wien2k has been considered as a simulating calculation software developed at Institute of Chemistry of materials in the Technical University of Vienna (Austria) by Peter Blaha et al. [73]. In order to improve it and make it adaptable to different physical properties calculations such as electronic, optical, elastic, act…., Wien2k software has been continuously revised since then and has undergone several updates. Wien2k software is a computer program written in FORTRAN language working under UNIX operating system, based on DFT theory and FP-LAPW+lo method, and it consists of multi-individual programs liked by C-SHEL script. **Figure.II.5** shows that the Wien2k software performs the calculations of a particular solid on two main parts:

***Initialization*:**

After struct generation "case.struct" file, we carry out the initialization by the command "init_lapw" to start multi-programs and executing in a successive way. These programs are as follows:

NN: Calculates the nearest neighbor distances of all atoms, checks whether atomic radius spheres are overlapping. It also checks if equivalent atoms are specified correctly in case.struct.

SGROUP: Determines the space group from case.struct file, as well as all point groups of non-equivalent sites

SYMMETRY: Generates the space group symmetry operations from the input data, and determines the point group of each atomic locations, and the rotation matrix corresponding to the operations which generates the spherical harmonics.

LSTART: A program, which generates the atomic densities and determines how the different orbitals are treated in the calculation of the band structure, like core states with or without local orbitals.

KGEN: Specifies the number of K-point in order to create a cell in the irreducible Brillouin zone (BZ).

DSTART: Generates an initial charge density for the Self-Consistent Field cycle by superimposing the atomic densities generated in LSTART.

Self-Consistent Field calculation:

When the initialization steps are complete, the SCF "Self-Consistent Field" cycle processes are then launched and iterated until the solution converges.

LAPW0: Generates the Coulomb (V_C) and exchange-correlation (V_{xc}) potentials as total potential (V) from the total electron density.

LAPW1: Sets up the matrix coefficients of the Hamiltonian in the LAPW wave base and finds, by diagonalization, the eigenvalues and the eigenvectors.

HF: Calculates the orbitals and eigenvalues for hybrid functionals using the 2nd variational procedure.

LAPWSO: Includes spin-orbit coupling (SOC) in a 2nd variational procedure and computes eigenvalues and eigenvectors using the scalar-relativistic wavefunctions from lapw1.

LAPW2: Calculates the valence densities from the eigenvectors and the Fermi energy.

LCORE: Determinates the core states inside the M spheres, keeping only the spherical part of the potential.

MIXER: Performs the mixing of the input and output densities (starting, valence and core).

If the calculations are performed without HF or SOC calculations HF and LAPWSO steps will removed.

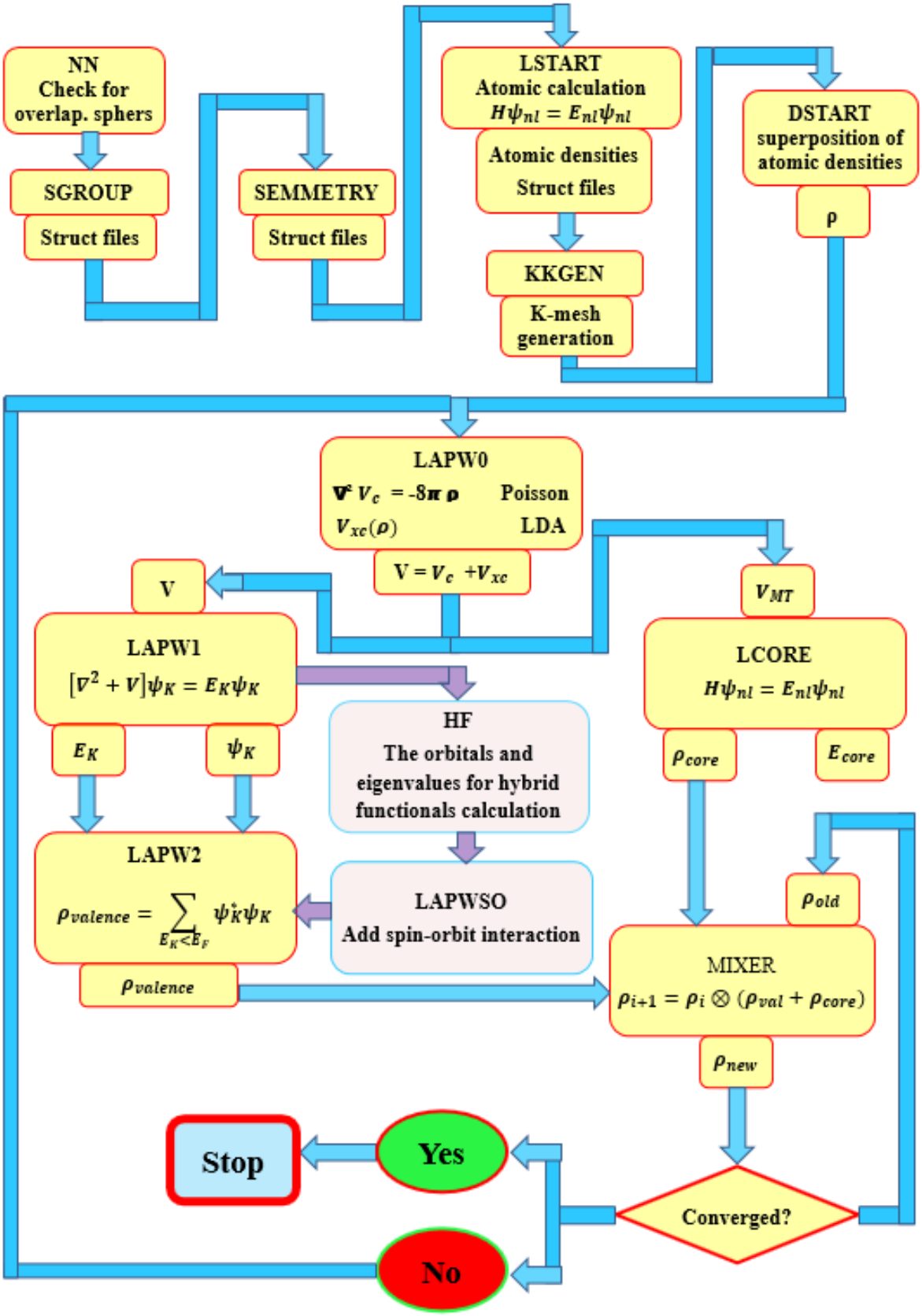

Figure II.5: Program flow in WIEN2k software

II. 3. 5. Boltzmann transport theory

Similar to numerous scientific discovers, the comprehension of the thermoelectric effect came through the common curiosity of the scientific community. In 1822s, Thomas Johann Seebeck observed the relationship between magnetism and heat. Moreover, in 1823s Seebeck presented the first thermoelectric generator which convert heat energy directly to electrical one calling this phenomenon by the thermoelectric effect [74]. Furthermore, the transport theory deals with the flow of charges and heat passing through a solid material under the effect of an external field (electric field (E) and/or gradient of temperature). Boltzmann's semi-classical transport theory has been proven its validity in many applications including the calculation of transport coefficients which could be easily compared to the experiment results. The Boltzmann transport equation is a powerful tool to describe the transport behavior of non-uniform temperature systems (non-thermodynamic equilibrium systems) [75].

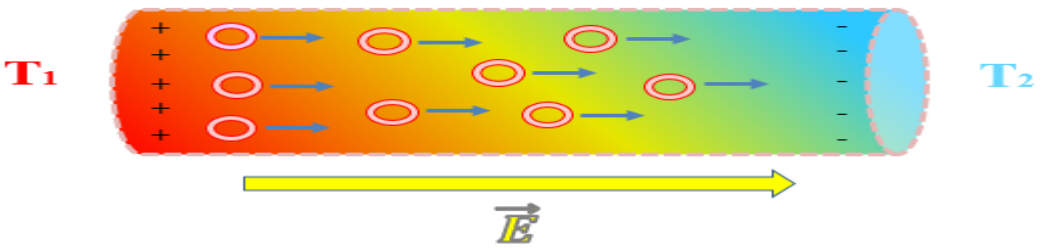

Figure II.6: Charge Carrier Diffusion ; where $T_1 > T_2$. In the example above, electrons are the charge carriers represented by the pink circles. The temperature gradient causes the charge carriers to move toward the cooler side until an equilibrium state is reached

II. 3. 5. 1. Boltzmann's equation

Boltzmann's transport theory provides a method of calculating the thermoelectric transport coefficients by describing describes the evolution of a distribution function *f* (n,*k*), influenced by an external electric field *E* and a temperature gradient ∇T. This distribution function *f*(*n*,*k*) provides the probability of finding an electron in band *n* with wave vector *k* at time t. Thus, the Boltzmann equation is:

$$-\left(\frac{\partial f^0(n,\vec{k})}{\partial \varepsilon\left(n,\vec{k}\right)}\right)\vec{v}\left(n,\vec{k}\right)\left[\frac{\varepsilon\left(n,\vec{k}\right)}{T}\nabla T + e\vec{E} - \nabla\mu\right] = -\left(\frac{\partial g(n,\vec{k})}{\partial t}\right)_{sc} \qquad \textbf{(Eq. II. 32)}$$

Herein, $\partial f^0(n,k,t)$ term represents the equilibrium distribution, $\partial\varepsilon(n,k,t)$ and $v\,(n,k,t)$ being the energy of an electron and velocity of an electron in band *n* with wave vector k at time

t, respectively. e is the electron charge, T is the temperature, *E* represents the external electric field, μ is the chemical potential while the difference between the equilibrium Fermi function $f^0(n,k,t)$ and the Fermi function influenced by an external electric field or temperature gradient $f(n,k,t)$ is represented by $g(n,k,t)$ term ($g(n,k,t) = f(n,k,t) - f^0(n,k,t)$), the distribution function $f(n,k,t)$ of an electron in band *n* with wave vector k at time t can vary due to the following three processes:

- The electrons diffusion by temperature or concentration gradients.
- The electrons acceleration by an external field.
- The electrons scattering by phonons, lattice defects or impurities.

The variation in time of the total distribution can be expressed as the sum of these three contributions:

$$\left(\frac{\partial f}{\partial t}\right) = \left(\frac{\partial f}{\partial t}\right)_{diffusion} + \left(\frac{\partial f}{\partial t}\right)_{field} + \left(\frac{\partial f}{\partial t}\right)_{scattering} \qquad \textbf{(Eq. II. 33)}$$

To simplify the Boltzmann's transport equation, the constant relaxation time approximation is adopted. The relaxation time (τ) represents the time it takes for an electron distribution to relax to the equilibrium Fermi distribution from a non-equilibrium state. In this approximation, the τ is assumed to be independent of position and velocity. The analytical expressions of the Boltzmann equation within the τ approximation becomes:

$$-\left(\frac{\partial f^0(n,\vec{k})}{\partial \varepsilon(n,\vec{k})}\right)\vec{v}(n,\vec{k})\left[\frac{\varepsilon(n,\vec{k})}{T}\nabla T + e\vec{E} - \nabla\mu\right] = -\frac{\partial g(n,\vec{k})}{\tau} \qquad \textbf{(Eq. II. 34)}$$

Where the group velocity is expressed as follows:

$$\vec{v}(n,\vec{k}) = \frac{1}{\hbar}\left(\frac{\partial \varepsilon(n,\vec{k})}{\partial \vec{k}}\right) \qquad \textbf{(Eq. II. 35)}$$

II. 3. 5. 2. Overview of the transport coefficients derivation and BoltzTrap Software

After the determination of the distribution function, the thermoelectric coefficients can be obtained through the electrical-current density and the heat current density known as the Onsager relations [76]:

$$j = \sigma E_0 + \sigma S \nabla T \qquad \textbf{(Eq. II. 36)}$$

$$j_Q = \sigma S T E_0 + \kappa \nabla T \qquad \textbf{(Eq. II. 37)}$$

Where σ, S being the electric conductivity the Seebeck coefficient, respectively. While κ term represents the thermal conductivity. Therefore, it is possible to investigate all the transport coefficients including the Seebecke coeffects, thermal and electrical conductivities from the conductivity distributions $f_\mu(T, \varepsilon)$ determined by the Boltzmann transport equation:

$$\mathbf{S}_{\alpha\beta}(T,\mu) = \frac{1}{eT\Omega\sigma(T,\mu)} \int \sigma(\varepsilon)(\varepsilon-\mu)\left[-\frac{\partial f_\mu(T,\varepsilon)}{\partial\varepsilon}\right] d\varepsilon \qquad \textbf{(Eq. II. 38)}$$

$$\sigma_{\alpha\beta}(T,\mu) = \frac{1}{\Omega} \int \sigma(\varepsilon)\left[-\frac{\partial f_\mu(T,\varepsilon)}{\partial\varepsilon}\right] d\varepsilon \qquad \textbf{(Eq. II. 39)}$$

$$\mathbf{k}(T,\mu) = \frac{1}{e^2 T\Omega} \int (\varepsilon-\mu)^2 \sigma(\varepsilon)\left[-\frac{\partial f_\mu(T,\varepsilon)}{\partial\varepsilon}\right] d\varepsilon \qquad \textbf{(Eq. II. 40)}$$

Where N represents the number of K-point for the integral in the Brillouin zone, Ω is the volume of the unit cell while σ (ε) represents the conductivity tensors which can be obtained from the following equation:

$$\sigma(\varepsilon) = \frac{1}{N} \sum_{i;k} \sigma(k) \frac{\partial(\varepsilon-\varepsilon_k)}{\partial(\varepsilon)} \qquad \textbf{(Eq. II. 41)}$$

In 2006s, Georg Madsen and David Singh developed the BoltzTrap software which allows to calculate the semi-classical transport coefficients based on a smoothed Fourier interpolation of the bands to solving the Boltzmann's equation using the relation time [77]. The interpolated band structure is used to calculate the transport coefficients. Thus, it is necessary to compute the band structure through wien2k software before using BoltzTrap software. Authoritative and comprehensive discussions of the transport coefficients derivation can be found in a range of excellent review articles [78,79] and textbooks [74,75,77].

II. 4. Conclusion

To conclude, the different theoretical methods and softwares used to determine the physical properties of the understudy compounds with different approximations that used in this thesis were described in this chapter.

Chapter III : The new eco-friendly lead-free zirconate perovskites doped with chalcogens for solar cells: Ab initio calculations

III. 1. Introduction

The most efficient solar cells are using Pb-based oxide perovskites. Regrettably, due to the high perceived toxicity of Pb, this may hinder the pace of commercialization of Pb oxide perovskites [38 – 42]. On the way to non-toxic perovskite solar cells, Lead-Free Zirconate perovskites $AZrO_3$ (A = Ca, Ba and Sr) have recently attracted widespread attention from researchers because they are environmentally friendly and as well as due to their outstanding properties [80 – 82], for instance: ferroelectricity, piezoelectricity [80 – 83] superconductivity, magnetoresistance, photoluminescence, nonlinear optical properties [84, 85], they have chemical inertness and high proton conductivity [82, 86], chemical and mechanical stability in a wide range of temperatures and a large dielectric constant [87, 88]. They can be synthesized using low-cost preparations methods such as sol-gel, propionic acid routes, solid-state reaction and sputtering [85, 89, 90]. They have a variety of a crystallographic structure which undergo a paraelectric transition from cubic to tetragonal, a ferroelectric transition from tetragonal to orthorhombic and lastly from orthorhombic to rhombohedral [84, 91]. The cubic symmetry (Pm3m) is the ideal structure for $AZrO_3$ [92, 93]. For these reasons, $AZrO_3$ (A = Ca, Ba and Sr) have a large and various of high technology applications, including photoelectric devices [86, 92 – 94], solid-oxide fuel cells, nuclear industry [86, 95], hydrogen sensors and hydrogen separation membranes [88, 96, 97], microelectronics industry [98], charge storage devices as well as electrolyzers [96, 97]. And they also led to emergence of novel oxide interfaces phenomena [99]. Currently, $AZrO_3$ become as one of the most promising optical devices [86, 92]. However, the large forbidden band width of $AZrO_3$ (4.85 eV – 5.7 eV) reduces the solar absorption, mainly in the visible spectrum which present the highest percentage of the solar spectrum [86, 92]. Until now, no satisfactory solution has been proposed. The wide forbidden band width of $AZrO_3$ can be narrowed by changing the composition of the materials, hence modifying the electronic structure properties. Based on this, several experimental and theoretical studies have been done to enhance the absorption in the visible spectrum including; Kunti et al. [100], successfully synthesized the undoped and Eu^{3+} doped $BaZrO_3$ phosphor using solid-state reaction method at 1400 °C for 4 hours via B-sites substitution which caused a reduction of the forbidden band width. Yuan et al. [101], studied structural, chemical and optical properties of $BaZr_{1-x}Sn_xO_3$ (x = 0, 0.25, 0.50) using density functional theory. They reported

that the increase of Sn content in the compound resulted in decreasing the forbidden band width. Furthermore, they synthesized successfully, Sn doped-$BaZrO_3$ by an improved Pechini-type process at 1000 °C for 6 hours, through which the theoretical results were confirmed. Similarly, Meng et al. [92], Borja-Urby et al. [102], and Khan et al. [103], reported the synthesis of the undoped and Fe, Bi and Ta doped- $BaZrO_3$ by solvothermal process using ethanediamine (EDA) as solvent, hydrothermal process at 100 °C for 24 hours and the precipitation from homogenous solution method at 1000 °C for 12 hours respectively. Showing the improvement of photocatalytic activity for hydrogen generation due to their reduction of forbidden band with visible light absorption, which in turn, was caused by Fe, Bi and Ta dopant.

This study sheds a new light on non-toxic Lead-Free zirconate perovskites semiconductors for solar cells application by studying the effect of different concentrations of chalcogens-doped $AZrO_3$ (A = Ba, Sr and Ca) on the electronic and optical properties.

III. 2. Computational technique methodology

Our ab initio calculations were performed basing Density Functional Theory [104], implemented in the WIEN2K software [73], using Kohn-Sham equations in the Full Potential Linearized Augmented Plane wave method within Local Density Approximation and modified Becke and Johnson (LDA+mBJ) [60, 67] have been used for the exchange correlation potential. In this study were Lead-Free Zirconate perovskites $AZrO_3$ (A = Ca, Ba and Sr) have been doped with oxygen group elements (chalcogens), while the oxygen atoms are substituted by the chalcogens (Sulfur (S), Selenium (Se) or Tellurium (Te)) with different concentrations of 4.1667%, 8.333%, and 12.500% corresponding to I, II, and III respectively. Hereafter, chalcogens-doped $AZrO_3$ structures are presented by X@OI, X@OII, and X@OIII, respectively. The unit-cell of the pure $AZrO_3$ (A = Ca, Ba and Sr) consisting 5 atoms 1*1*1 supercell (1 A atom, 1 Zr atom and 3 O atoms) have been used in the geometrical optimization, while 40 atoms (8 A atoms, 8 Zr atoms and 24 O atoms) 2*2*2 supercell were utilized for the electronic and optical properties. The Monkhorst–Pack k-mesh in Brillouin zone were selected as 6×6×6 and 4×4×4 for the optimization of the lattice parameters and the calculations of electronic and optical properties respectively.

III. 3. Results and discussion

III. 3. 1. Structural properties

The optimization of lattice parameters of $CaZrO_3$ (CZO), $BaZrO_3$ (BZO) and $SrZrO_3$ (SZO) was carried out. BZO and SZO are by 0.86% and 0.16% smaller than the detecting experimental data values of 4.19 Å [100] and 4.109 Å [105] for BZO and SZO respectively, while CZO is by 1.23% larger than the experimentally corresponded data value of 4.02 Å [106], and all deviations are below 1.3%. **Table III.1** illustrates that there is a perfect agreement between our results and the experimental data, as well as other theoretical results. Murnaghan's equation of state was used to optimize the crystal structures. **Figure III.1** pinpoints the atomic occupations and the unit cell and total energy versus the volume fitting of CZO, BZO and SZO respectively.

Table III.1: Relaxed structures of CZO, BZO and CZO in this work, compared with the experimental data and other theoretical results

	Lattice parameter a (Å)		
Compound	**Present work**	**Experimental**	**Theoretical**
CZO	4.0696	4.0200 [106]	4.0635 [107]
BZO	4.1540	4.1900 [100]	4.1570 [87]
SZO	4.1023	4.1090 [105]	4.1950 [98]

CZO

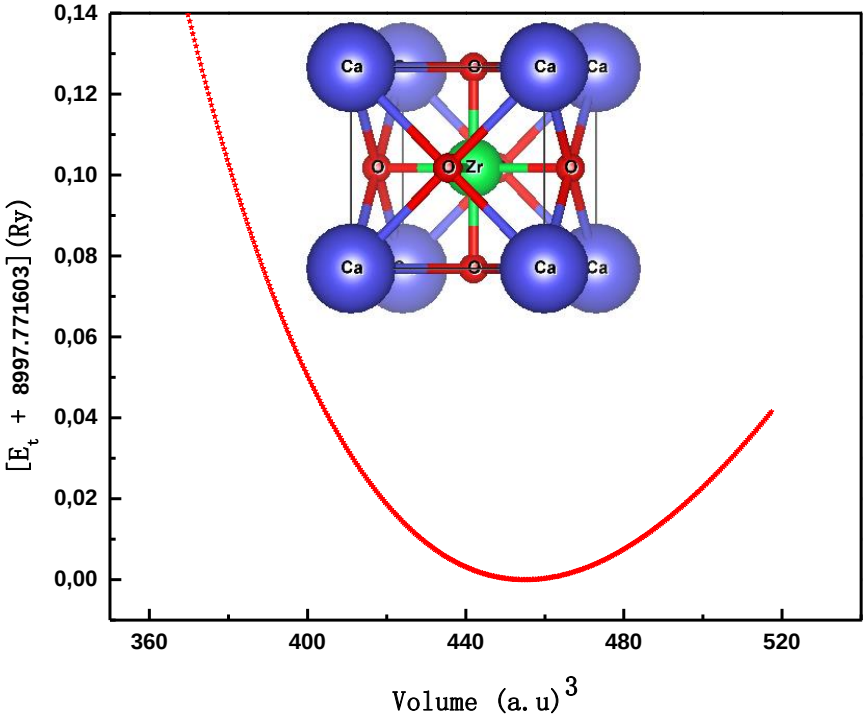
0,14
0,12
0,10
0,08
0,06
0,04
0,02
0,00
[E_t + 8997.771603] (Ry)
360
400
440
480
520
Volume (a.u)^3
Ca
O
Zr

BZO

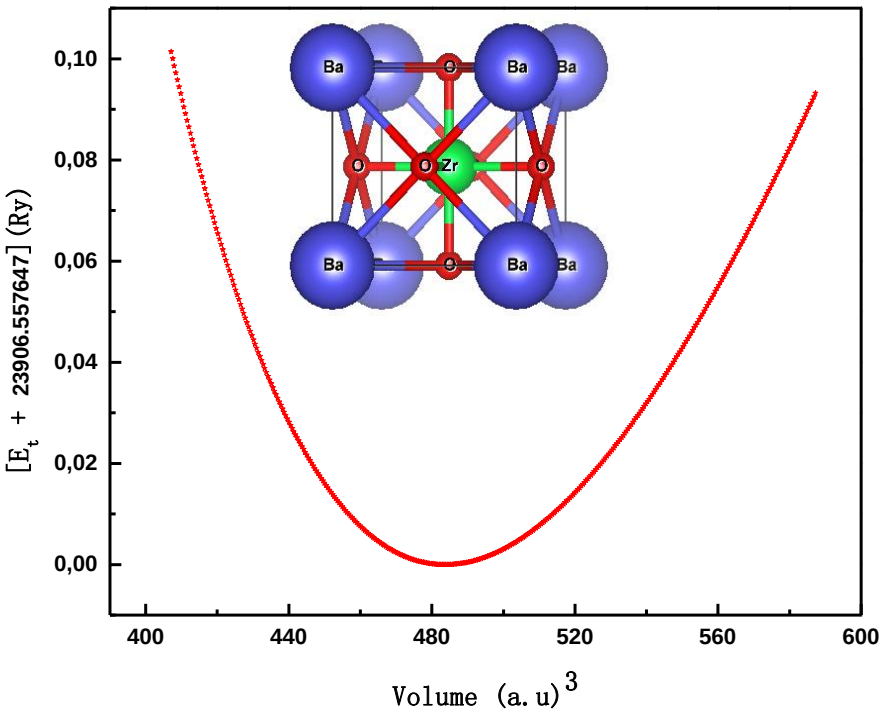
0,10
0,08
0,06
0,04
0,02
0,00
[E_t + 23906.557647] (Ry)
400
440
480
520
560
600
Volume (a.u)^3
Ba
O
Zr

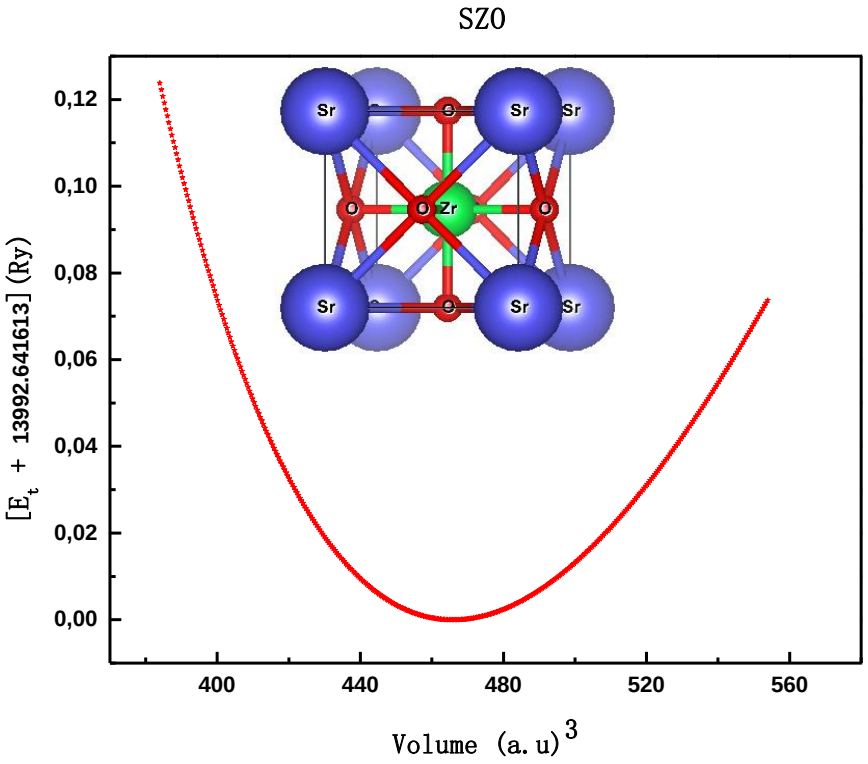

Figure III.1: The unit cell, and the total energy versus the volume of CZO, BZO and SZO

III. 3. 2. Electronic properties

The Total densities of states (TDOS) of undoped and doped $AZrO_3$ (A = Ca, Ba and Sr) are plotted in **Figure II.2**. In accordance with **Figure II.2** the upper VB of all compounds is predominantly composed of O-2p orbitals with some admixture of Zr-4d orbitals. Moreover, the bottom CB is principally composed of Zr-4d orbitals with a slight admixture of Ba-5d orbitals for BZO, Zr-4d orbitals with a small admixture of Sr-4d orbitals for SZO, and mostly composed of Ca-3d and Zr-4d orbitals for CZO. These outcomes of the pure $AZrO_3$ are in complete agreement with the experimental data [108], as well as other theoretical results [107]. Consequently, the calculated forbidden bands values are 4.963 eV, 4.645 eV and 4.949 eV for CZO, BZO and SZO respectively. These findings are in good agreement with the experimental data values of (4.850 eV – 5.350 eV) [100, 108] and 5.600 eV [109] for BZO and SZO, respectively. For CZO the forbidden band width of the cubic phase has not been measured experimentally. For the orthorhombic phase, the experimental value of forbidden band width is 5.700 eV [85]. **Table II.2** summaries the results obtained in comparison with the reported experimental data values, as well as previous studies. While after doping $AZrO_3$ with oxygen group elements (X = Se, Te and S), new states have been appearing in the valence and conduction bands. Hence, the overall nature of the densities of states of all compound are

altered. The upper VB is principally composed of O-2p and X-p orbitals in all cases, with 3p, 4p and 5p orbitals for S, Se and Te, respectively. Moreover, the VB maxima (VBM) above the Fermi level is composed by X-p orbitals for all compounds. Furthermore, when the O sites are replaced with chalcogens, the DOS illustrate that with the increase of chalcogens' concentration, the bottom CB is mostly consisting of Ca-3d and Zr-4d for CZO, Zr-4d and Sr-4d orbitals for SRO and of Zr-4d and Ba-5d orbitals for BZO. On the other hand, the CB minima (CBM) of AZOX is mainly composed by X-d, Zr-4d, A-d and O-2p orbitals, with X-d = S-3d, Se-4d and Te-5d states, A-d = Ca-3d, Sr-4d and Ba-5d states. Indicating that the doping with oxygen group elements has a noticeable influence on the VBM and CBM of $AZrO_3$ compounds. **Table II.2** illustrates that the forbidden band of all compounds was reduced by different degrees due to the substitution of chalcogens by oxygen atoms. Moreover, the forbidden band decreases with increasing the chalcogens' concentration due to the enhances of its charge carriers' mobility, Specially for Te and Se substitutions. Moreover, with 8.333% of Se the forbidden band in all cases is below 0.5 eV. Additionally, at 12.500% the Te causes overlapping valence and conduction bands. Hence, AZOX became conductors. Whereas the ideal value corresponding to the maximum theoretical of the PCE, for a semiconductor PV solar cells is 1.4 eV [110].

Table III.2: The calculated forbidden band (Eg) for the pure and doped $AZrO_3$

		Eg (eV)		
	Concentration (%)	**CZOX**	**BZOX**	**SZOX**
	Pure	4.963 5.700 [85] 3.283 [107]	4.645 4.850 [108] - 5.350 [100] 4.790 [111]	4.949 5.600 [109] 4.700 [80]
X=S	4.167	3. 673	3.632	3.728
	8.334	3.509	3.497	3.576
	12.500	1.531	1.842	1.706
X=Se	4.167	2.955	3.019	3.045
	8.334	2.779	2.864	2.886
	12.500	0.040	0.490	0.251
X=Te	4.167	1.531	1.740	1.659
	8.334	1.333	1.552	1.476
	12.500	0.000	0.000	0.000

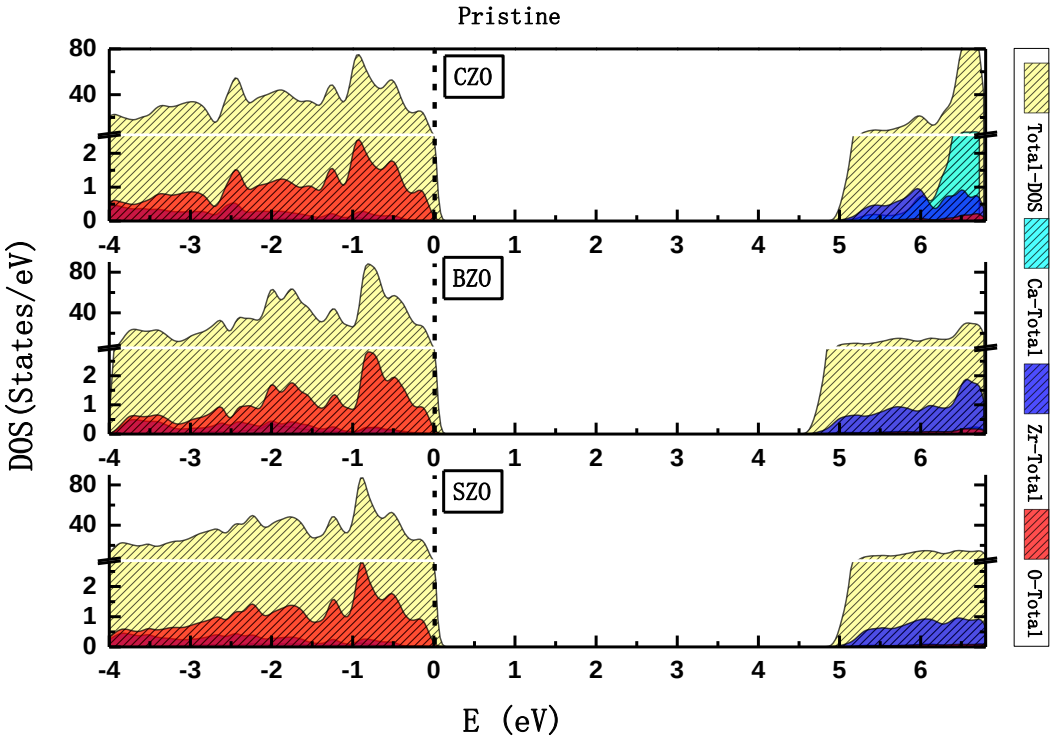
Pristine
CZO
BZO
SZO
DOS (States/eV)
E (eV)
Total-DOS
Ca-Total
Zr-Total
O-Total

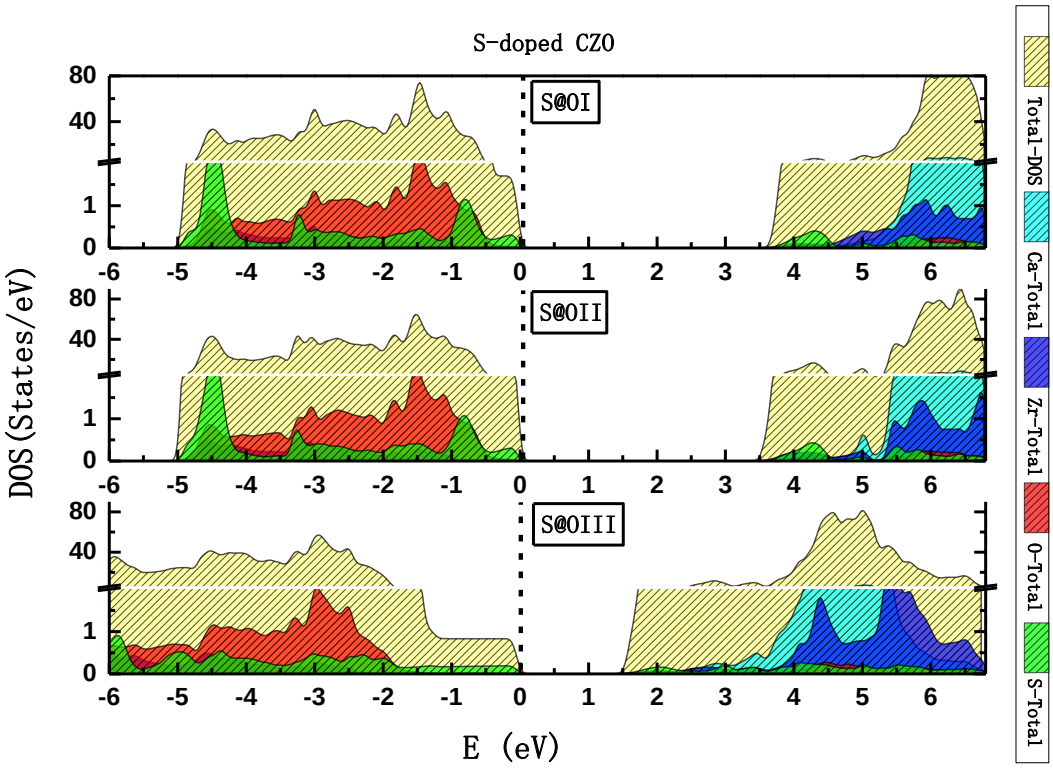
S-doped CZO
S@OI
S@OII
S@OIII
DOS (States/eV)
E (eV)
Total-DOS
Ca-Total
Zr-Total
O-Total
S-Total

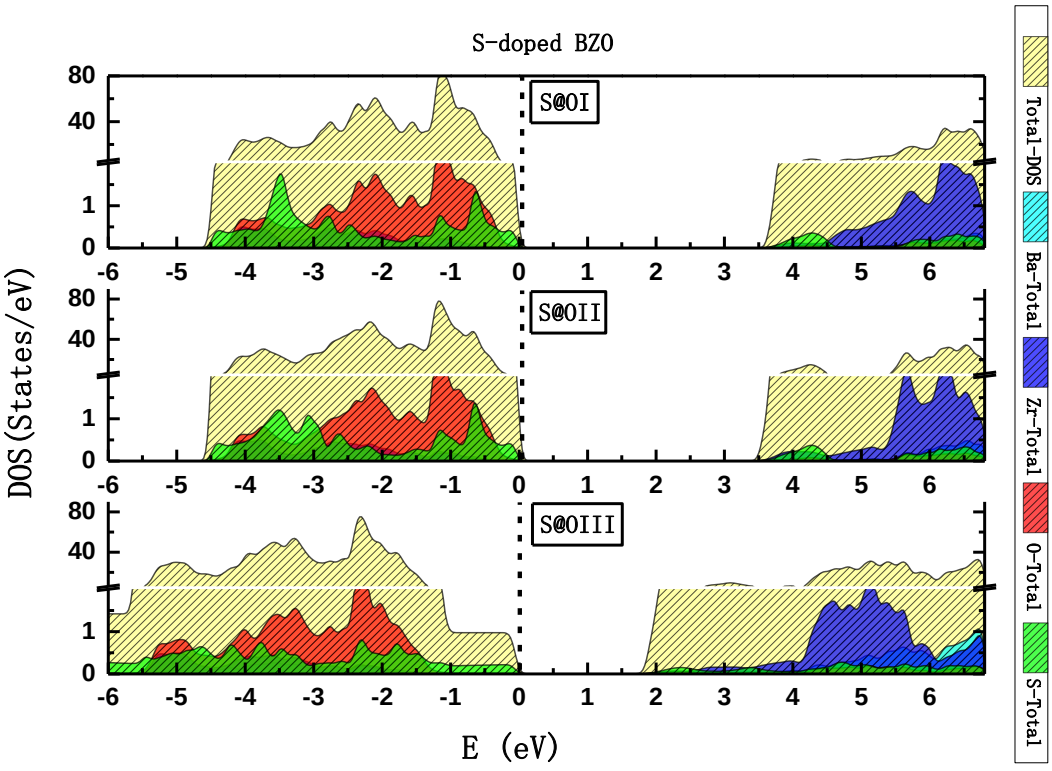
S-doped BZO
S@OI
S@OII
S@OIII
DOS(States/eV)
E (eV)
Total-DOS
Ba-Total
Zr-Total
O-Total
S-Total

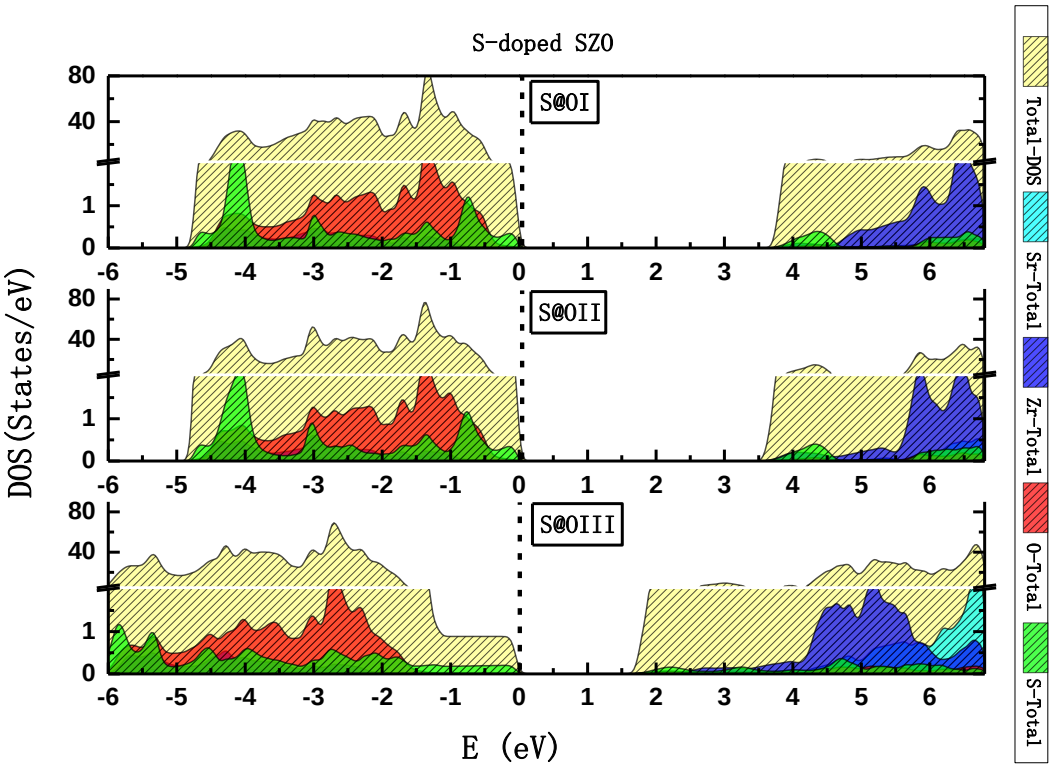
S-doped SZO
S@OI
S@OII
S@OIII
DOS(States/eV)
E (eV)
Total-DOS
Sr-Total
Zr-Total
O-Total
S-Total

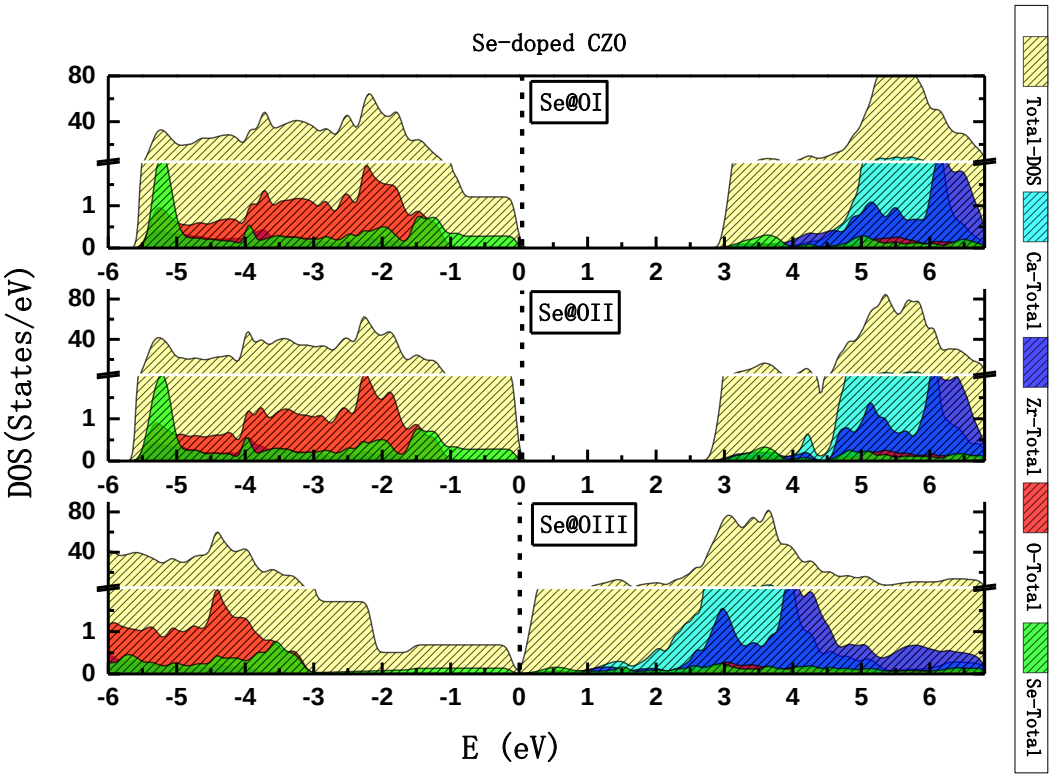
Se-doped CZO
Se@OI
Se@OII
Se@OIII
DOS(States/eV)
E (eV)
Total-DOS
Ca-Total
Zr-Total
O-Total
Se-Total

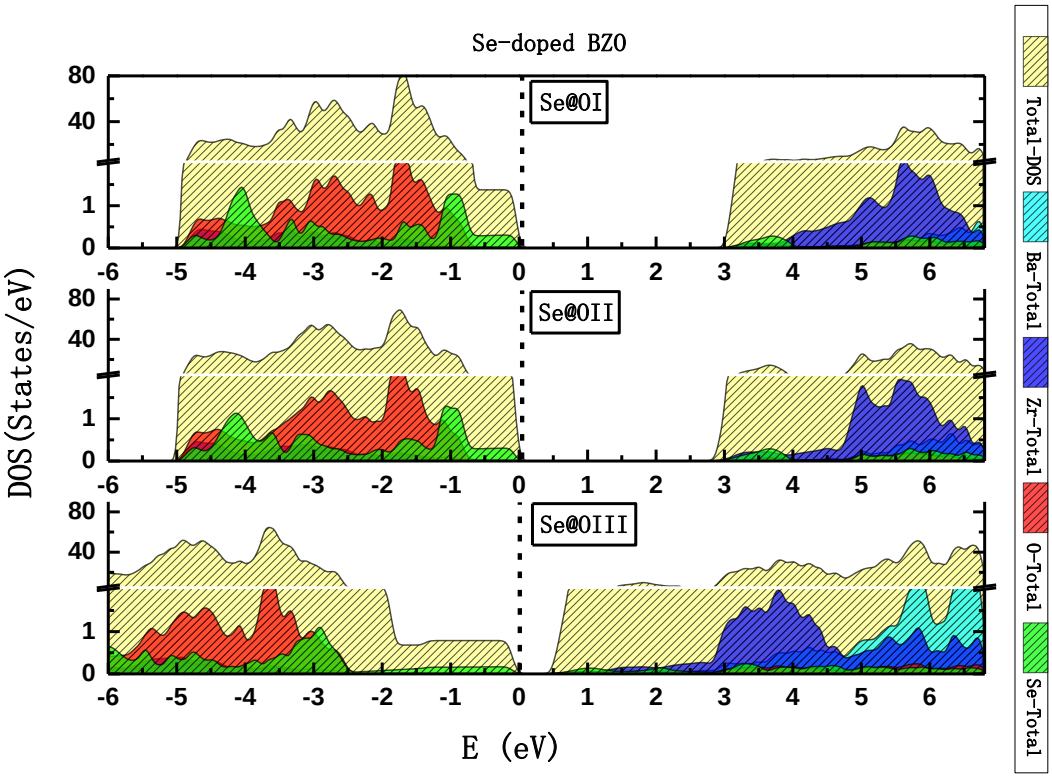
Se-doped BZO
Se@OI
Se@OII
Se@OIII
DOS(States/eV)
E (eV)
Total-DOS
Ba-Total
Zr-Total
O-Total
Se-Total

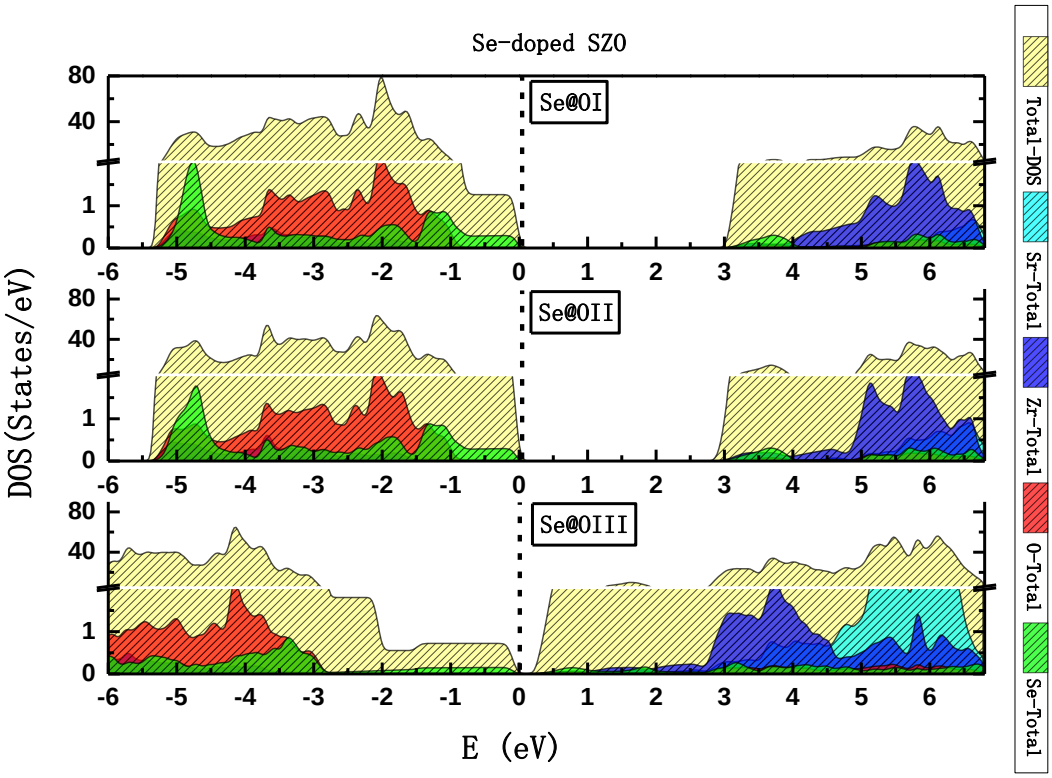
Se-doped SZO
Se@OI
Se@OII
Se@OIII
DOS (States/eV)
E (eV)
Total-DOS
Sr-Total
Zr-Total
O-Total
Se-Total

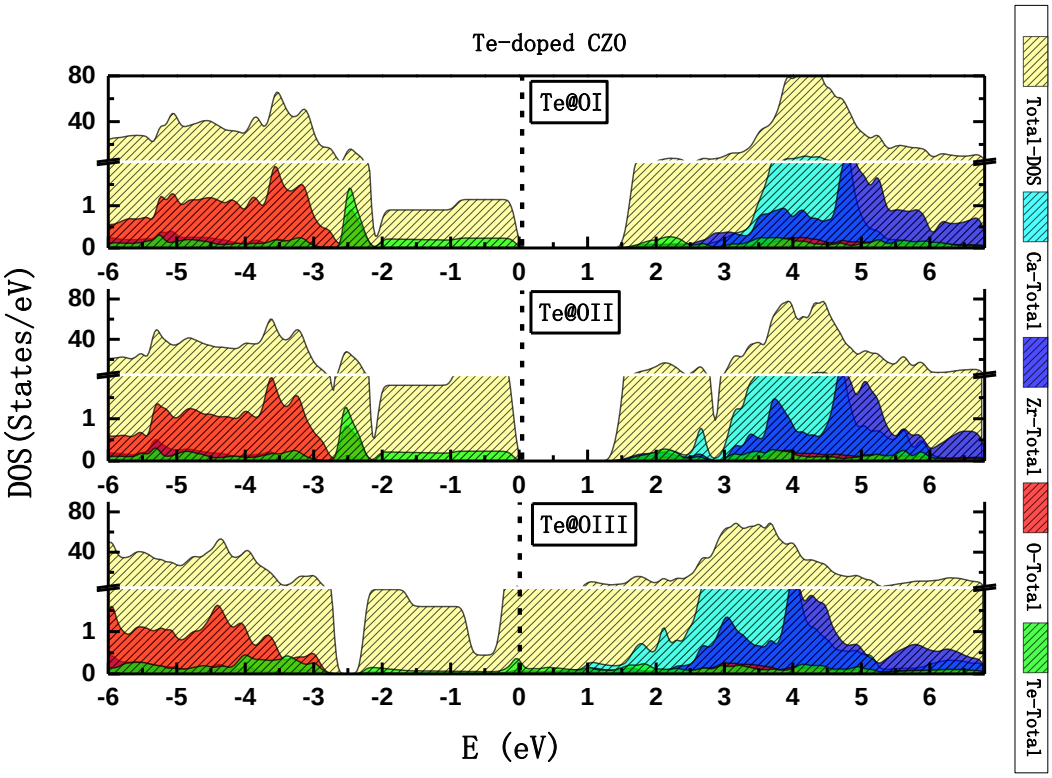
Te-doped CZO
Te@OI
Te@OII
Te@OIII
DOS (States/eV)
E (eV)
Total-DOS
Ca-Total
Zr-Total
O-Total
Te-Total

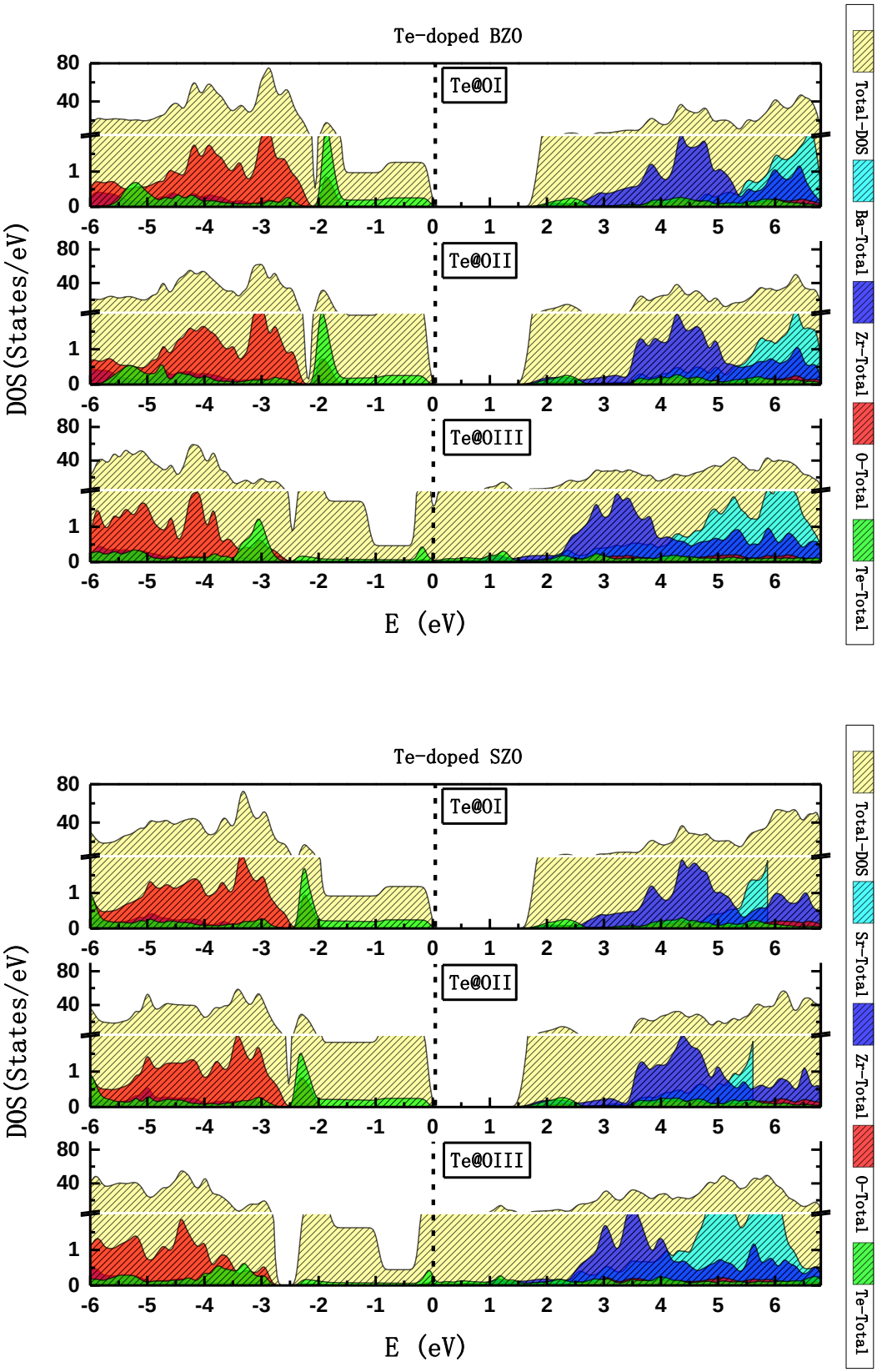

Figure III.2: Total and partial densities of states for the pure and doped $AZrO_3$

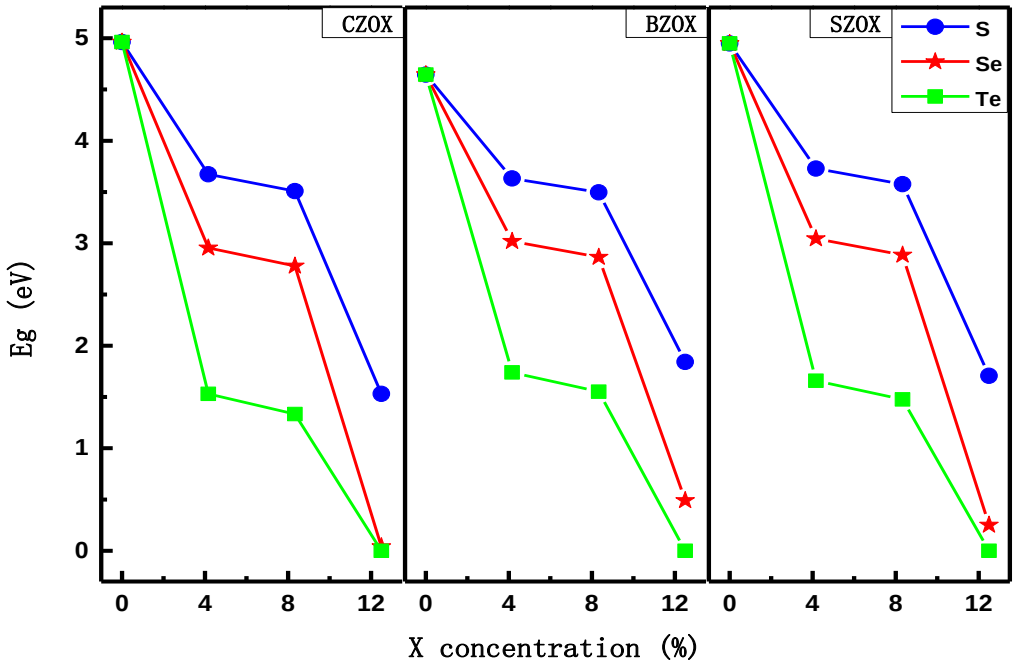

Figure III.3: Forbidden band of AZOX as a function of chalcogens' concentration with X = S, Se and Te

III. 3. 3. Optical properties

The efficient absorption of sunlight essentially the absorption of the visible light is a must drive the photovoltaic performance of materials, which indicates that the abundantly solar radiations are utilized effectively. Besides, the absorption coefficient α(ω), can be obtained based on the dielectric function from the following equation [112].

$$\alpha(\omega) = \sqrt{2}\,\omega\,[\sqrt{\varepsilon_1(\omega)^2 + \varepsilon_2(\omega)^2} - \varepsilon_1(\omega)]^{1/2} \qquad \textbf{(Eq. III.1)}$$

Where the complex dielectric functions (the real $\varepsilon_1(\omega)$ and imaginary $\varepsilon_2(\omega)$ parts) are calculated using the below equation.

$$\varepsilon_1(\omega) = 1 + \frac{2}{\pi}\rho_0 \int_0^{\infty} \frac{\omega' \varepsilon 2(\omega)}{\omega'^2 - \omega^2}\, d\omega \qquad \textbf{(Eq. III.2)}$$

$$\varepsilon_2(\omega) = \frac{4\pi^2}{m^2\omega^2} \sum_{C,V} \int_{BZ} \frac{2}{(2\pi)^3} \left| M_{C,V}(k) \right|^2 \delta\,(E_C^k - E_V^K - h\omega)\, d^3k \qquad \textbf{(Eq. III.3)}$$

Where ω is the angular frequency, subscripts C and V represent conduction band and valence band, respectively. BZ is the first Brillouin zone, $|M_{C,V}(k)|$ is the momentum matrix element, k is reciprocal lattice vector, E_C^K and E_V^K are intrinsic energy level of the conduction band and valence band, respectively. **Figure II.4** illustrate that the absorption starts as the incident

radiations energy rises above the forbidden band energy, demonstrating that the pure $AZrO_3$ can only absorb the ultraviolet light for wavelengths less than 250 nm. Our findings appear to be well supported by the experimental data [92 ,93, 103], as well as other theoretical results [85, 113, 114]. Fortunately, a significant enhancement of absorption in the visible spectrum was observed when $AZrO_3$ doped with oxygen group elements. Furthermore, the enhancement increases with the increase of chalcogens' concentration up to 12.500%. **Figure II.4** illustrates that there are no peaks for the pure $AZrO_3$ in the visible spectrum, while a broad peak appears when $AZrO_3$ doped with Te (4.1667% - 8.333%). These enhancements of absorption in the visible spectrum are due to the reduction of the forbidden band energy which increases the number of photons absorbed in $AZrO_3$. Based on this, we have plotted the absorption coefficient as percentage of the pure and AZrOT structures (all results are plotted in the original paper [115]). It is worth mentioning that R+T+A=100%, the significance of this equation is that all the incident power is either absorbed, reflected or transmitted, where A, T, and R denotes the optical absorption, transmittance, and reflectivity respectively. At 456 nm (441 nm), the absorption coefficient is 16% for the pure CZO (SZO), 53% for 4.1667% of Te doped CZO (SZO), and 71% of 8.3333% of Te doped CZO (SZO). Moreover, at 443 nm, the absorption coefficient is 17% for the pure BZO, 56% for 4.1667% of Te doped BZO, and 73% of 8.3333% of Te doped BZO.

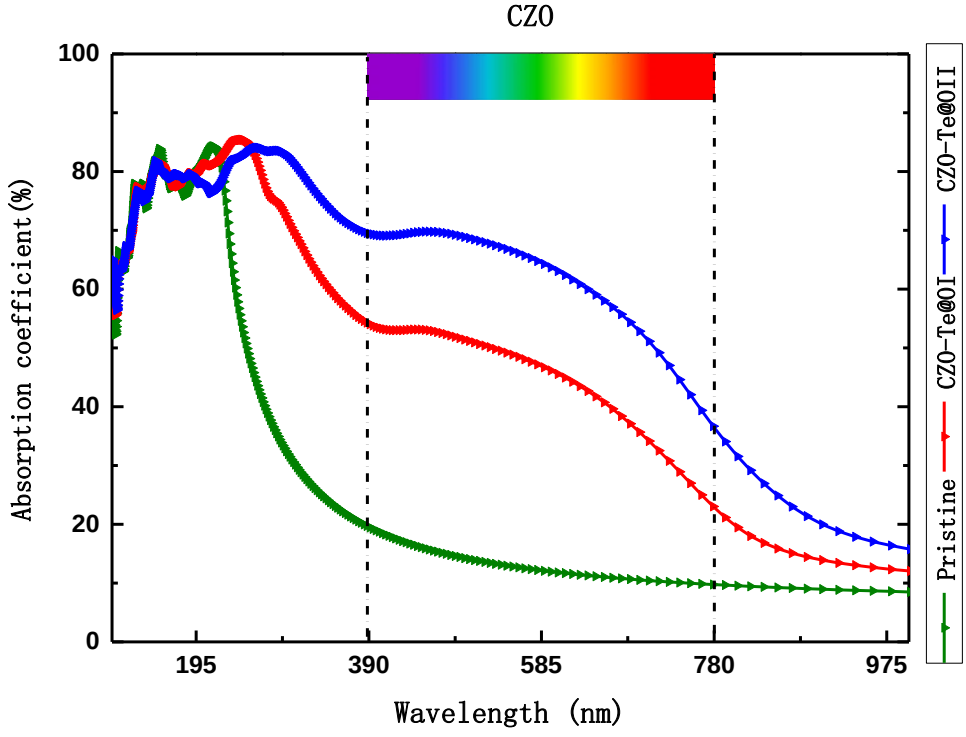

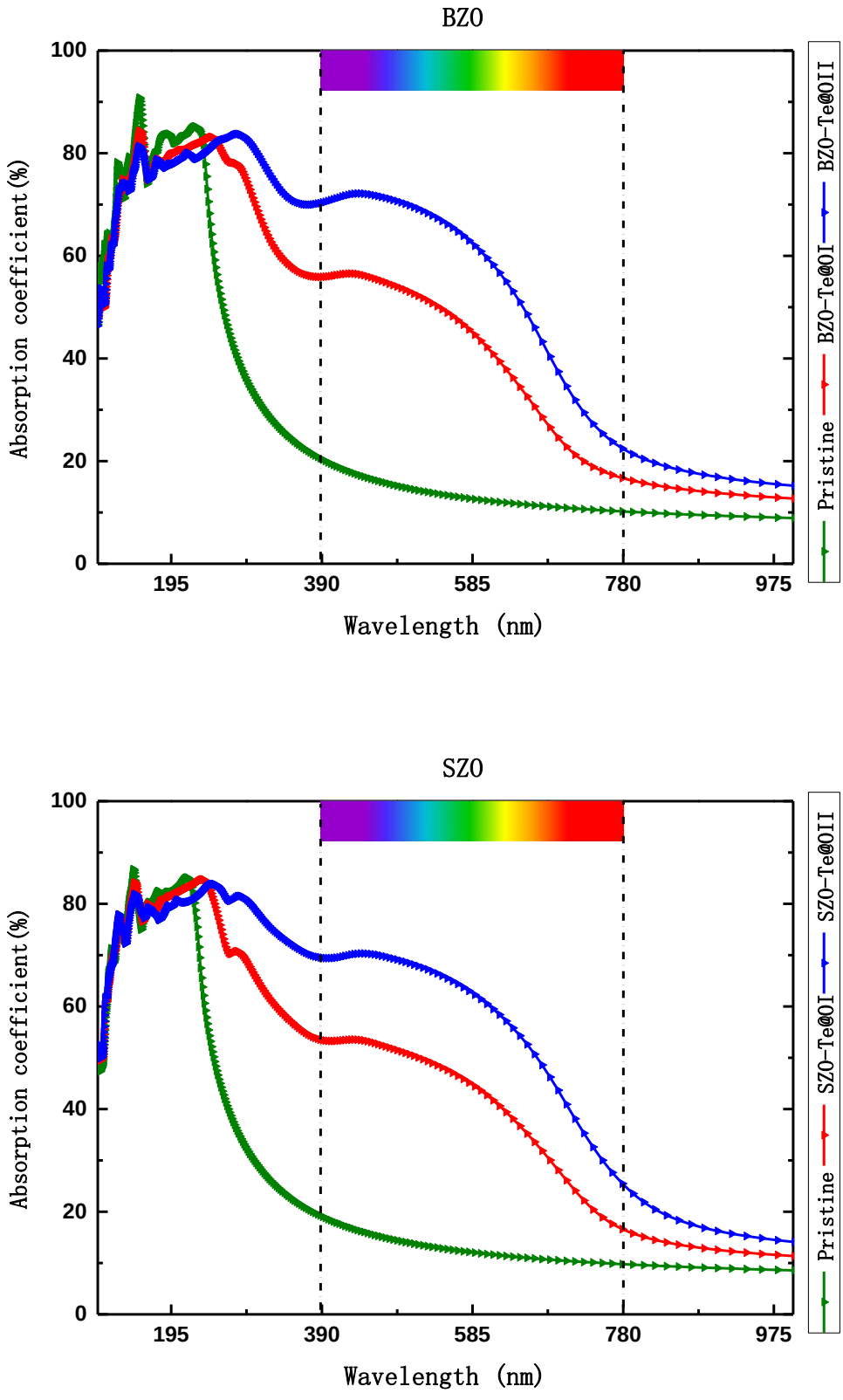

Figure III.4: Absorption coefficient for the pure and doped $AZrO_3$ with X = S, Se and Te

III. 4. Conclusion

In conclusion, we have studied the electronic and optical properties of Lead-Free Zirconate perovskites $AZrO_3$ (A = Ca, Ba and Sr) doped with different concentrations of chalcogens impurities (S, Se and Te) basing on density functional theory. This study has led to conclude that the doping with oxygen group elements has a noticeable influence on the VBM and CBM of $AZrO_3$. Hence, the Forbidden band of all studied compounds decreases with the increase of chalcogens' concentration up to 7.5%. Consequently, the absorption coefficient and the optical conductivity edge were progressively shifted to the visible spectrum especially for Te-doped $AZrO_3$. At the end of our research we obtained (AZrOTe) compounds which are good potential candidates for photovoltaic devices. Therefore, we encourage further research on our results, and we propose to synthesize this type of material using the Pechini-type sol-gel process [117].

Chapter IV : Chalcogens' impurities and a single F-center in perovskite $CaZrO_3$, $CaHfO_3$ and $SrHfO_3$ compounds: Ab initio calculations

IV. 1. Introduction

The Pb-free oxide perovskites solar cells (ABO_3) have received much attention over the last few decades, and they have emerged as promising materials for the next generation of solar cells [112, 115], Among the family of lead-free perovskites ABO_3, Calcium Zirconate ($CaZrO_3$), Calcium Hafnate $CaHfO_3$ (CHO) and Strontium Hafnate $SrHfO_3$ (SHO) perovskites have been considered as the most studied alkaline-metal zirconate and hafnate perovskites [115, 116], and they have gained substantial interest from the scientific community due to their high chemical and mechanical stabilities, they can be manufactured using low-cost preparations methods such as, propionic acid routes, sputtering and Pechini-type sol-gel process [89, 90, 117]. Their unique properties make CZO, CHO and SHO suitable for a very large range of applications, such as; coatings and mechanical filters [118], metal-oxide-semiconductor field-effect transistors (MOSFETs) [119], high-temperature technology (HTT) [120], and thermal barrier coatings (TBC) [121]. Therefore, the understudy compounds have been experimentally and theoretically studied extensively due to their outstanding properties. Moses Abraham et al. [122] investigated the structural, electronic, and lattice dynamical properties of CZO under high pressure up to 30 GPa, and it was found that the calculated phonon dispersion curves show the dynamical stability of CZO under studied pressure range while the obtained forbidden gap shows insulating behavior of CZO material and the increase in the forbidden gap under pressure is mainly due to anti-bonding and nonbonding nature of bands near the Fermi level. Erwan et al. [123] reported the photoluminescence properties of CHO, they observed that CHO has unexpectedly strong photoluminescence in the visible spectrum over a wide temperature range, exhibiting sensitivity exposure time to ultraviolet light as well. In 2004, Keisuke et al. [124] showed that it is possible to grow an insulating thin film of CHO on $SrTiO_3$. Moreover, in 2007 they found that interfaces between amorphous CHO films and $SrTiO_3$ substrates showed a high conductivity with no polar discontinuity [125]. Using molecular-beam epitaxy, Rossel et al. [126] synthesized the epitaxial deposition of thick layers below 1 nm on Si (100), indicating that SHO is a potential gate dielectric for metal-oxide-semiconductor field-effect transistors application due to its large bandgap (6.1 eV- 6.5 eV) [119, 127]. Alay-e-Abbas et al. [128] reported thermodynamic stability and vacancy defect formation energies in SHO, it was found that the oxygen vacancies in SHO produce defect levels between the conduction band and the

valence band, while cation defects lead the system into the hole-doped state, and the oxygen vacancies in HfO layers are energetically favorable. Despite this interest, no one as far as we know has studied the photocatalytic hydrogen production from water splitting properties of CZO, CHO and SHO perovskites and just a few works have studied the photovoltaic properties of the studied compounds due to their wide forbidden band (5.7 eV-6.5 eV) [85, 119, 123, 127], hence the understudy compounds are considered as insulators. It is worthwhile noting that the most common intrinsic defects in oxide materials are the oxygen vacancies which could be formed under high-energy particle irradiation or during the reduction process [129,130 – 132]. Moreover, Popov et al. [133] and Jayashree et al. [134] have already noted that the oxygen vacancies have several charges states: F^{++} center (O vacancy without electrons), F^{+} center (O vacancy with one-electron), F center (O vacancy with two-electrons), and F^{-} center (O vacancy with three electrons). Based on this, this paper takes the challenge to enable CZO, CHO and SHO to be applied as semiconductors for photovoltaic and photocatalytic hydrogen production from water splitting devices by the substitution of oxygen atoms by chalcogens impurities (S, Se, and Te) with different concentrations up to 12.5% taking into account the F-center defect (a neutral oxygen vacancy). To date, this study has not been applied to CZO, CHO and SHO perovskites. This paper is divided into four sections; the second section gives a brief overview of the computational details. In the third section, the results of the electronic, optical, and hydrogen production from water splitting properties of pristine CZO, CHO and SHO and chalcogens-doped CZO, CHO and SHO with and without the presence of F center defect in the understudy compounds are described. Our conclusions are presented in the final section.

IV. 2. Computational technique methodology

Undoped, chalcogens-doped CZO, CHO and SHO as well as chalcogens-doped with the presence of F-center in CZO, CHO and SHO compounds were carried out using Density Functional Theory [104], by adopting the Full Potential Linearized Augmented Plane Wave method implemented in the WIEN2K software [73] with spin-polarized calculations. It is worthwhile noting that the Local Density Approximation [60] underestimates the forbidden band value of semiconductor materials. In order to achieve an excellent agreement between the experimental forbidden band and the theoretical one, the LDA + the modified Becke and Johnson [60, 67] gives excellent results. Based on this, in our calculations, LDA+mBJ were used to describe the exchange-correlation potential to obtain the accurate forbidden band of the studied compounds. The alkaline-metal CZO, CHO and SHO crystallize in the ideal cubic

structure (Pm-3m) containing 5 atoms. A 2*2*2 supercell was done in order to get concentrations' impurities (X = S, Se, and Te) of 4.1667%, 8.33%, and 12.5% corresponding to I, II, and III respectively. In this work, the considered defect is the F-center because it is well known that the F centers are formed in oxide perovskites when neutral O atoms are removed from the regular lattice sites [135]. To simulate the F center defect (O vacancy with two-electrons), one O atom (δ = 4.1667%) was removed from 2*2*2 supercell. Hereafter, chalcogens-doped CZO, CHO and SHO structures are presented by X@OI, X@OII, and X@OIII, while the chalcogens-doped CZO, CHO and SHO with the presence of F center defect (an oxygen vacancy defect (Ov)) structures are presented by X@OI+Ov, X@OII+Ov, and X@OIII+Ov. The Monkhorst–Pack k-mesh in the Brillouin zone was selected as 7×7×7 and 4×4×4 for the lattice parameters optimization and the calculations of electronic and optical properties respectively.

IV. 3. Results and discussion

IV. 3. 1. Structural and electronic properties

IV. 3. 1. 1. Pristine SHO

Before examining the effect of chalcogens impurities and the oxygen vacancy defect on electronic, optical and photocatalytic properties of the understudy compounds, we must scrutinize the performance of LDA+mBJ functional in recreating the experimentally marked properties of bulk CZO, CHO and SHO. The optimized lattice constant of pristine compounds was carried out by fitting the plot of the total energy as a function of the volume using the Murnaghan equation and LDA approximation **(**see **Figure IV.1)**. As can be seen in **Table IV.1**, our result is in perfect agreement with the experimental data value as well as other theoretical results.

Table IV.1: Relaxed structures of CZO, CHO and SHO compared with the experimental data and other theoretical results

	Lattice parameter a (Å)		
Compound	**Present work**	**Experimental**	**Theoretical**
CZO	4.0696	4.0200 [106]	4.0635 [107]
CHO	4.0390	3.9900 [123]	4.0380 [136]
SHO	4.0738	4.0770 [137]	4.1250 [120]

CZO

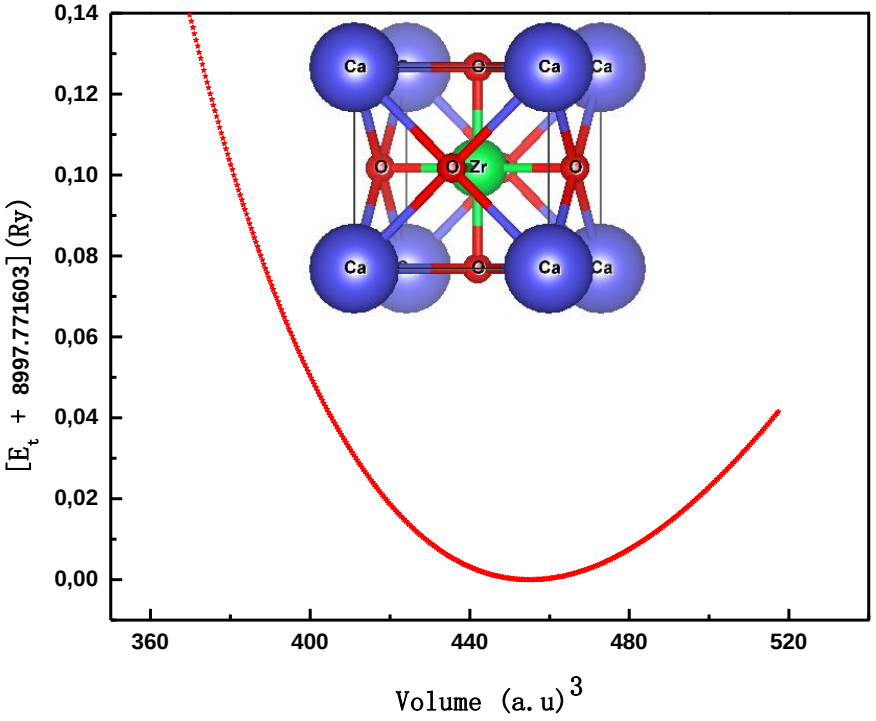
0,14
0,12
0,10
0,08
0,06
0,04
0,02
0,00
[E_t + 8997.771603] (Ry)
360
400
440
480
520
Volume (a.u)^3
Ca
O
Zr

CHO

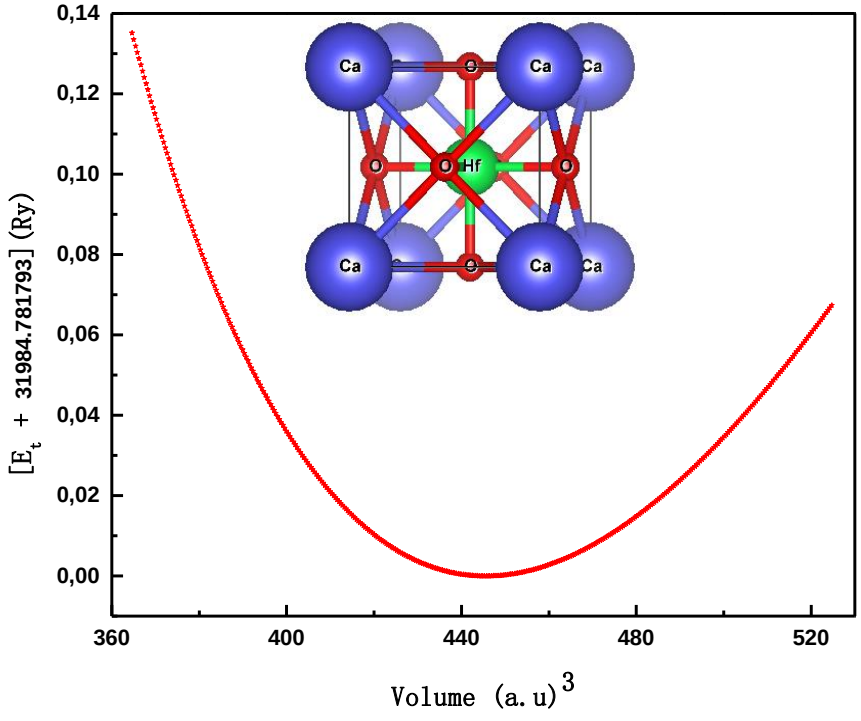
0,14
0,12
0,10
0,08
0,06
0,04
0,02
0,00
[E_t + 31984.781793] (Ry)
360
400
440
480
520
Volume (a.u)^3
Ca
O
Hf

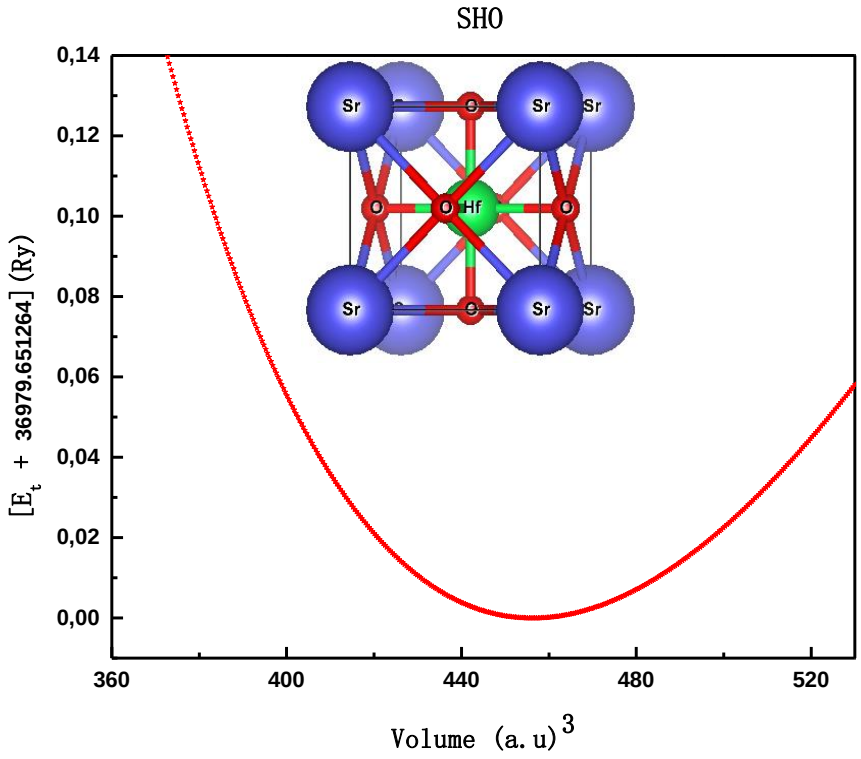

Figure IV.1: The unit cell, and the total energy versus the volume of CZO, CHO and SHO

The partial densities of electronic states of CZO, CHO and SHO have been plotted in **Figure IV.2**. The electronic structures of the studied compounds show insulators behavior. Moreover, the energy between the HOMO and the LUMO by LDA approximation is equal to 3.266 eV, 3.606 eV and 3.737 eV for CZO, CHO and SHO, respectively which lend support to previous findings in the literature [138, 139]. While it was found that the energy between the HOMO and LUMO by LDA+mBJ approximations is 4.963 eV, 5.830 eV and 6.071 eV for CZO, CHO and SHO, respectively. Therefore, the LDA+mBJ functional did not show any significant differences between our results and the experimental ones (see **Table IV.2**). As shown in **Figure IV.2**, the pristine CZO, CHO and SHO are indirect semiconductors because the HOMO is situated at R point while the LUMO is located at Γ point. Besides, O-2p orbitals are the most prominent in the upper VB with some admixture of Zr-4d / Hf-5d orbitals. Moreover, the bottom CB shows a strong hybridization between Ca-3d / Sr-3d and Zr-4d / Hf-5d orbitals with admixture of O-2p orbitales. The Fermi level is taken as the zero of energy and it is situated at the peak of HOMO, implying that pristine CZO, CHO and SHO have p-type electrical conductivities behaviors. These findings of pristine studied compounds are in complete agreement with previous studies [136, 139, 140].

Table IV.2: The calculated forbidden band of CZO, CHO and SHO compared with the experimental data and other theoretical results

	Eg (eV)		
Compound	**Present work**	**Experimental value**	**Theoretical study**
CZO	3.266 -LDA 4.963 -LDA+mBJ	------	3.283 [107] -LDA 4.600 [141] -TB-mBJ
CHO	3.606 LDA 5.830 -LDA+mBJ	6.200 [123]	5.270 [136] -TB-mBJ
SHO	3.737 LDA 6.071 -LDA+mBJ	6.1±0.1 [119]	3.500 [138] -LDA

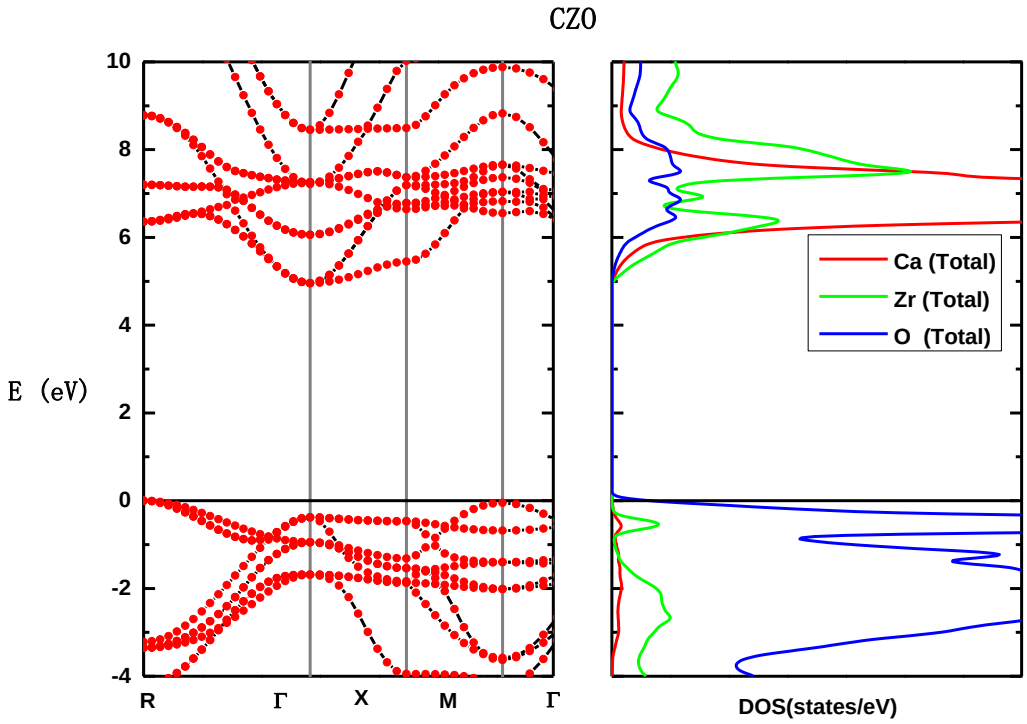

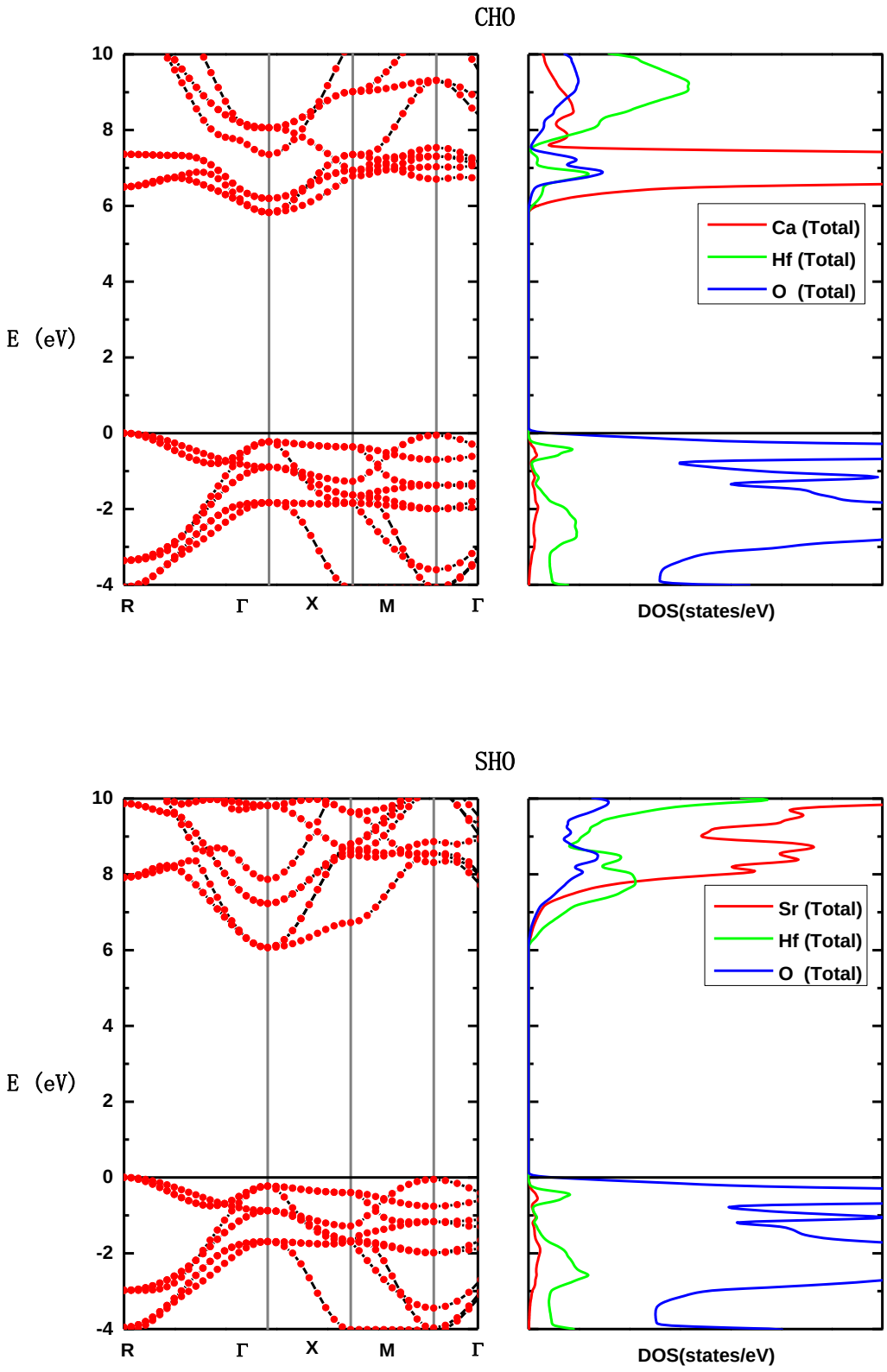

Figure IV.2: Partial densities of states and the band structure for the pristine CZO, CHO and SHO perovskites

IV. 3. 1. 2. Oxygen vacancy defect in CZO, CHO and SHO.

After the pristine calculations, one O atom was removed from the C_{4v} local symmetry. Thereafter, the atomic configuration of surrounding atoms is re-optimized, and it was found that the lattice parameter with the presence of F center defect is less than 0.3% smaller than the pristine compounds (0.122% for CZO,0.1968% for CHO, and 0.202% for SHO), indicating there is no structural phase transition accrues and the CZO/CHO/SHO+Ov have cubic structures. Furthermore, TDOS and the band structure of CZO, CHO and SHO with the presence of an Ov are illustrated in **Figure IV.3**. This figure shows significant differences between TDOS, PDOS and band structure when the understudy compounds contain an Ov, which means that an Ov is significantly influenced the electronic properties of CZO CHO and SHO. Moreover, a single intermediate band (red line) is formed between the HOMO and LUMO, because an Ov defect is usually trapped two electrons (two electrons in an oxygen-vacancy) [131 – 133]. Furthermore, **Figure IV.3** shows that the upper VB and the bottom CB compositions have similar characters as that of pristine CZO, CHO and SHO compounds. However, the forbidden band is slightly decreased by 0.3630 eV, 0.4100 eV and 0.1346 eV compared to pristine CZO, CHO and SHO, respectively due to the formation of an intermediate band. Furthermore, the intermediate band positioned above the Fermi level which is composed of Ca-3d orbitals for CZO compound and of O-2p orbitals for CHO and SHO compounds. In the SHO+Ov case, at **Γ** point the intermediate band is located 2.36 eV above the HOMO and 1.33 eV below the LUMO by LDA approximation. This supports previous findings in the literature. Abass et al. [128] found that the intermediate band of SHO is situated 2.331 eV above the HOMO and 1.518 eV below the LUMO while Lupina et al.[138] found the intermediate band is too close (closer than 1 eV) to the CB by LDA approximation. Otherwise, we are already demonstrated that the LDA approximation did not give the accurate forbidden band of pristine compounds while the LDA+mBJ functional did not show any significant differences between our results and the experimental ones. Hence, the accurate position of the intermediate band is 2.2863 eV above the HOMO and 2.5989 eV below the LUMO for CZO, 2.25983 eV above the HOMO and 3.4651 eV below the LUMO for CHO, and in the case of SHO is 2.46 eV above the HOMO and 3.53 eV below the LUMO by the LDA+mBJ function.

CZO+0v

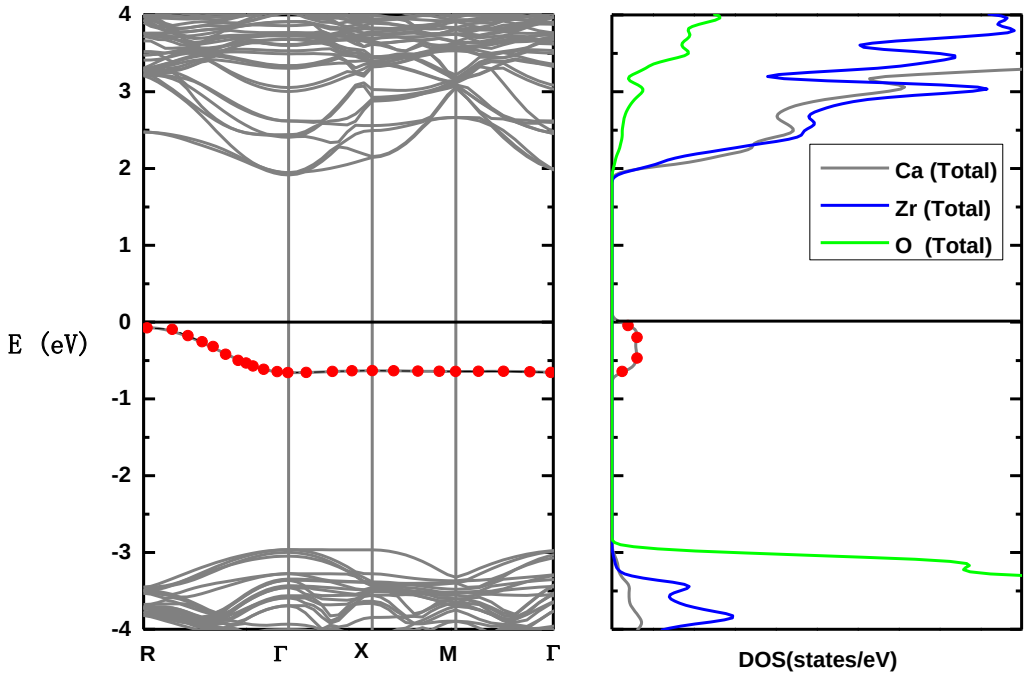
E (eV)
4
3
2
1
0
-1
-2
-3
-4
R
Γ
X
M
Γ
Ca (Total)
Zr (Total)
O (Total)
DOS(states/eV)

CHO+0v

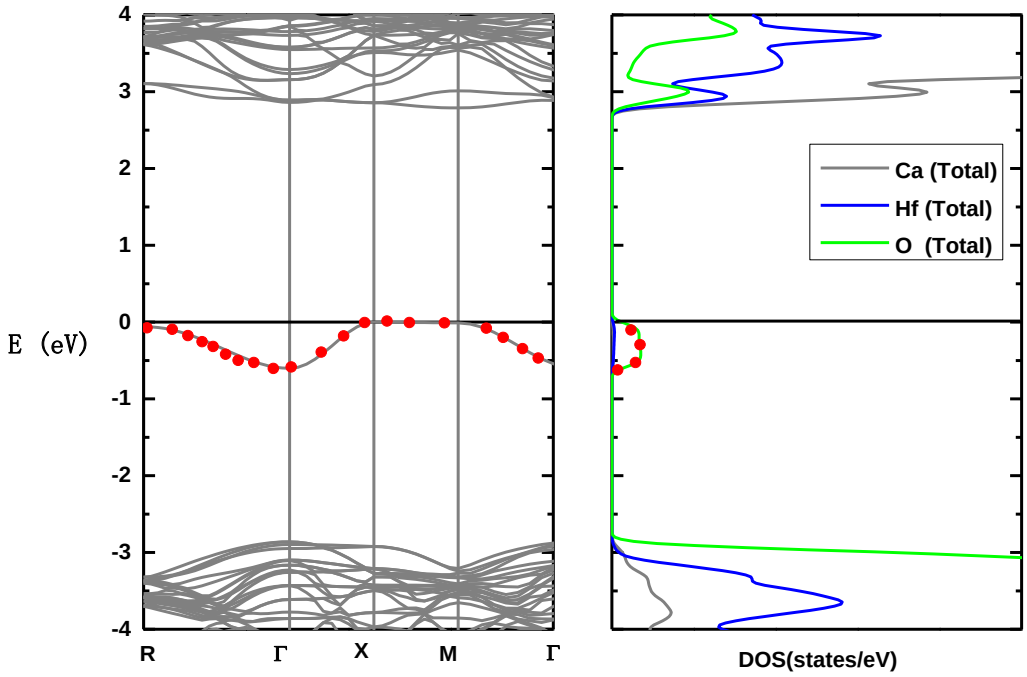
E (eV)
4
3
2
1
0
-1
-2
-3
-4
R
Γ
X
M
Γ
Ca (Total)
Hf (Total)
O (Total)
DOS(states/eV)

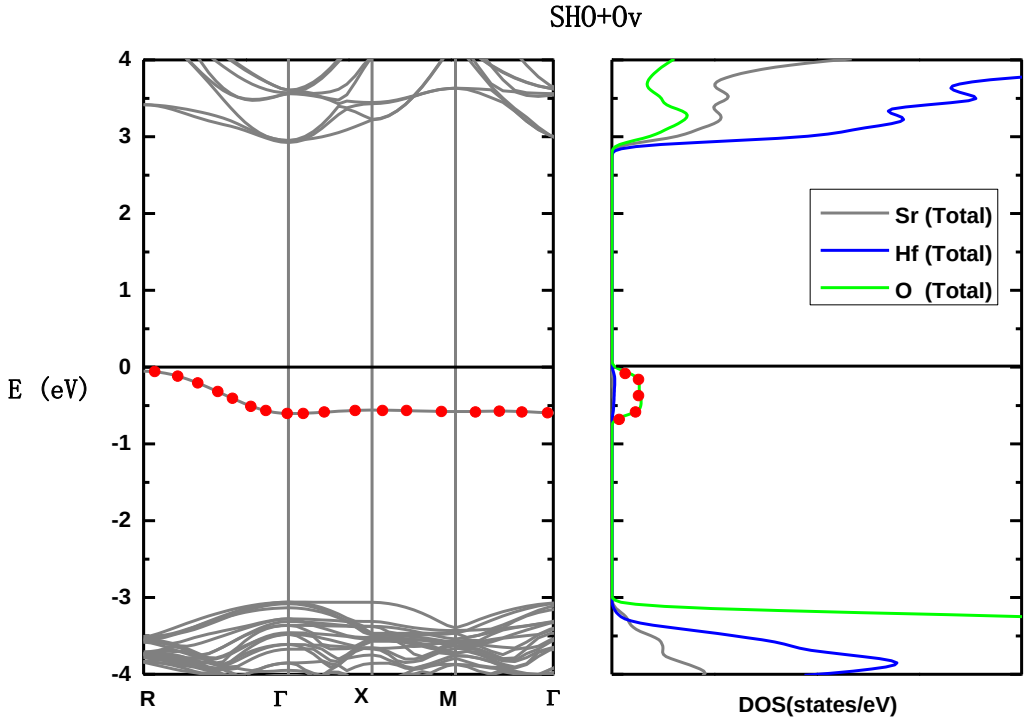

Figure IV.3: Partial densities of state and the band structure of CZO, CHO and SHO containing an F-center defect

IV. 3. 1. 3. Chalcogens-doped CZO, CHO and SHO.

The TDOS of chalcogens-doped SHO are demonstrated in **Figure IV. 4**. The overall nature of DOS for pristine CZO/CHO/SHO are modified when these compounds are doped with chalcogens impurities due to the appearance of their new orbitals in the valence and conduction bands. Moreover, the upper VB is principally composed of O-2p orbitals and p-orbitals of chalcogens' impurities (S-3p, Se-4p, or Te-5p orbitals) with some admixture of Zr-4d/Hf-5d orbitals. On the other hand, the bottom CB is mainly composed of Ca-4d/Sr-4d and Zr-4d/Hf-5d orbitals with minor d-chalcogens orbitals admixture (S-3d, Se-4d, or Te-5d orbitals). Moreover, the CBM is made by a strong hybridization between Zr-4d/Hf-5d and d-chalcogens orbitals. Furthermore, the LUMO is shifted to the Fermi level compared with pristine CZO/CHO/SHO introducing the forbidden band's reduction. This reduction is triggered by the chalcogens' impurities in the studied compounds. Additionally, the forbidden band decreases with increasing the chalcogens concentrations up to 12.5%, especially for Te and Se substitutions (see **Table IV.3**). Besides, with 12.5% of Te the VB overlaps the CB for all understudy compounds.

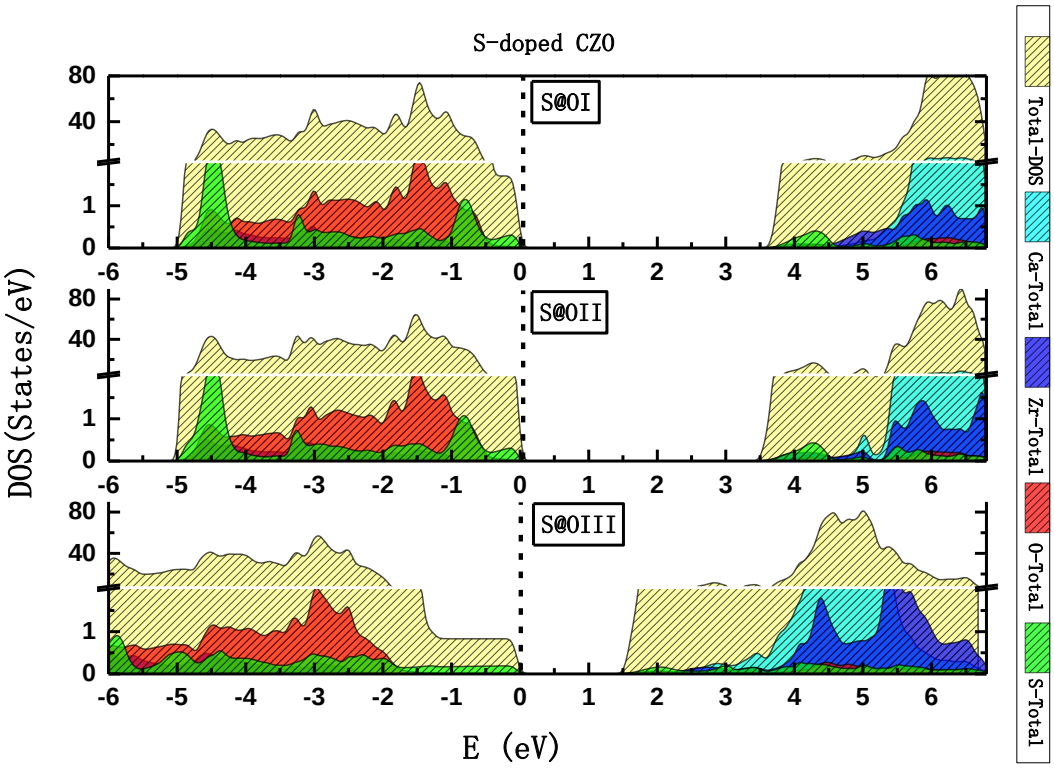
S-doped CZO
S@OI
S@OII
S@OIII
DOS(States/eV)
E (eV)
Total-DOS
Ca-Total
Zr-Total
O-Total
S-Total

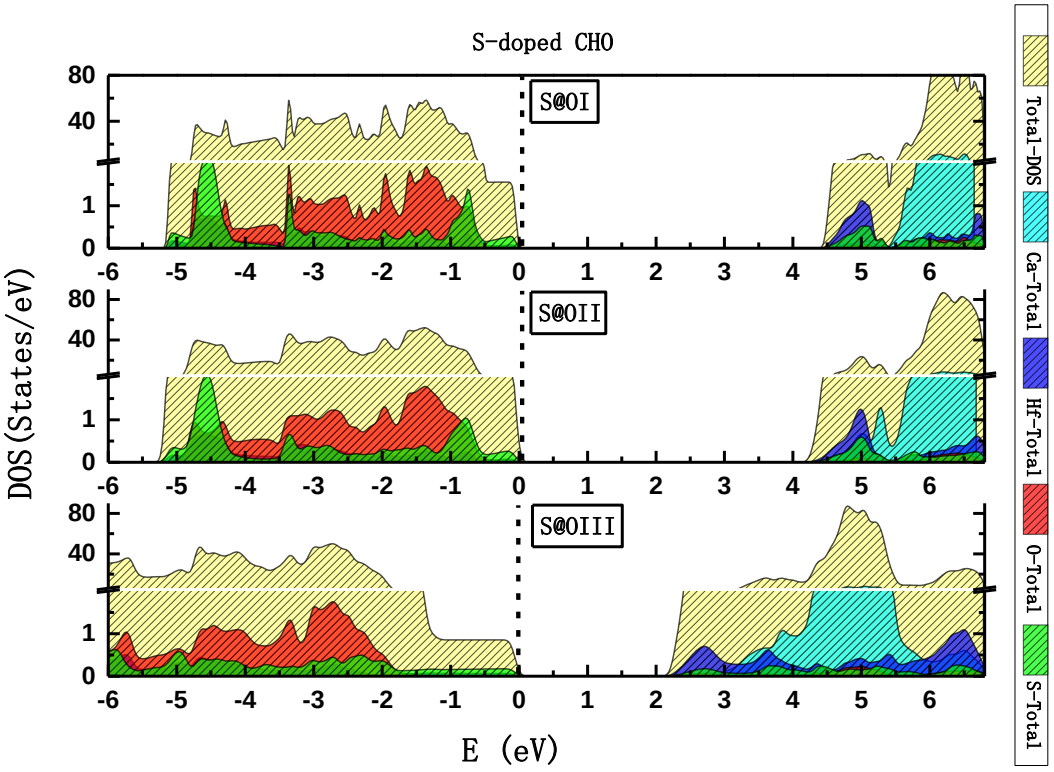
S-doped CHO
S@OI
S@OII
S@OIII
DOS(States/eV)
E (eV)
Total-DOS
Ca-Total
Hf-Total
O-Total
S-Total

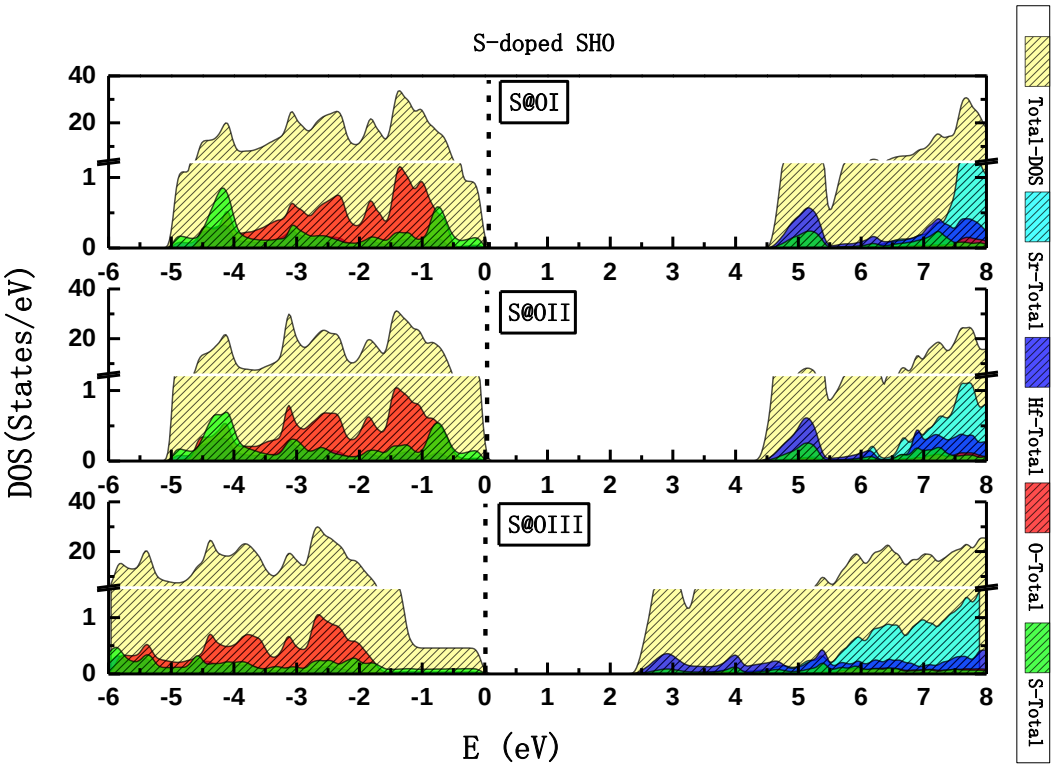
S-doped SHO
S@OI
S@OII
S@OIII
DOS(States/eV)
E (eV)
Total-DOS
Sr-Total
Hf-Total
O-Total
S-Total

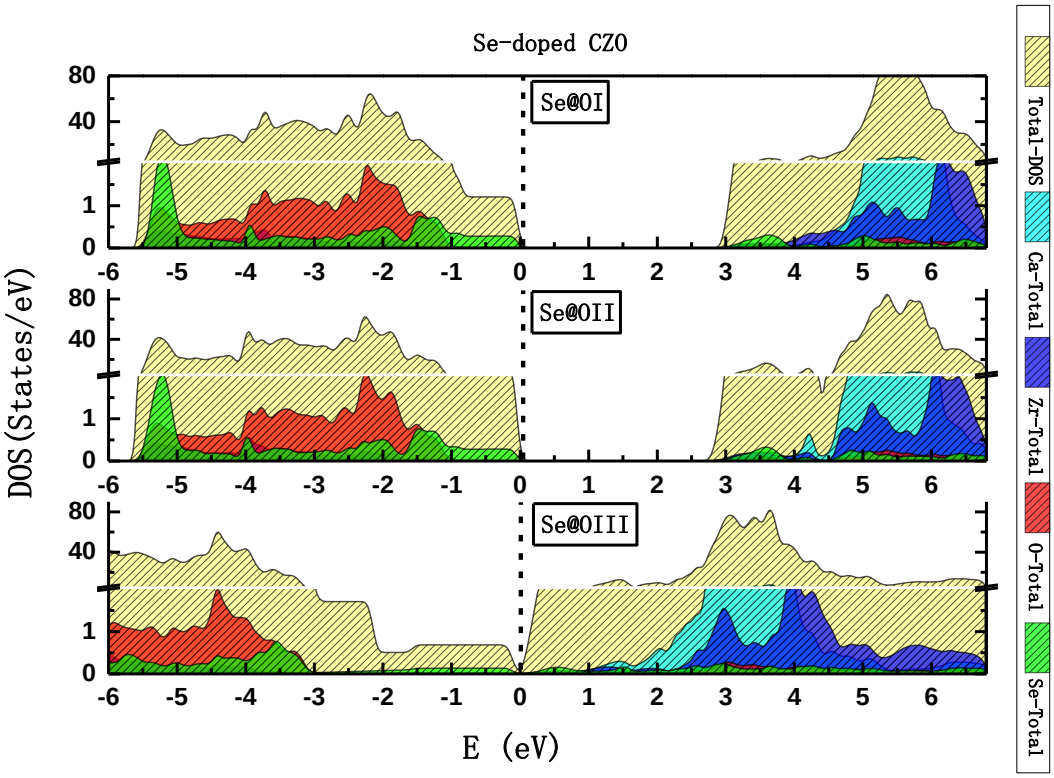
Se-doped CZO
Se@OI
Se@OII
Se@OIII
DOS(States/eV)
E (eV)
Total-DOS
Ca-Total
Zr-Total
O-Total
Se-Total

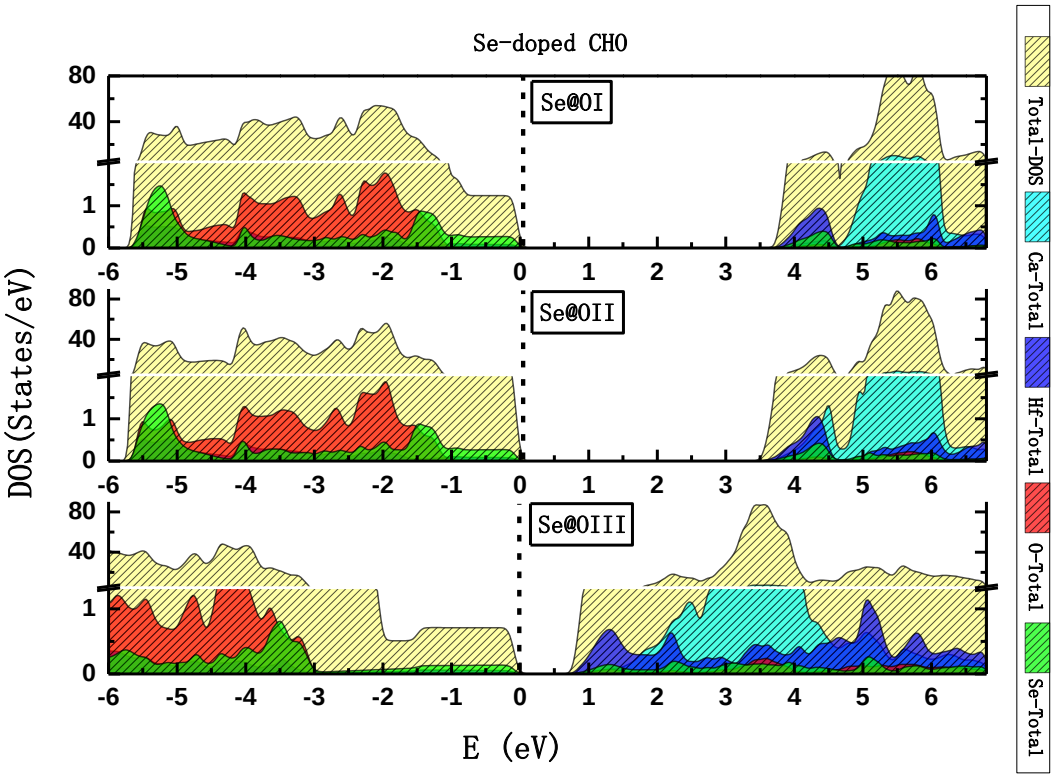
Se-doped CHO
Se@OI
Se@OII
Se@OIII
DOS(States/eV)
E (eV)
Total-DOS
Ca-Total
Hf-Total
O-Total
Se-Total

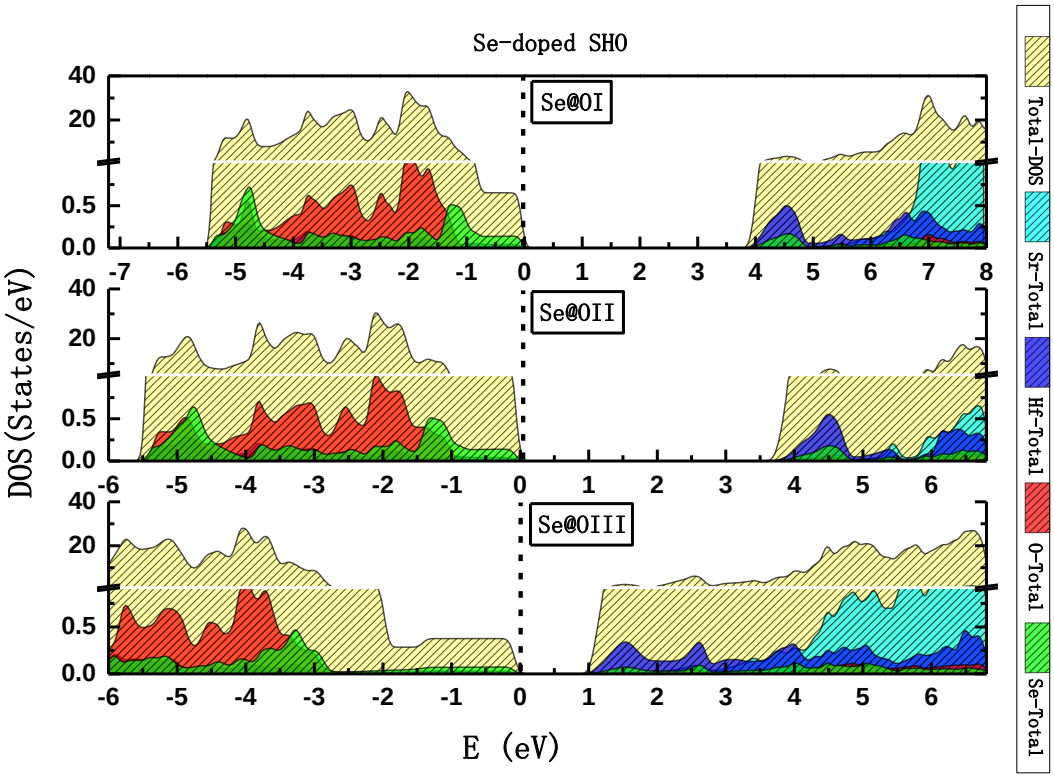
Se-doped SHO
Se@OI
Se@OII
Se@OIII
DOS(States/eV)
E (eV)
Total-DOS
Sr-Total
Hf-Total
O-Total
Se-Total

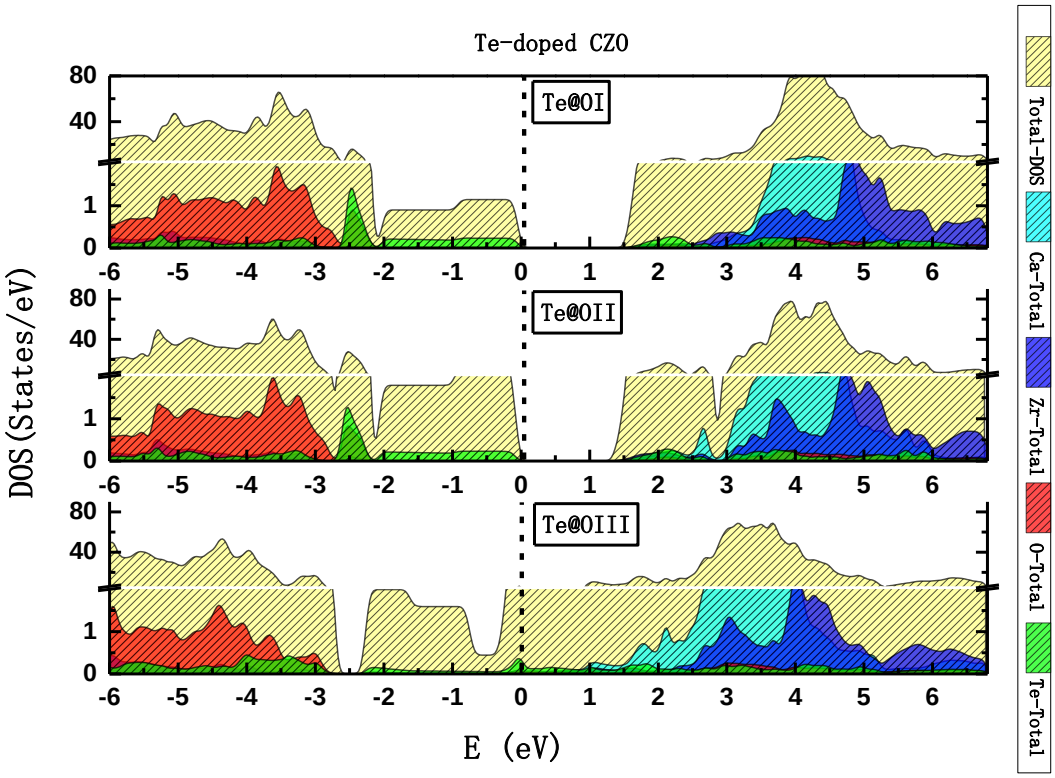
Te-doped CZO
Te@OI
Te@OII
Te@OIII
DOS (States/eV)
E (eV)
Total-DOS
Ca-Total
Zr-Total
O-Total
Te-Total

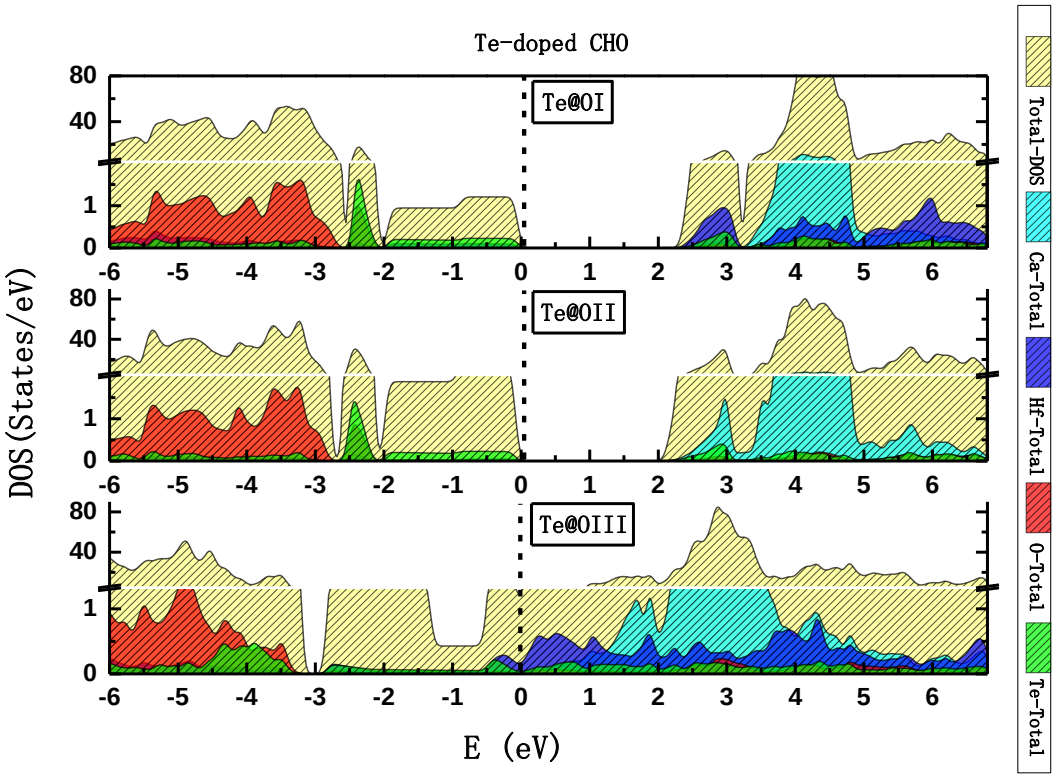
Te-doped CHO
Te@OI
Te@OII
Te@OIII
DOS (States/eV)
E (eV)
Total-DOS
Ca-Total
Hf-Total
O-Total
Te-Total

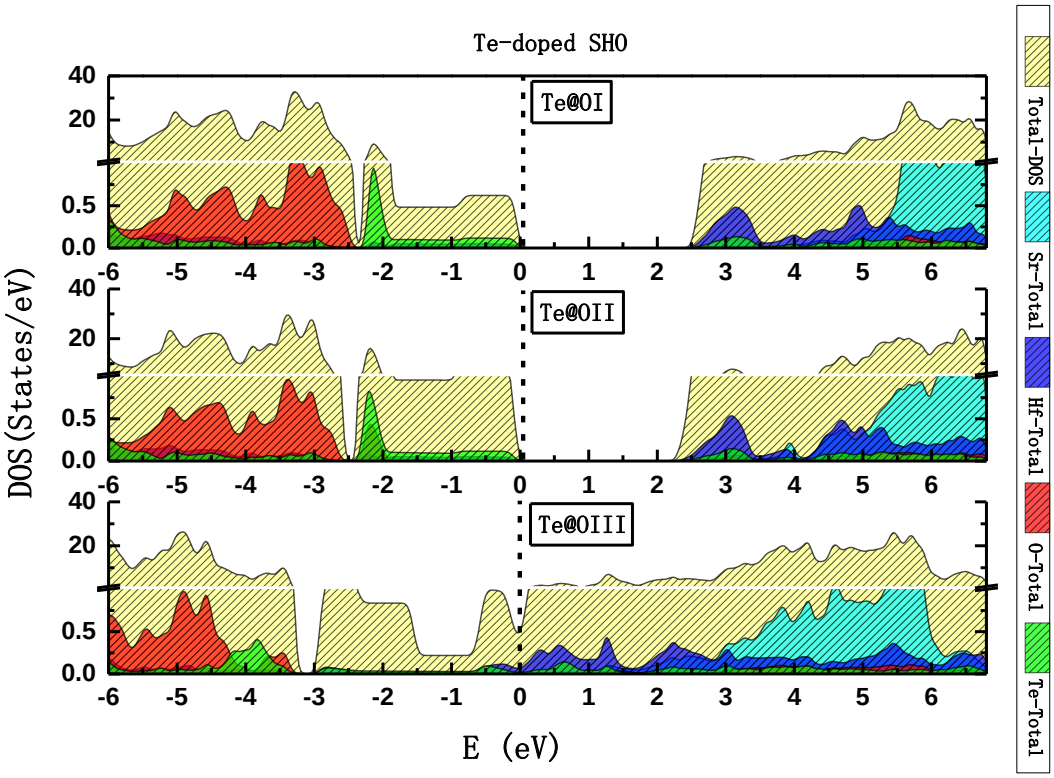

Figure IV.4: Total and partial densities of states for chalcogens-doped CZO, CHO and SHO

IV. 3. 1. 4. Chalcogens doped CZO, CHO and SHO + Ov

In order to establish the effect of electronic properties of CZO, CHO and SHO when chalcogens impurities meet the F-center defect, different systems are demonstrated in **Figure IV.5**. From this figure we can note that the upper VB of all studied compounds is principally composed of O-2p orbitals with a clear hybridization between p-orbitals of chalcogens' impurities (S-3p, Se-4p, or Te-5p) and Zr-4d/Hf-5d orbitals while the bottom CB is mainly composed of Ca-4d/Sr-4d and Zr-4d/Hf-5d orbitals with minor d-chalcogens orbitals admix (S-3d, Se-4d, or Te-5d) and O-2p orbitals. On the other hand, due to the presence of F-center defect an intermediate band has appeared in all cases. Besides, in the case of CZO perovskite, the intermediate band is mostly consisted of Ca-4d and Zr-4d orbitals in the case of S/Se/Te@OI+Ov, of Ca-4d, S-3p or Se-4p or Te-5p, S-3d or Se-4d or Te-5d and Zr-4d orbitals in S/Se/Te@OII+Ov cases, of Ca-4d, O-2p, S-3p or Se-4p or Te-5p, S-3d or Se-4d or Te-5d and Zr-4d orbitals in S/Se@OIII+Ov case, and of Ca-4d orbitales for Te@OII/OIII+Ov cases. While for CHO compound, Ca-4d orbitals dominate the intermediate band in the case of S/Se/Te@OI+Ov while it is principally formed by a hybridization between Hf-5d, Ca-4d and O-2p orbitales in the case of

S/Se/Te@OII+Ov, and by Ca-4d, O-2p, S-3p or Se-4p, S-3d or Se-4d and Hf-5d orbitals in the case of S/Se@OIII+Ov, and by Ca-4d orbitales in Te@OII/OIII+Ov cases. For SHO compound, the intermediate band is composed by hybridization between Sr-4d and O-2p orbitals in the case of S/Se/Te@OI+Ov, and mostly composed by hybridization of Hf-5d and Sr-4d orbitals in the case of S/Se@OII+Ov, and principally composed by a hybridization between S-3d, S-3p, and Hf-5d orbitals in the case of S@OIII+Ov, Sr-4d, O-2p, Se-4p, and Hf-5d orbitals in the case of Se@OIII+Ov, Sr-4d orbitales in the case of Te@OII+Ov, and by a hybridization between Sr-4d and O-2p orbitales inn Te@OIII+Ov case. As shown in **Figure IV.2** and **Figure IV.5** the Fermi level is situated at the HOMO, while when S or Se impurities meet an Ov defect in CZO, CHO and SHO the Fermi level is shifted to the LUMO compared with pristine and doped structures, indicating the introduction of additional electrons into the system which give rise to enhancement of the electrical (electronic) conductivity, therefore the enhancement of the quantity of electrons in all studied materials. Otherwise, the oxygen vacancies have long been known to be responsible for the n-type electrical conductivity in perovskite oxides [142, 143], which indeed enhances the electrical conductivity which consists with our results.

Table IV.3: Calculated forbidden band (Eg) for pristine, chalcogens-doped CZO, CHO and SHO with and without the presence of an Ov defect

Crystal	X (%)	CZO	CHO	SHO
Pristine	0.000	4.963	5.830	6.071
Compound +Ov	4.167	4.600	5.42	5.936
S-doped compound	4.167	3. 673	4.448	4.579
	8.334	3.509	4.233	4.383
	12.500	1.531	2.213	2.419
S-doped compound + Ov	4.167 + 4.167	3.573	4.260	4.495
	8.334 + 4.167	3.378	4.000	4.304
	12.500 + 4.167	2.855	3.441	2.375
Se-doped compound	4.167	2.955	3.740	3.907
	8.334	2.779	3.514	3.693
	12.500	0.040	0.780	1.017
Se-doped compound + Ov	4.167 + 4.167	2.810	3.653	3.838
	8.334 + 4.167	2.506	3.305	3.619
	12.500 + 4.167	2.167	2.678	2.865
Te-doped compound	4.167	1.531	2.324	2.515
	8.334	1.333	2.074	2.271
	12.500	0.000	0.000	0.000
Te-doped compound + Ov	4.167 + 4.167	1.400	1.975	2.427
	8.334 + 4.167	0.954	1.776	1.640
	12.500 + 4.167	0.369	1.128	0.921

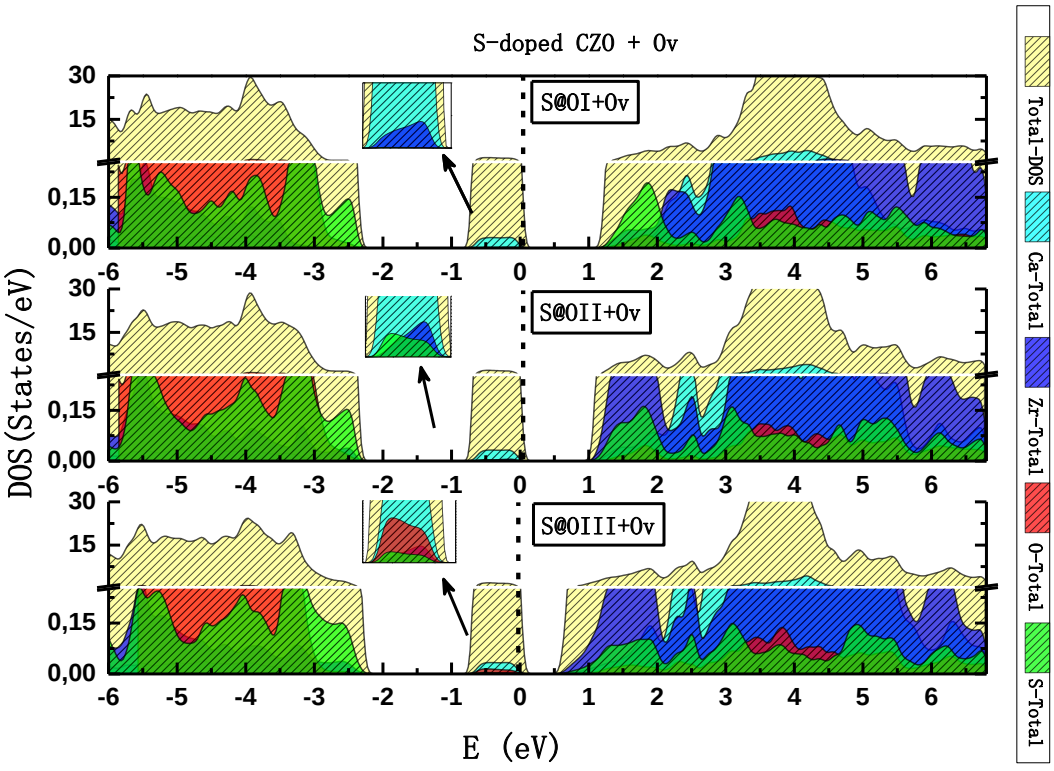
S-doped CZO + 0v
S@OI+0v
S@OII+0v
S@OIII+0v
DOS(States/eV)
E (eV)
Total-DOS
Ca-Total
Zr-Total
O-Total
S-Total

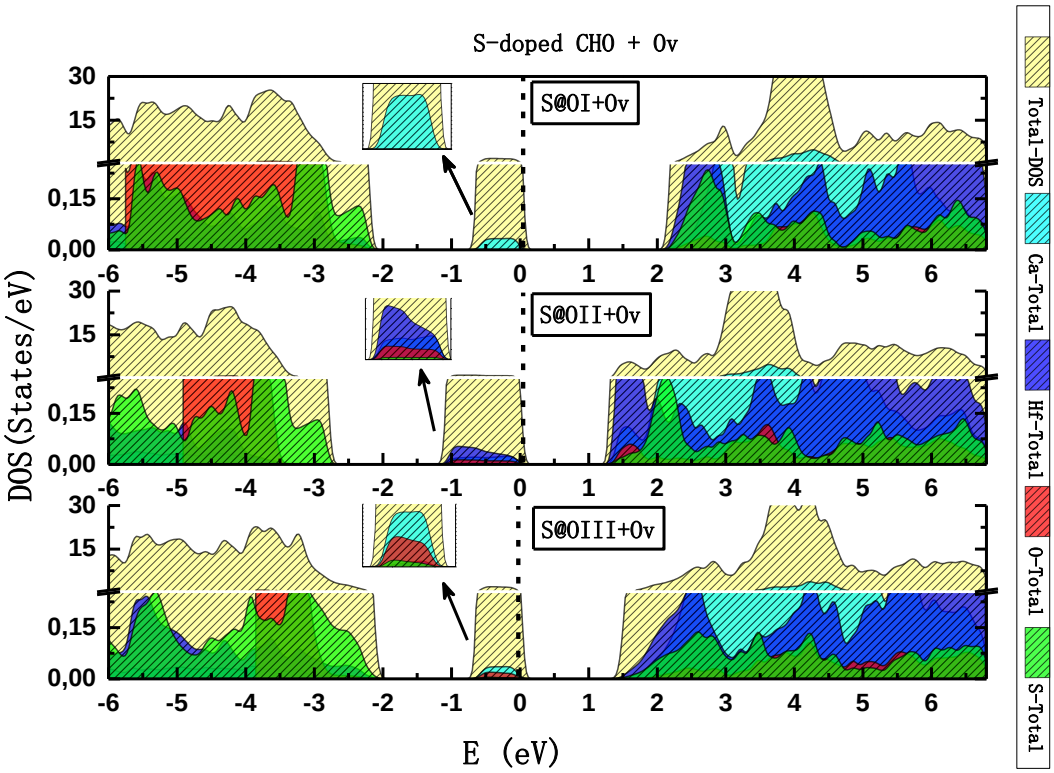
S-doped CHO + 0v
S@OI+0v
S@OII+0v
S@OIII+0v
DOS(States/eV)
E (eV)
Total-DOS
Ca-Total
Hf-Total
O-Total
S-Total

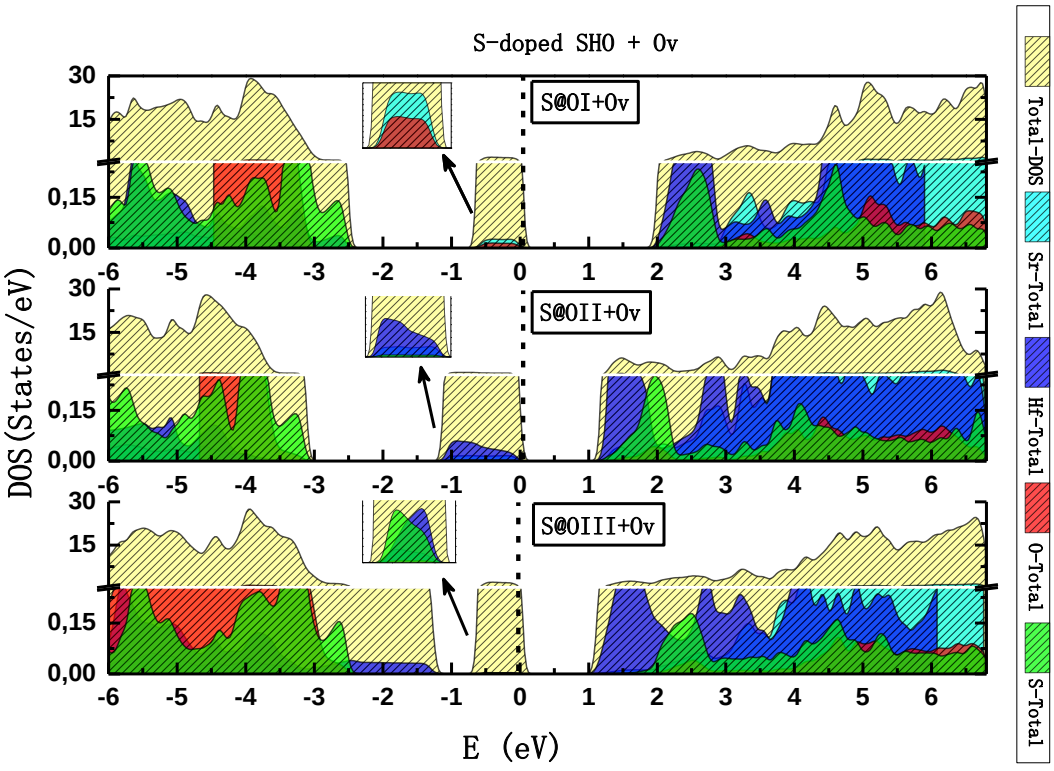
S-doped SHO + Ov
S@OI+Ov
S@OII+Ov
S@OIII+Ov
DOS(States/eV)
E (eV)
Total-DOS
Sr-Total
Hf-Total
O-Total
S-Total

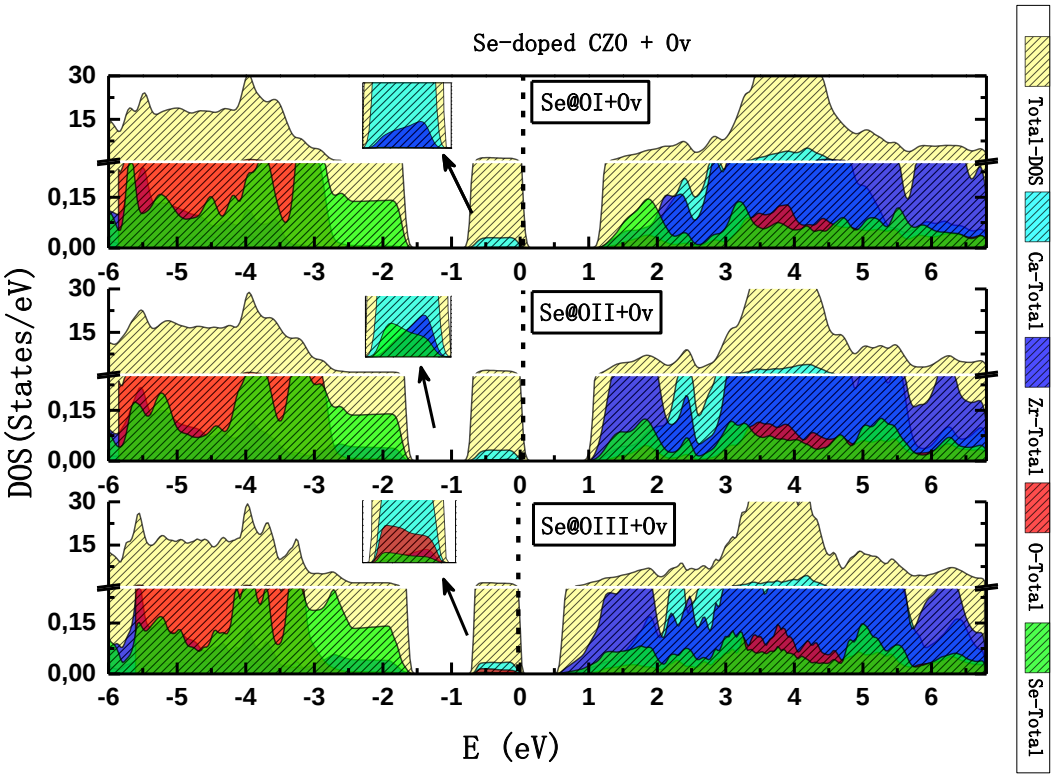
Se-doped CZO + Ov
Se@OI+Ov
Se@OII+Ov
Se@OIII+Ov
DOS(States/eV)
E (eV)
Total-DOS
Ca-Total
Zr-Total
O-Total
Se-Total

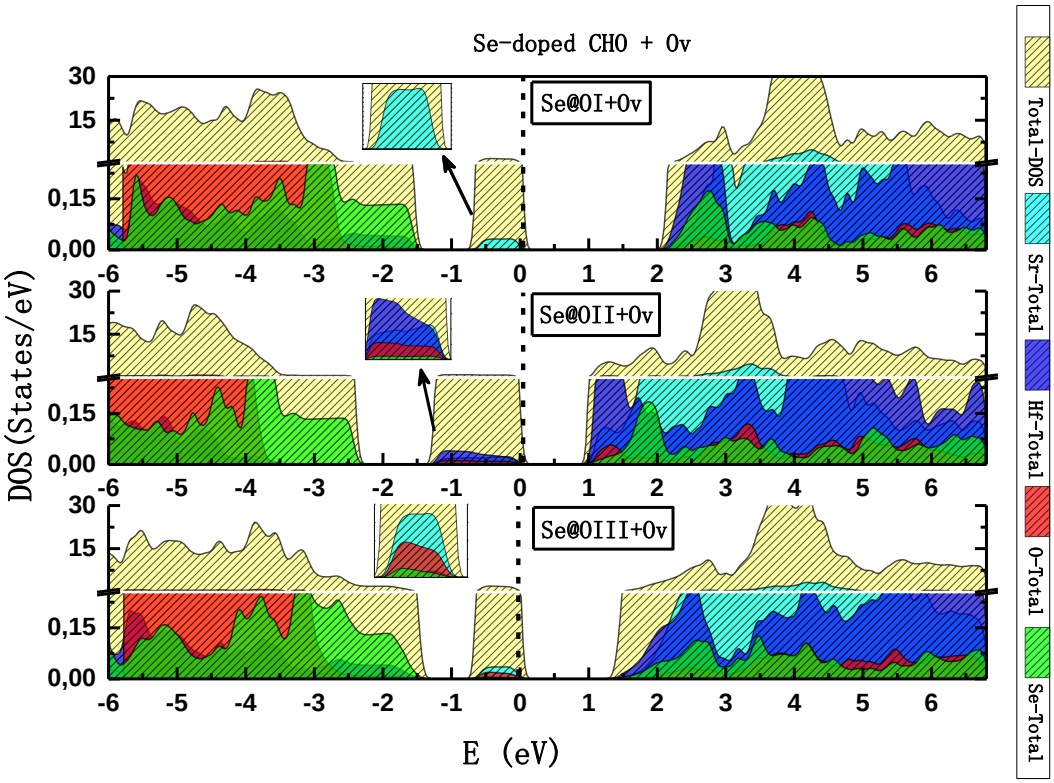
Se-doped CHO + Ov
Se@OI+Ov
Se@OII+Ov
Se@OIII+Ov
DOS(States/eV)
E (eV)
Total-DOS
Sr-Total
Hf-Total
O-Total
Se-Total

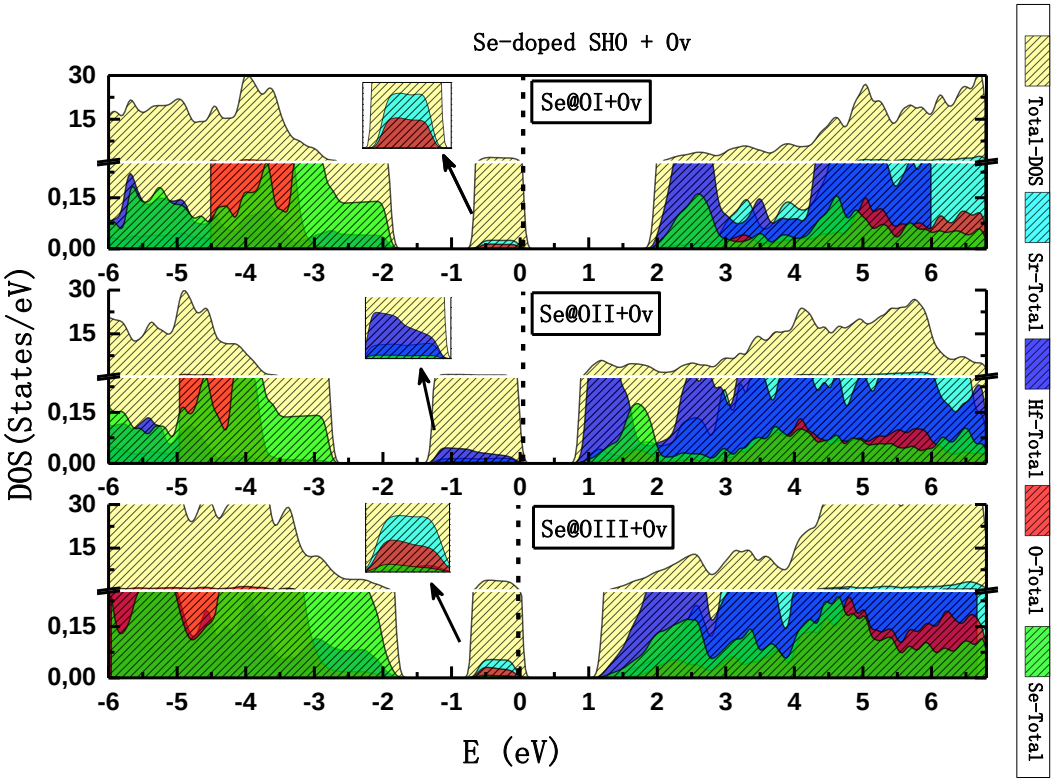
Se-doped SHO + Ov
Se@OI+Ov
Se@OII+Ov
Se@OIII+Ov
DOS(States/eV)
E (eV)
Total-DOS
Sr-Total
Hf-Total
O-Total
Se-Total

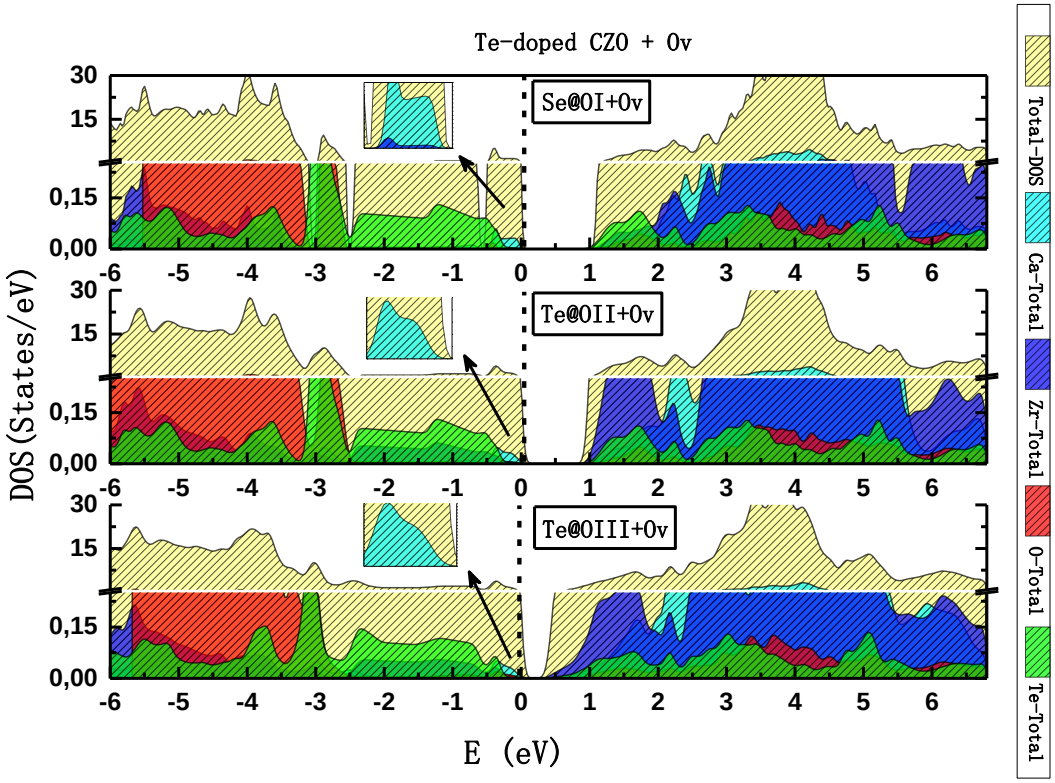
Te-doped CZO + Ov
Se@OI+Ov
Te@OII+Ov
Te@OIII+Ov
DOS(States/eV)
E (eV)
Total-DOS
Ca-Total
Zr-Total
O-Total
Te-Total

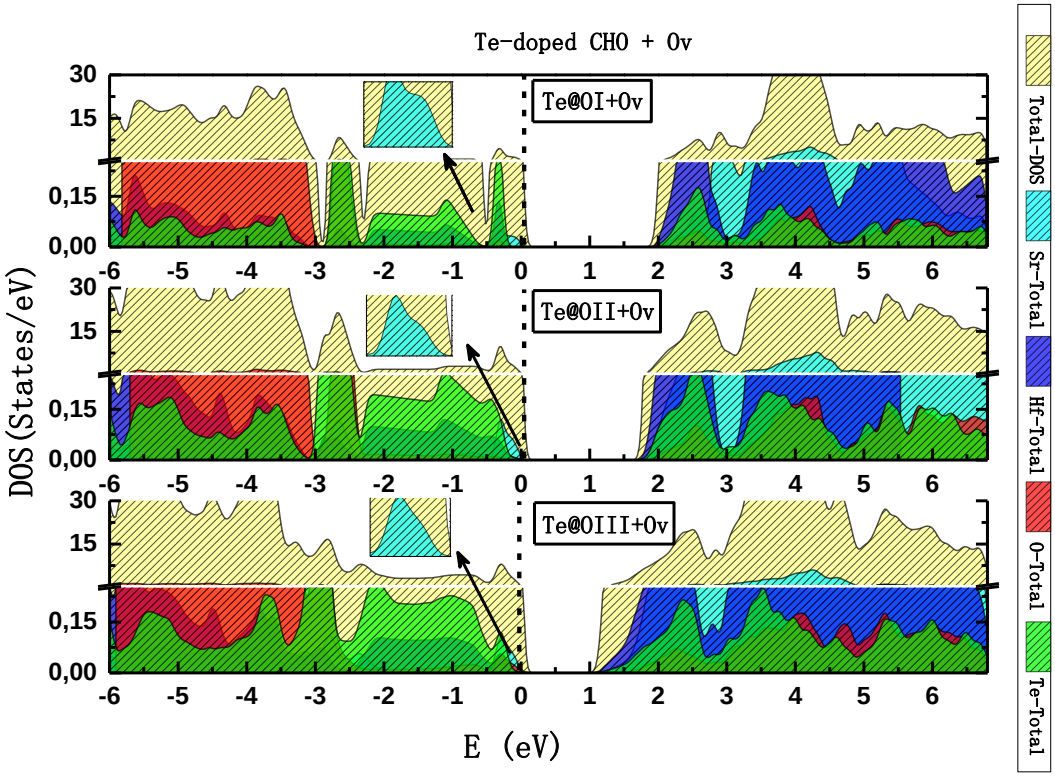
Te-doped CHO + Ov
Te@OI+Ov
Te@OII+Ov
Te@OIII+Ov
DOS(States/eV)
E (eV)
Total-DOS
Sr-Total
Hf-Total
O-Total
Te-Total

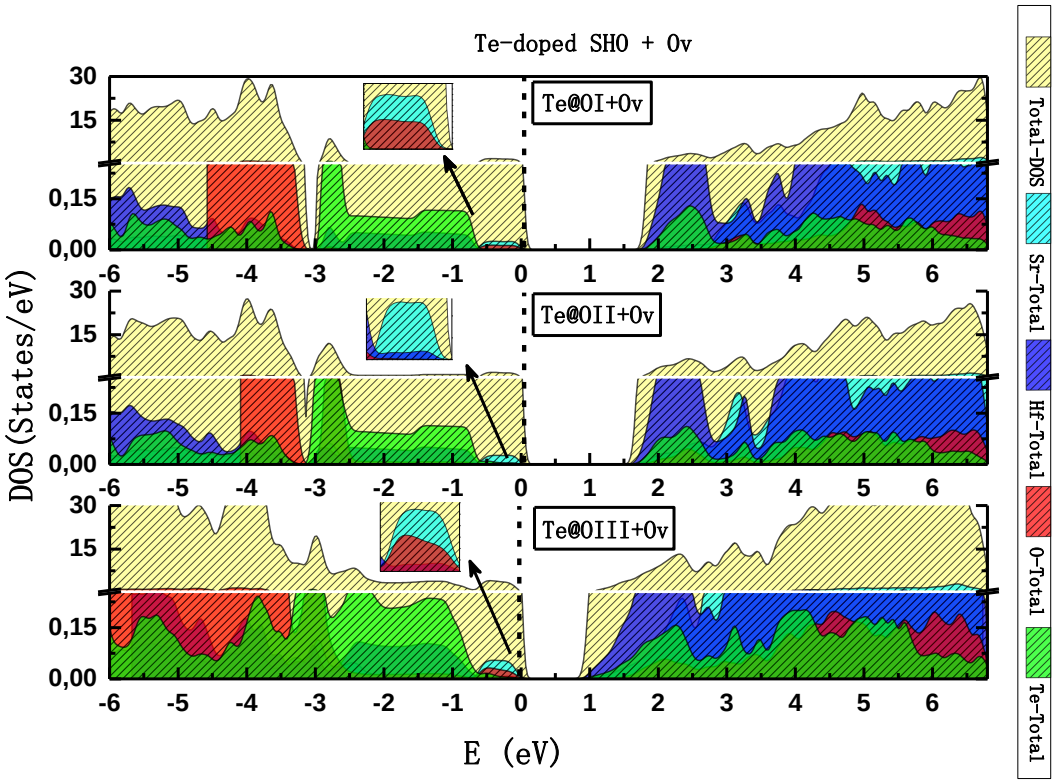

Figure IV.5: Total and partial densities of states for chalcogens-doped CZO, CHO and SHO with the presence of an F-center defect

IV. 3. 2. Optical properties

The results of the absorption coefficient of all studied compounds are presented in percentage in **Figure IV.6**. From this Figure we can note that there is no absorption of visible light for the pristine compounds. Our results are in line with previous theoretical results [107, 136, 138], as well as with the experimental results [119, 123], indicating that the pristine CZO, CHO and SHO are only excited by UV light due to their wide forbidden band values. Furthermore, the presence of an Ov itself in understudy compounds is optically inactive in the visible spectrum (See [170, 183] references), our results are in accordance with previous theoretical results [128]. As shown in [170, 183], there is no significant enhancement of the absorption coefficient in the visible spectrum for the doped structures. Fourteenthly, when chalcogens impurities meet an Ov defect in CZO/CHO or SHO compounds the absorption coefficient is significantly enhanced along the visible spectrum with a broad absorption coefficient peak in the visible spectrum of the order of 10^4 cm^{-1}. These results are in consistent with Kotomin results [144], which is proved that the optical absorption by F centers is due to the transition of an electron from the ground state to an excited state, which is located below the bottom of the conduction band. Moreover, the shifting of the Fermi level to LUMO caused the n-type semiconductor behavior in all cases,

and the reduction of the forbidden band which reduced the electrons' transitions distance give rise to the improvement of carrier concentrations (numbers of electrons and/or holes are generated inside the CB and VB), hence a huge enhancement of the absorption coefficient was observed especially in the case of S/Se/Te@OI+Ov, S/Se/Te@OII+Ov and S/Se@OIII+Ov for CZO compound and S/Se/Te@OII+Ov and Te@OIII+Ov structures for CHO, and S/Se/Te@OII+Ov and Se/Te@OIII+Ov for SHO compound.

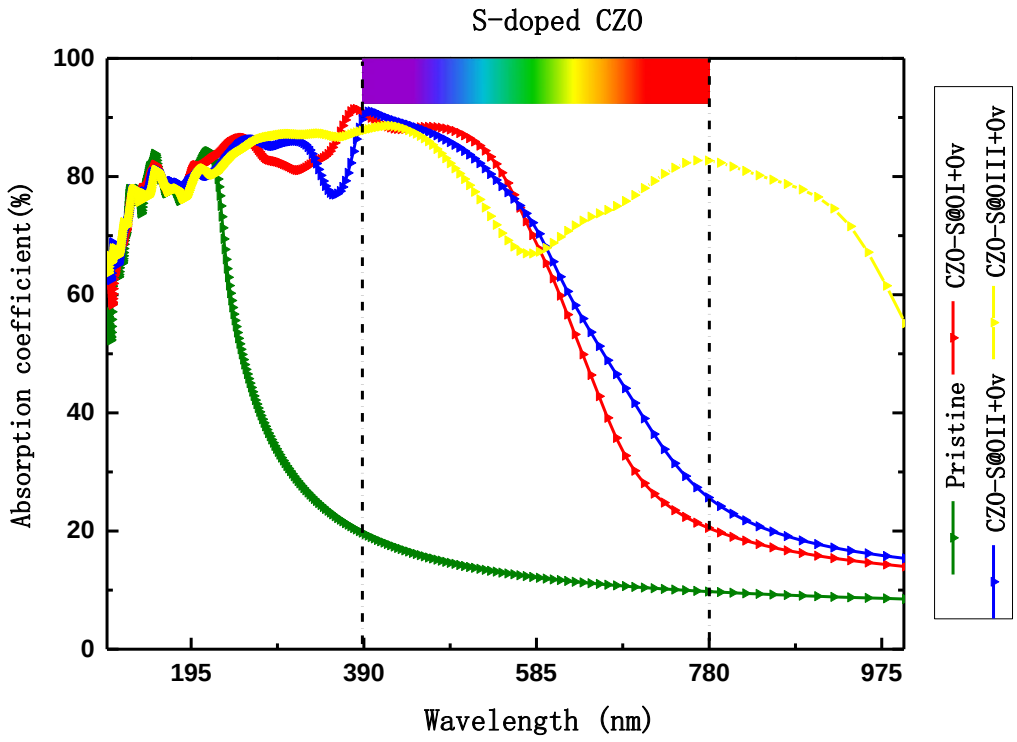

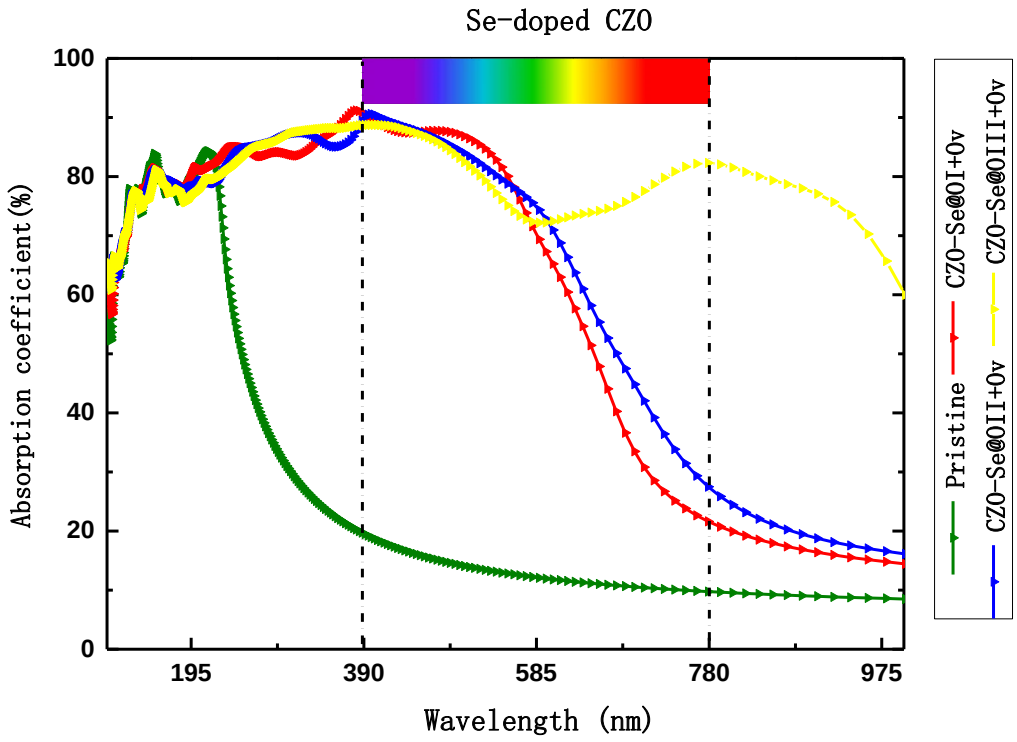
Se-doped CZO
Absorption coefficient(%)
Wavelength (nm)
100
80
60
40
20
0
195
390
585
780
975
Pristine
CZO-Se@OI+Ov
CZO-Se@OII+Ov
CZO-Se@OIII+Ov

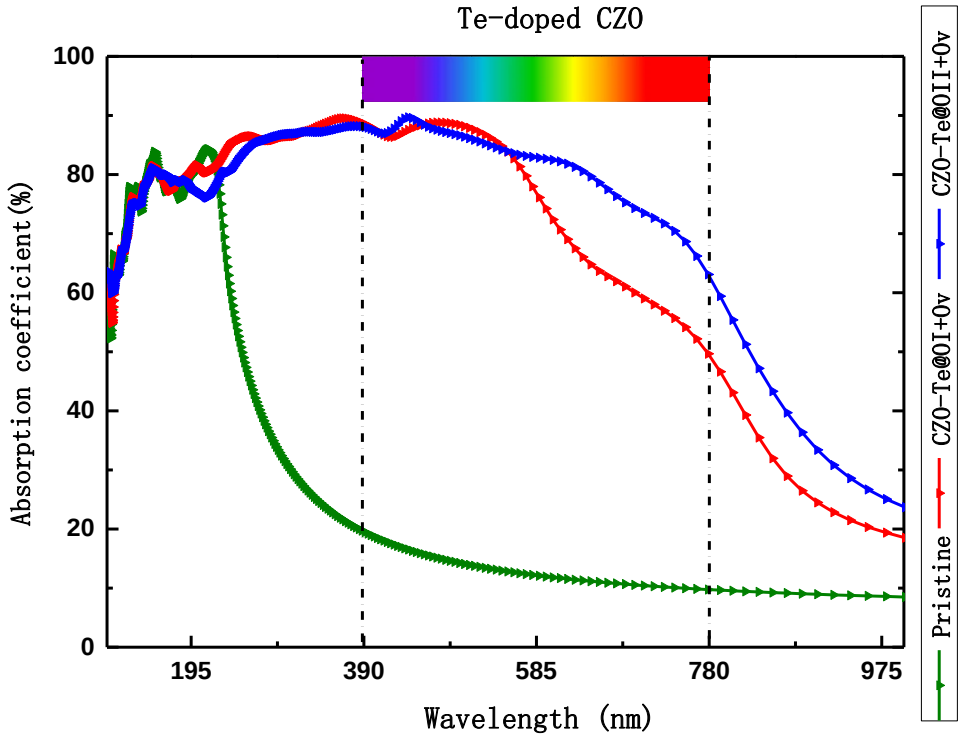
Te-doped CZO
Absorption coefficient(%)
Wavelength (nm)
100
80
60
40
20
0
195
390
585
780
975
Pristine
CZO-Te@OI+Ov
CZO-Te@OII+Ov

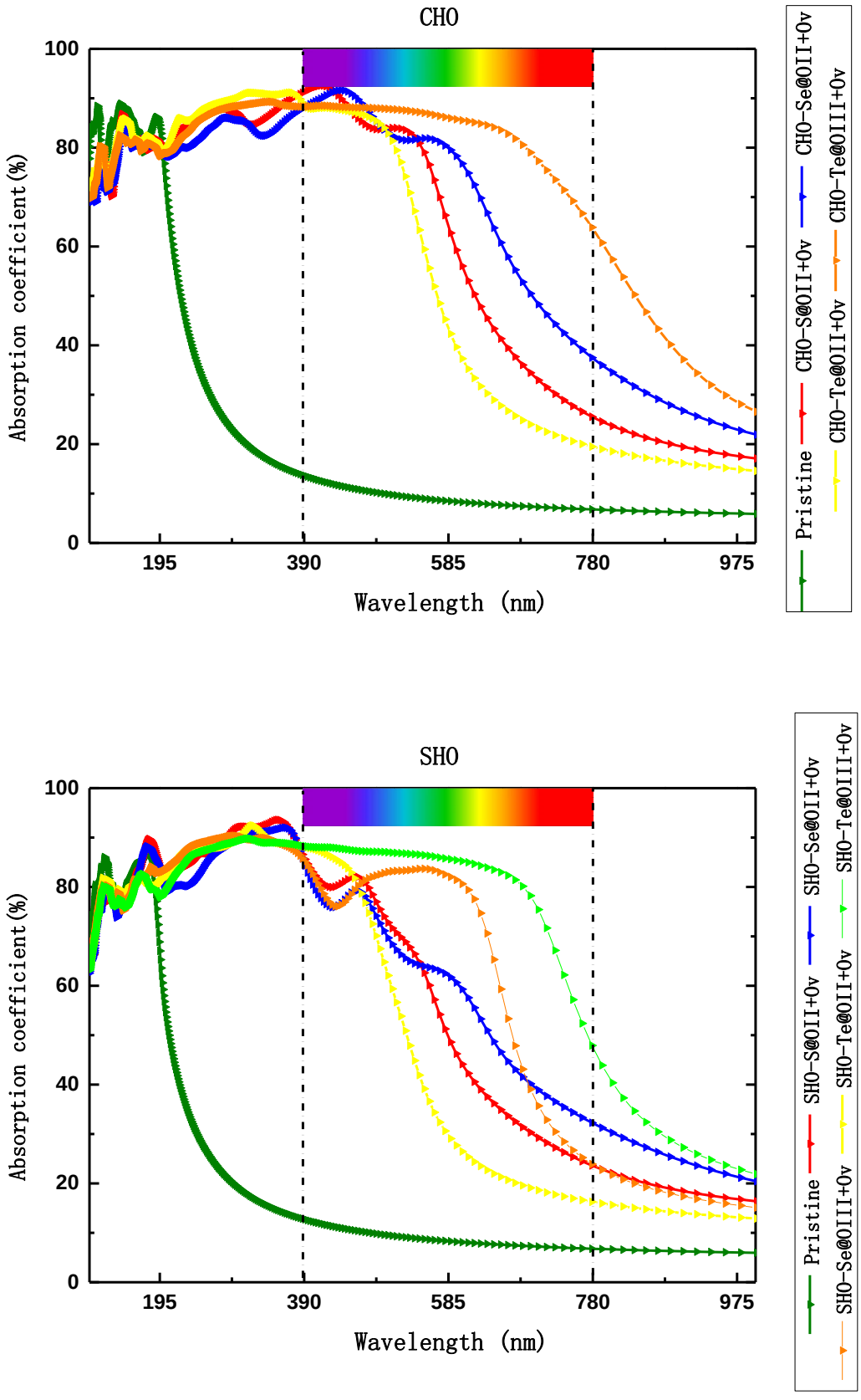

Figure IV.6: The absorption coefficient doped-CZO/CHO or SHO with the presence of an F-center defect

IV. 3. 3. Hydrogen production

According to reactions IV. 1 and IV. 2, four holes and two electrons are needed to produce an O_2 molecule and an H_2 molecule for driving the oxidation and reduction procedure respectively for giving rise to hydrogen through water splitting based on photocatalysis [47].

Reaction IV. 1: Water oxidation: $\mathbf{2H_2O + 4h^+ \rightarrow O_2 + 4H^+}$

Reaction IV. 2: Proton reduction: $\mathbf{2H^+ + 2e^- \rightarrow H_2}$

Moreover, the positions of HOMO and LUMO are necessary for photocatalytic water splitting to evaluate the oxidation and reduction ability of semiconductors. The HOMO must be positioned below the water oxidation potential $E_{\mathrm{H2O/O2}}^{HOMO} \geq 1.23\ eV$ and the LUMO must be situated above the proton reduction potential $E_{\mathrm{H+/H2}}^{LUMO} \leq 0\ eV$ to generate photo-excited charge carriers and carry out redox reactions. The energy levels of HOMO and LUMO were calculated using the following equations [145]:

$$\boldsymbol{E_{LUMO} = \chi + E_0 - \frac{E_g}{2}} \qquad \textbf{(Eq.IV.1)}$$

$$\boldsymbol{E_{HOMO} = \chi + E_0 + \frac{E_g}{2}} \qquad \textbf{(Eq.IV.2)}$$

Where χ is the electronegativity of the compound, E_0 is the Normal Hydrogen Electrode potential (NHE) with a value of -4.5 eV and Eg is the forbidden energy of the semiconductor. **Figure IV. 7 (a)** shows that the HOMO of pristine compound is situated 1.846 eV, 2.324 eV and 2.347 eV below the water oxidation potential (H_2O/O_2), while the LUMO is positioned 1.887 eV, 2.276 eV and 2.493 eV above the proton reduction (H^+/H_2) for CZO, CHO and SHO, respectively. Hence to use CZO, CHO and SHO for splitting water photons having energies greater than forbidden band are needed (4.963 eV for CZO, 5.830 eV for CHO and 6.071 eV for SHO). Besides, the presence of chalcogens impurities in CZO, CHO and SHO leads to the upward and downward shifting of the HOMO and LUMO respectively due to the reduction of the forbidden band width of pristine compounds. **Figure IV.7 (a)** reports the HOMO and LUMO of the doped structures are positioned below the water oxidation and above the proton reduction respectively, which means that the doped structures can be used as semiconductors for photocatalytic water splitting except Se/Te@OIII structures. On the other hand, **Figure IV. 7 (b)** shows that the HOMO and LUMO positions of all compounds containing an Ov respect the limits necessary to split water except Te@OI/OII/OIII+Ov structures for CZO, and Te@OIII+Ov structure for CHO and SHO compounds. Furthermore, the upward and the

downward shifting of the HOMO and LUMO indicate that these structures exhibit strong reduction/oxidation ability. Moreover, the presence of an intermediate band (between the VB and the CB) (**Figure OV. 7 (b)**) guarantees the efficiency of the charge transfer. Additionally, **Figure IV. 6** illustrates that S/Se@OI/OII/OIII+Ov structures for CZO and S/Se/Te@OII+Ov structures for CHO and SHO can effectively absorb the visible light which is a requirement for photocatalysis. Additionally, the intermediate band which guarantees the efficiency of the charge transfer, and these structures have the ability to split water which enhanced the hydrogen production. Hence, these structures are the most preferable structures for photocatalytic hydrogen production from water splitting under visible light.

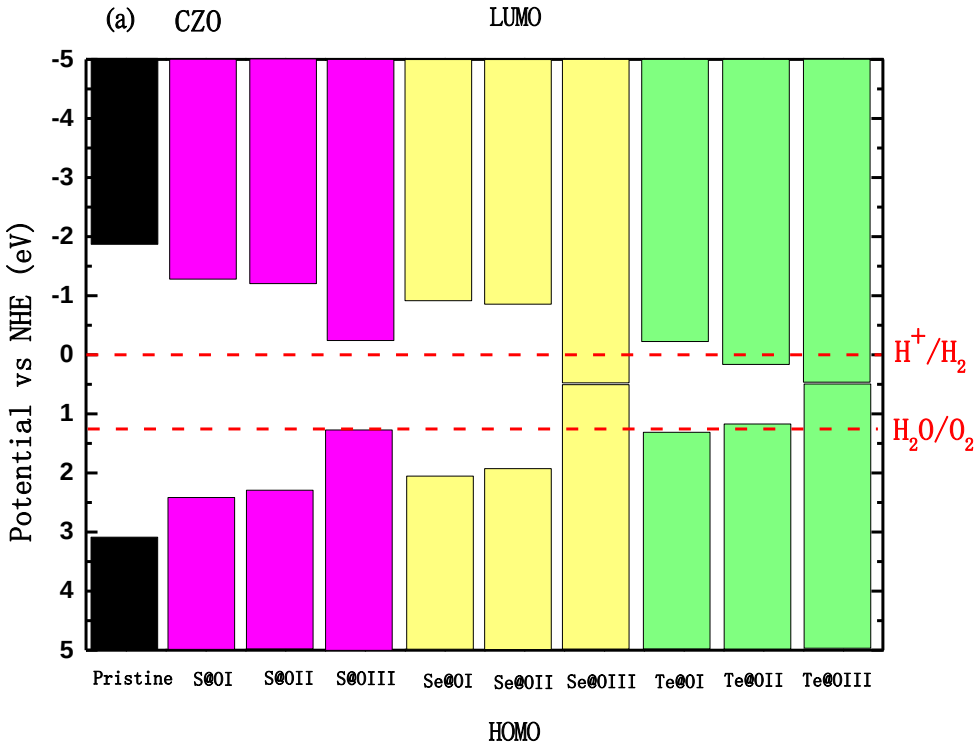

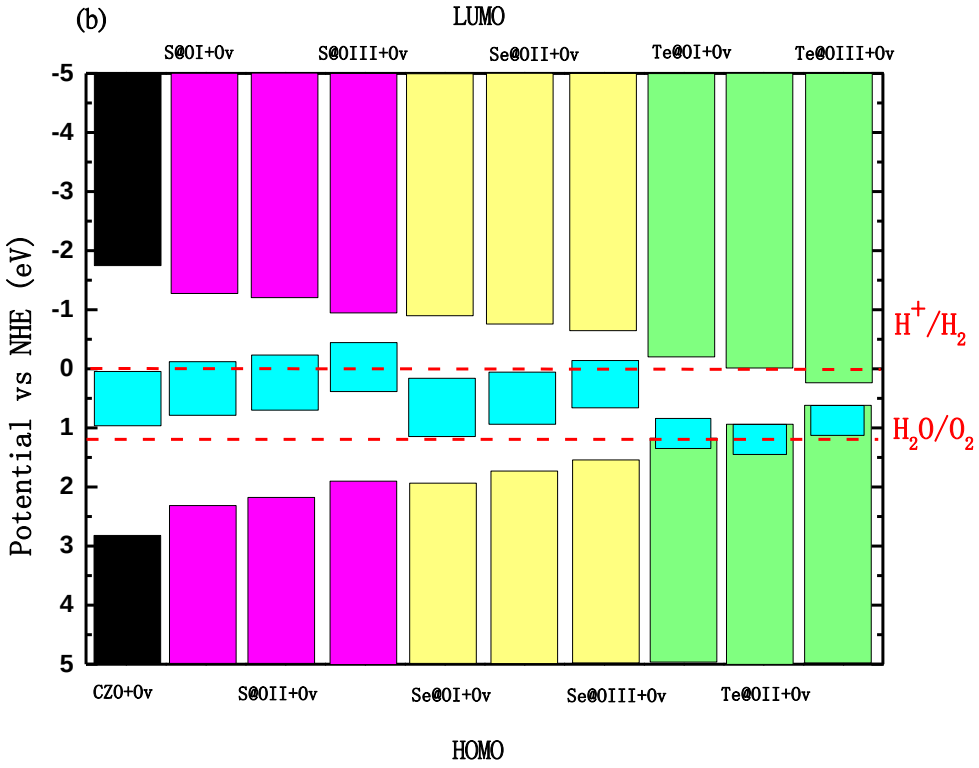
(b)
LUMO
S@OI+Ov
S@OIII+Ov
Se@OII+Ov
Te@OI+Ov
Te@OIII+Ov
Potential vs NHE (eV)
-5
-4
-3
-2
-1
0
1
2
3
4
5
H+/H2
H2O/O2
CZO+Ov
S@OII+Ov
Se@OI+Ov
Se@OIII+Ov
Te@OII+Ov
HOMO

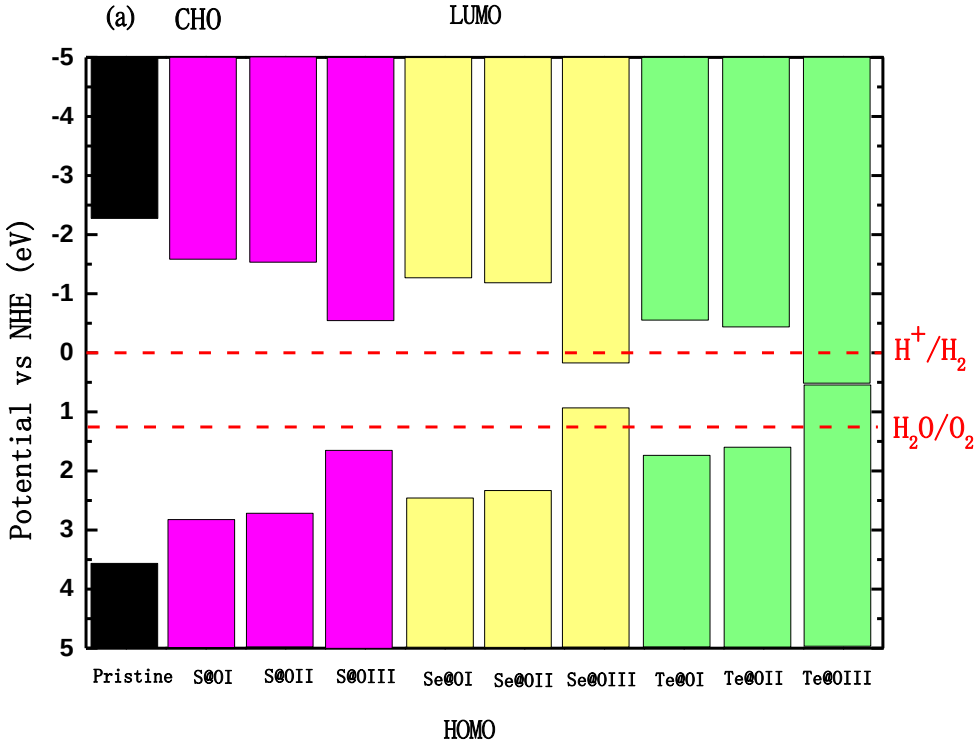
(a)
CHO
LUMO
Potential vs NHE (eV)
-5
-4
-3
-2
-1
0
1
2
3
4
5
H+/H2
H2O/O2
Pristine
S@OI
S@OII
S@OIII
Se@OI
Se@OII
Se@OIII
Te@OI
Te@OII
Te@OIII
HOMO

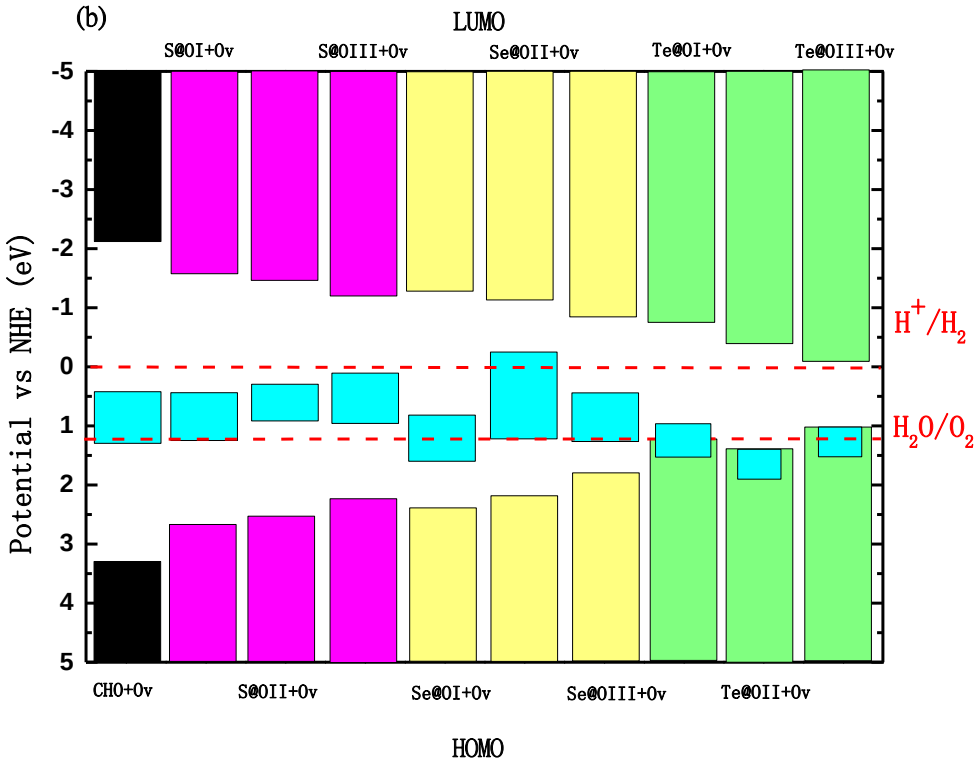
(b)
LUMO
S@OI+Ov
S@OIII+Ov
Se@OII+Ov
Te@OI+Ov
Te@OIII+Ov
Potential vs NHE (eV)
-5
-4
-3
-2
-1
0
1
2
3
4
5
H+/H2
H2O/O2
CHO+Ov
S@OII+Ov
Se@OI+Ov
Se@OIII+Ov
Te@OII+Ov
HOMO

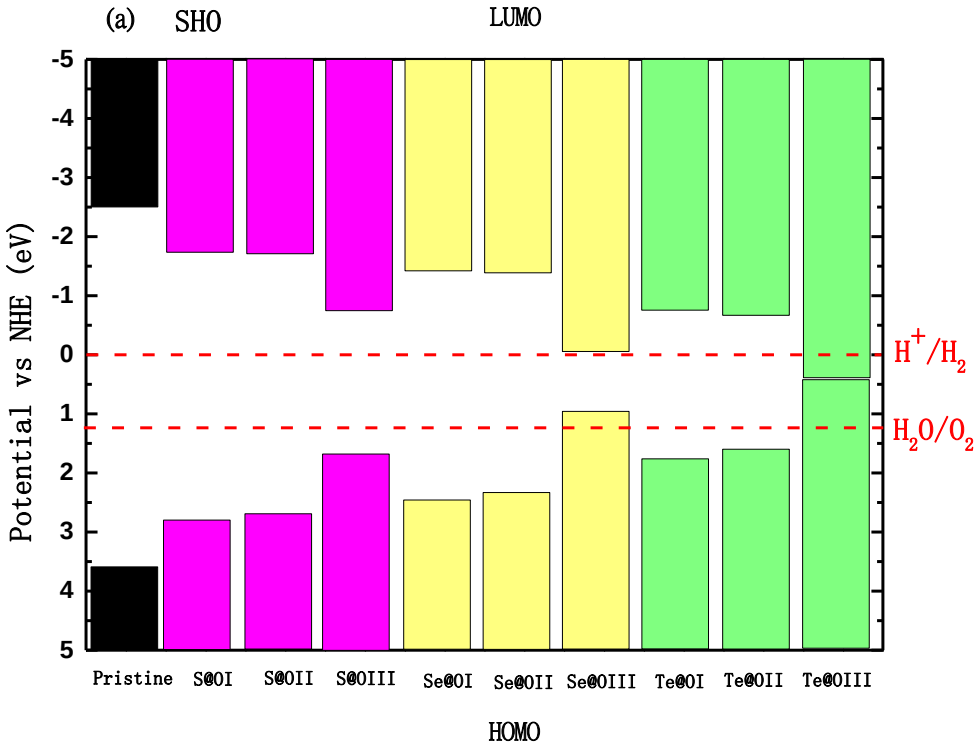
(a) SHO
LUMO
Potential vs NHE (eV)
-5
-4
-3
-2
-1
0
1
2
3
4
5
H+/H2
H2O/O2
Pristine
S@OI
S@OII
S@OIII
Se@OI
Se@OII
Se@OIII
Te@OI
Te@OII
Te@OIII
HOMO

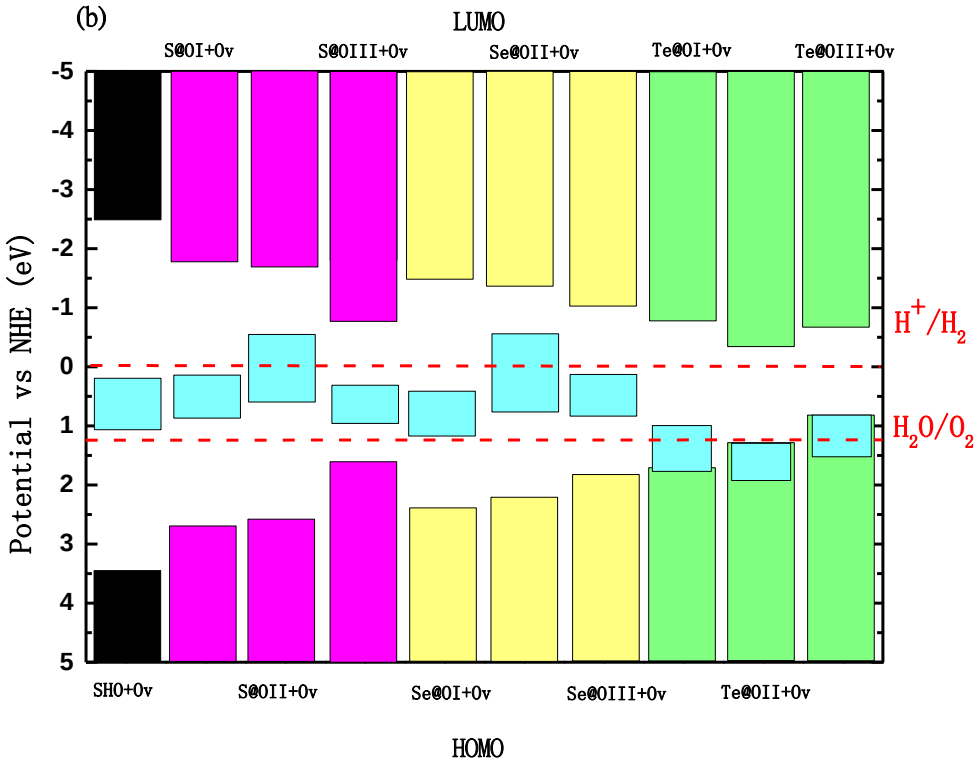

Figure IV.7: The HOMO and LUMO energy positions of the pristine, chalcogens doped-CZO/CHO or SHO without (a), and with (b) the presence of an F-center defect relative to the Normal Hydrogen Electrode (NHE) potential

IV. 3. 4. Thermodynamic stability

The feasibility of synthesis of a compound can be evaluated by enthalpy of formation which can be calculated according to the following equation (taking SHO compound as an example) [145]:

$$\Delta H_f = \frac{1}{N}(E(ABO_{3-\delta-X}Y_X) - E(pristine) - n\mu_{S/Se/Te} + n\mu_O) \quad \textbf{(Eq. IV.3)}$$

Where ΔH_f is the enthalpy of formation, E (doped) and E (pristine) are the total energy of $ABO_{3-\delta}$-xYx ($X \neq 0$ and $\delta \neq 0$) (where A = Ca or Sr, and B = Zr or Hf) structures and pristine in the supercell respectively, N is the total number of atoms in the supercell, n is the number of the doped atoms and μ represents the chemical potential of S, Se, Te and O atoms. The calculated enthalpy of formation values are presented in **Figure IV. 8**. As is well known, the negative sign of enthalpy of formation for a compound shows that the heat energy is released to the outside environment during the formation. Therefore, the formation reaction is exothermic which means that the compound is stable and can be easily synthesized at ambient conditions [145]. From **Figure IV. 8** we can note that the stability of chalcogens doped-CZO/CHO or SHO is

slightly reduced when chalcogens doping concentration increases compared with pristine ABO_3, especially for Te-doped CZO//CHO or SHO. On the other hand, it is clear that the value of formation energy is smaller when chalcogens impurities meet an oxygen vacancy which makes these structures are more stable than the pristine ones especially for CHO compound. Hence, from the enthalpy of formation, we can certify that all studied structures are thermodynamically stables and they can easily synthesize at ambient conditions.

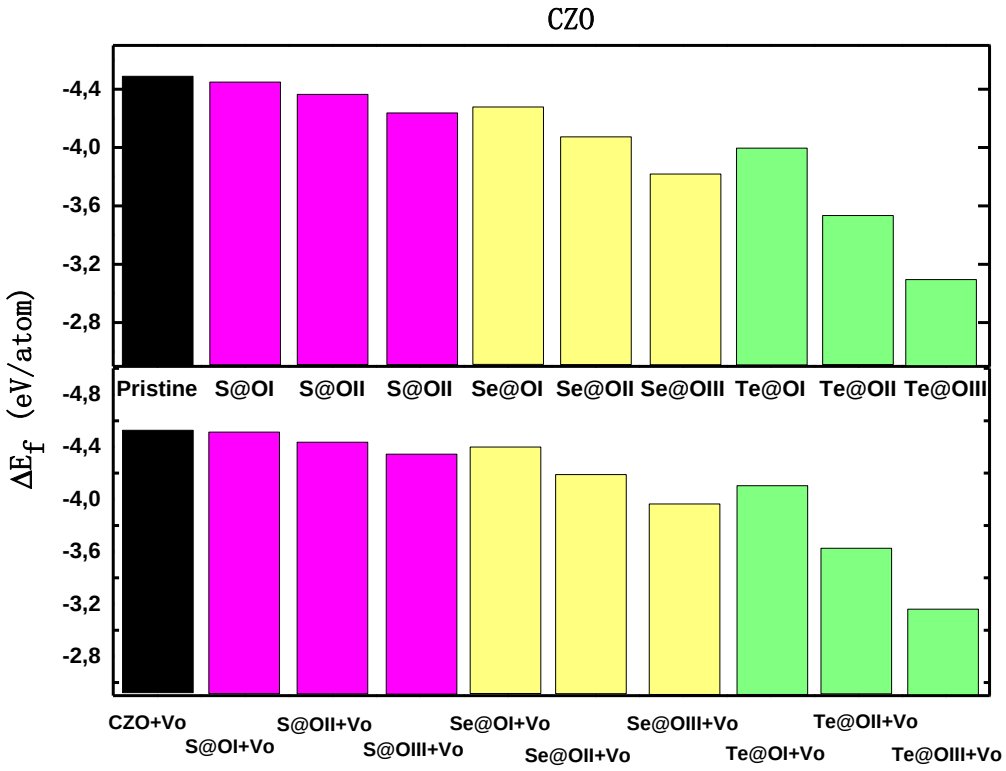

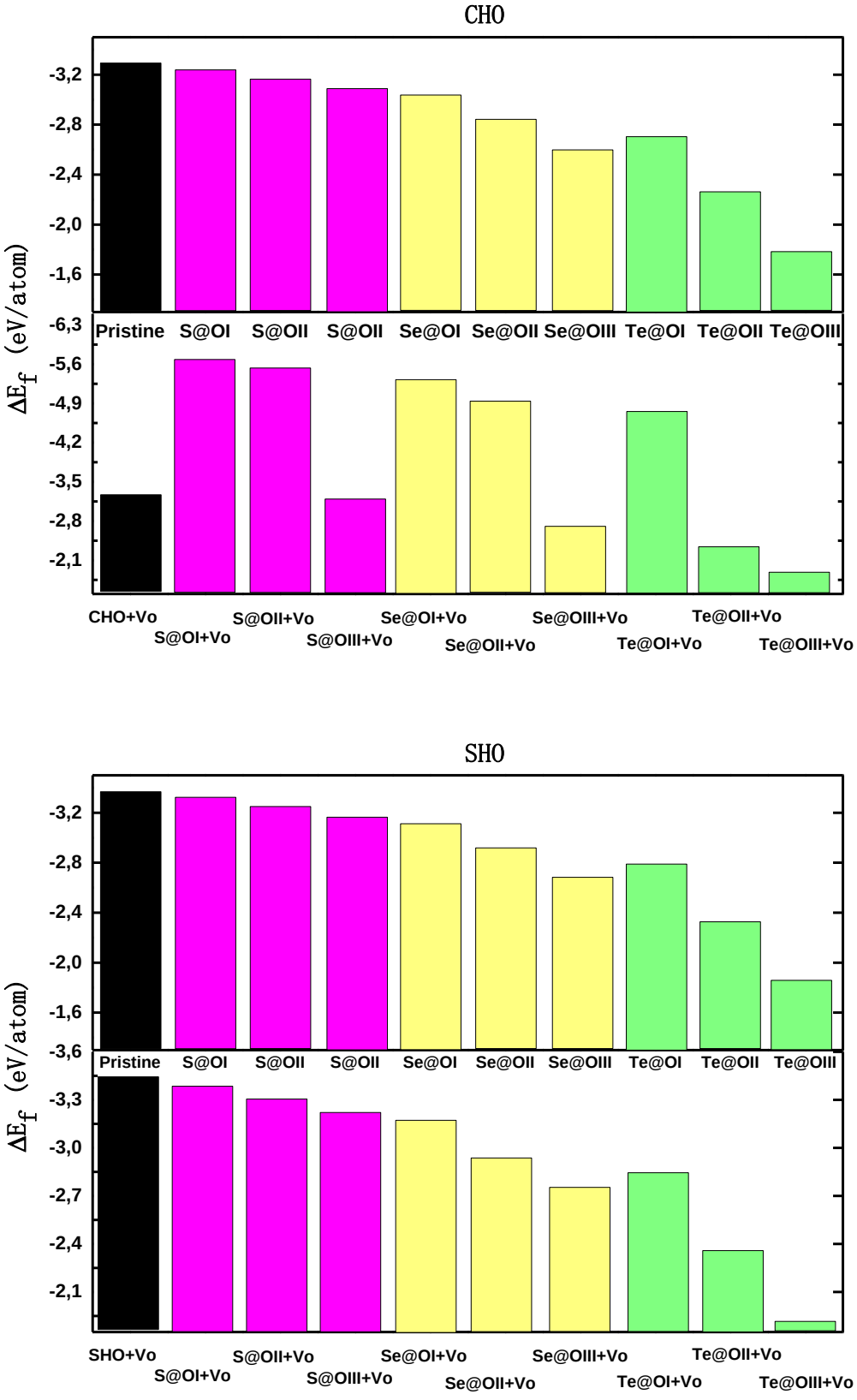

Figure IV.8: The enthalpy of formation of chalcogens doped-CZO/CHO or SHO without and with the presence of an F-center defect

IV. 4. Conclusion

In the present study, the effect of chalcogens-doped CZO, CHO and SHO with and without the presence of F-center on electronic, optical, and photocatalytic properties were carried out, based DFT using LDA+mBJ approximation which did not show any significant differences between the results obtained and the experimental ones. Our results corroborate that new orbital have been appearing in the VB and CB of CZO, CHO and SHO when oxygen atoms were replaced by chalcogens' impurities which decreased the forbidden band effectively. Moreover, an intermediate band was appeared in the middle of the forbidden band in all structures having an F-center defect. On the other hand, the absorption coefficient extends in the visible spectrum when chalcogens impurities meet an F-center defect due to the shifting of the Fermi level to LUMO structures caused the n-type semiconductor behavior giving rise to the enhancement of carrier concentrations. In addition, the upward of the HOMO and downward of LUMO positions of all studied compounds indicate that the structures exhibit strong reduction/oxidation ability, and the intermediate band guarantees the efficiency of the charge transfer especially for S/Se@OI/OII/OIII+Ov structures for CZO and S/Se/Te@OII+Ov structures for CHO and SHO structures which is a basic requirement for photovoltaic and photocatalytic under visible light devices. Finally, from the enthalpy of formation, we can certify that all studied structures are thermodynamically stables.

Chapter V : Importance of spin-orbit coupling on photovoltaic properties of Pb-free vacancy ordered double perovskites halides X_2TeY_6 (X = Cs, Rb, and Y = I, Br, Cl): First-principles calculations

V. 1. Introduction

Halide Perovskites (HPs) solar cells are attracting widespread interest from the scientific community because they have been proved as considerable light absorbers [146 – 148], they have a high PCE [149] and simple manufacturing process [150]. In order to have Pb-free HPs with high PCE, several attempts have been made in order to substitute Pb element by inorganic metal cation such as; silver (Ag) [151], titanium (Ti) [152], tin (Sn) [153,154], copper (Cu) [155], bismuth (Bi) [156], Palladium (Pd) [157], Selenium (Se) [158], and tellurium (Te) [159]. Moreover, the lead-free double HPs types A_2BX_6 have been considered as promising semiconductors perovskites because they are environmentally benevolent perovskites and due to their long-term stabilities. Besides, several experimental and theoretical studies have been done to study the physical properties of A_2BX_6 double HPs including; Shodruz et al. [153], synthesized A-site tailoring in Cs_2SnI_6 by adding monovalent cation (Rb and Ag), which leads to a small reduction in the forbidden band from 1.41 ± 0.02 eV (pristine) to 1.31 ± 0.02 eV ($(Cs_{1-x}A_x)_2SnI_6$ where X = Rb or Ag), which enhances the photovoltaic parameters such as V_{OC} (from 0.191± 0.051 V to ~ 0.38 V), and the efficiency (from 0.103 ± 0.051% to 0.258 ± 0.018% and 0.659 ± 0.022 % for X = Rb and Ag, respectively), as well as an excellent thermal stability in ambient air was observed. Xiaofeng et al. [154] synthesized the air-stable Cs_2SnI_6 with a bandgap of 1.48eV and high absorption coefficient (over10^5 cm^{-1} from 1.7eV) which can be utilized as an effective light absorber material in a simple planar n-i-p solar cell structures. Recently, Malak et al. [158] considered Cs_2SeCl_6 and Cs_2TeCl_6 perovskites as novel promising compounds for thermoelectric materials for power generation at high temperatures due to their high stabilities and high figure of merit (ZT) values compared to Pb HPs. Ju et al. [146] synthesized Ti-based HPs ($Cs_2TiI_xBr_{6-x}$) with the ideal values 1.38 eV for $Cs_2TiI_2Br_4$ and 1.78 eV for Cs_2TiBr_6 with high stability. Bhamu et al. [157] performed the density functional investigations for Cs_2PdX_6 (X=Cl and Br), and it was found that these compounds have indirect forbidden bands with values of 2.29 eV and 1.22 eV for Cs_2PdCl_6 and Cs_2PdBr_6 respectively, and the optical absorption confirms the utilization of Cs_2PdX_6 (X=Cl and Br) as solar cells and as low-temperature thermoelectric compounds. Freshly, Alshahrani et al. [160] examined the role of 5d electrons spin in quantum ferromagnetism and transport properties of double

perovskites Cs_2ZCl/Br_6 (Z = Ta, W) for spintronic applications. As mentioned by Malak et al. [161], Cs_2NpBr_6 material is highly recommended to use for spintronics applications. Rehan et al. [162,163] calculated the structural, electronic, magnetic, optical, and thermoelectric properties of K_2OsX_6 (X = Cl and Br) and Cs_2NbI_6 compounds. A recent researcher examined the transport and optoelectronic properties of Rb/Cs_2TeI_6, and it was found that these materials are effectively suitable for thermoelectric materials and solar cell applications [164]. A new study has also been published on Rb_2TeX_6 (where X=Cl, Br, and I) [165], and it was found that these compounds have forbidden bands to exhibit from 3.2 eV to 1.8 eV shifting the absorption to the visible region and increasing the ZT by the substitution of Cl by Br and I ions boosting the optoelectronics, solar cells applications and thermoelectric generators performances of Rb_2TeX_6. These studies approve the use of A_2BX_6 in variant fields. Therefore, we got the motivation to carry a research on Pb-free the vacancy ordered double perovskites halides X_2TeY_6 (X = Cs, Rb, and Y = I, Br, and Cl) because these compounds are still poorly studied in the literature. Moreover, as far as we know, no other authors have investigated the Spin Orbit-Coupling (SOC) effects on X_2TeY_6 compound. Thus, the aim of the present work is to investigate the role of SOC on the physical properties of X_2TeY_6 double perovskites Halides (DHPs) due to the presence of heavy elements Cs/I. We believe that our study will improve knowledge and serve as a base for future studies on Cs_2TeI_6 (CTI), Cs_2TeBr_6 (CTB), Cs_2TeCl_6 (CTC), Rb_2TeI_6 (RTI), Rb_2TeBr_6 (RTB), and Rb_2TeCl_6 (RTC) compounds.

V. 2. Computational technique methodology

The equation of Schrodinger wave is solved using the Density Functional Theory [104] computational WIEN2K software [73], within full-potential linearized augmented plane wave method in order to investigate the crystal structures, electronic properties, optical properties, and the stabilities of X_2TeY_6 (where X = Cs and Rb; Y = I, Br, and Cl) DHPs. The Wu Cohen-generalized gradient approximation [61] was used to optimize the crystal structures of X_2TeY_6 which gives high precision. On the other hand, WC-GGA failed to provide the accurate forbidden band and electronic properties on which the optical properties are dependent. Therefore, improving the forbidden bandgap until high precision is necessary. The modified Becke and Johnson potential of Trans and Blaha (TB-mBJ) [67] was added to the WC-GGA approximation to have the accurate forbidden band. The SOC interaction is taken into account in our calculations [166]. The cutoff energy was set to -6.0 Ry, $R_{MT} \times K_{max} = 8$ with 10×10×10 Monkhorst–Pack k-mesh in the first Brillouin zone.

V. 3. Results and discussion

V. 3. 1. Crystal optimization, thermodynamic stability, and cohesive energy

The Pb-free vacancy ordered DHPs X_2TeY_6 (X = Cs and Rb; Y = I, Br, and Cl) crystallize into face centered cubic structures with space group Fm-3m (No 225). The experimental studies have confirmed that X (X = Cs or Rb) atoms occupy 8c Wyckoff site (0.25, 0.25, 0.25), Te atom occupy 4a Wyckoff site (0, 0, 0) and Y atoms (Y = I, Br, and Cl) take 24e Wyckoff site (**u**, 0, 0). A Hardly any variation of the anion displacement (u), therefore, in our study **u** was taken value 0.252 for each material. Murnaghan's equation of state was used to optimize the crystal structures. **Figure V. 1** pinpoints the atomic occupations and the unit cell and total energy versus the volume fitting of X_2TeY_6 DHPs. The optimized crystal structures by different approximations are presented in **Table V.1**, from this table we can note that the lattice parameter increases with the increase of the atomic size from Cl, I to Br. Furthermore, lattice parameters obtained from WC-GGA approximation are the closest to the experimental ones compared to Pbe-GGA, Pbsol-GGA, and LDA approximations except that of CTC and RTC because they obtained lattice parameters from WC-GGA approximation is by 0.68% and 0.83% smaller than the experimental ones [167,169], while Pbe-GGA approximation gives lattice parameters smaller by 0.19% and larger by 0.73% compared to the experimental one for CTI and RTC respectively. Hence, the deviations between our results and the experimental results are below 1% which makes the results obtained by WC-GGA, Pbe-GGA, Pbsol-GGA, and LDA close to the experimental ones.

Table V.1: Presents optimized lattice parameter of CTI, CTB, CTC, RTI, RTB, and RTC DPHs with available experimental and theoretical results

	Lattice parameter a (Å)					
Compound	**Pbe-GGA**	**Pbsol-GGA**	**WC-GGA**	**LDA**	**Theoretical**	**Experimental**
CTI	11.9075	11.6262	11.6368	11.4513	11.6423[164]	11.700 [167]
CTB	11.0313	10.7908	10.8027	10.6252	-----	10.888 [167]
CTC	10.4246	10.4246	10.2334	10.0717	10.603 [168]	10.445 [167]
RTI	11.8255	11.5769	11.5940	11.3972	11.588 [164]	11.670 [169]
RTB	10.9329	10.7228	10.7444	10.5558	10.910 [165]	10.773 [167]
RTC	10.3085	10.1285	10.1486	9.9729	10.390 [165]	10.233 [167]

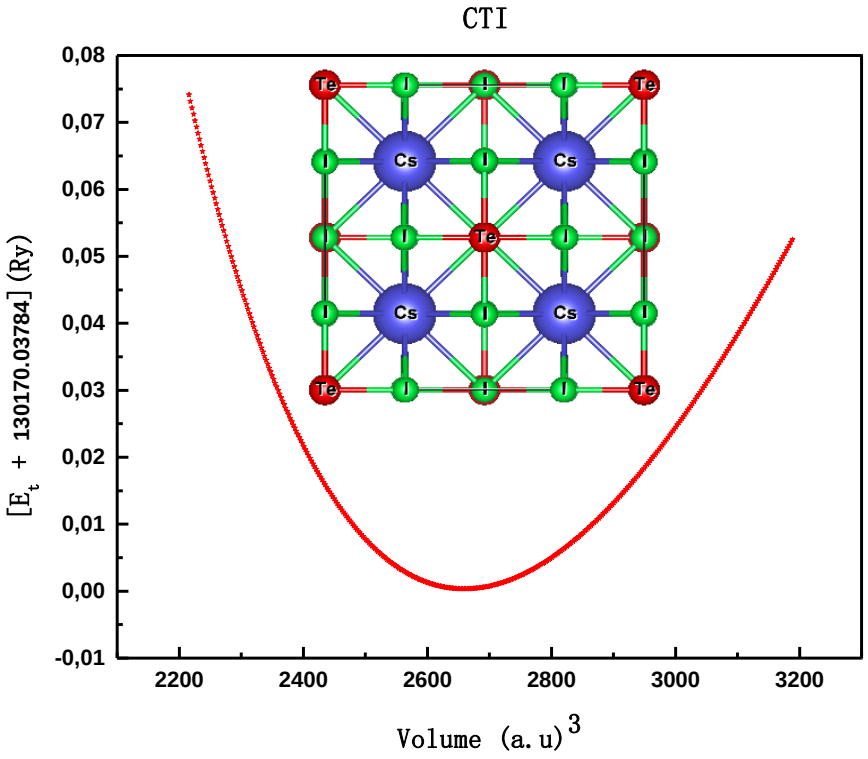
CTI
0,08
0,07
0,06
0,05
0,04
0,03
0,02
0,01
0,00
-0,01
[E_t + 130170.03784] (Ry)
2200
2400
2600
2800
3000
3200
Volume (a.u)^3
Te
I
Cs

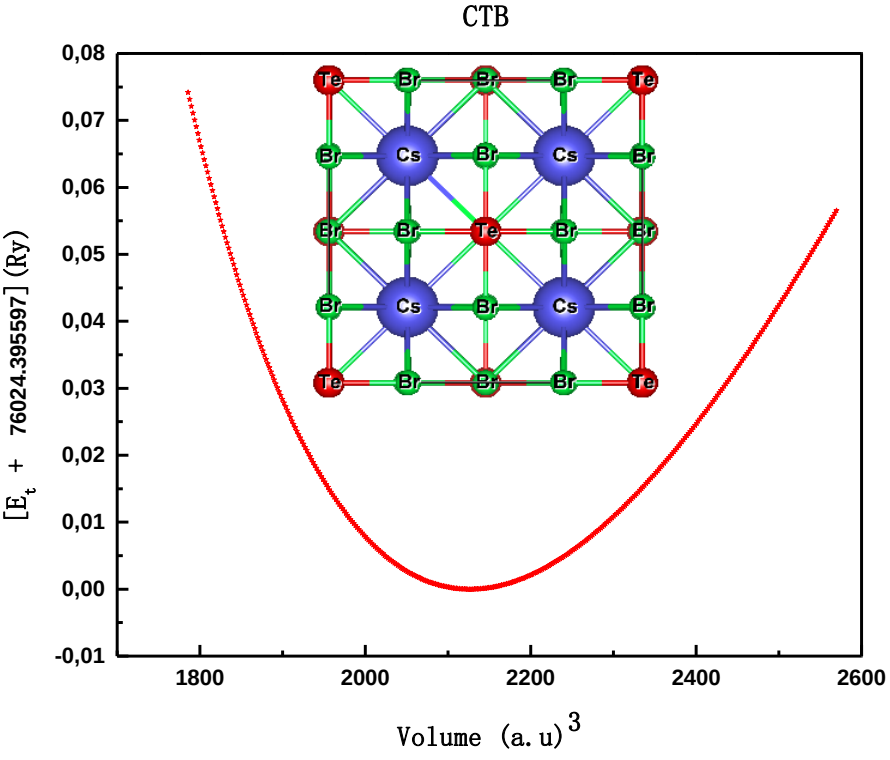
CTB
0,08
0,07
0,06
0,05
0,04
0,03
0,02
0,01
0,00
-0,01
[E_t + 76024.395597] (Ry)
1800
2000
2200
2400
2600
Volume (a.u)^3
Te
Br
Cs

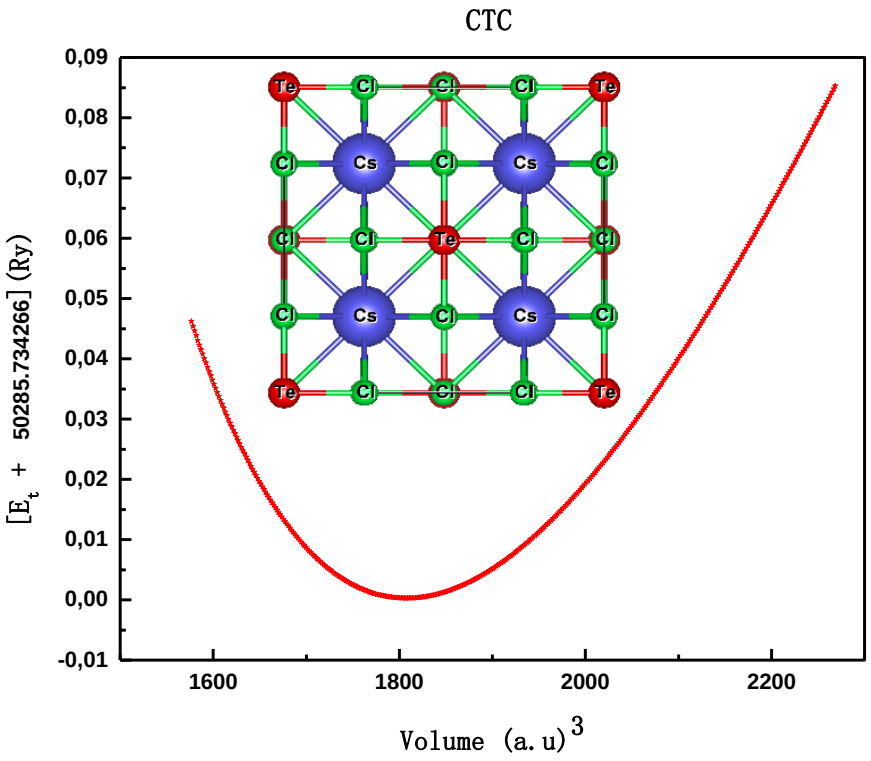
CTC
0,09
0,08
0,07
0,06
0,05
0,04
0,03
0,02
0,01
0,00
-0,01
[E_t + 50285.734266] (Ry)
1600
1800
2000
2200
Volume (a.u)^3
Te
Cl
Cs

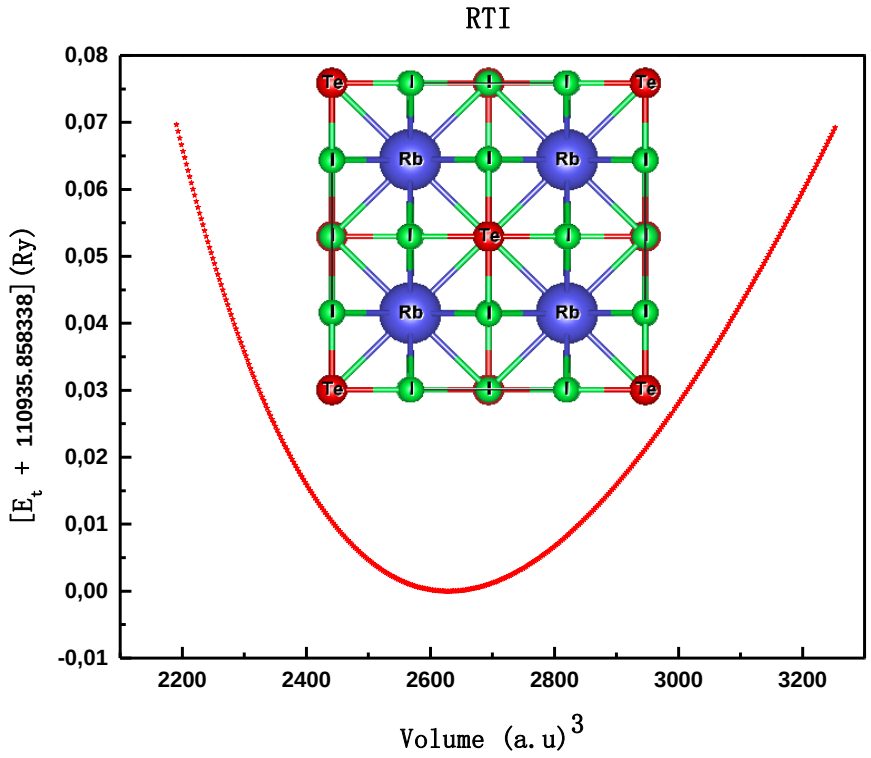
RTI
0,08
0,07
0,06
0,05
0,04
0,03
0,02
0,01
0,00
-0,01
[E_t + 110935.858338] (Ry)
2200
2400
2600
2800
3000
3200
Volume (a.u)^3
Te
I
Rb

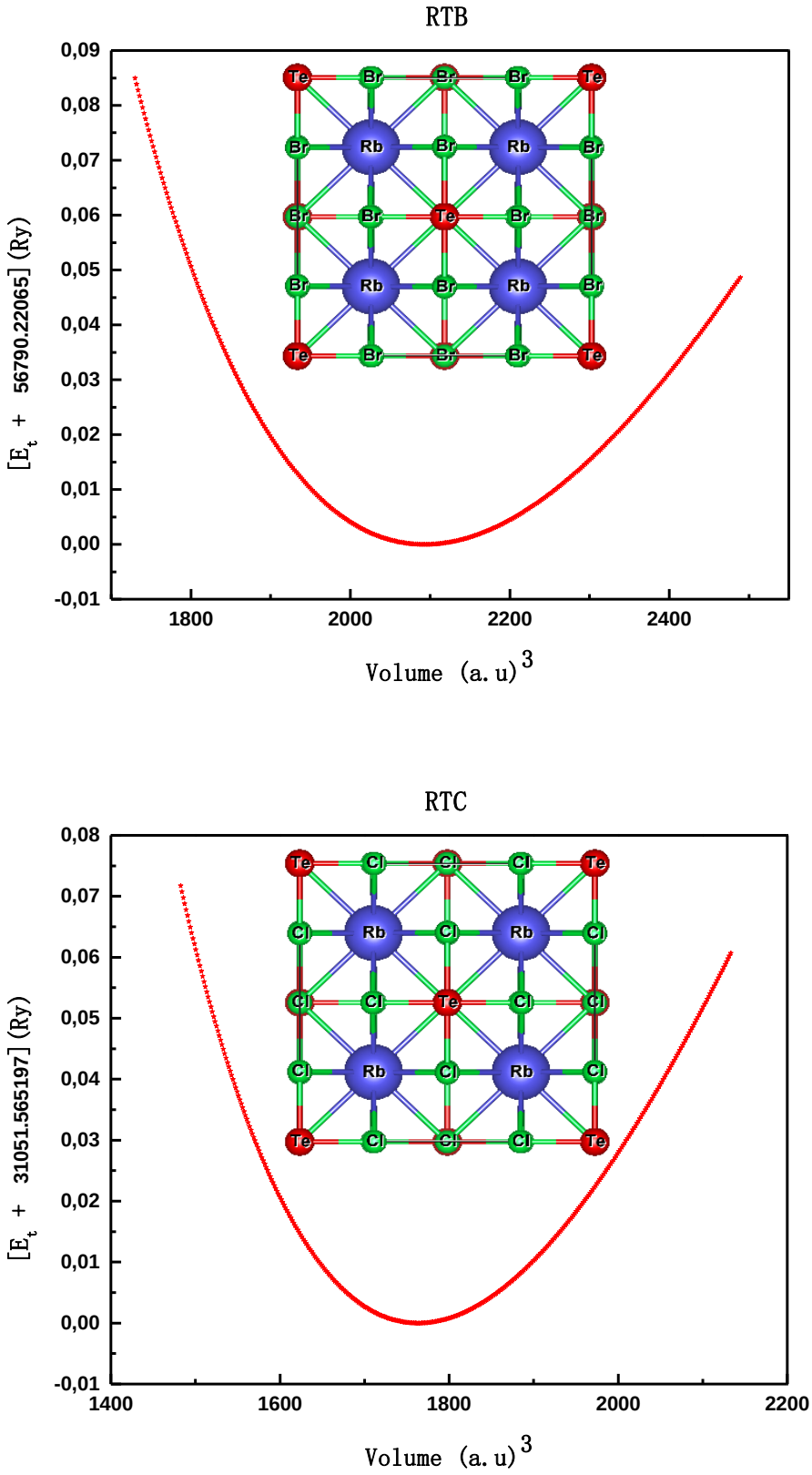

Figure V.1: The unit cell, and the total energy versus the volume of of X_2TeY_6 (X = Cs, Rb; Y = I, Br, and Cl) of DPHs using GGA-WC

After crystal structures optimization, the enthalpy of formation was calculated in order to explore the thermodynamic stability of X_2TeY_6 (X = Cs and Rb; Y = I, Br, and Cl) compounds using the following formula [170]:

$$\Delta H_f = (E_{total}(X_2TeY_6) - 2E(X) - E(Te) - 6E(Y)) \quad \textbf{(Eq. V.1)}$$

Herein, E_{total} (X_2TeY_6) represents the total ground state energy of X_2TeY_6, E(X), E(Te), and E(Y) are the ground state energies of X (body center cubic), Te (hexagonal), and Y(orthorhombic) in the bulk form. **Table V. 2** proves that the ΔH_f values affirm that CTI, CTB, CTC, RTI, RTB, and RTC phases are energetically favorable from the point of view of thermodynamics, and these structures can be formed during experiments. Moreover, the ΔH_f value decreases by substituting I by Br and Cl. Therefore, the thermodynamic stability is gradually increased from X_2TeI_6, X_2TeBr_6 to X_2TeCl_6. Our findings appear to be well supported by the experimental data [171], in which the standard heat of formation of RTC has been found to be -294.4 kcal mol^{-1} at 298 K which ensures its stability. Further, **Table V. 2** demonstrates that our results are in complete agreement with other simulation results [158,164].

The cohesive (or binding) energy (E_{Coh}), is a measure of the strength of the forces that bind the individual atoms together in solids and is helpful in determining the phase stability of any compound. The cohesive energy per atom of X_2TeY_6 DHPs can be determined via the following equation [172]:

$$E_{Coh}^{X_2TeY_6} = \frac{[2E_{atom}^{X} + E_{atom}^{Te} + 6E_{atom}^{Y}] - E_{X_2TeY_6}}{9} \quad (\textbf{Eq. V. 2})$$

Where E_{atom}^{X}, E_{atom}^{Te}, and E_{atom}^{Y} are isolated atomic energies of X, Te, and Y atoms, respectively. Moreover, the calculated cohesive energies of X_2TeY_6 compounds are presented in **Table V. 2**, and from this table, the high E_{Coh} values indicate that the individual atoms are strongly held together in the crystal lattice of all studied compounds.

Table V.2: The calculated enthalpy of formation (ΔH_f) and cohesive energy (E_{Coh}) of CTI, CTB, CTC, RTI, RTB, and RTC DPHs with available theoretical results

	CTI	CTB	CTC	RTI	RTB	RTC
ΔH_f (eV)	-13.4102 -13.6600 [164]	-19.6381 ------	-23.9548 -24.1300 [158]	-14.0315 -14.2400 [164]	-20.2088 ------	-24.5521 ------
E_{coh} (eV/atom)	1.5170	2.1905	2.6613	1.5823	2.2667	2.7416

V. 3. 2. Electronic density of states and band structures

The optical characteristics of solar cell devices depend on the electronics properties. Thus, the total, partial densities of states and the band structure, of X_2TeY_6 (X = Cs and Rb; Y = I, Br, and Cl) were depicted in **Figure V. 2.** Furthermore, WC-GGA**,** WC-GGA+TB-mBJ, and WC-GGA+TB-mBJ+SOC approximations were used to calculate the electronics properties of DHPs compounds, and the results are compared in **Table V. 3**. We can note that WC-GGA approximation underestimates the forbidden band of X_2TeY_6. It is worthwhile noting that the DFT-GGA underestimates the forbidden band of semiconductor materials [173]. Therefore, various theoretical approaches have been proposed to overcome this deficiency including the TB-mBJ [67]. It can be seen in **Table V. 3** that WC-GGA+TB-mBJ and WC-GGA+TB-mBJ+SOC exchange-correlation potentials provide forbidden bands values close to the experimental ones [173 – 176], and these values increase as we move up the halogen in the periodic table (from I to Cl). In addition, when relative effects are included, the forbidden band value has been slightly reduced for all studied compounds, such calculations have also evidenced the major role of SOC reduces the forbidden band by splitting the first degenerated conduction levels. Otherwise, the TDOS and PDOS of X_2TeY_6 have similar profiles with and without SOC, but only the LUMO is shifted towards the Fermi Level (E_F) which results in the forbidden band reduction in all cases due to SOC effects. Further, the $5p^5$/ $4p^5$/$3p^5$ states of I/Br/Cl hybridize with $5s^2$ and $5p^4$ states of Te in the upper VB while the bottom CB is primly occupied by $5p^4$ Te states and $5p^5$/$4p^5$/$3p^5$ states of I/Br/Cl. Meanwhile, **Figure V. 2** demonstrates that the HOMO of all studies compounds (X_2TeY_6) lies at W (0.5, 0.25, 0.75) high-symmetry point while the LUMO lie at L (0.5, 0.5, 0.5) high-symmetry point in the first Brillouin zone, thus X_2TeY_6 DHPs exhibit indirect forbidden bands behaviors in W→L direction. Our results appear to be well substantiated by the literature's results [158,164,165]. On the other hand, when relativistic SOC interaction is included, the HOMO is unchanged for all studied compounds except that of CTI and RTI, which is shifted from W (0.5, 0.25, 0.75) to X (0.5, 0.0, 0.5) high-symmetry point. Our findings are in good agreement with the experimental data [175], demonstrating that CTI has an indirect forbidden band along the X→L direction. Similarly, Rehan Ullah et al. [177] found that when SOC is included, the HOMO of Cs_2HfI_6 (CHI) double perovskite was changed from X (0.5, 0.0, 0.5) toΓ (0.0, 0.0, 0.0) high-symmetry point which suggests that the SOC is necessary to study the HOMO of A_2BI_6 DHPs due to the presence of Iodine (I) because it is considered as a heavy element. Besides, due to the large SOC, CB splits into two bands separated by about 0.46 eV (CTI), 0.481 eV (CTB),

0.584 eV (CTC), 0.452 eV (RTI), 0.494 eV (RTB), and 0.588 eV (RTC) at Γ point, respectively. This shows that the CB shape is completely different due to the relativistic spin-orbit coupling effects. Hence, the inclusion of SOC is crucial for the correct description of the CB edge of X_2TeY_6 DHPs. For comparison, in the case of $Cs_2BiAgCl_6$ ($Cs_2SbAgCl_6$) [178], the CB edge splits in two bands separated by >1.5 eV (0.5 eV) at the Γ point, and upon inclusion of relativistic effects, the shape of the conduction band is drastic because the character of the bottom CB is of primarily Bi-p character. Besides, in the case of $(FC_6H_5C_2H_4NH_3)_2PbI_4$ [179], the energy spacing between the $(CBM_1+CBM_2)/2$ and CBM_3 (Conduction Band Minima) is about 1 eV, and the effect of the spin-orbit interaction is huge at the CBM leading to a large spin-orbit splitting between the two first conduction states, bearing resemblance to the case of $Cs_2BiAgCl_6$, $Cs_2BiAgBr_6$ [152], and $CH_3NH_3PbI_3$ [180].

Table V.3: Calculated forbidden bands (Eg) of CTI, CTB, CTC, RTI, RTB, and RTC DPHs along with experimental and theoretical values

	Eg (eV)					
Compound	**WC**	**WC+SOC**	**WC+mBJ**	**WC+mBJ+SOC**	**Theoretical**	**Experimental**
CTI	1.129	0.914	1.596	1.422	1.344 [164] 1.521 [164]	1.590 [175] 1.500 [176]
CTB	1.801	1.728	2.359	2.281	------	2.120 [181] 2.200 [182]
CTC	2.336	2.253	3.096	2.971	3.100 [158]	------
RTI	1.124	0.909	1.621	1.469	1.820 [165] 1.321 [164] 1.482 [164] 1.830 [175]	1.400 [176]
RTB	1.815	1.740	2.414	2.338	2.460 [165]	2.140 [181] 2.190 [182]
RTC	2.355	2.275	3.190	3.067	3.200 [165]	------

CTI

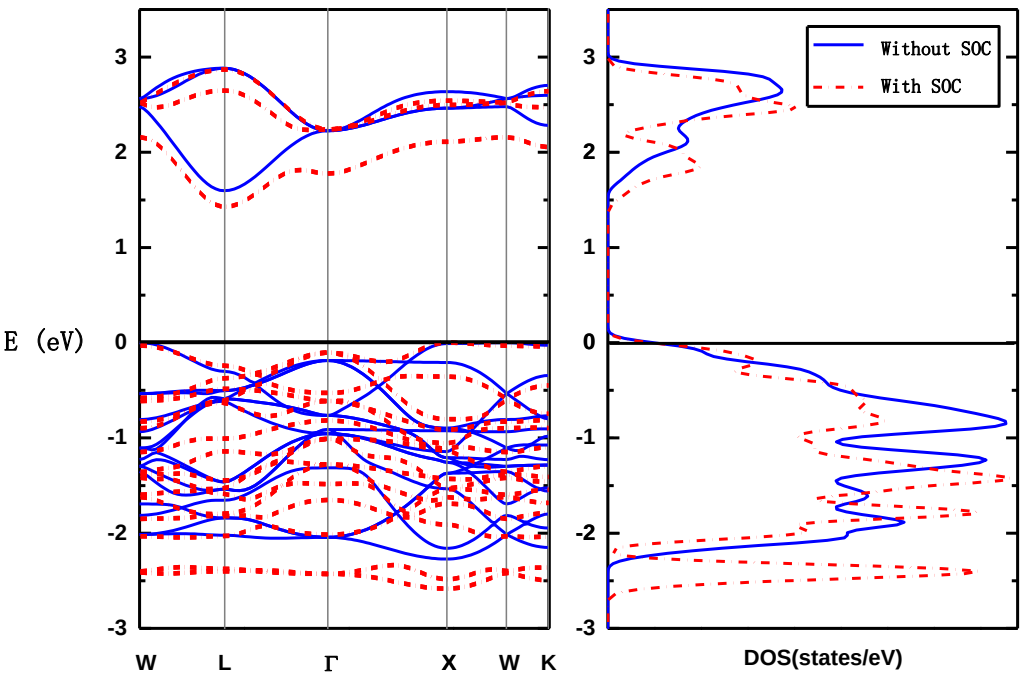
E (eV)
3
2
1
0
-1
-2
-3
W
L
Γ
X
W
K
Without SOC
With SOC
DOS(states/eV)

CTB

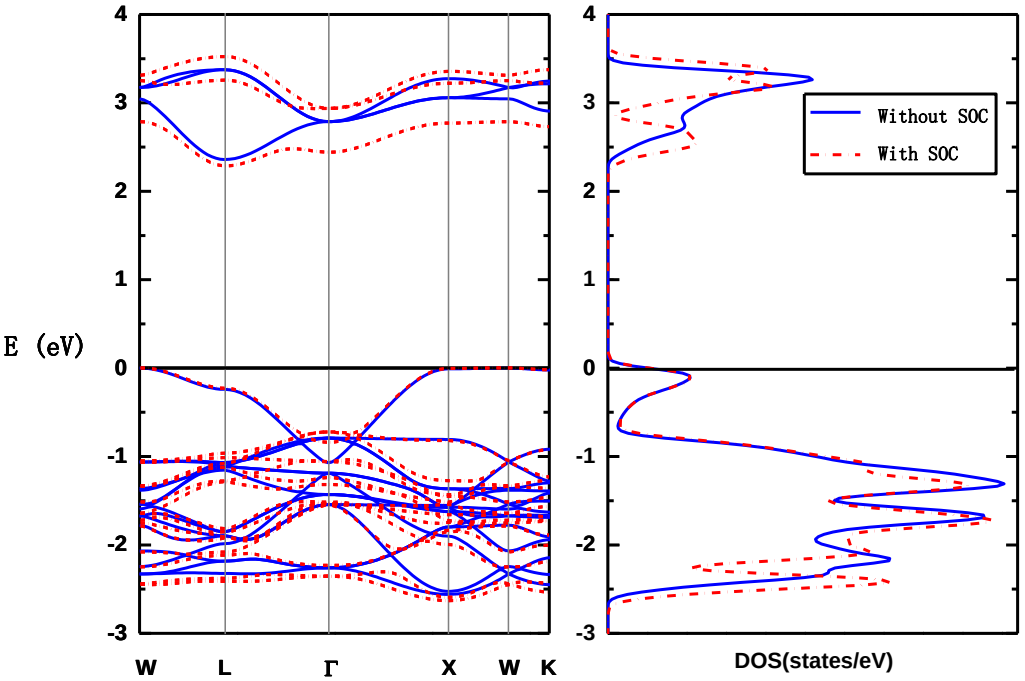
E (eV)
4
3
2
1
0
-1
-2
-3
W
L
Γ
X
W
K
Without SOC
With SOC
DOS(states/eV)

CTC

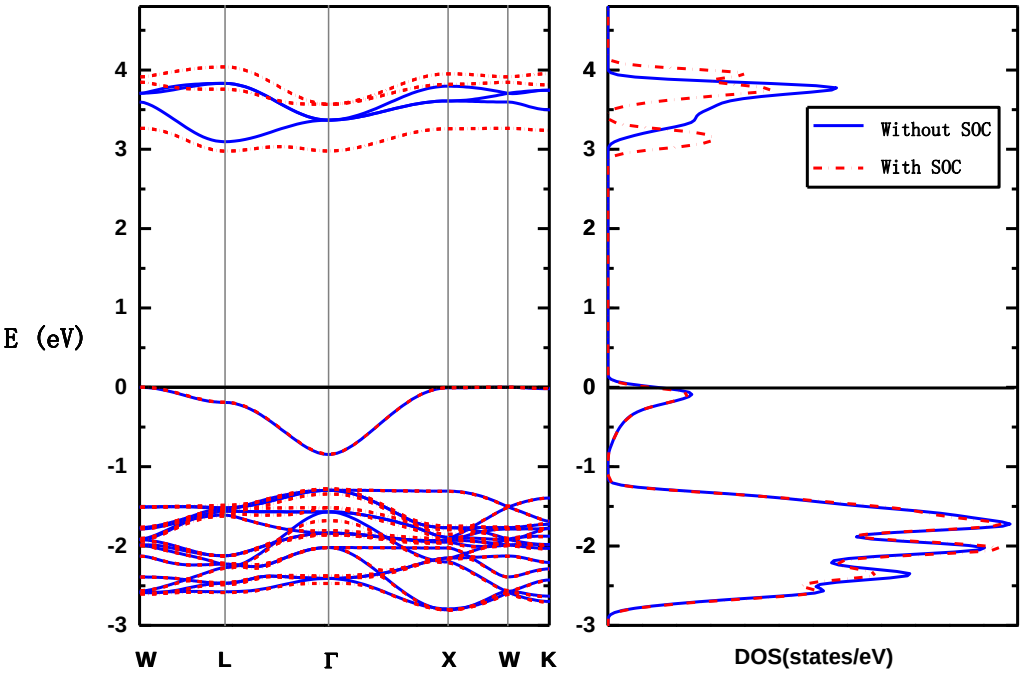
E (eV)
4
3
2
1
0
-1
-2
-3
W
L
Γ
X
W
K
Without SOC
With SOC
DOS(states/eV)

RTI

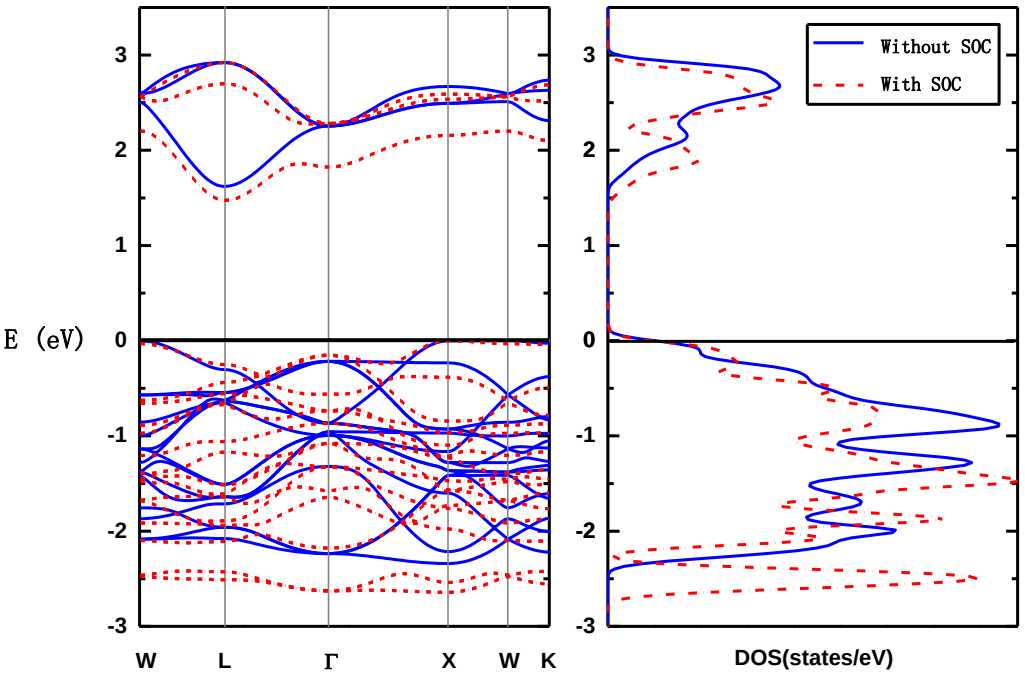
E (eV)
3
2
1
0
-1
-2
-3
W
L
Γ
X
W
K
Without SOC
With SOC
DOS(states/eV)

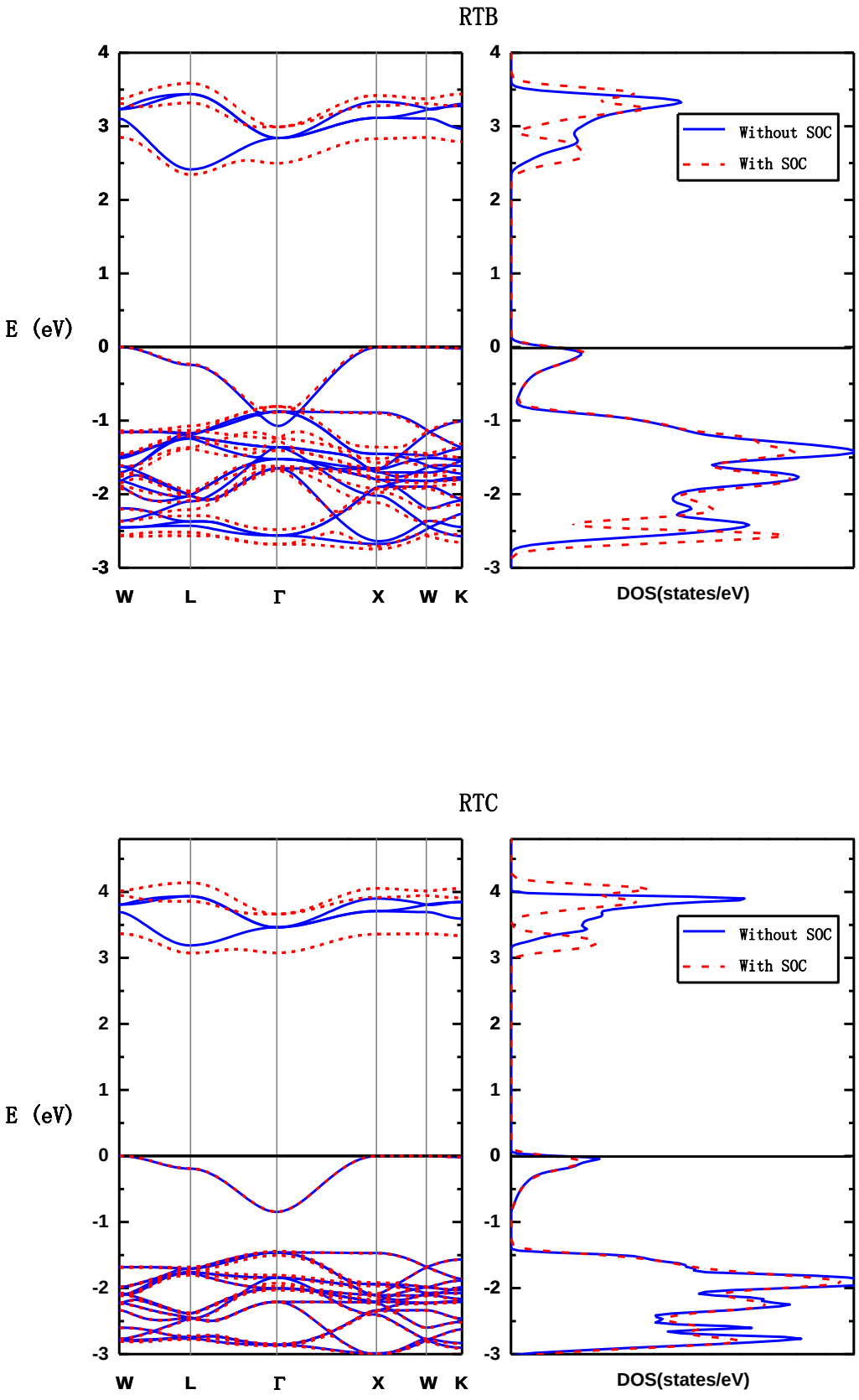

Figure V.2: The bands structures and TDOS of X_2TeY_6 (X = Cs and Rb; Y = I, Br, and Cl)

V. 3. 3. Optical properties

The optical properties are the keys to investigate the inter-band transitions of DHPs semiconductors for photovoltaic devices [112,115,170,183]. It is worth mentioning that the optical properties were performed using WC(GGA)+TB-mBJ+SOC functional, due to its high precision in the determination of the band structures for X_2TeY_6 (X = Cs and Rb; Y = I, Br, and Cl). Furthermore, the optical reflectance, transmittance, and absorption coefficient of X_2TeY_6 are plotted as percentages (%) in **Figure V. 3**. It is apparent from this figure that along the visible spectrum [390 nm – 780 nm] [170], the CTI and RTI compounds exhibit a high absorption coefficient around 62% - 75% and 57% - 76% for CTI and RTI, respectively while CTB (RTB) displays average absorption coefficient peaks of around 84% at 418 nm, and 78% at 494 nm (85% at 408 nm, and 78% at 483 nm for RTB). Moreover, it should be noted that for solar cells, a forbidden band in the range of (1 eV - 1.6 eV) is highly recommended, because it leads to matches well the absorption coefficient and the solar spectrum, as well as it maximizes solar cell efficiency [154]. Based on this, the suitable forbidden band (1.422 eV for CTI, and 1.469 eV for RTI) and the strong absorption in the whole visible spectrum make both CTI and RTI new potential candidate compounds for single-junction solar cells. On the other hand, all studied compounds have large absorption coefficients in the Ultraviolet (UV) region which makes these compounds be used for optical applications in the UV region. Additionally, both CTC and RTC show good transparencies and low absorption coefficients in the visible spectrum indicating that these materials can be used as transparent systems for solar cells.

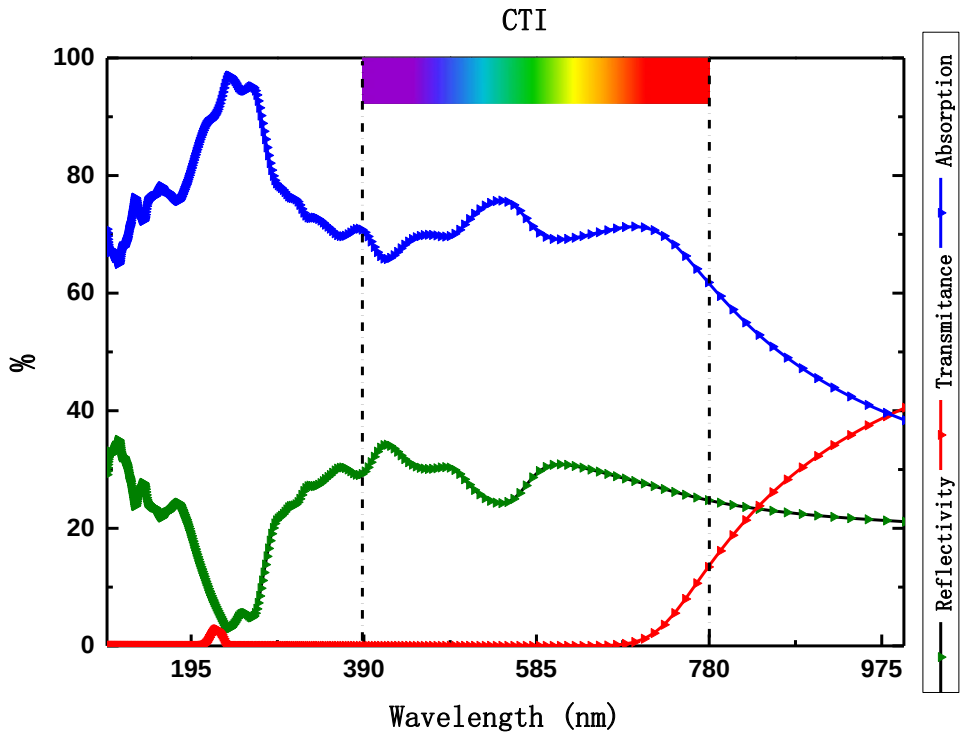
CTI
100
80
60
40
20
0
%
195
390
585
780
975
Wavelength (nm)
Absorption
Transmitance
Reflectivity

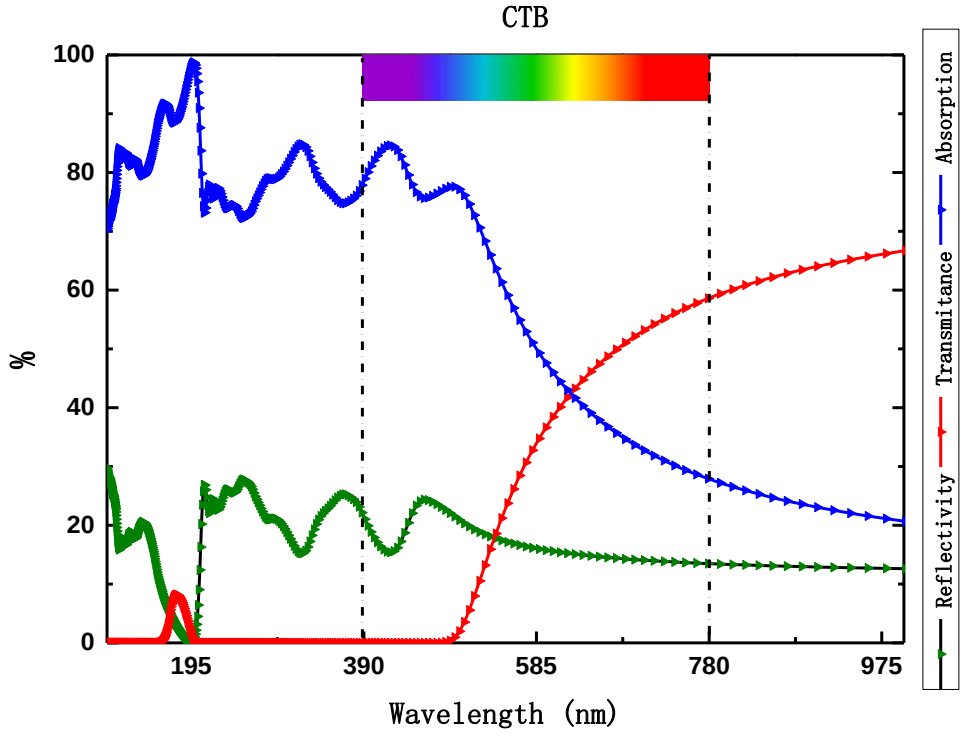
CTB
100
80
60
40
20
0
%
195
390
585
780
975
Wavelength (nm)
Absorption
Transmitance
Reflectivity

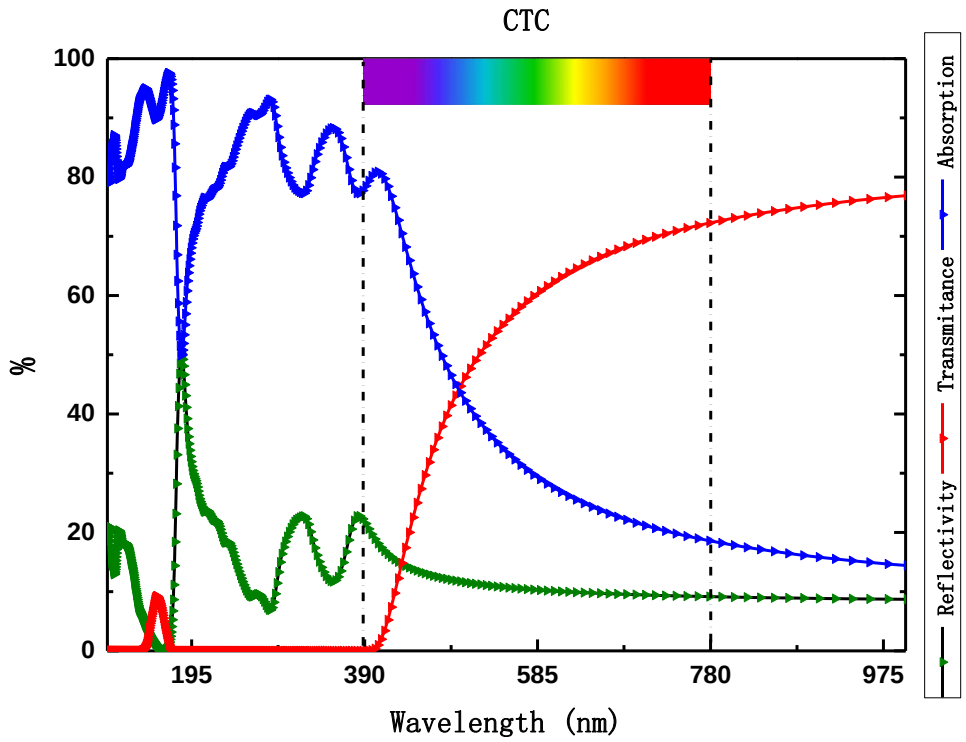
CTC
100
80
60
40
20
0
%
195
390
585
780
975
Wavelength (nm)
Absorption
Transmitance
Reflectivity

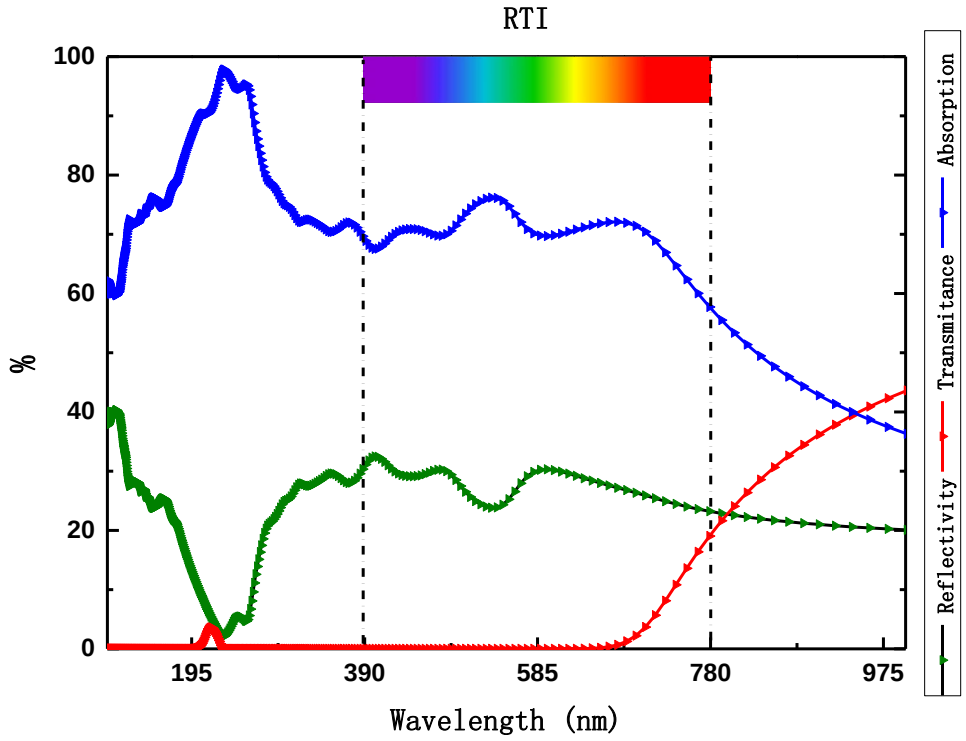
RTI
100
80
60
40
20
0
%
195
390
585
780
975
Wavelength (nm)
Absorption
Transmitance
Reflectivity

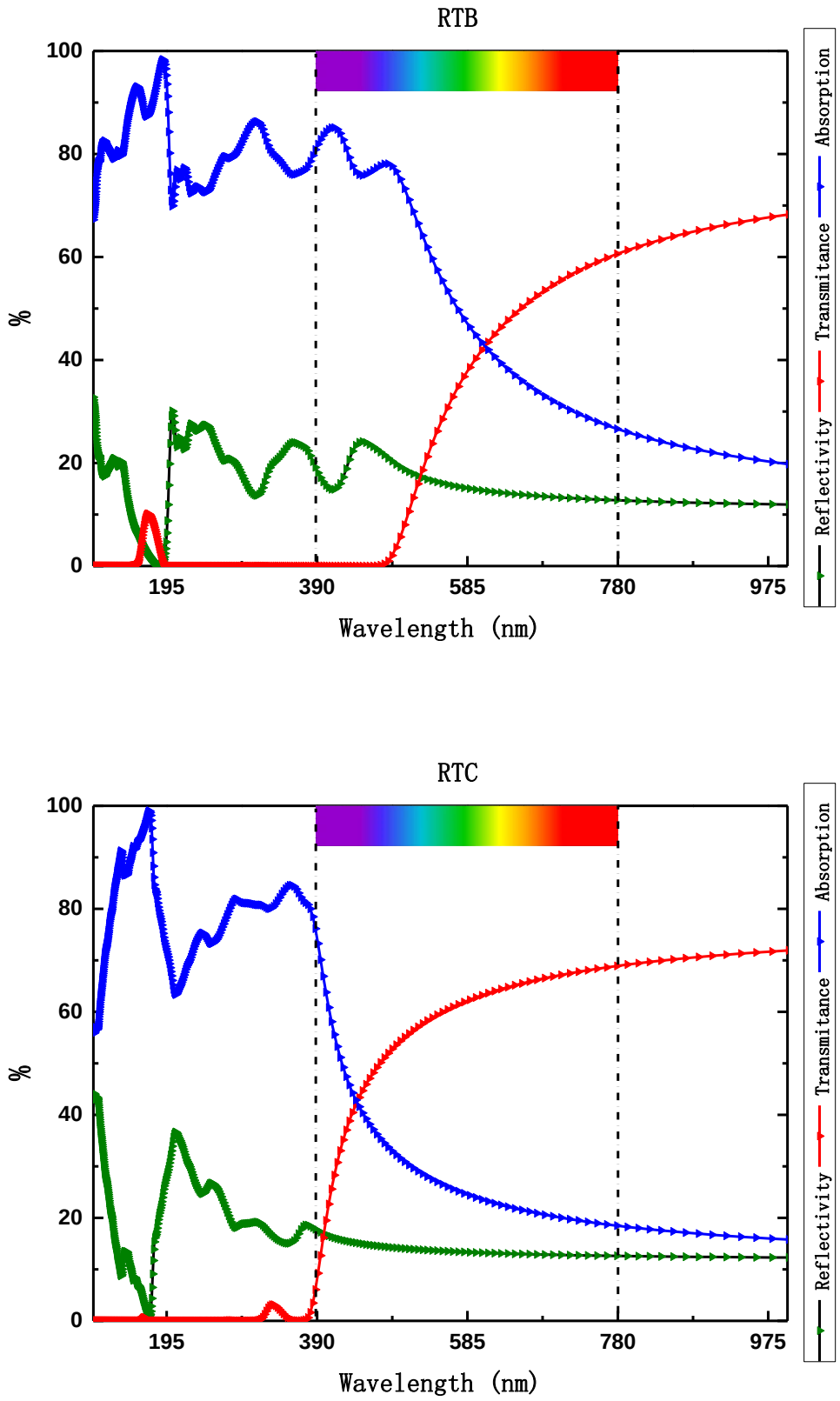

Figure V.3: The absorption coefficient, reflectivity and transmittance of X_2TeY_6 (X = Cs and Rb; Y = I, Br, and Cl)

V. 4. Conclusion

The density functional theory employed in Wien2k software was used to investigate crystal structures, thermodynamic stability, electronic densities of states, bands structures, and optical properties of Pb-free vacancy ordered DHPs X_2TeY_6 (X = Cs and Rb; Y = I, Br, and Cl). The computed lattice parameters are found in close resemblance with available experimental results. Moreover, the calculated negative formation energy values show that the reaction involved in the formation of all studied compounds is exothermic which confirms that X_2TeY_6 compounds are thermodynamically stable. Furthermore, the electronic densities of states of X_2TeY_6 show that the major contribution in the bottom CB is from $5p^5$/ $4p^5$/ $3p^5$ states of I/Br/Cl states while the principal contrition in the upper VB is from $5p^4$ Te states. Meanwhile, the band's structures ensured that the inclusion of SOC is necessary to have the correct characterization of the CB of X_2TeY_6 compounds. Our findings are in good agreement with the experimental data. Further, from the optical properties, we can note that all studied compounds exhibit large absorption coefficients in the UV region boosting the UV optoelectronic performances of X_2TeY_6 materials. In addition, CTI and RTI demonstrate strong absorption coefficients in the visible region and suitable forbidden bands values of 1.422 eV (CTI) and 1.469 eV (RTI) which boost the potential of CTI and RTI as solar cells for photovoltaic applications. These findings suggest the following directions for future research: the study of the defect tolerance in X_2TeY_6 compound, as well as the study on the optoelectronic properties of mixed-vacancy, ordered double perovskites halides $Cs_2TeI_{6-x-y}Br_xCl_y$.

Chapter VI : Earth-Abundant Nontoxic ternary calcium nitrides inverse perovskites for single-junction solar cells; ab-initio simulations

VI. 1. Introduction

On the way of hunting for efficient semiconductor compounds, the solar cells which have direct forbidden band gap values covering both infrared and visible energies (1 eV - 4 eV) [184], have been aroused immense interests in photovoltaic and optoelectronic applications. The photovoltaic technology relies primarily on monocrystalline silicon as a photons' absorber due to their astounding accomplishments in the photons absorption rates [184, 185]. Monocrystalline silicon is a semiconductor material with indirect forbidden band gap of 1.1 eV [186]. Knowing that, the direct semiconductors compounds have extra beneficials than the indirect ones, because the indirect electronic transitions demand the participation of additional photons to guarantee the momentum conservation [112,187,188]. Accordingly, this research targets semiconducting materials with direct forbidden band gap to boost the quantity of photons absorbed. The inexpensive and nontoxic ternary calcium nitrides Ca_3MN (M= P, As, Sb and Bi) inverse perovskites (anti-perovskites) compounds have been aroused immense interests over the past decade due to their phenomena and remarkable features [189 – 191], including ; the low recombination rate and low charge carrier effective masse were observed in Ca_3PN [184]. Dynamical stability of Ca_3PN was confirmed by Hao Cheng et al. [192]. The study of elastic, electronic and optical properties of $BiNCa_3$ and $SbNCa_3$ was reported by Moakafi et al. [193], by applying the full relativistic version of the full-potential with the mixed basis augmented plane wave plus local orbitals method (APW+lo). Ferromagnetism induced by cation and/or anion vacancies in Ca_3BiP was studied by Kadiri et al. [194] using the spin-polarized density functional theory calculations. The pressure- dependence of the structural and electronic properties, and the phase transition from orthorhombic to cubic was observed at 59 GPa for Ca_3XN (X = P, As and Bi) were carried out by Martins [195]. Using first-principles density functional calculations to study the effect of high pressures up to 40 GPa on structural and elastic properties of Ca_3AN (A = P, As, Sb, and Bi) was reported by Haddadi et al. [196]. The synthesis of Ca_3AN (A = P, As, Sb, and Bi) compounds was done by Ming et al. [197]. Recently, the optoelectronic and thermoelectric properties of Ca_3AsN in both orthorhombic and cubic phases were discussed by Hafiz et al. [198], using Generalized Gradient Approximation with the modified Becke- Johnson. Despite these studies, there is still a need of information about some of physical properties of Ca_3AN (A = P, As, Sb, and Bi). Based on this, our study

provides a considerable insight into physical properties of the non-silicon based ternary calcium nitrides Ca_3MN (M = P, As, Sb, and Bi) inverse perovskites by reporting the structural optimization, thermodynamic stability, mechanical stability, elastic properties, electronic structure, the percentage of ionic character, effective mass charge carrier, optical and thermoelectric properties.

VI. 2. Computational technique methodology

In the formwork, the equation of Schrodinger wave is solved using the Density Functional Theory [104], within Wien2k software [73] are used, where the full potential linearized augmented plane wave has been implemented. The generalized gradient approximation developed by Perdew, Burke and Ernzerhof [63], the modified Becke and Johnson potential of Trans and Blaha [67], and the hybrid function which was discovered by Yukawa screened PBE0 [69], were used in order to describe the exchange-correlation potential. the semi-classical Boltzmann equation was used in order to simulate the thermoelectric properties using BoltzTrap software [77]. For achieving energy convergence, the charge density Fourier coefficient expansion (G_{max}) was set as 12 (a.u.) while the RMT × Kmax product is considering to be 7. The k-space integration in the irreducible Brillouin zone was selected as 10 × 10 × 10 meshes.

VI. 3. Results and discussion

VI. 3. 1. Structural properties and thermodynamic stability

The optimized geometry structural parameters (a_0) and bulk modulus at zero pressure and T = 0 K (B_0), and its pressure derivative (B') of the cubic structure of Ca_3PN (CPN), Ca_3AsN (CAN), Ca_3SbN (CSN) and Ca_3BiN (CBN) inverse perovskites were determined using Brich-Munarghan equation of state (**Eq. VI. 1**) [199], by fitting the total energy of the system versus the volume of unit cell. The optimized volume of the system is that corresponds to the lowest energy. The calculated a_0, B_0 and B' of all studied compounds are summarized in **Table VI. 1** along with the theoretical and the experimental data. As illustrated in **Table VI. 1**, the optimized structures parameters in this work are in complete agreement with the experimental data results [197], as well as other reported theoretical results [184, 196, 199, 200]. Moreover, the error ratio between our results and the experimental results are below 0.6000%. On one hand, it is apparent from **Table VI. 1** that the a_0 raises by substituting the anion from P to Bi due to the raise of atomic number and the ionic size. On the other hand, the B_0 reduces when the volume

is increased, indicating that material hardiness reduces. Furthermore, the unit cell and total energy versus the volume fitting of Ca_3MN (M = P, As, Sb, and Bi) are shown in **Figure VI. 1.**

$$\mathbf{E\,(V) = E_0 + \frac{9V_0B}{16}\left\{\left[\left(\frac{V_0}{V}\right)^{\frac{2}{3}} - 1\right]^3 B' + \left[\left(\frac{V_0}{V}\right)^{\frac{2}{3}} - 1\right]^2 \left[6 - 4\left(\frac{V_0}{V}\right)^{\frac{2}{3}}\right]\right\}} \qquad \textbf{(Eq. VI.1)}$$

Table VI.1: The calculated a_0 (Å), bulk modulus B_0 (GPa), and its pressure derivative B' at zero pressure and T = 0 K, through GGA-PBE compared with the theoretical and the experimental data of Ca_3MN

Compound	Parameter	This work	Theoritical	Experimental
CPN	a_0 (Å)	4.7261	4.7357 [199] 4.7300 [184] 4.7030 [196]	4.7300 [197]
	B_0 (GPa)	63.4215	63.2300 [184] 65.3500 [196]	----
	B'	4.1209	3.9500 [196]	----
CAN	a_0 (Å)	4.7695	4.7797 [199] 4.7118 [200] 4.7370 [196]	4.7700 [197]
	B_0 (GPa)	60.8908	61.0991 [200] 60.5900 [196]	----
	B'	4.1289	4.1700 [196]	----
CSN	a_0 (Å)	4.8708	4.8743 [199] 4.8755 [200] 4.8310 [196]	4.8541 [197]
	B_0 (GPa)	58.1429	58.5464 [200] 60.9000 [196]	----
	B'	4.2907	3.9700 [196]	----
CBN	a_0 (Å)	4.9161	4.9196 [199] 4.9196 [200] 4.8640 [196]	4.8884 [197]
	B_0 (GPa)	54.0552	53.4628 [200] 57.0700 [196]	----
	B'	4.1219	4.0200 [196]	----

CPN

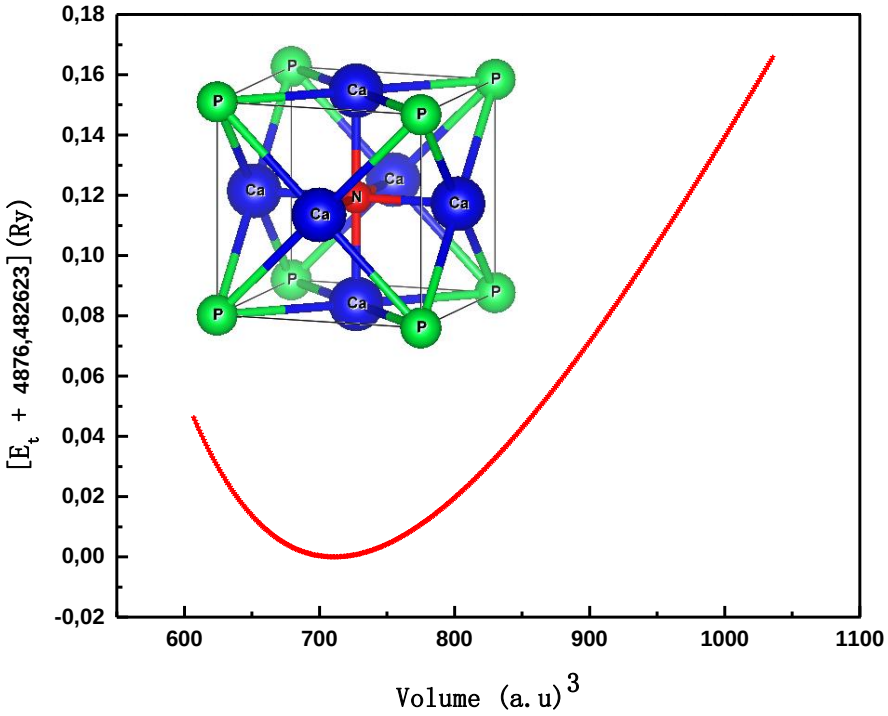
0,18
0,16
0,14
0,12
0,10
0,08
0,06
0,04
0,02
0,00
-0,02
600
700
800
900
1000
1100
[E_t + 4876,482623] (Ry)
Volume (a.u)^3
P
Ca
N

CAN

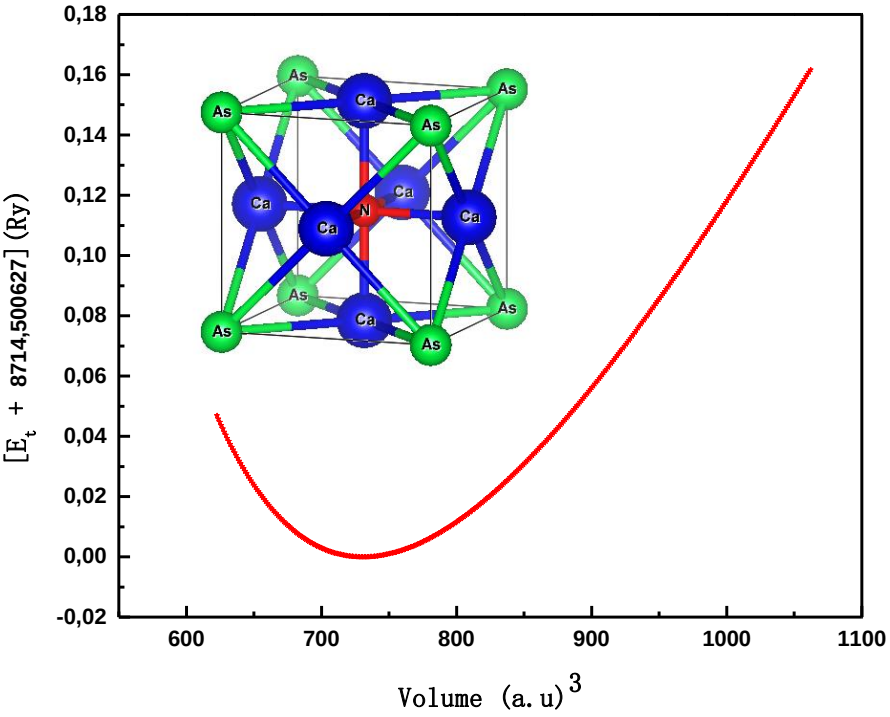
0,18
0,16
0,14
0,12
0,10
0,08
0,06
0,04
0,02
0,00
-0,02
600
700
800
900
1000
1100
[E_t + 8714,500627] (Ry)
Volume (a.u)^3
As
Ca
N

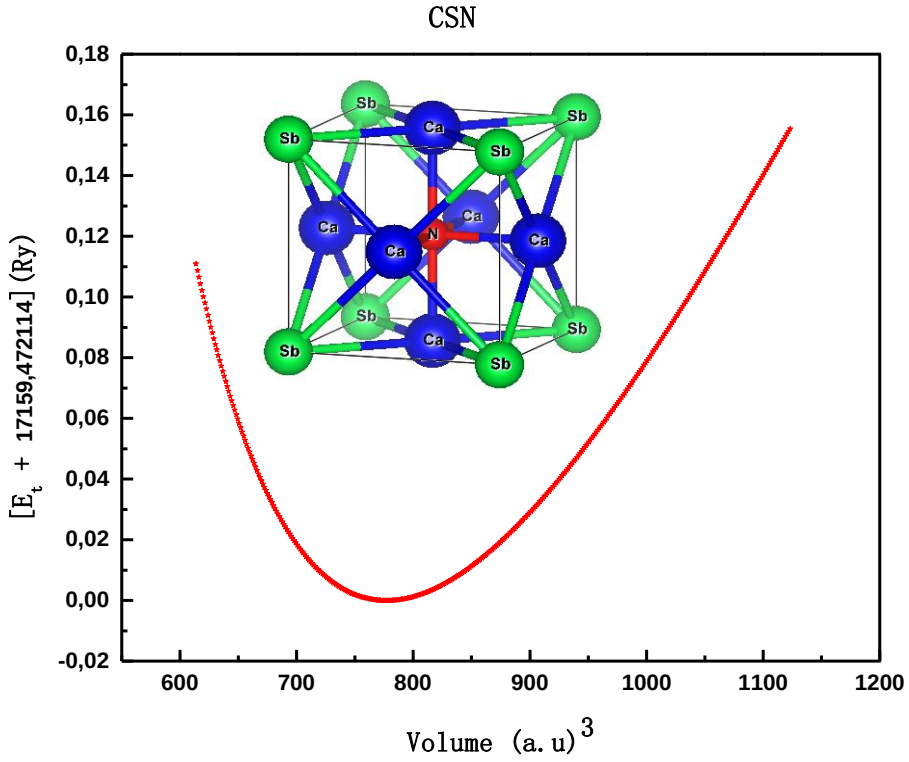

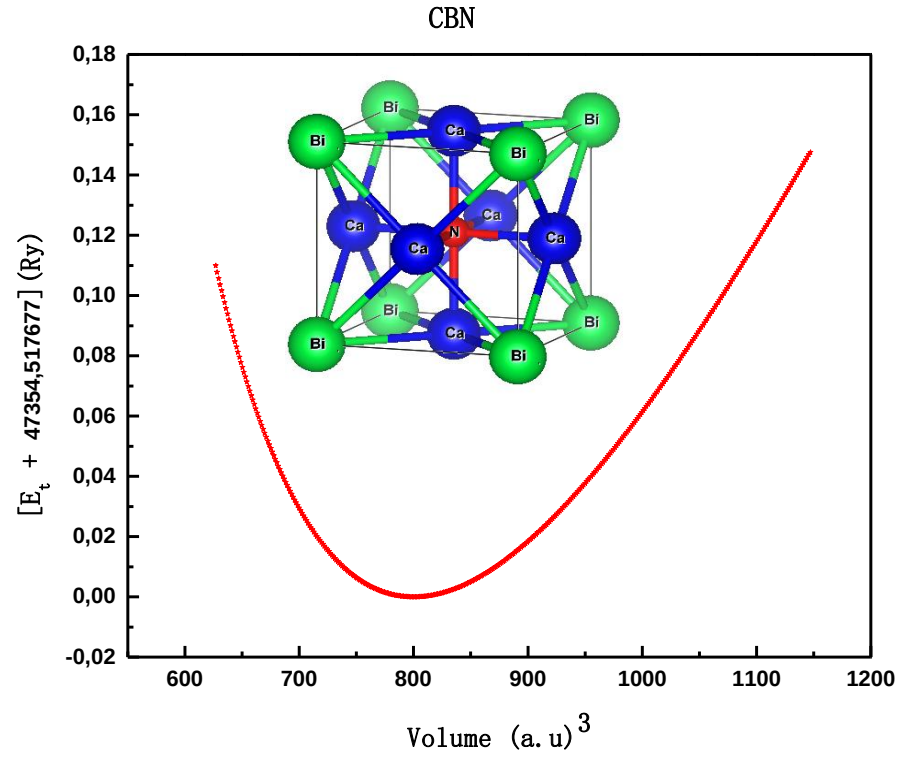

Figure VI.1: The unit cell, and the total energy versus the volume of CPN, CAN, CSN and CBN compounds

Once a_0, B_0 and B' had been done, we then calculated the enthalpy of formation (ΔH_f) in order to verify the thermodynamic stability of CPN, CAN, CSN and CBN compounds. It is worthwhile noting that the negative sign of ΔH_f indicates that the synthesis reaction formation is exothermic which provide the stability of the compound [201, 202]. Therefore, **Figure VI. 2** provides the thermodynamic stability of all studies compounds.

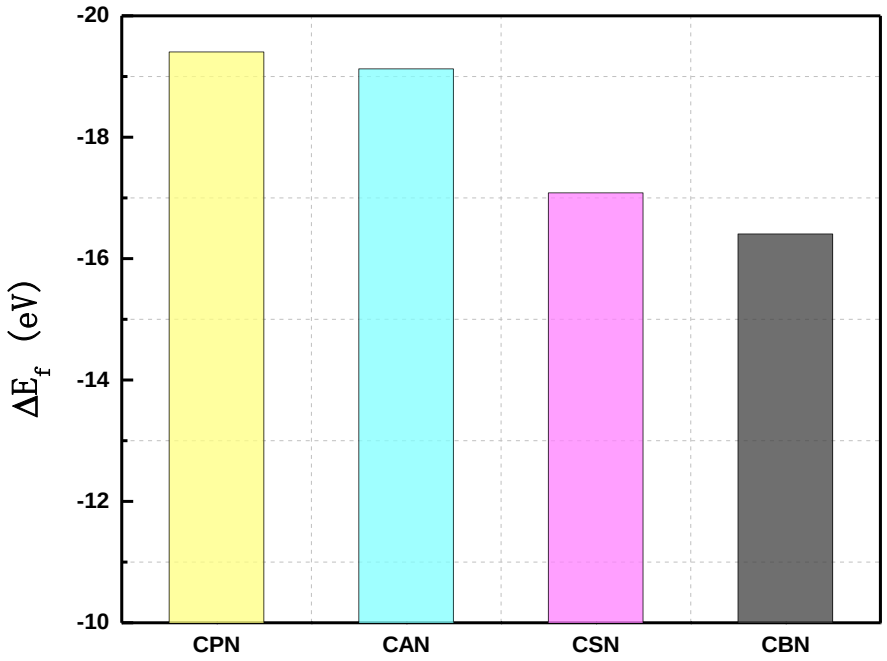

Figure VI.2: The enthalpy of formation of CPN, CAN, CSN and CBN

VI. 3. 2. Elastic properties and mechanical stability

The description when a compound undergoes stress, misshape and then recuperates its original shape, is given by the investigation of the elastic properties (mechanical properties) [203, 204]. Moreover, the anisotropy, mechanical stability, structural stability, bonding and chemical characteristics of a cubic compound can be extracted by the comprehension of elastic stiffness constants C_{11}, C_{12} and C_{44} (C_{ij}) [203 – 208]. It is worth mentioning, to investigate the mechanical stability of the cubic Ca_3MN compounds, the three independent elastic stiffness coefficients (C_{ij}) should satisfy the cubic Born stability criteria [209]:

$$(C_{11} - C_{12}) > 0 \quad , \quad C_{11} > 0 \quad , \quad C_{44} > 0 \quad , \quad (C_{11} + 2C_{12}) > 0 \qquad \textbf{(Eq. VI.2)}$$

From the **Table VI. 2**, we can note that all studied compounds satisfy the Born stability conditions which confirms the mechanical stability of the cubic Ca_3AN (A = P, As, Sb, and Bi) at ambient pressure. The elastic anisotropy factor (A) of a crystal which can be obtained using elastic stiffness coefficients through the following equation [209]:

$$\mathbf{A} = \frac{2C_{44}}{C_{11} - C_{12}} \quad \textbf{if} \quad \begin{cases} \mathbf{A = 1 \text{ the compound is isotropic}} \\ \mathbf{A \neq 1 \text{ the compound is anisotropic}} \end{cases} \qquad \textbf{(Eq.VI.3)}$$

The elastic anisotropy factors A of Ca_3MN are calculated and listed in the **Table VI. 2**. We observe from **Table VI. 2** that CPN, CAN, CSN and CBN are anisotropic crystals. Furthermore, the magnitude deviation from the anisotropy behavior reduces in the sequence CPN → CAN → CSN → CBN, which indicates that the CSN and CBN crystals are not characterized by a thorough anisotropy behavior. The **Table VI. 2** shows that the Bulk modulus (B) reduce in magnitude moving down a periodic table group V (from P to Bi). Further, **Tables VI. 1** and **2** show that the obtained Bulk modulus values from Brich-Munarghan equation of state fitting have roughly the selfsame values as those calculated using the elastic stiffness coefficients. This confirms the accuracy and reliability of the elastic stiffness coefficients calculated in this work. The shear modulus (G) reflects the strength of a compound under plastic deformation. Besides, once the Bulk and shear modulus are calculated we can use the Pugh's proportion to measure the ductility of the matters using the following expressions [205]:

$$\mathbf{B} = \frac{C_{11} + 2C_{12}}{3} \qquad \textbf{(Eq. VI. 4)}$$

$$\mathbf{G} = \frac{G_V + G_R}{2} \qquad \textbf{where} \qquad \begin{cases} G_R = \frac{5C_{44}\,(C_{11} - C_{12})}{[4C_{44} + 3\,(C_{11} - C_{12})} \\ G_V = \frac{[C_{11} - C_{12} + 3C_{44}]}{5} \end{cases} \qquad \textbf{(Eq. VI. 5)}$$

$$\textbf{Pugh's proportion:} \qquad \textbf{if} \quad \begin{cases} \frac{B}{G} > \mathbf{1.75 \text{ the compound is ductile}} \\ \frac{B}{G} < \mathbf{1.75 \text{ the compound is brittle}} \end{cases}$$

The obtained B/G ratio is less than 1.75 (see **Table VI. 2**). Based on Pugh's proportion the Ca_3AN (A = P, As, Sb, and Bi) compounds have brittle behaviors. Meanwhile, if the Poisson's ratio (u) of a crystal is less than 0.25, the crystal exhibiting with none-central bands while if its

value between 0.25 and 0.5, the crystal displaying with central forces [205, 210, 211]. The values of Poisson's ratio are calculated as a function of the Young's modulus (E) and the bulk modulus (B) using the following equation [196]:

$$\mathbf{u} = \frac{3B-E}{6B} \qquad \textbf{Where} \quad \mathbf{E} = \frac{9BG}{(3B+G)} \qquad \textbf{(Eq. VI. 6)}$$

Therefore, the tabulated data confirms that Ca_3AN (A = P, As, Sb, and Bi) compounds exhibit central forces. On the top of that, the high melting temperature (T_M) values of all studied compounds demonstrate that these compounds can effectively resist the high temperature effects. A simple relationship links the Debye temperature (Θ_D) with numerous physical properties including; melting point, the elastic stiffness coefficients as well as specific heat [193]. The Debye temperature is derived from the average wave velocity (ν_m) using the below relation [212]:

$$\Theta = \frac{h}{K_B}\left[\frac{3n}{4\pi V_a}\right]^{1/3} \nu_m \qquad \textbf{(Eq. VI. 7)}$$

Herein, h is the Plank's constant, K_B represents the Boltzmann's constant, n is the atoms number per formula unit, V_a reparents the atomic volume while ν_m is the average wave velocity which can be described using the following expressions [204]:

$$\nu_m = \left[\frac{1}{3}\left(\frac{2}{\nu_t^3} + \frac{1}{\nu_l^3}\right)\right]^{-1/3} \qquad \textbf{Where} \qquad \begin{cases} \nu_t = \left(\frac{G}{\rho}\right)^{1/2} \\ \nu_l = \left(\frac{3B+4G}{3\rho}\right)^{1/2} \end{cases} \qquad \textbf{(Eq. VI. 8)}$$

Where ρ represents the density of the compound, while ν_t and ν_l are the transverse and the longitudinal elastic wave velocities, respectively, for an isotropic compound. Since the Debye temperature of a compound show their interatomic force. From **Table VI. 2** the magnitude deviation of the strength covalent bonding reduces in the sequence CPN → CAN → CSN → CBN. As far as we know, there is no experimental data on the elastic properties for CPN, CAN, CSN and CBN compounds, and just few theoretical studies have been done in which our results are in complete agreement with [193, 196].

Table VI.2: The calculated elastic stiffness coefficients (Cij), anisotropy factor (A), Bulk (B), Shear (G) and Young (E) modulus, Pugh's ratio (B/G), Poisson's ratio (u), melting temperature (T_M), average wave velocity (v_m) and Debye temperature (Θ_D) at zero-pressure for CPN, CAN, CSN and CBN compounds.

	CPN	**CAN**	**CSN**	**CBN**
C_{11} (GPa)	151.1583 151±0.6 [196]	138.7163 146 ±0.9 [196]	120.7185 113.0400 [193] 134 ± 0.5000 [196]	121.3679 117.9600 [193] 124 ± 0.8400 [196]
C_{12} (GPa)	20.6523 23±0.2 [196]	21.7745 23±0.03 [196]	24.4946 26.5700 [193] 28 ± 0.6000 [196]	26.0784 22.0300 [193] 25.4 ± 0.24000 [196]
C_{44} (GPa)	48.2152 48±0.1 [196]	47.3501 50±0.05 [196]	50.2550 43.8200 [193] 53 ± 0.1000 [196]	51.4672 45.4300 [193] 50 ± 0.1000 [196]
A	0.7389 0.75 [196]	0.8100 0.81 [196]	1.0445 1.02 [196] 1.01 [193]	1.08022 1.01 [196] 0.94 [193]
B (GPa)	64.1540 66±0.2 [196]	60.7551 64 ±0.4 [196]	56.5690 63±0.6 [196]	57.8410 58±0.3 [196]
G (GPa)	54.4340	51.5239	49.3860 43.58 [193]	49.9010 46.42 [193]
E (GPa)	127.2980	120.5000	114.7610 103.5800 [193]	116.2670 108.2600 [193]
B/G	1.1785	1.1790	1.1454	1.1591
υ	0.1690	0.1690	0.1610	0.1640
T_M (K) ± 300	1446.3455	1372.8133	1266.4463	1270.2842
v_m (m/s)	5036.25	4414.85	4029.02	3547.74
Θ_D (K)	542.5090	471.2430	421.1150	367.3950

VI. 3. 3. Electronic properties and chemical bonding

To fully understand the electronic properties of Ca_3MN (M= P, As, Sb and Bi) compounds, the examination of the band structure and Density Of States were carried out. The forbidden band of all studied compounds are calculated using GGA, TB-mBJ and YS-PBE0 approximations and they are listed in **Table VI.3**. As shown in this figure, the GGA approximation underestimates the forbidden band values of all studied compounds compared to those obtained using TB-mBJ and YS-PBE0 approximations of all studied compounds. It is noteworthy that the underestimation of the forbidden band value obtained by GGA approximation is due to the overestimation of the bonding interactions [184]. Hence, the TB-mBJ as well as the Hybrid-Function implanted in YS-PBE0 exchanges correlations functionals were chosen in order to get control of these issues. Manifestly from **Table VI. 3**, the forbidden band value become smaller in the sequence CPN → CAN → CSN → CBN. These reduces of the forbidden bands values is due to the reduce of the electronegativity from CPN to CBN compounds (from P to Bi anions) (see **Figure VI. 3**). Despite this interest, no one to the best of our knowledge has reported the forbidden band values of the understudy compounds. Besides, from experimental electrical conductivity measurements, M. Y. Chern et al. [197] are reported that by varying the central anions (Ca_3MN where M= P, As, Sb and Bi), the properties change from semiconducting with small band gaps (CBN and CSN), to insulating (CAN and CPN). However, no experimentally measured forbidden band value is given. Moreover, it is clear that the tabulated theoretical data assures that our calculated forbidden band values of Ca_3MN are corroborate with previous results [184, 198, 199, 200, 213]. However, there is no significant appreciable differences were found between the TB-mBJ and YS-PBE0 forbidden band values. Thus, the electronic structures, and all next simulated properties are preformed using the most accurate YS-PBE0 exchange correlation functional. Furthermore, the probability of distribution of an electron in an energy range is described by investigating the DOS, and the results of DOS are presented in **Figure VI. 4**. We observe from **Figure VI. 4** that the originate of the upper VB of Ca_3MN is from the p-p anions interactions, while the originate of the bottom CB is from the mix of d-p/cation-anion interactions. As highlighted in **Figure VI. 4**, the dispersion curves of the electronic band along the R – Γ – X – M – Γ integration path of the Brillouin zone are plotted for Ca_3MN compounds. It is apparent from **Figure VI. 4** that the HOMO and the LUMO have common position (Γ point), indicating a direct semiconducting behavior of Ca_3MN compounds, these findings are consistent well with other theoretical findings [184, 198, 199, 200, 213].

Table VI.3: The calculated forbidden band (Eg) of CPN, CAN, CSN and CBN from GGA-PBE, TB-mBJ and YS-PBE0 compared with the theoretical results and the experimental data.

	Eg (eV)				
	GGA	**TB-mBJ**	**YS-PBE0**	**Theoritical**	**Experimental**
CPN	0.808	1.603	1.635	0.810 [184] 1.630 [184] 0.736 [199] 1.497 [199] 1.203 [199] 1.743 [199]	Insulator [197]
CAN	0.750	1.448	1.514	1.500 [198] 0.651 [199] 1.448 [199] 1.080 [199] 1.355 [199] 1.390 [200] 1.390 [213]	Insulator [197]
CSN	0.448	1.006	1.134	0.344 [199] 1.006 [199] 0.712 [199] 0.808 [199] 0.980 [200] 0.940 [213]	Semicon. [197]
CBN	0.403	1.018	1.103	0.245 [199] 0.957 [199] 0.663 [199] 0.471 [199] 1.010 [200] 0.580 [213]	Semicon. [197]

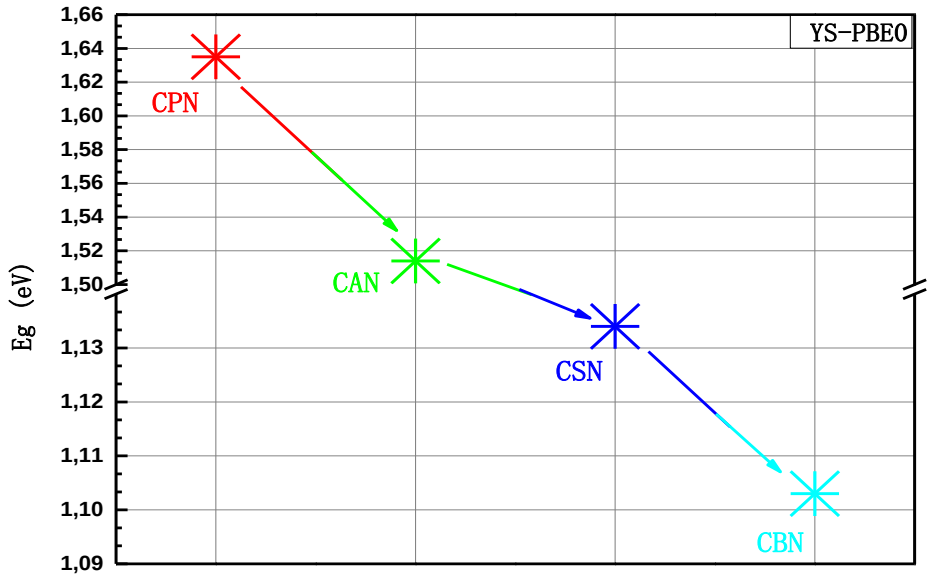

Figure VI.3: The calculated forbidden band of CPN, CAN, CSN and CBN using YS-PBE0

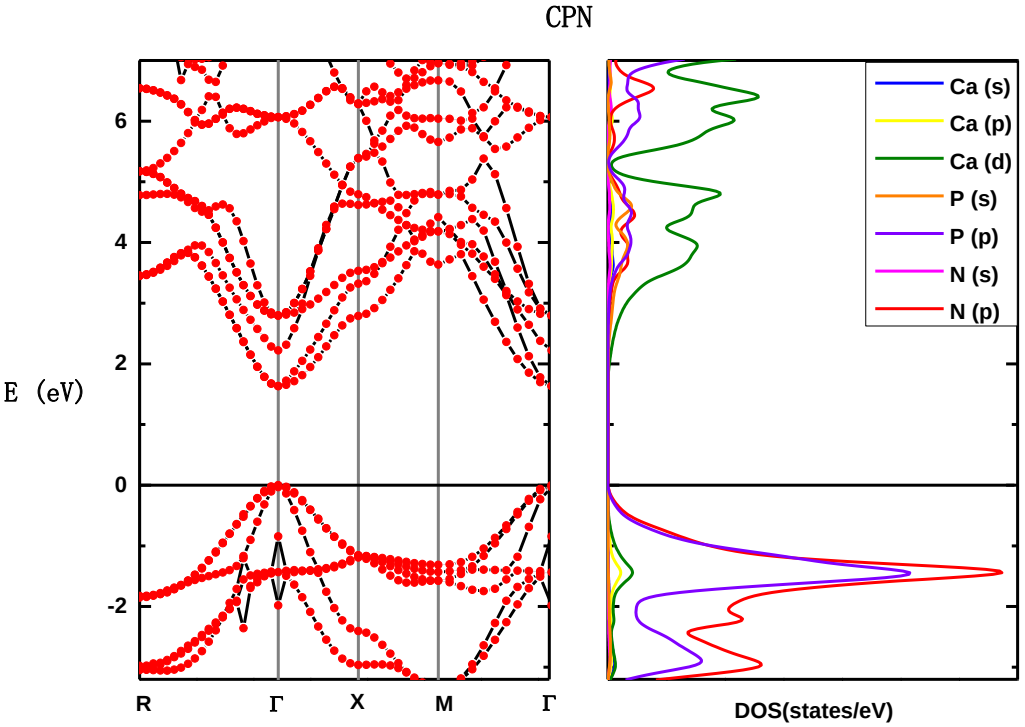

CAN

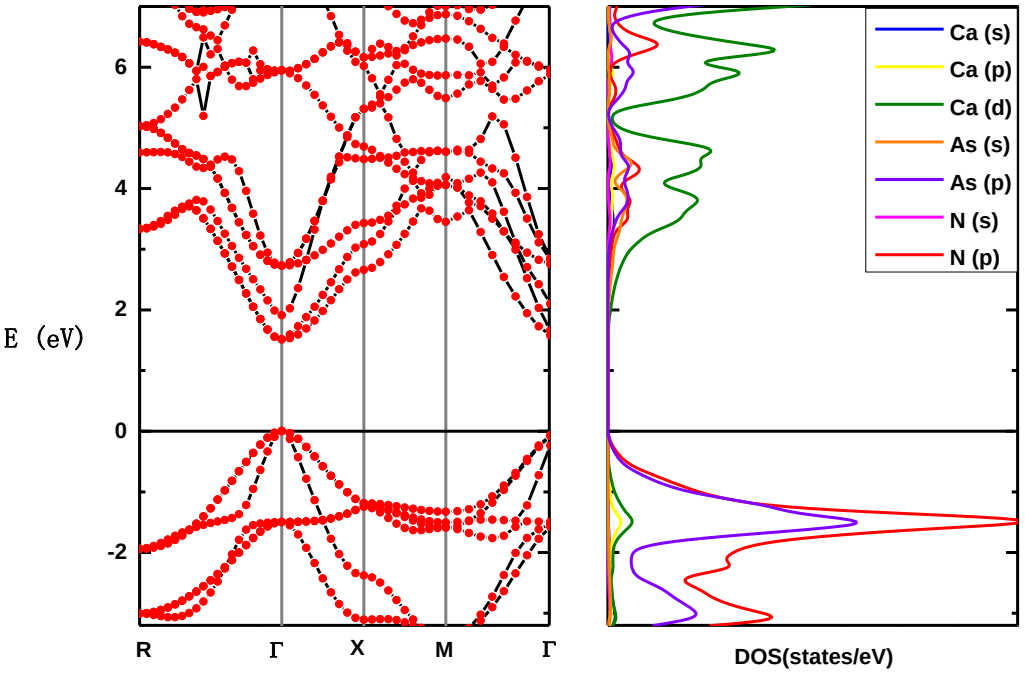
E (eV)
6
4
2
0
-2
R
Γ
X
M
Γ
Ca (s)
Ca (p)
Ca (d)
As (s)
As (p)
N (s)
N (p)
DOS(states/eV)

CSN

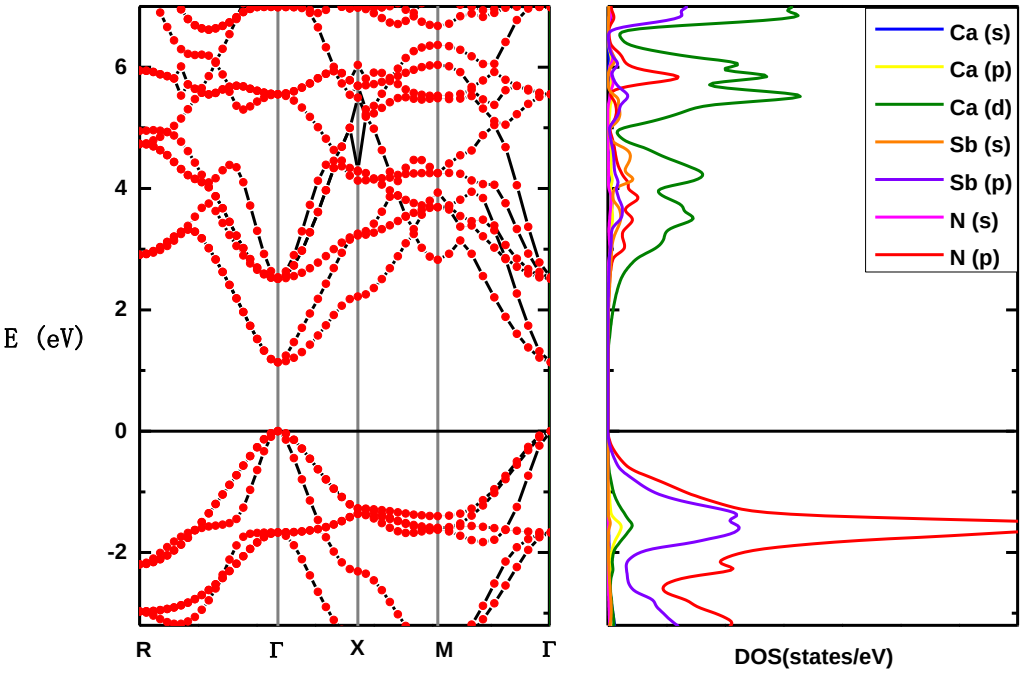
E (eV)
6
4
2
0
-2
R
Γ
X
M
Γ
Ca (s)
Ca (p)
Ca (d)
Sb (s)
Sb (p)
N (s)
N (p)
DOS(states/eV)

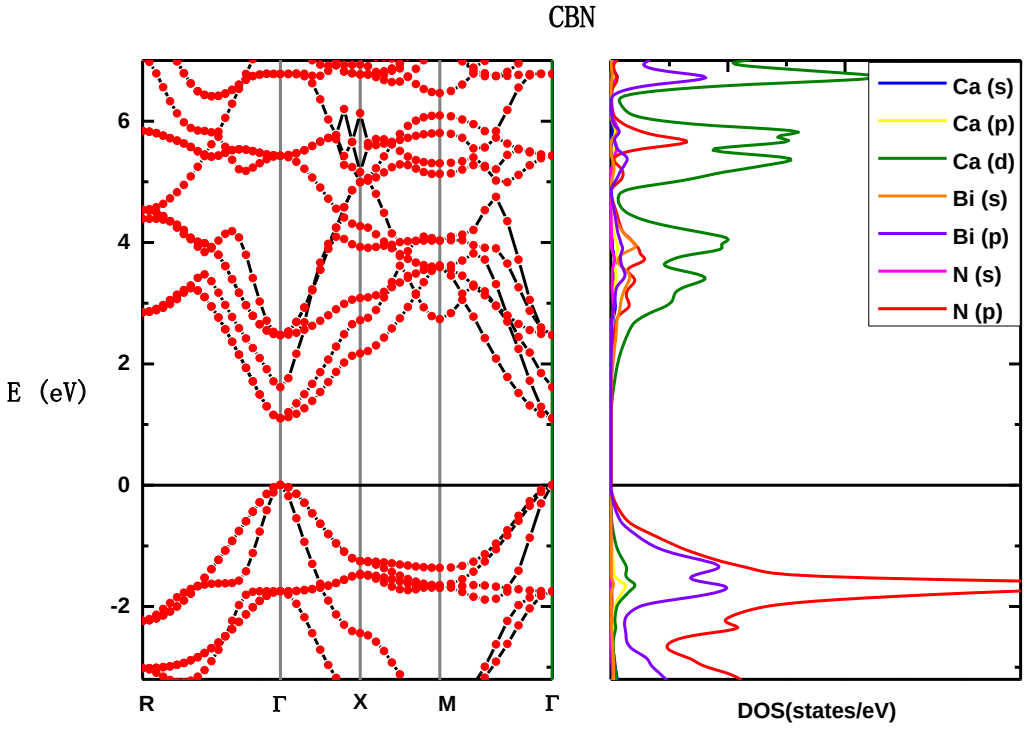

Figure VI.4: The band structure and PDOS of CPN, CAN, CSN and CBN using YS-PBE0

To determine the charge distribution of the electronic density of Ca_3MN compounds and the bonding nature between anions and cations, we used the electronic charge density distribution map as presented in **Figure VI. 5**. Therefore, **Figure VI. 5** illustrates that there is a mixture of ionic-covalent interatomic bonds. The electron cloud which surrounding M atom is rounded and distortion free, proving that the banding between M and surrounding atoms are principally ionic and partially covalent. Contrary, the overlapping spherical electron clouds around Ca and N atoms showing that the band between these two atoms is mainly covalent and partially ionic. It should be mentioned that the difference in the electronegativity between atoms describes the bonding character. Additionally, as the electronegativity value between two atoms increases, the attraction of an electron increases. From the calculated ionic character percentage (CI%) (**Table VI. 4**), we observe that the IC% values of Ca-M and N-M are larger than 50%, implies that the interatomic bonds are ionic. Otherwise, the IC% values of Ca-N is smaller than 50% which indicates the presence of polar covalent character. Consequently, the electrons are transferred between M and surrounded atoms, while the electrons are shared unequally between Ca and N atoms.

Table VI.4: The tabulated IC% of CPN, CAN, CSN and CBN using Pauling electronegativity values

	IC (%)			
	M = P	**M = As**	**M = Sb**	**M = Bi**
Ca-M	70.2000	70.6000	79.4300	77.1000
N-M	83.4700	83.1100	74.700	77.1000
Ca-N		35.3300		

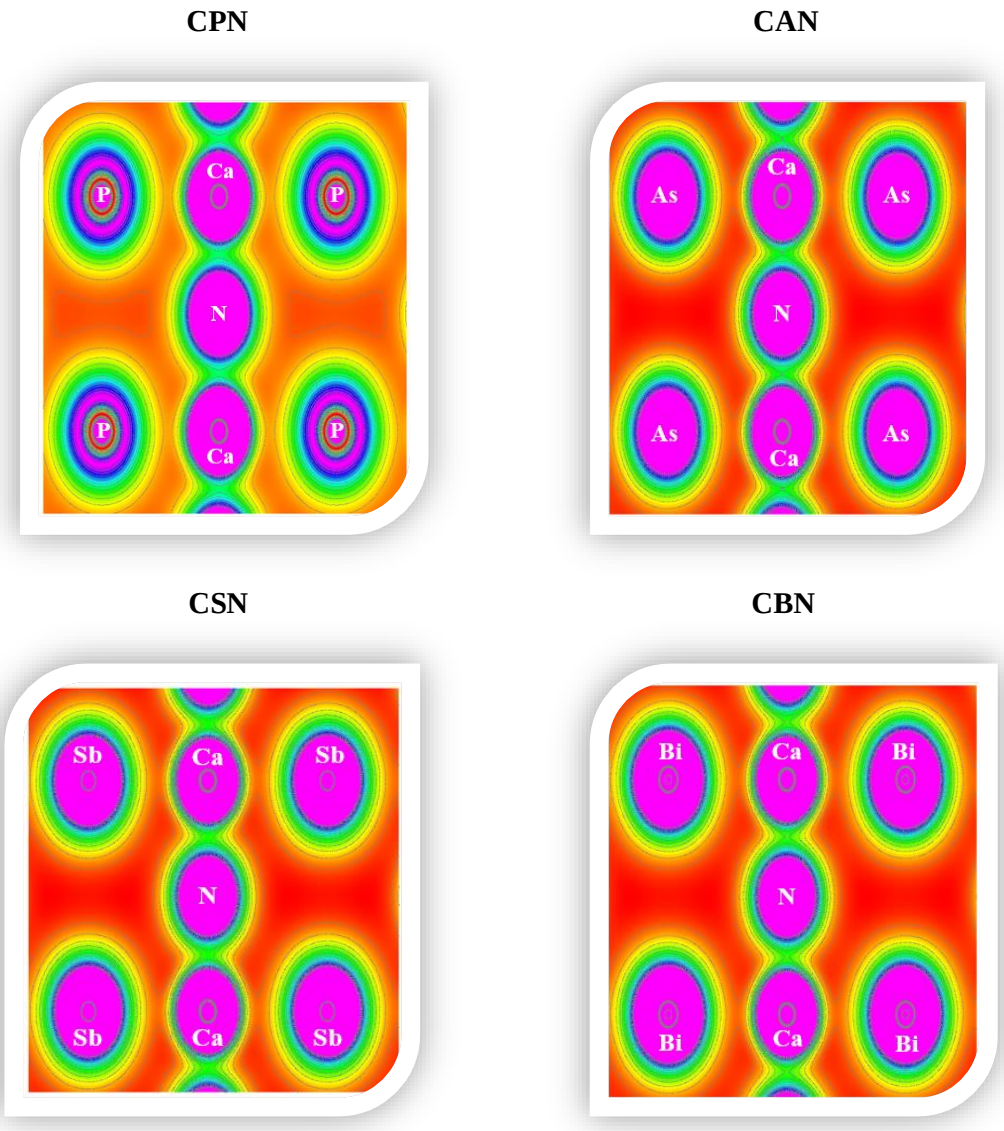

Figure VI.5: The Electronic densities of CPN, CAN, CSN and CBN using YS-PBE0

VI. 3. 4. The charge carrier effective masses and their recombination rate

The charge carrier effective masses (hole (m_h^*) and electron (m_e^*)), is one of the most important indicators of semiconductor materials due to its description of the carrier's transport properties which is immediately associated with the electronic band structure [184]. Therefore, the effective masses of holes and electrons are proportional conversely to the upper valence band and bottom conduction band curvatures. The adopted procedure to investigate the charge carrier effective masses is by using the second derivative of the electronic energy of Bloch wave dispersion (E (k)) through the parabola fitting according to the following equation [214]:

$$\frac{1}{m^*} = \frac{1}{\hbar^2}\frac{\delta^2 E\ (k)}{\delta k^2} \qquad \textbf{(Eq.VI. 9)}$$

Herein, m^* represents the effective mass of hole or the electron, $\hbar$ describes the reduced Plank's constant while k defines the wave vector. The charge carrier effective masses (m_h^* and m_e^*) along different crystallographic directions (Γ→R and Γ→X) were carried out, and the results obtained in this work with other theoretical results are tabulated in **Table VI. 5**. More importantly, **Figure VI. 4** depicts that the upper VB and bottom CB along Γ→R direction are significantly less flat than those along Γ→X direction. Consequently, the charge carriers' effective masses along Γ→R direction are lighter than those along Γ→X direction. Remarkably, the calculated effective masses are less than 0.5 (m_0) along the both studied crystallographic directions except m_e* of CAN, CSN and CBN along Γ→X direction. Kishore et al. [215] , and Bahers et al. [216] reported that at least in one crystallographic direction, the effective masses ought to be less than 0.5 (m_0) (m_0 being the free electron mass), in order to achieve an excellent charge carrier mobility. Accordingly, Ca_3MN materials have excellent charge carries mobility hence high conductivity. Note that there is a relation between the charge carrier effective masses and their recombination rate. Therefore, once the charge carrier effective masses values have been determined, we are able to calculated the electron-hole pairs recombination ratio (D) as follows [184]:

$$D = \frac{m_e^*}{m_h^*} \qquad \textbf{(Eq.VI.10)}$$

From equation above, we can note that, a smaller value of D implies a narrow difference in the electron-hole mobility which boosts the electron-hole pairs recombination. From the tabulated results (**Table VI. 5**), the D values of Ca_3MN compounds along Γ→R and Γ→X

crystallographic directions are in the range of [0.6200 - 1.7570]. These small values of D reflect high mobility of charge carries for Ca_3MN compounds.

Table VI.5: The calculated carrier effective masses and their recombination rate of CPN, CAN, CSN and CBN compounds compared with the theoretical results.

	m_h^* (m_0)		m_e^* (m_0)		D	
Compound	**Γ - R**	**Γ - X**	**Γ - R**	**Γ - X**	**Γ - R**	**Γ - X**
CPN	0.4238	0.4260	0.2630	0.4130	0.6200	0.9691
	0.3990 [184]	0.4600 [184]	0.2910 [184]	0.4190 [184]	----	----
	0.2100 [185]		0.2900 [185]			
	0.3800 [217]		0.4200 [217]			
CAN	0,3860	0,4515	0,2550	0,7940	0.6600	1.7570
	0.3700 [213]	0.4300 [213]	0.2800 [213]	0.8000 [213]	----	----
CSN	0.2410	0.3240	0.1900	0.5276	0.7884	1.6320
	0.2400 [213]	0.3600 [213]	0.2200 [213]	0.8000 [213]	----	----
CBN	0.3524	0.3930	0.2415	0.5256	0.6851	1.3368
	0.1200 [213]	0.3000 [213]	0.1900 [213]	0.8000 [213]	----	----

VI. 3. 5. Transport and optical properties

The thermoelectric (TE) technology is the key to convert the heat energy to the electrical one. Therefore, the TE properties of Ca_3MN inverse perovskites compounds were examined using the semiclassical Boltzmann transport theory implanted in BoltzTrap package [77]. Based on the melting temperature obtained from the calculated elastic properties, the TE properties are examined from 50 K to 1000 K. The thermopower (or Seebeck coefficient (S)) defines the voltage ratio generated by the temperature difference as well as the efficiency of thermocouples. The calculated thermopower values of Ca_3MN are given in **Figure VI. 6**. It is apparent from figure 6 that the thermopower values of understudy compounds rise with rising temperature up to 1000 K. Besides, the thermopower values of CPN, CAN and CSN indicate that these materials undergo from n-type to p-type semiconductors behaviors due to the transition from the negative to the positive values. Denoting that the electrons are the essentially charge carrier from 0 K to 400 K for CPN, to 261 K for CAN, and to 200 K for CSN, while up to these

temperatures the holes are the predominantly charge carrier. Otherwise, the CBN compound is a p-type semiconductor due to positives thermoelectric values. Further, charge carriers' flow is calculated by the electrical conductivity (κ_e). **Figure VI. 6** shows an almost exponential downward trend of electrical conductivity of CPN and CBN moving from the low to the high temperature. On the other hand, the electrical conductivity of CAN compound is increased from 50 K to 250 K and then starts to decrease with increasing temperature, while the electrical conductivity of CSN material reduces from 500 K to 200 K, then it boosts up to 400 K, thereafter it lessens. Otherwise, the calculated lattice thermal conductivity (κ_l) shows an almost exponential downward trend of the understudy compounds which can be explained by the vibrations of atoms in the crystals lattice are increased with increasing temperature which in turn leads to increased collisions between the vibrating atoms and moving electrons. Thus, the electrons are scattered more frequently by lattice vibrations, or phonons, which causes the decrease of lattice thermal conductivity and the increase of resistivity. Our findings appear to be well supported by the experimental data [197], showing that the resistivity of CBN shows upward trend with the increasing temperature. It is worthwhile mentioned that κ represents the sum of the electrical and the lattice thermal conductivities, and due to the large deference between κ_e and κ_l, in present calculations only κ_e is considered and κ_ℓ is ignored. Besides, the heat conductivity produced by the electron's movements are calculated and plotted in **Figure VI. 6**. Accordingly, the heat conductivity of understudy compounds raised almost linearly in throughout investigated temperatures. Additionally, the performance of a TE compound is given by the figure of merit (ZT), according to figure 6 the ZT performance decreased with increasing temperature up to 400 K for CPN, 250 K for CAN, 200 K for CSN and CBN, respectively, then it starts to increase. From in **Figure VI. 6.,** CSN compound has better characteristics in TE applications at 50 K where the ZT value is 80%

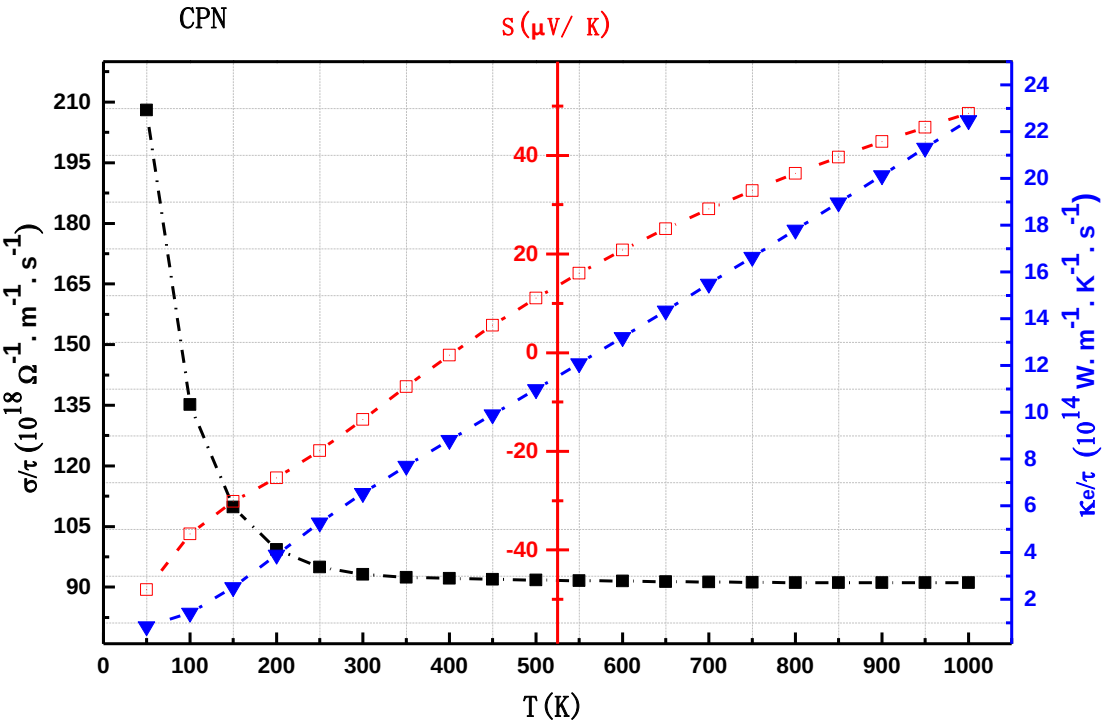
CPN
S(μV/ K)
σ/τ (10^18 Ω^-1 . m^-1 . s^-1)
κe/τ (10^14 W. m^-1 . K^-1 . s^-1)
T (K)

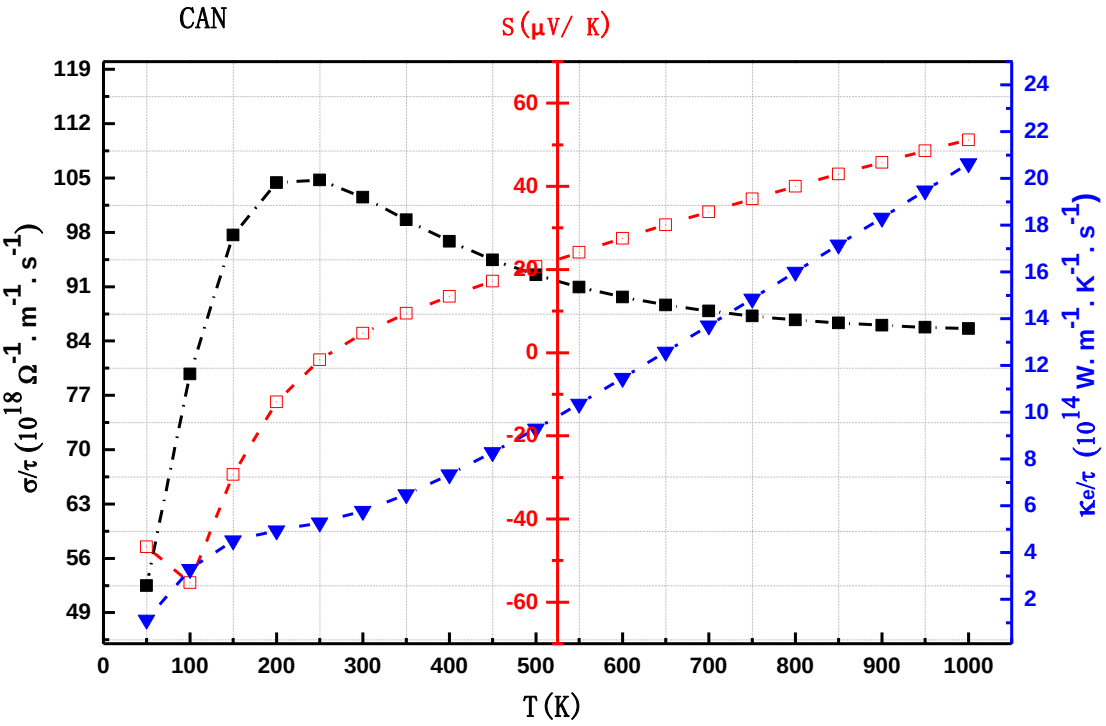
CAN
S(μV/ K)
σ/τ (10^18 Ω^-1 . m^-1 . s^-1)
κe/τ (10^14 W. m^-1 . K^-1 . s^-1)
T (K)

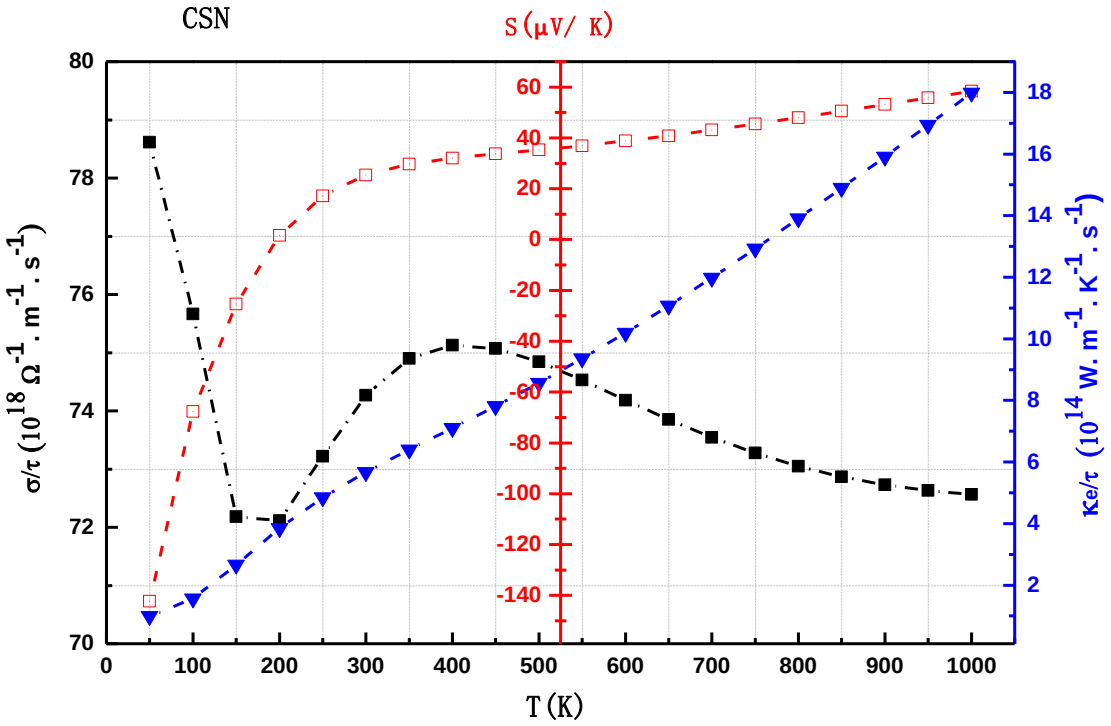
CSN
S(μV/ K)
σ/τ (10^18 Ω^-1 . m^-1 . s^-1)
κe/τ (10^14 W. m^-1 . K^-1 . s^-1)
T(K)

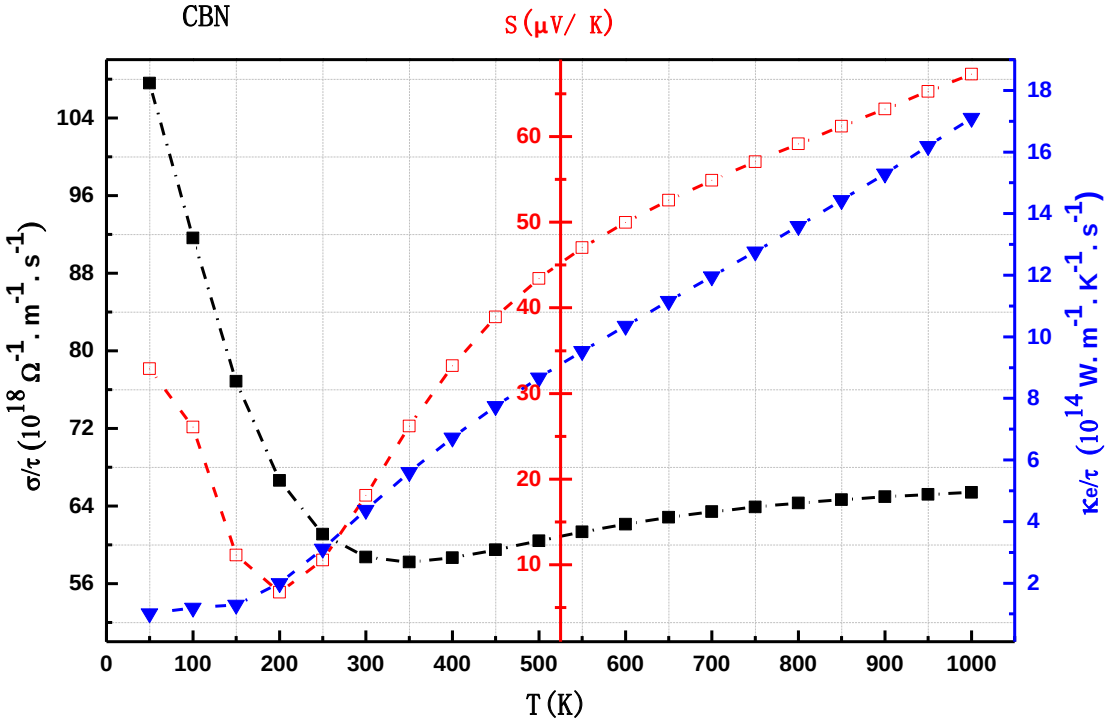
CBN
S(μV/ K)
σ/τ (10^18 Ω^-1 . m^-1 . s^-1)
κe/τ (10^14 W. m^-1 . K^-1 . s^-1)
T(K)

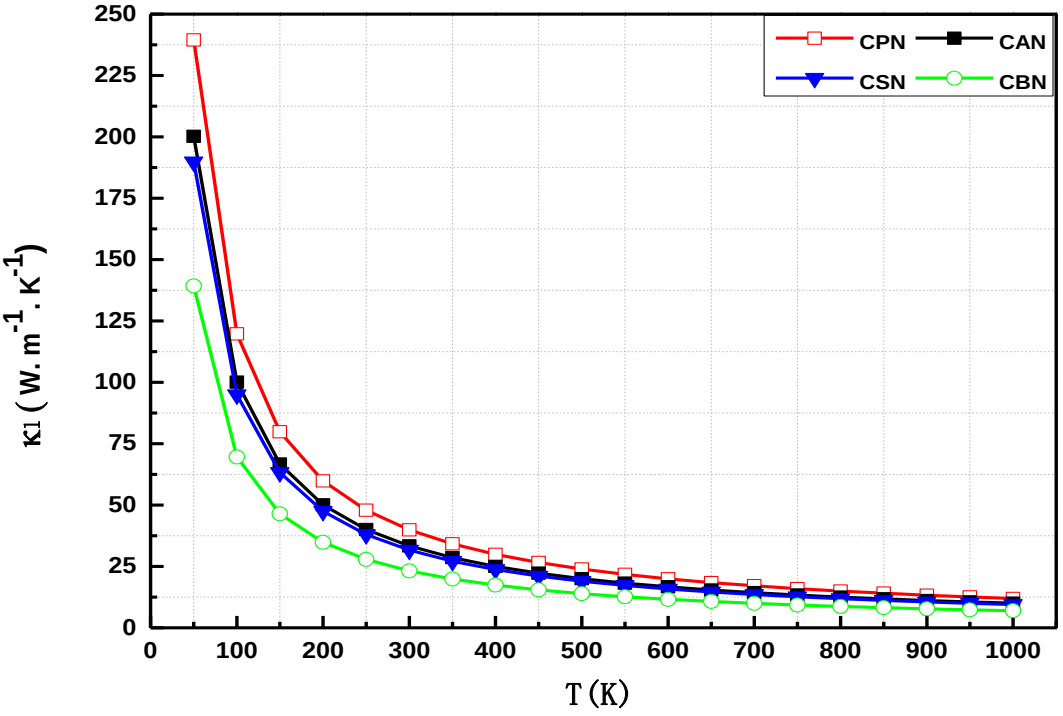

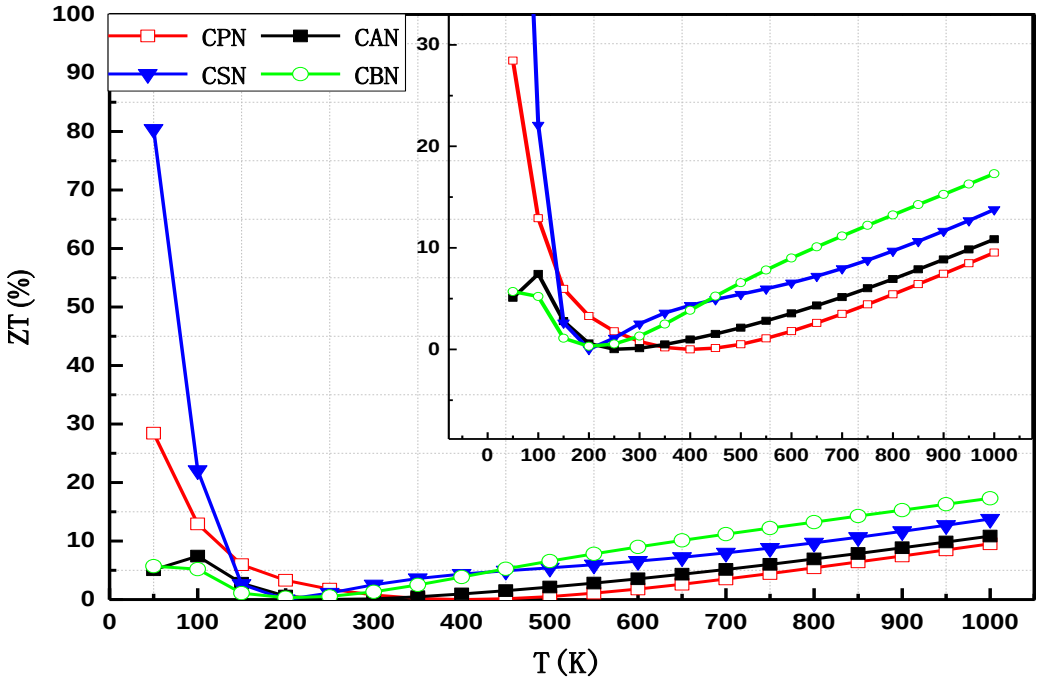

Figure VI.6: The thermopower, electrical and heat conductivities, as well as figure of merit of CPN, CAN, CSN and CBN compounds

The optical spectra which derivates based on the inter-band transition from the VB to the CB of a material [112, 115, 170, 183]. The optical absorption coefficient, transmittance and reflectivity of Ca_3MN inverse perovskites compounds are plotted as percentages (%) in **Figure VI. 7**. The analyzed optical inter-band transition displays that in the visible spectrum, the understudy compounds present an immense absorption coefficient percentage around 80%. These immense absorption coefficient percentage of Ca_3MN compounds is essentially from the inter-band transition of p states of N and M atoms in the VB to d states of Ca atoms in the CB, as well as from the extra beneficials of the direct forbidden band of understudy compounds which boosts the quantity of photons absorbed. Note that the forbidden band value in [1 eV – 1.6 eV] zone boosts solar cell efficiency, hence is extremely recommended for solar cells. Therefore, the outstudying Ca_3MN properties make these compounds as new single-junction solar cells.

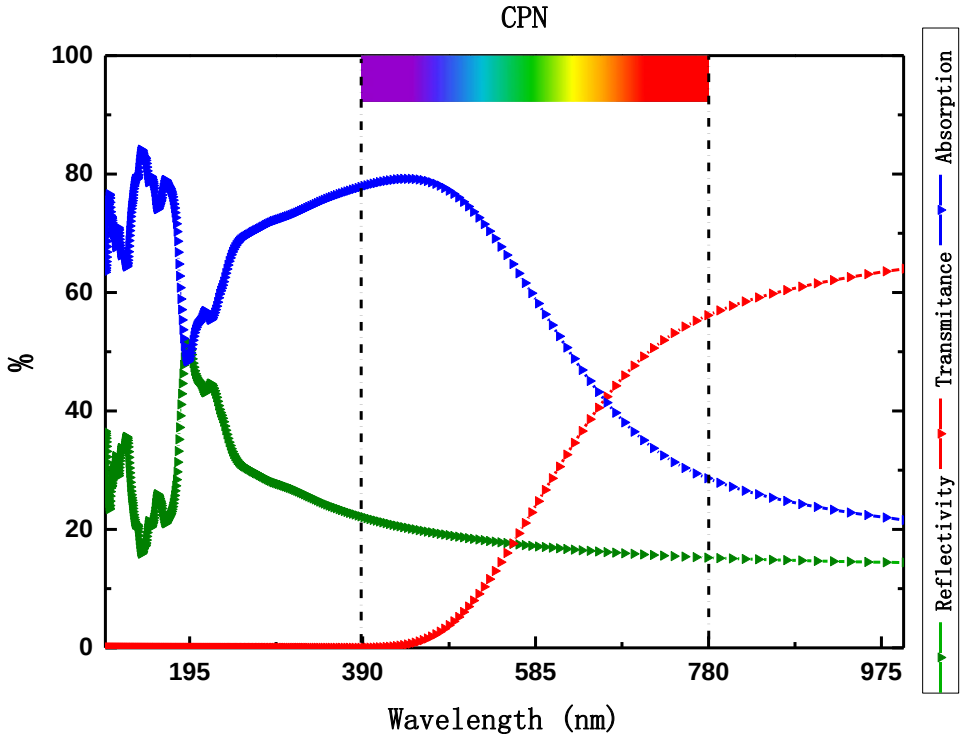

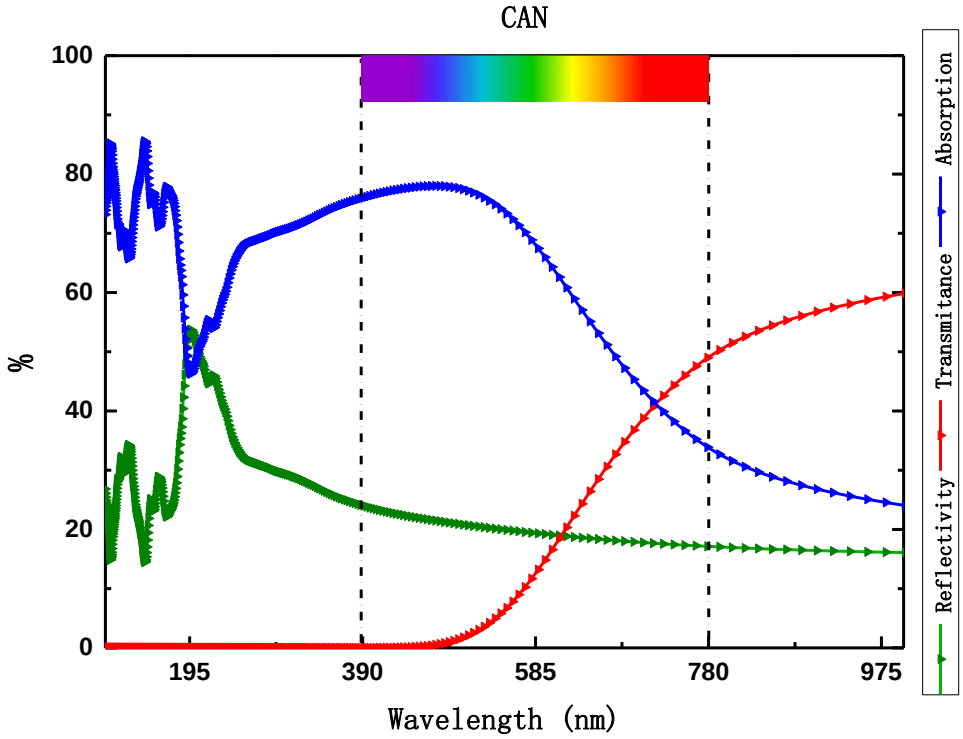
CAN
100
80
60
40
20
0
%
195
390
585
780
975
Wavelength (nm)
Absorption
Transmitance
Reflectivity

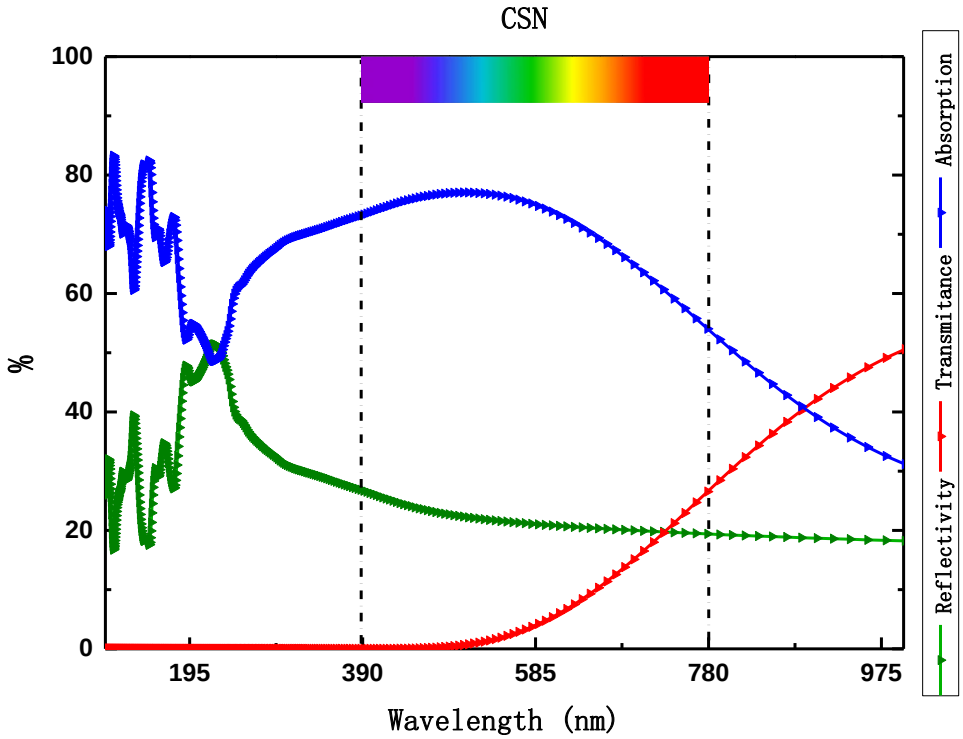
CSN
100
80
60
40
20
0
%
195
390
585
780
975
Wavelength (nm)
Absorption
Transmitance
Reflectivity

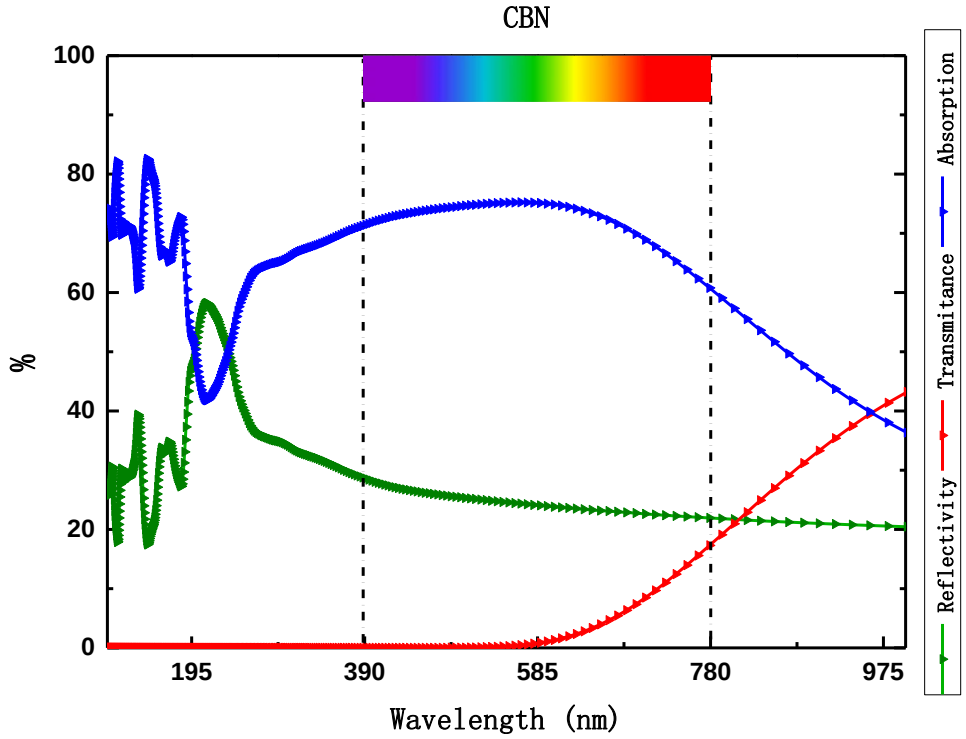

Figure VI.7: The absorption coefficient, reflectivity and transmittance of CPN, CAN, CSN and CBN compounds

VI. 4. Conclusion

To sum up, the structural, thermodynamic and elastic stabilities, elastic stiffness constants, elastic anisotropy factor, Bulk, Young's and shear modulus, Poisson's ratio, Pugh's proportion, average wave velocity, melting and Debye temperatures, electronic structure, chemical bonding nature, the charge carrier effective masses, recombination ratio, thermopower, electrical and heat conductivities, absorption coefficient, reflectivity and transmittance of non-silicon based inverse perovskites Ca_3MN (M= P, As, Sb and Bi) were explored using first principals calculations. It was found that the structural optimization of Ca_3MN compounds in this work are in complete agreement with the experimental data. Moreover, all studied compounds are found to be thermodynamically and elastically stable at ambient pressure and they classified as anisotropic and brittle compounds. The dispersion curves of the electronic band highlights that the HOMO and LUMO are situated at Γ point with the suitable solar cells forbidden band values. Furthermore, the charge distribution of the electronic density demonstrates that the electrons are transferred between M and surrounded atoms, while the electrons are shared unequally between Ca and N atoms. The charge carrier effective masses calculations illustrate

low charge carrier effective lasses and low recombination ratio which exhibit excellent charge carries mobility of the understudy compounds. Besides, the transport properties show that the thermopower and heat conductivity of all studied compounds increase with increasing temperature up to 1000 K. While CSN has better characteristics in TE applications at 50 K where the ZT value is 80%. Additionally, the optical properties demonstrate that the understudy compounds are excellent absorbers for photovoltaic applications.

General conclusion

In this thesis, we have studied various perovskites materials types; simple, double and inverse in order to explore the physical properties of CZO, BZO, SZO, CHO, SHO, CTI, CTB, CTC, RTI, RTB, RTC, CPN, CAN, CSN, and CBN compounds synthesized by DFT calculations, and adjust these to make the compounds promising in solar and photocatalytic applications.

The first part of this these was devoted to perform the effects of Sulfur, Selenium or Tellurium-doped $AZrO_3$ (A = Ca, Ba and Sr) on electronic and optical properties have been investigated using ab initio calculations. The results confirm that the forbidden band decreases with the increase of chalcogens' concentration, especially for Te and Se doped $AZrO_3$. Moreover, the absorption coefficient in the visible spectrum were stimulated essentially for Te doped $AZrO_3$. Hence, Te would be the better substitute of O in Lead-Free Zirconate perovskites for a new class of promising eco-friendly solar cells.

Following the former study, we focused on the effects of Sulfur, Selenium, or Tellurium doped CZO, CHO and SHO on the electronic, optical and photocatalytic properties have been investigated using Density Functional Theory, but in this time the intrinsic F-center defect (Ov) in oxide materials were taken into account. The findings showed that the substitution of oxygen atoms by chalcogens impurities decreased the forbidden band of the understudy compounds. effectively. Furthermore, there is a huge improvement of the absorption coefficient in the visible spectrum when chalcogens' impurities meet an Ov defect in the understudy compounds, especially case case of S/Se/Te@OI+Ov, S/Se/Te@OII+Ov and S/Se@OIII+Ov for CZO compound and S/Se/Te@OII+Ov and Te@OIII+Ov structures for CHO, and S/Se/Te@OII+Ov and Se/Te@OIII+Ov for SHO compound due to the shifting of the Fermi level to the lowest unoccupied molecular orbital which caused the n-type semiconductor behavior giving rise to the enhancement of carrier concentrations. Otherwise, the S/Se@OI/OII/OIII+Ov structures for CZO and S/Se/Te@OII+Ov structures for CHO and SHO can effectively absorb the visible light and they respects the limits necessary to split water and the intermediate band guarantees the efficiency of the charge transfer which is a requirement for photocatalysis. therefore, these structures have the ability to split water which enhanced the hydrogen production. In addition, the enthalpy of formation confirms that all studied structures are thermodynamically stables. We believe that our research will serve as a base for future studies on CZO, CHO and SHO to be used

as semiconductors for photovoltaic and photocatalytic hydrogen production from water sp litting applications.

After that, the crystal structures, thermodynamic stability, electronic densities of states, band structures, and optical properties of the non-toxic Pb-free vacancy ordered double perovskites halides X_2TeY_6 (X = Cs, Rb, and Y = I, Br, Cl) were investigated using first-principles calculations. It was found that at Γ point, the CB splits into two bands upon inclusion of SOC interaction for X_2TeY_6 compound. Besides, the highest occupied molecular orbital is unchanged for all studied compounds except that of X_2TeI_6, which is shifted from W to X point. Our findings appear to be well supported by the experimental data [Annalise E. Maughan et al., J. Am. Chem. Soc. 138 (2016) 8453–8464]. This shows a contradiction with the theoretical work found by [Malak Azmat Ali et al., Int. J. Energy Res. 45 (2020) 8448-8455]. Hence, the inclusion of SOC is crucial for the correct characterization of the electronic properties of the X_2TeY_6 compound. Otherwise, the absorption coefficients shift to the visible region by the substitution of Cl by Br and I ions. Thus, the excellent absorption coefficients percentages of Cs_2TeI_6 (62% - 75%) and Rb_2TeI_6 (57% - 76%) along the visible region, their suitable forbidden bands (1.422 eV for Cs_2TeI_6, and 1.469 eV for Rb_2TeI_6) and their high stabilities make both Cs_2TeI_6 and Rb_2TeI_6 as new potential candidates' compounds for single-junction solar cells.

Finally, a single-junction solar cell with direct and ideal photovoltaic forbidden band gap value which maximizes the phonon absorbed is needed for diversity of solar energy conversion, as well as other optoelectronics applications. Here, the ternary calcium nitrides inverse perovskites Ca_3PN, Ca_3AsN, Ca_3SbN and Ca_3BiN were investigated in the frame of Density Functional Theory. The principal novelty of this research essentially projects a detailed information on the structural, elastic, electronic, transport and optical properties for Ca_3PN, Ca_3AsN, Ca_3SbN and Ca_3BiN compounds. The understudy compounds are founded to be thermodynamically and elastically stable at ambient pressure. The electronic properties demonstrate that the understudy compounds have direct semiconductor behaviors with the ideal solar cells forbidden band gaps values which overlap very well with the visible zone of solar spectrum leading to these materials high absorption coefficients percentage around 80%, low reflectance and transmittance along this zone. The interatomic bonds between M and surrounded atoms are ionic while Ca-N interatomic bond is polar covalent. Otherwise, the understudy compounds exhibit low recombination rates as well as low charge carriers effective masses which boost the carrier mobility. In addition, with rising temperature up to 1000 K, the Ca_3PN, Ca_3AsN and Ca_3SbN

compounds undergo from n to p-type semiconductor behaviors while Ca_3BiN shows a p-type semiconductor behavior. Accordingly, these outstudying properties make the understudy compounds as new single-junction solar cells non-silicon based.

References

[1] International Energy Agency, «World Energy Outlook 2011,» *OECD Publishing*, 2011, Scientific american in 2010, [En ligne]. Available: https://www.scientificamerican.com/article/global-emissions-predicted-to-grow/.

[2] M. D. Webster, M. Babiker, M. Maye, J.M. Reilly, J, Harnisch, R. Hyman and C. Wang, « Uncertainty in emissions projections for climate models,» *Atmos. Environ*, vol. 36, p. 3659-3670, 2002.

[3] World Bank, «Guide to Climate Change Adaptation in Cities,» *Science*, 2011.

[4] J. Chen, D. He and N-G. Park, «Methologies for >30% efficient perovskites solar cells via enhancement of voltage and fill factor,» *Sol. RRL*, vol. 6, p. 2100767, 2022.

[5] A. Rafiee and K. R. Khalilpour, «Chapter 11 - Renewable Hybridization of Oil and Gas Supply Chains,» Polygeneration with Polystorage for Chemical and Energy Hubs, For Energy and Chemicals, pp. 331-372, 2019.

[6] V. Smil, « Energy Transitions: History, Requirements and Prospects,» Ed. ABC-CLIO, 2010.

[7] W. Matt Jolly et al, «Climate-induced variations in global wildfire danger from 1979 to 2013,» *Nature Communications*, vol. 6, p. 7537, 2015.

[8] C. McGlade and P. Ekins, «The geographical distribution of fossil fuels unused when limiting global warming to 2 °C,» Nature , vol. 517, p. 187–190, 2015.

[9] «National Aeronautics and Space Administration, Goddard Institute for Space Studies (GISS) in New York,» [En ligne]. Available: https://www.giss.nasa.gov/research/news/20220113/.

[10] National Aeronautics and Space Administration, Goddard Institute for Space Studies (GISS) in New York,» [En ligne]. Available: https://www.giss.nasa.gov/research/news/20220113b/.

[11] M. Hussain, M. Rashid, A. Ali and M. F. Bhopal , «Systematic study of optoelectronic and transport properties of cesium lead halide (Cs_2PbX_6; X=Cl, Br, I) double perovskites for solar cell applications,» Ceram. Int., vol. 46, p. 21378–21387, 2020.

[12] J. Potočnik, «Renewable Energy Sources and the Realities of Setting an Energy Agenda,» Science , vol. 315, pp. 810-811, 2007.

[13] Q. Schiermeier, J. Tollefson, T. Scully, A. Witze et O. Morton, «Energy alternatives: Electricity without carbon,» Nature, vol. 454, pp. 816-823, 2008.

[14] L. P. Verma, N. K. Lohani and S. Kumar, «The sun,» Philosophy and Social Action, vol. 31, p. 23, 2005.

[15] J. Luceño-Sánchez, A. Díez-Pascual et R. Capilla, «Materials for photovoltaics: State of art and recent developments,» International Journal of Molcular Sciences, vol. 20, p. 976, 2019.

[16] B. P. Jelle, «Electrochromic smart windows for dynamic daylight and solar energy control in buildings,» Electrochromic Materials and Devices. Wiley-VCH Weinheim, 2015.

[17] A. I. Sterhov and I. Y. Loshkarev, «Determination of the proportion of natural light in solar radiation using the method of conversion of lighting units into energy,» Journal of Physics: Conference Series, vol. 1353, p. 012002, 2019.

[18] R. Williams, «Becquerel Photovoltaic Effect in Binary Compounds,» J. Chem. Phys, vol. 32, pp. 1505-1514, 1960.

[19] G. D. Kubiak and K. W. Kolasinski, «Normally unoccupied states on C (111)(diamond)(2× 1): Support for a relaxed π-bonded chain model,» Phys. Rev. B, vol. 39, p. 1381, 1989.

[20] R. Foster, M. Ghassemi and A. Cota, Solar Energy: renewable Energy and the Environment, 2010.

[21] J. S. Lacerda et Jeroen C.J.M. Van den Bergh, «Diversity in solar photovoltaic energy: Implications for innovation and policy,» *Renew. Sust. Energ. Rev. RENEW SUST ENERG REV,* vol. 54, pp. 331-340, 2016.

[22] U. Gangopadhyay, S. Jana and S. Das, «State of Art of Solar Photovoltaic Technology,» chez *Proceedings of International Conference on Solar Energy Photovoltaics*, 2013.

[23] P. G. V. Sampaio and M. . O. A. González, «Photovoltaic solar energy: Conceptual framework,» *Renew. Sust. Energ. Rev. Renew Susut Energ Rev,* vol. 74, p. 590–601, 2017.

[24] D. Lincot, «Where is the photovoltaic conversion of solar energy?,» *Photonics*, vol. 93, pp. 37-43, 2018.

[25] «Fraunhofer Institute for Solar Energy System, Photovoltaic report,» 2019. [En ligne]. Available: https://www.ise.fraunhofer.de.

[26] B. O'Regan and M. Grätzel, «A low-cost, high-efficiency solar cell based on dye-sensitized colloidal TiO2 films,» *Nature,* vol. 353, p. 737–740, 1991.

[27] S. Grini, «Band gap grading and impurities,» 2019.

[28] V. Aroutiounian, S. Petrosyan and A. Khachatryan, «Studies of the photocurrent in quantum dot solar cells by the application of a new theoretical model,» *Energy Mater. Sol. Cells,* vol. 89, p. 165–173, 2005.

[29] W. Wang, W. Feng, J. Du, W. Xue, L. Zhang, L. Zhao, Y. Li and X. Zhong, «Cosensitized quantum dot solar cells with conversion efficiency over 12%,» *Adv. Mater,* vol. 30, p. 1705746 , 2018.

[30] J. V. Lagemaat, T. Barnes, G. Rumbles, S. Shaheen, T. Coutts, C. Weeks, I. Levitsky, J. Peltola and P. Glatkowski , «Organic solar cells with carbon nanotubes replacing as the transparent electrode,» *Appl. Phys. Lett,* vol. 88, p. 233506, 2006.

[31] M. W. Rowell, M. A. Topinka, M. D. McGehee, H. J. Prall, G. Dennler, N. S. Sariciftci, L. Hu and G. Gruner , «Organic solar cells with carbon nanotube network electrodes,» *Appl. Phys. Lett,* vol. 88, p. 233503, 2006.

[32] D. König, K. Casalenuovo, K. Takeda et G. Conibeer, «Hot carrier solar cells: Principles, materials and design,» *Phys. E: Low-Dimens. Syst. Nanostructures,* vol. 42, p. 2862–2866, 2010.

[33] R. Toss and A. Nozik, «Efficiency of hot-carrier solar energy converters,» *J. Appl. Phys,* vol. 53, pp. 3813-3816, 1982.

[34] T. Ameri, G. Dennler, C. Lungenschmied and C. J. Brabec, «Organic tandem solar cells: A review,» *Energy Environ. Sci,* vol. 2, pp. 347-363, 2009.

[35] C. A. Nelson, N. R. Monahan and X. Y. Zhu, «Exceeding the Shockley–Queisser limit in solar energy conversion,» *Energy Environ. Sci,* vol. 6, pp. 3508-3519, 2013.

[36] G. Conibeer, «Third-generation photovoltaics,» *Mater. Today,* vol. 10, pp. 42-50, 2007.

[37] A. Navrotsky and D. J. Weidner, Perovskite: a structure of great interest to geo- physics and materials science, Washington DC American Geophysical Union Geo-physical Monograph Series, vol. 45, 2013.

[38] D. Zhou, T. Zhou, Y. Tian, X. Zhu and Y. Tu, «Perovskite-Based Solar Cells: Materials, Methods, and Future Perspectives,» *J. Nanomater,* vol. 2018, p. 8148072, 2018.

[39] N.-G. Park, «Perovskite solar cells: An emerging photovoltaic technology,» *Mater. Today,* vol. 18, pp. 65-72, 2015.

[40] M. A. Green, E. D. Dunlop, J. Hohl-Ebinger, M. Yoshita, N. Kopidakis and X. Hao, «Solar cell efficiency tables (Version 58),» *Prog. Photovolt. Res. Appl,* vol. 29, p. 657–667, 2021.

[41] A. M. Elseman el al., «Superior Stability and Efficiency Over 20% Perovskite Solar Cells Achieved by a Novel Molecularly Engineered Rutin–AgNPs/Thiophene Copolymer,» *Adv. Sci,* vol. 5, p. 1800568, 2018.

[42] C. J. Xiao, C. Q. Jin and X. H. Wang, «Crystal structure of dense nanocrystalline BaTiO3 ceramics,» *Mater. Chem. Phys,* vol. 111, pp. 209-212, 2008

[43] C. J. Kennedy, C. J. Howard et B. C. Chakoumakos, «High-temperature phase transitions in SrHfO3,» *Phys. Rev. B,* vol. 60, p. 2972, 1999

[44] A. Barua, S. K. Dey, S. K. Sabyasachi and S. Kumar, «Structural and dielectric characterization of triple perovskites Ba3NiTaNbO9 and Ba3NiTaSbO9,» *J. Alloys Compd,* vol. 854, p. 157217, 2021.

[45] P. Zhou, N. Li, Y. Chao, W. Zhang, F. Lv, K. Wang, K. Yang, P. Gao and P. Guo, «Thermolysis of Noble Metal Nanoparticles into Electron-Rich Phosphorus-Coordinated Noble Metal Single Atoms at Low Temperature,» *J. Angew. Chem. Int. Ed,* vol. 58, p. 14184–14188, 2019

[46] F. Bensebaa, M. Khalfallah and M. Ouchen, «Decentralized and direct solar hydrogen production: Towards a hydrogen economy in MENA region,» [En ligne]. Available: https://www.osti.gov/etdeweb/servlets/purl/21397664.

[47] J. H. Kim, D. Hansora, P. Sharma, J. W. Jang and J. S. Lee, «Toward practical solar hydrogen production – an artificial photosynthetic leaf-to-farm challenge,» *Chem. Soc. Rev,* vol. 48, p. 1908–1971, 2019.

[48] E. Schrödinger, «An undulatory theory of the mechanics of atoms and molecules,» *Phys. Rev,* vol. 28, p. 1049, 1926.

[49] V. Shukla, «Computational Studies of 2D Materials: Application to Energy Storage and Electron Transport in Nanoscale Devices,» 2019.

[50] M. Born and R. Oppenheimer, «Quantum Theory of Molecules,» *Ann. Phys,* vol. 84, pp. 0457-0484, 1927.

[51] V. Fock, «Näherungsmethode zur Lösung des quantenmechanischen Mehrkörperproblems,» *Zeitschrift für Physik ,* vol. 61, pp. 126-148, 1930.

[52] J. C. Slater, «Note on Hartree's method,» *Phys. Rev,* vol. 35, p. 210, 1930.

[53] L. H. Thomas, «The Calculation of Atomic Fields,» *Math. Proc. Camb. Philos. Soc,* vol. 23, pp. 542-548, 1927.

[54] P. C. Hohenberg and W. Kohn, «Inhomogeneous Electron Gas,» *Phys. Rev. B,* vol. 136, p. 864, 1964.

[55] W. Kohn and L. J. Sham, «Self-Consistent Equations Including Exchange and Correlation Effects,» *Phys. Rev,* vol. 2, p. 19, 1965

[56] D. Shechtman, I. Blech, D. Gratias and J. W. Cahn, «Metallic Phase with Long-Range Orientational Order and No Translational Symmetry,» *Phys. Rev. Lett,* vol. 53, p. 1951, 1984.

[57] F. De Proft and P. Geerlings, «Conceptual and computational DFT in the study,» *Chem. Rev,* vol. 101, pp. 1451-1464, 2001.

[58] A. Görling, «Density-functional theory beyond the Hohenberg-Kohn theorem,» *Phys. Rev. A,* vol. 59, p. 3359, 1999.

[59] W. Kohn and L. J. Sham, «Self-Consistent Equations Including Exchange and Correlation Effects,» *Phys. Rev,* vol. 140, p. A1133 , 1965.

[60] S. Kurth, M. Marques, M. Lüders and E. K. U. Gross, «Local Density Approximation for Superconductors,» *hys. Rev. Lett,* vol. 83, p. 2628, 1999.

[61] Z. Wu and R. E. Cohen, «More accurate generalized gradient approximation for solids,» *Phys. Rev. B,* vol. 73, p. 235116, 2006.

[62] J. P. Perdew ad Y. Wang, «Pair-distribution function and its coupling-constant average for the spin-polarized electron gas,» *Phys. Rev. B,* vol. 46, p. 12947, 1992.

[63] J. P. Perdew, K. Burke and M. Ernzerhof, «Generalized gradient approximation,» *Phys. Rev. Let,* vol. 77, p. 3865, 1996.

[64] F. Zahariev, S. S. Leang, and Mark S. Gordon, «Functional derivatives of meta-generalized gradient approximation (meta-GGA) type exchange-correlation density functionals,» J. Chem. Phys, vol. 138, p. 244108, 2013.

[65] E. Engel and S. H. Vosko, «Exact exchange-only potentials and the virial relation as microscopic criteria for generalized gradient approximations,» *Phys. Rev. B,* vol. 47, p. 13164, 1993.

[66] A. D. Becke and E. R. Johnson, «A simple effective potential for exchange,» *J. Chem. Phys,* vol. 124, p. 221101, 2006.

[67] F. Tran and P. Blaha, «Accurate Band Gaps of Semiconductors and Insulators with a Semilocal Exchange-Correlation Potential,» *Phys. Rev. Lett,* vol. 102, p. 226401, 2009.

[68] A. D. Becke, «A new mixing of Hartree-Fock and local density-functional theories ,» *J. Chem. Phys,* vol. 98, p. 1372–1377, 1993.

[69] F. Tran and P. Blah, «Implementation of screened hybrid functionals based on the Yukawa potential within the LAPW basis set,» *Phys. Rev. B,* vol. 83, p. 235118, 2011.

[70] O. K. Andersen, «Linear methods in band theory,» *Phys. Rev. B,* vol. 12, p. 3060, 1975.

[71] E. Sjöstedt, L. Nordström et D. Singh, «An alternative way of linearizing the augmented plane-wave method,» *Solid State Commun,* vol. 114, pp. 15-20, 2000.

[72] J. C. Slater, «Wave Functions in a Periodic Potential,» *Phys. Rev. B,* vol. 51, p. 846, 1937.

[73] P. Blaha , K. Schwarz, G. K. H. Madsen, D. Kvasnicka and J. Luitz, «WIEN2K, an Augmented Plane Wave Plus Local Orbitals Program for Calculating Crystal Properties,» *Vienna University of Technology, Austria,* 2001.

[74] D. M. Rowe, In Thermoelecrics handbook (macro to nano), 2006.

[75] N. P. Blake and M. Metiu, «in Chemistry, Physics, and Materials Science of Thermoelectric Materials: Beyond Bismuth Telluride,» 2003.

[76] J. I. Gersten and F. W. Smith, The Physics and Chemistry of Materials, 2001.

[77] G. KH. Madsen and D. J. Singh, «BoltzTraP. A code for calculating band-structure dependent quantities,» *Comput. Phys. Commun,* vol. 175, pp. 67-71, 2006.

[78] N. Tahiri, S. Dahbi, O. El Bounagui and H. Ez-Zahraouy, «Magnetic, magnetocaloric and thermoelectric investigations of perovskite LaFeO3 compound: First principles and Monte Carlo calculations,» *Comput. Theor. Chem,* vol. 1204, p. 113421, 2021.

[79] N. Tahiri, S. Dahbi, O. El Bounagui and H. Ez-Zahraouy, «Magnetocaloric and thermoelectric properties of the perovskite LaMnO3 material: A DFT study and Monte Carlo thechnique,» *Ph. Transit,* vol. 94, pp. 826-834, 2021.

[80] L. Weston, A. Janotti, X. Y. Cui, C. Stampfl and C. G. Van de Walle, «Hybrid functional calculations of point defects and hydrogen in SrZrO3,» *Phys. Rev. B,* vol. 89, p. 184109, 2014.

[81] S. M. Alay-e-Abbas et al, «Evaluation of thermodynamics, formation energetics and electronic properties of vacancy defects in CaZrO3, » *Sci. Rep,* vol. 7, p. 8439, 2017.

[82] A. Yoko, J. Wang, N. Umezawa, T. Ohno and Y. Oshima, «A-Site Cation Bulk and Surface Diffusion in A- Site-Deficient BaZrO3 and SrZrO3 Perovskites,» *J. Phys. Chem. C,* vol. 121, pp. 12220-12229, 2017.

[83] D. Amoroso, A. Cano and P. Ghosez, «First-principles study of (Ba , Ca)TiO_3 and Ba(Ti , Zr)O3 solid solutions, » *Phys. Rev. B,* vol. 97, p. 174108, 2018.

[84] Z. Song, J. Zhao, and Q. Liu, «Luminescent perovskites: Recent advances in theory and experiments, » *Inorg. Chem. Front,* vol. 6, p. 2969-3011, 2019.

[85] I. L. V. Rosa et al., «A theoretical investigation of the structural and electronic properties of orthorhombic $CaZrO_3$,» Ceram. Int, vol. 41, p. 3069-3074, 2014.

[86] S. C. Middleburgh et al., «Peroxide defect formation in zirconate perovskites, » *J. Mater. Chem. A,* vol. p. 2, 15883-15888, 2014.

[87] J. W. Bennett, I. Grinberg, and A. M. Rappe, «Effect of symmetry lowering on the dielectric response of $BaZrO_3$,» *Phys. Rev. B,* vol. 73, p. 180102, 2006.

[88] S. Muhammad Alay-e-Abbas, S. Nazir, and A. Shaukat, «Formation energies and electronic structure of intrinsic vacancy defects and oxygen vacancy clustering in $BaZrO_3$,» *Phys. Chem. Chem. Phys,* vol. 18, p. 23737-23745, 2016.

[89] I. Grinberg et al., « Perovskite oxides for visible-light-absorbing ferroelectric and photovoltaic materials,» *Nature*, vol. 503, p. 509-512, 2013.

[90] D. Cao, C. Wang, F. Zheng, W. Dong, L. Fang, and M. Shen, «High-Efficiency Ferroelectric-Film Solar Cells with an n-type Cu_2O Cathode Buffer Layer, » *Nano Lett*, vol. 12, p. 2803-2809, 2012.

[91] B. J. Kennedy, C. J. Howard, and B. C. Chakoumakos, «High-temperature phase transitions in $SrZrO_3$, ». *Phys. Rev. B*, vol. 59, p. 4023-2027, 1999.

[92] J. Meng et al., « $BaZrO_3$ hollow nanostructure with Fe (III) doping for photocatalytic hydrogen evolution under visible light, » *Int. J. Hydrog. Energy*, vol. 43, p. 9224-9232, 2018.

[93] Y. Yuan et al., « Synthesis and photocatalytic characterization of a new photocatalyst $BaZrO_3$, » *Int. J. Hydrog. Energy*, vol. 33, p. 5941-5946, 2008.

[94] A. Bihari Swain, D. Murali, B. R. K. Nanda, and P. Murugavel, « Large Bulk Photovoltaic Response by Symmetry-Breaking Structural Transformation in Ferroelectric $[Ba(Zr_{0.2}Ti_{0.8})O_3]_{0.5}[(Ba_{0.7}Ca_{0.3})TiO_3]_{0.5}$, » *Phys. Rev. Applied*, vol. 11, p. 044007 ,2019.

[95] P. G. Sundell, M. E. Björketun, and G. Wahnström, « Thermodynamics of doping and vacancy formation in $BaZrO_3$ perovskite oxide from density functional calculations, » *Phys. Rev. B*, vol. 73, p. 104112 ,2006.

[96] N. Bork, N. Bonanos, J. Rossmeisl, and T. Vegge, «Simple descriptors for proton-conducting perovskites from density functional theory, » *Phys. Rev. B*, vol. 82, p. 014103 ,2010.

[97] A. Lindman, P. Erhart, and G. Wahnström, «Implications of the band gap problem on oxidation and hydration in acceptor-doped barium zirconate, » *Phys. Rev. B, vol.* 91, p. 245114 ,2015.

[98] R. I. Eglitis, «Ab initio hybrid DFT calculations of $BaTiO_3$, $PbTiO_3$, $SrZrO_3$ and $PbZrO_3$ (111) surfaces, » *Appl. Surf. Sci*, vol. 358, p. 556–562, 2015.

[99] H. Y. Hwang, Y. Iwasa, M. Kawasaki, B. Keimer, N. Nagaosa, and Y. Tokura, «Emergent phenomena at oxide interfaces, » *Nature Mater*, vol. 11, no. 2, p. 103–113, 2012.

[100] A. K. Kunti et al., «Local Structure and Spectroscopic Properties of Eu^{3+}-Doped $BaZrO_3$,» *Inorg. Chem, vol.* 58, p. 3073-3089 ,2019.

[101] Y. Yuan et al., «Polymerizable complex synthesis of $BaZr_{1-x}Sn_xO_3$ photocatalysts Role of Sn in the band structure and their photocatalytic water splitting activities, » *J. Mater. Chem*, vol. 20, p. 6772-6779, 2010.

[102] R. Borja-Urby et al., «Structural study, photoluminescence, and photocatalytic activity of semiconducting $BaZrO_3$: Bi nanocrystals, » *Mater. Sci. Eng*: B, vol. 176, p. 1382-1387, 2011.

[103] Z. Khan and M. Qureshi, «Tantalum doped $BaZrO_3$ for efficient photocatalytic hydrogen generation by water splitting, » *Catal. Commun*, vol. 28, p. 82-85, 2012.

[104] L. J. Sham and M. Schlüter, « Density-Functional Theory of the Energy Gap,» *Phys. Rev. Lett*, vol. 51, p. 1888-1891 ,1983.

[105] A. J. Smith and A. J. E. Welch, «Some mixed metal oxides of perovskite structure, » *Acta Cryst*, vol. 13, p. 653-656, 1960.

[106] R. W. G. Wyckoff, «Crystal structures, » *Acta Cryst*, vol. 18, p.139-139, 1965.

[107] M. G. Brik, C.-G. Ma, and V. Krasnenko, «First-principles calculations of the structural and electronic properties of the cubic CaZrO3 (001) surfaces, » Surf. Sci, vol. 608, p. 146-153, 2012.

[108] L. S. Cavalcante et al., «Experimental and theoretical correlation of very intense visible green photoluminescence in $BaZrO_3$ powders, » *J. Appl. Phys*, vol. 103, p. 063527, 2008.

[109] Y. S. Lee et al., «Systematic trends in the electronic structure parameters of the 4-d transition-metal oxides $SrMO_3$ (M = Zr, Mo, Ru, and Rh),» *Phys. Rev. B*, vol. 67, p.113101, 2003.

[110] R. Nechache et al., « Bandgap tuning of multiferroic oxide solar cells,» *Nat. Photon*, vol. 9, p. 61-67, 2014.

[111] R. I. Eglitis ,«Ab initio calculations of the atomic and electronic structure of $BaZrO_3$ (111) surfaces. *Solid State Ion*,» vol. 230, p. 43-47, 2012.

[112] S. Dahbi, N. Tahiri, O. El Bounagui and H. Ez-Zahraouy, «Electronic, optical, and thermoelectric properties of perovskite $BaTiO_3$ compound under the effect of compressive strain, » *J. Chem. Phys*, vol. 544, p. 111105, 2021.

[113] S. M. Alay-e-Abbas et al., «Theoretical investigation of thermodynamic and optoelectronic properties
of Ce4+ doped $SrZrO_3$ ceramics: A DFT study,» *Ceram. Int*, vol. 45, p. 18281-18290, 2019.

[114] S. M. Alay-e-Abbas et al., «Density Functional Theory Evaluation of Ceramics Suitable for Hybrid Advanced Oxidation Processes: A Case Study for Ce^{4+} -Doped $BaZrO_3$,» *J. Phys. Chem.* C, vol. 123, p. 6044-6053, 2019.

[115] S. Dahbi, N. Tahiri, O. El Bounagui and H. Ez-Zahraouy, «The new eco-friendly lead-free zirconate perovskites doped with chalcogens for solar cells: Ab initio calculations,» *Opt. Mater*, vol. 109, p. 110442, 2020.

[116] E. Mihóková, et al., «Intrinsic and impurity-induced emission bands in SrHfO3, » *Phys. Rev. B*, vol. 82, p. 165115, 2010.

[117] P.Maggio Pechini, «Method of Preparing Lead and Alkaline Earth Titanates and Niobates and Coating Method Using the Same to Form a Capacitor,» US Patent No, 1963, p. 3330697.

[118] R. S. André, S. M. Zanetti, J. A. Varela and E. Longo, «Synthesis by a chemical method and characterization of CaZrO3 powders: Potential application as humidity sensors,» *Ceram. Int*, vol. 40, p. 16627, 2014.

[119] M. Sousa, et al., «Optical properties of epitaxial SrHfO3 thin films grown on Si, » *J. Appl. Phys*, vol. 102, p. 104103, 2007.

[120] R.A. Evarestov, A.V. Bandura, E.N. Blokhin ,«Surface relaxation and tilting in SrHfO3 orthorhombic perovskite: hybrid HF-DFT LCAO calculations,» *Surf. Sci*, vol. 602, p. 3674, 2008.

[121] S. Yamanaka, T. Maekawa, H. Muta, T. Matsuda, S. Kobayashi and K. Kurosaki, «Thermal and mechanical properties of SrHfO3», *J. Alloys Compd*, vol. 381, p. 295, 2004.

[122] B. Moses Abraham, N. Yedukondalu and G. Vaitheeswaran, «Structural, electronic and lattice dynamical properties of perovskite CaZrO3 under high pressure,» AIP Conference Proceedings, vol. 1832, p. 090042, 2017.

[123] E. Rauwel, A. Galeckas, P. Rauwel and H. Fjellvåg, «Unusual photoluminescence of CaHfO3 and SrHfO3 nanoparticles, » *Adv. Funct. Mater*, vol. 22, p. 1174–1179, 2012.

[124] K. Shibuya, T. Ohnishi, M. Lippmaa, M. Kawasaki and H. Koinuma, «Domain structure of epitaxial CaHfO3 gate insulator films on SrTiO3,» *Appl. Phys. Lett*, vol. 84, p. 2142–2144, 2004.

[125] K. Shibuya, T. Ohnishi, M. Lippmaa and M. Oshima, «Metallic conductivity at the CaHfO3/SrTiO3 interface», *Appl. Phys. Lett*, vol. 91, p. 232106, 2007.

[126] C. Rossel, et al., «Field-effect transistors with SrHfO3 as gate oxide,» *Appl. Phys. Lett*, vol. 89, p. 053506, 2006.

[127] C. Rossel, et al., «SrHfO3 as gate dielectric for future CMOS technology,» *Microelectron. Eng*, vol. 84, p. 1869, 2007.

[128] S.M. Alay-e-Abbas, S. Nazir, N.A. Noor, N. Amin and A. Shaukat, « Thermodynamic stability and vacancy defect formation energies in SrHfO3, » *J. Phys. Chem*, vol. 118, p. 19625, 2014.

[129] R.I. Eglitis and S. Piskunov, «First principles calculations of SrZrO3 bulk and ZrO2- terminated (001) surface F centers, » *Comput. Condens. Matter*, vol. 7, p. 1, 2016.

[130] A.I. Popov, E.A. Koto and M.M. Kukl, «Quantum chemical calculations of the electron center diffusion in MgO crystals, » *Phys. Stat. sol. B*, vol. 195, p. 61, 1996.

[131] H. Pinto, S. Elliott andA. Stashans, «Theoretical study of structural and optical properties of F-centers in tetragonal BaTiO3, » *Proc. SPIE-Int. Soc. Opt. Eng*, vol. 5122, p. 303, 2003.

[132] E.A. Kotomin, R.I. Eglitis and A.I. Popov, «Charge distribution and optical properties of and F+ and F centres in KNbO3 crystals, » *J. Phys. Condens. Matter*, vol. 9, p. L315, 1997.

[133] A.I. Popov, E.A. Kotomin and J. Maier, «Basic properties of the F-type centers in halides, oxides and perovskites, » Nucl. Instrum. *Methods Phys. Res. B: Beam Interact. Mater*, vol. 268, p. 3084, 2010.

[134] Jayashree Swaminathan and Meiyazhagan Ashokkumar, «Switchable intrinsic defect chemistry of Titania for catalytic applications, » *Catalysts*, vol. 8, p. 601, 2018.

[135] R.I. Eglitis, «Comparative first-principles calculations of SrTiO3, BaTiO3, PbTiO3 and CaTiO3 (001), (011) and (111) surfaces,» *Ferroelectrics*, vol. 483, p. 53, 2015.

[136] D.M. Hoat, J.F.R. Silva and A.M. Blas, «First principles study of structural, electronic and optical properties of perovskites CaZrO3 and CaHfO3 in cubic phase,» *Solid State Commun*, vol. 275, p. 29–34, 2018.

[137] A. Feteira and D.C. Sinclair, «Crystal structure and microwave dielectric properties of alkaline-earth hafnates, AHfO3 (Ba, Sr, Ca),» *J. Am. Ceram. Soc*, vol. 91, p. 893, 2008.

[138] G. Lupina, G. Kozłowski, J. Dabrowski, P. Dudek, G. Lippert and H.-J. Müssig, «Dielectric and structural properties of thin SrHfO3 layers on TiN,» *Appl. Phys. Lett*, vol. 93, p. 252907, 2008.

[139] L. Qi-Jun, L. Zheng-Tang, F. Li-Ping and T. Hao, «Electronic and optical properties of cubic SrHfO3,» *Commun. Theor. Phys*, vol. 54, p. 908, 2010.

[140] C. S. Prasanth, H. Padma Kumar, R. Pazhani, Sam Solomon and J. K. Thomas, «Synthesis, characterization and microwave dielectric properties of nanocrystalline CaZrO3 ceramics,» *J. Alloys. Compd*, vol. 464, p. 306, 2008.

[141] U. Saif, I. Tausif, R. Gul and A. Iftikhar, «Electronic and optical properties of group IIA-IVB cubic perovskite oxides: Improved TB-mBJ study,» *Chem. Phys. Lett*, vol. 757, p.139887, 2020.

[142] S.M. Alay-e-Abbas, S. Nazir, S. Cottenier and A. Shaukat, «Evaluation of thermodynamics, formation energetics and electronic properties of vacancy defects in CaZrO3,» *Sci. Rep*, vol. 7, p. 8439, 2017.

[143] W. Luo, W. Duan, S.G. Louie and M.L. Cohen, «Structural and electronic properties of n-doped and p-doped SrTiO3,» *Phys. Rev*. B, vol. 70, p. 214109, 2014.

[144] E.A. Kotomin, et al., «Calculations of the geometry and optical properties of F_{Mg} centers,» *Phys. Rev*. B, vol. 51, p. 8770, 1995.

[145] H. -C. Huang, C. -L. Yang, M. -S. Wang and X.-G. Ma, «Chalcogens doped $BaTiO_3$ for visible light photocatalytic hydrogen production from water splitting, Spectrochim,» *Acta A Mol. Biomol. Spectrosc*, vol. 208, p. 65, 2019.

[146] M-G. Ju, M. Chen, Y. Zhou, H. F. Garces, J. Dai, L. Ma, N. P. Padture and X. Ch. Zeng, «Earth-Abundant Nontoxic Titanium (IV)-based Vacancy-Ordered Double Perovskite Halides with Tunable 1.0 to 1.8 eV Bandgaps for Photovoltaic Applications,» *ACS. Energy Lett*, vol. 3, p. 297−304, 2018.

[147] G. E. Eperon et al., «Perovskite-perovskite tandem photovoltaic's with optimized bandgap, » *Science*, vol. 354, p. 861−865, 2016.

[148] H. J. Snaith, «Present status and future prospects of perovskite Photovoltaics,» *Nat. Mater*, vol. 17, p. 372–376, 2018.

[149] X. H. Zhao, Y. L. Tang, T. Y. Tang, X. F. Diao, L. K. Gao, Q. Xie, B. Shi, L. Yuan and L. M. Lu, «Study on mechanical, electronic and optical properties of Pb-free double halide perovskites In_2TiX_6 (X = Cl, Br, I) for solar cells based on first-principles, Mater,» *Today Commum*, vol. 26 ,p. 102180, 2021.

[150] A. Kojima , K. Teshima, Y. Shirai and T. Miyasaka, «T. Organometal halide perovskites as visible-light sensitizers for photovoltaic cells,» *J.Am. Chem. Soc*, vol. 131, p. 6050−6051, 2009.

[151] M. R. Filip, S. Hillman, A. A. Haghighirad, H. J. Snaith and F. Giustino, «Band Gaps of the Lead-Free Halide Double Perovskites $Cs_2BiAgCl_6$ and $Cs_2BiAgBr_6$ from Theory and Experiment,» *J. Phys. Chem. Lett*, vol. 7, p. 2579–2585, 2016.

[152] D. Liu and R. Sa, «Theoretical study of Zr doping on the stability, mechanical, electronic and optical properties of Cs_2TiI_6,» *Opt. Mater*, vol. 110, p. 110497, 2020.

[153] S. T. Umedov, D. B. Khadka, M. Yanagida, A. Grigorieva and Y. Shirai, «A-site tailoring in the vacancy-ordered double perovskite semiconductor Cs_2SnI_6 for photovoltaic application,» *Sol. Energy Mater Sol. Cells*, vol. 230, p. 111180, 2021.

[154] Xiaofeng Qiu et al., «From unstable $CsSnI_3$ to air-stable Cs_2SnI_6: A lead-free perovskite solar cell light absorber with bandgap of 1.48 eV and high absorption coefficient,» *Sol. Energy Mater Sol. Cells*, vol. 159, p. 227–234, 2017.

[155] D. Cortecchia et al. ,«Lead-free $MA_2CuCl_xBr_{4-x}$ hybrid perovskites,» *Inorg. Chem*, vol. 55, p. 1044–1052, 2016.

[156] O.A. Lozhkina, A.A. Murashkina, M.S. Elizarov, V.V. Shilovskikh, A.A.Zolotarev, Yu.V. Kapitonov, R. Kevorkyants, A.V. Emeline and T. Miyasaka, «Microstructural analysis and optical properties of the halide double perovskite $Cs_2BiAgBr_6$ single crystals,» *Chem. Phys. Lett*, vol. 694, p. 12-22, 2018.

[157] K.C. Bhamu, A. Soni, J. Sahariya, «Revealing optoelectronic and transport properties of potential perovskites Cs_2PdX_6 (X=Cl, Br): A probe from density functional theory (DFT),» *Sol. Energy*, vol. 162, p. 336–343, 2018.

[158] M. A. Ali, T. Alshahrani, G. Murtaza, «Defective perovskites Cs_2SeCl_6 and Cs_2TeCl_6 as novel high temperature potential thermoelectric materials,» *Mater. Sci. Semicond. Process*, vol. 127, p. 105728, 2021.

[159] X. Du, D. He, H. Mei, Y. Liu, N. Cheng, «Mechanical, electronic and optical properties of K2TeX6 (X=Cl, Br, I) perovskite derivatives using density functional theory»**,** *Mater. Sci. Semicond. Process*, vol. 123, p. 105579, 2021.

[160] T. Alshahrani and Q. Mahmood and M. Rashid, «The role of 5d electrons spin in quantum ferromagnetism and transport properties of double perovskites Cs_2ZCl/Br_6 (Z = Ta, W) for spintronic applications», *Eur. Phys. J. Plus*, vol. 136, p. 297, 2021.

[161] M. A. Ali, G. Murtaza and A. Laref, «Exploring the ferromagnetic half metallic nature of Cs_2NpBr_6 via spin polarized density functional theory», *Chin. Phys B*, vol. 29, p. 066102, 2020.

[162] R. Ullah, M. Az. Ali, G. Murtaza, A. Khan and A. Mahmood, «Ab initio study for the structural, electronic, magnetic, optical, and thermoelectric properties of K_2OsX_6 (X = Cl, Br) compounds», *Int. J. Energy. Res*, vol. 44, p. 9035-9049, 2020.

[163] R. Ullah, M. A. Ali, G. Murtaza, A. Mahmood and S. M. Ramay, «The significance of anti-fluorite Cs_2NbI_6 via its structural, electronic, magnetic, optical and thermoelectric properties», *Int. J. Energy. Res*, vol. 44, p. 10179-10191, 2020.

[164] M. A. Ali, A. H. Reshak, G. Murtaza, M. AL-Anazy, H. Althib, T. H. Flemban, J. Bila, «Optoelectronic and transport properties of Rb/Cs_2TeI_6 defective perovskites for green energy applications», *Int. J. Energy. Res*, vol. 45, p. 8448-8455, 2020.

[165] Q. Mahmood, M.H. Alhossainy, M.S. Rashid, Tahani H. Flemban, Hind Althib, ThamraaAlshahrani, M. Rashid and A. Laref, «First-principles study of lead-free double perovskites Rb_2TeX_6 (X = Cl, Br, and I) for solar cells and renewable energy», *Mater. Sci. Eng B*, vol. 266, p. 115064, 2021.

[166] Dinesh Kumar Yadav, Shalika Ram Bhandari,Bishnu Prasad Belbase, Gopi Chandra Kaphle, Dibya Prakash Rai and Madhav Prasad Ghimire, «Effects of electron-correlation, spin-orbit coupling, and modified Becke Johnson potential in double perovskites $SrLaBB'O_6$ (B = Ni, Fe; B′ = Os, Ru)», *Comput. Mater. Sci*, vol. 170, p.109168, 2019.

[167] Anjie Cheng, Chenyang Lyu, Tianyi Shi, Ziheng Wang and Robert Palgrave, «Geometric Analysis and Formability of the Cubic A_2BX_6 VacancyOrdered Double Perovskite Structure», *Chem. Mater*, vol. 32, p. 9573–9583, 2020.

[168] V. Sidey, «A simplified empirical model for predicting the lattice parameters for the cubic perovskite-related inorganic A_2BX_6 halides», *J. Phys. Chem. Solids*, vol. 126, p. 310–313, 2019.

[169] W. Abriel, «Crystal structure and phase transition of Rb_2TeI_6», *Mat. Res. Bull*, vol. 17, p. 1341-1346, 1982.

[170] S. Dahbi, N. Tahiri, O. El Bounagui, H. Ez-Zahraouy, «Chalcogens' impurities and a single F-center in perovskite $SrHfO_3$ compound: Ab initio calculations», *Mater. Sci. Semicond. Process*, vol. 138, p. 106271, 2022.

[171] Michael Webster and Paul H. Collins, «Structural and Thermochemical Studies on Rb_2TeCI_6 and Comparison with Rb_2SnCI_6», *J. Chem. Soc., Dalton. Trans*, p. 588-594, 1973.

[172] A. Yakoubi, O. Baraka, and B. Bouhafs, «Structural and electronic properties of the Laves phase based on rare earth type BaM2 (M = Rh, Pd, Pt)», *Results Phys*, vol. 2, p. 58-65, 2012.

[173] John P. Perdew and Stefan Kurth, «Accurate Density Functional with Correct Formal Properties: A Step Beyond the Generalized Gradient Approximation», *Phys. Rev. Lett*, vol. 82, p. 2544, 1999.

[174] Jun-Hui Yuan, Qi Chen, Leonardo R C Fonseca, Ming Xu, Kan-Hao Xue and Xiang-Shui Miao, «GGA-1/2 self-energy correction for accurate band structure calculations: the case of resistive switching oxides», *J. Phys. Commun*, vol. 2, p. 105005, 2018.

[175] Annalise E. Maughan, Alex M. Ganose, Mitchell M. Bordelon, Elisa M. Miller, David O. Scanlon and James R. Neilson, «Defect Tolerance to Intolerance in the Vacancy-Ordered Double Perovskite Semiconductors Cs_2SnI_6 and Cs_2TeI_6», *J. Am. Chem. Soc*, vol. 138, p. 8453–8464, 2016.

[176] E. Yu. Peresh, O. V. Zubaka, V. I. Sidei, I. E. Barchii, S. V. Kun and A. V. Kun, «Preparation, Stability Regions, and Properties of M2TeI6 (M = Rb, Cs, Tl) Crystals», *Inorg. Mater*, vol. 38, p. 859-863, 2002.

[177] Rehan Ullah, Malak Azmat Ali, Afzal Khan, G. Murtaza, Asif Mahmood and Shahid M. Ramay, «Influence of the spin-orbit coupling effect on the electronic and thermoelectric properties of Cs2MI6 (M = Zr, Hf) variant perovskites», *Mater. Res. Bull*, vol. 134, p. 111112, 2021.

[178] G. Volonakis, M. R. Filip, A. A. Haghighirad, N. Sakai, B. Wenger, H. J. Snaith and F. Giustino, «Lead-free halide double perovskites via heterovalent substitution of noble metals», *J. Phys. Chem. Lett*, vol. 7, p. 1254–1259, 2016.

[179] J. Even, L. Pedesseau, M.-A. Dupertuis, J.-M. Jancu, and C. Katan, «Electronic model for self-assembled hybrid organic/perovskite semiconductors: Reverse band edge electronic states ordering and spin-orbit coupling», *Phys. Rev. B*, vol. 86, p. 205301, 2012.

[180] Jacky Even, Laurent Pedesseau, Jean-Marc Jancu and Claudine Katan, «Importance of Spin−Orbit Coupling in Hybrid Organic/Inorganic Perovskites for Photovoltaic Applications», *J. Phys. Chem. Lett*, vol. 4, p. 2999–3005, 2013.

[181] E. Yu. Peresh, O. V. Zubaka, S. V. Kun, I. V. Galagovets, I. E. Barchii, and M. Yu. Sabov, «Stability Limits and Properties of Tl_2TeBr_6, Cs_2TeBr_6, and Rb_2TeBr_6», *Inorg. Mater*, vol. 37, p. 849-852, 2001.

[182] E. Yu. Peresh, V. I. Sidei, O. V. Zubaka and I. P. Stercho, «$K_2(Rb_2,Cs_2,Tl_2)TeBr_6(I_6)$ and $Rb_3(Cs_3)Sb_2(Bi_2)Br_9(I_9)$ Perovskite Compounds», *Inorg. Mater*, vol. 47, p. 208-212, 2011.

[183] S. Dahbi, N. Tahiri, O. El Bounagui, H. Ez-Zahraouy, «Calcium hafnate perovskite from an insulator to a semiconductor for photovoltaic and photocatalytic hydrogen production from water splitting applications», *Superlattices Microstruct*, vol. 160, p.107058, 2021.

[184] P.D. Sreedevi, R. Vidya, P. Ravindran, «Earth-abundant nontoxic direct band gap semiconductors for photovoltaic applications by ab-initio simulations», *Sol. Energy*, vol. 190, p. 350–360, 2019.

[185] K. Kuhar, M. Pandey, K. S. Thygesen, and K. W. Jacobsen, «High-Throughput Computational Assessment of Previously Synthesized Semiconductors for Photovoltaic and Photoelectrochemical Devices», *ACS Energy Lett*, vol. 3, p. 436–446, 2018.

[186] D. Sun, Y. Xiong, Y. Sun, I. Dabo, and R. E. Schaak, «Solution-Synthesized In4SnSe4 Semiconductor Microwires with a Direct Band Gap», *Chem. Mater*, vol. 29, p. 1095–1098, 2017.

[187] Fatima et al., «Photoexcited Electron Lifetimes Influenced by Momentum Dispersion in Silicon Nanowires», J. Phys. Chem. C 2019, 123 (2019) 7457–7466.

[188] Fatima, J. Vogel, T. Inerbaev, N. Oncel, D. Kilin, «FirstPrinciples Study of Charge Carrier Dynamics with Explicit Treatment of Momentum Dispersion on Si Nanowires Along⟨211⟩ Crystallographic Directions», *MRS Adv*, vol. 3, p. 3477−3482, 2018.

[189] S. V. Krivovichev, «Minerals with antiperovskite structure: a review», *Zeitschrift für Kristallographie*, vol. 223, p. 109-113, 2008.

[190] M. Bilal, S. Jalali-Asadabadi, Rashid Ahmad, and Iftikhar Ahmad, «Electronic Properties of Antiperovskite Materials from State-of-the-Art Density Functional Theory», *J. Chem*, vol. p. 2015 495131, 2015.

[191] P. D Sreedevi, P. Ravindran, R. Vidya, «First principles prediction of the ground state crystal structures of antiperovskite compounds A3PN (A= Be, Mg, Ca, Sr, Ba and Zn)», *Mater. Today: Proc*, vol. 8, p. 294–300, 2019.

[192] H. Cheng et al., «Semiconductor-to-Metal Reconstructive Phase Transition and Superconductivity of Anti-perovskite Ca3PN under Hydrostatic Pressure», *J. Mater. Chem. C*, vol. 8, p. 13072-13078, 2020.

[193] M. Moakafi, R. Khenata, A. Bouhemadou, F. Semari, Ali H. Reshak, M. Rabah, «Elastic, electronic and optical properties of cubic antiperovskites SbNCa3 and BiNCa3», *Comput. Mater. Sci*, vol. 46, p. 1051–1057, 2009.

[194] A. Kadiri, A. Zaoui, M. Belhadj, S. Kacimi, S. Menezla, «Ferromagnetism induced by calcium vacancies in Ca3BiP anti-perovskite: An ab-initio Calculation», *J. Solid State Chem*, vol. 289, p. 121520, 2020.

[195] P. R. Vansant, P. E. Van Camp, and V. E. Van Doren, «Variable-cell-shape-based structural optimization applied to calcium nitrides», *Phys. Rev. B*, vol. 57, p. 7615- 7620, 1998.

[196] K. Haddadi, A. Bouhemadou, L. Louail, S. Maabed and D. Maouche, «Structural and elastic properties under pressure effect of the cubic antiperovskite compounds ANCa3 (A = P, As, Sb, and Bi)», *Phys. Lett. A*, vol. 373, p. 1777–1781, 2009.

[197] M. Y. Chern, D. A. Vennos, and F. J. DIisalvo, «Synthesis, Structure, and Properties of Anti-perovskite Nitrides Ca3MN, M = P, As, Sb, Bi, Ge, Sn, and Pb», *J. Solid State Chem*, vol. 96, p. 415-425, 1992.

[198] H. M. T. Farid et al., «Optoelectronic and thermoelectric properties of A3AsN (A = Mg, Ca, Sr and Ba) in cubic and orthorhombic phase», *J. Mater. Res. Technol*, vol. 13, p.1485-1495, 2021.

[199] S. Iqbal et al., «Electronic and Optical Properties of Ca3MN (M = Ge, Sn,Pb, P, As, Sb and Bi) Antiperovskite Compounds», *J. Electron. Mater*, vol. 45, p. 4188-4196, 2016.

[200] I. Ullah et el., «Structural and Optoelectronic Properties of X3ZN (X = Ca, Sr, Ba; Z = As, Sb, Bi) Anti-Perovskite Compounds», *J. Electron. Mater*, vol. 45, p. 3059-3068, 2016.

[201] X. Qiu et al., «From unstable CsSnI3 to air-stable Cs2SnI6: A lead-free perovskite solar cell light absorber with bandgap of 1.48 eV and high absorption coefficient», *Sol. Energy Mater Sol. Cells*, vol. 159, p. 227–234, 2017.

[202] S. Dahbi, N. Tahiri, O. El Bounagui and H. Ez-Zahraouy, «Importance of spin-orbit coupling on photovoltaic properties of Pb-free vacancy ordered double perovskites halides X_2TeY_6 (X = Cs, Rb, and Y = I, Br, Cl): first-principles calculations», *Int. J. Energy Res*, vol. 46, p. 8433-8442, 2022.

[203] Y. Bouhadda, M. Bououdina, N. Fenineche and Y. Boudouma, «Elastic properties of perovskite-type hydride NaMgH3 for hydrogen storage», *Int. J. Hydrog. Energy*, vol. 38, p. 1484-1489, 2013.

[204] B. Rehmat et al., «Elastic properties of perovskite-type hydrides LiBeH3 and NaBeH3 for hydrogen storage», *Int. J. Hydrog. Energy*, vol. 42, p. 10038-10046, 2017.

[205] S. A. Khandy, I. Islam, K. Kaur, A. Nazir and A. Laref, «Electronic structure, magnetism and elastic properties of inverse perovskite carbide: A first principles study», *Phys. B: Condens. Matter*, vol. 578, p. 411839, 2020.

[206] Y. Liu, G. Xu, C. Song, Z. Ren, G. Han and Y. Zheng, «First-principles study of elastic properties in perovskite PbTiO3», *Mater. Sci. Eng. A*, vol. 472, p. 269–272, 2018.

[207] S. A. Khandy and D. C. Gupta, «Structural, elastic and thermo-electronic properties of paramagnetic perovskite PbTaO3», *RSC Adv*, vol. 6, p. 48009-48015, 2016.

[208] Kai Li at al., «Electronic structures and elastic properties of a family of metal-free perovskites», Mater. Chem. Front, vol. 3, p.1678, 2019.

[209] M. Born ,«On the stability of crystal lattices. I», Math. Proc. *Cambridge Philos*, vol. 36, p. 160-172, 1940.

[210] S. A. Khandy et al., «DFT investigations on the electronic structure, magnetism, thermodynamic and elastic properties of newly predicted cobalt based antiperovskites: Co3XN (X = Pd, Pt & Rh) », *Results Phys*, vol. 17, p.103112, 2020.

[211] L.Boumia et al., «Structural, electronic and magnetic properties of new full Heusler alloys Rh2CrZ (Z = Al, Ga, In): First-principles calculations», *Chin. J. Phys*, vol. 59, p. 281-290, 2019.

[212] K. Haddadi, A. Bouhemadou_, L. Louail and Y. Medkour, «Structural, elastic and electronic properties of XNCa3 (X= Ge, Sn and Pb) compounds», *Solid State Commun*, vol.149, p. 619-624, 2009.

[213] Y. Mochizuki, Ha-Jun Sung, A. Takahashi, Y. Kumagai, and F. Oba, «Theoretical exploration of mixed-anion antiperovskite semiconductors M3XN (M = Mg, Ca, Sr, Ba; X = P, As, Sb, Bi) », *Phys. Rev. Mater*, vol. 4, p. 044601, 2020.

[214] Heng-Rui Liu, S. Chen, Ying-Teng Zhai, H. J. Xiang, X. G. Gong, and Su-Huai Wei, «First-principles study on the effective masses of zinc-blend-derived Cu2Zn-IV-VI4 (IV=Sn, Ge, Si and VI=S, Se) », *Int. J. Appl. Phys*, vol. 112, p. 093717, 2012.

[215] M.R. Ashwin Kishore, and Ponniah Ravindran, «Tailoring the Electronic Band Gap and Band Edge Positions in C2N Monolayer by P and As Substitution for Photocatalytic Water Splitting», *J. Phys. Chem. C*, vol. 121, p. 22216–22224, 2017.

[216] T. L. Bahers, M. Rérat, and P. Sautet, «Semiconductors Used in Photovoltaic and Photocatalytic Devices: Assessing Fundamental Properties from DFT», *J. Phys. Chem. C*, vol. 118, p. 5997–6008, 2014.

[217] W. Setyawan, R. M. Gaume, S. Lam, R. S. Feigelson, and S. Curtarolo, «High-Throughput Combinatorial Database of Electronic Band Structures for Inorganic Scintillator Materials», *ACS Comb. Sci*, vol. 13, p. 382–390, 2011.

Abstract

In the framework of this Ph.D. thesis, first-principle calculations based on the density functional theory is employed to reveal and fully understand structures and physical properties of simple, double and inverse perovskites nanomaterials. In this context, tree different applications are considered: absorbing materials for photovoltaic application, semiconductor for photocatalytic water splitting and thermoelectric applications. The first part of this thesis deals with simulating structural, electronic and optical properties of non-toxic zirconate perovskites $AZrO_3$ (A = Ca, Ba and Sr) doped with chalcogens impurities. And it was found that the wide forbidden band decreases with the increase of chalcogens' concentration, especially for Tellurium and Selenium doped $AZrO_3$. In the second part, the effects of Sulfur, Selenium, or Tellurium doped $CaZrO_3$, $CaHfO_3$ and $SrHfO_3$ on the electronic, optical and photocatalytic properties and structures stability with the presence of the intrinsic F-center defect in oxide materials were carried out. The findings show that there is a huge improvement of the absorption coefficient along the visible spectrum when chalcogens' impurities meet an F-center defect in understudy compounds due to the enhancement of carrier concentrations. The third part investigates the spin orbit coupling effects on physical properties of the non-toxic Lead-free vacancy ordered double perovskites halides X_2TeY_6 (X = Cs, Rb, and Y = I, Br, Cl) using first-principles calculations. The results confirm that the inclusion of spin orbit coupling is crucial for the correct characterization of the electronic properties of the X_2TeY_6 compound. The final part projects a detailed information on physical properties of Ca_3PN, Ca_3AsN, Ca_3SbN and Ca_3BiN inverse perovskites.

Keywords: Non-silicon-based compounds, Solar cells, DFT, Perovskites compounds, Absorption coefficient, Ab-initio simulations, Stability, Forbidden band gap.

Résumé

Dans le cadre de cette thèse, les calculs de premier principe basés sur la théorie de la fonctionnelle de la densité sont utilisés pour révéler et comprendre les structures et les propriétés physiques des nanomatériaux pérovskites simples, doubles et inverses. Dans ce contexte, trois applications différentes sont envisagées : les matériaux absorbants pour l'application photovoltaïque et les semi-conducteurs pour les applications photocatalyse pour la séparation de l'eau pour la production d'hydrogène et la thermoélectricité. La première partie de cette thèse porte sur la simulation des propriétés structurales, électroniques et optiques des pérovskites zirconates $AZrO_3$ (A = Ca, Ba et Sr) dopées par les éléments de chalcogènes. Et il a été constaté que la large bande interdite diminue avec l'augmentation de la concentration des chalcogènes, en particulier pour l'$AZrO_3$ dopé par tellure ou par sélénium. Dans la deuxième partie, les effets des $CaZrO_3$, $CaHfO_3$ et $SrHfO_3$ dopés par le soufre, sélénium ou tellure sur les propriétés électroniques, optiques et photocatalyse et la stabilité de ces structures avec la présence d'une lacune d'oxygène dans les matériaux oxydes ont été étudiés. Les résultats montrent qu'il y a une énorme amélioration du coefficient d'absorption le long du spectre visible lorsque les impuretés des chalcogènes rencontrent les lacunes d'oxygène grâce à l'amélioration des concentrations de porteurs de charges (trou et/ou électron). Dans la troisième partie de cette thèse, nous avons étudié les effets du spin-orbite sur les propriétés physiques des doubles halogénures pérovskites type X_2TeY_6 (X = Cs, Rb et Y = I, Br, Cl). Les résultats confirment que l'inclusion du spin-orbite est cruciale pour la caractérisation correcte des propriétés électroniques du composé X_2TeY_6. La dernière partie projette une information détaillée sur les propriétés physiques des pérovskites inverses Ca_3PN, Ca_3AsN, Ca_3SbN et Ca_3BiN.

Mots clés : Composés sans silicium, Cellules solaires, DFT, Composés pérovskites, Coefficient d'absorption, Simulations ab-initio, Stabilité, Bande interdite.

✉ Faculté des Sciences, avenue Ibn Battouta, BP. 1014 RP, Rabat –Maroc
☎ 00212(0) 5 37 77 18 76 🖷 00212(0) 5 37 77 42 61 ; http://www.um5a.ac.ma